FINAL TECHNICAL REPORT

September 1994

DTIC
ELECTE
FEB 17 1995
S
G
D

INNOVATIVE PROCESSING
OF
COMPOSITES FOR ULTRA-HIGH
TEMPERATURE APPLICATIONS

CLEARED
FOR OPEN PUBLICATION

by

JAN 31 1995   6

DIRECTORATE FOR FREEDOM OF INFORMATION
AND SECURITY REVIEW (OASD-PA)
DEPARTMENT OF DEFENSE

Reza Abbaschian
Department of Materials Science and Engineering
University of Florida
Gainesville, Florida

19950207 057

BOOK II of IV

DTIS

Executive Summary

The overall objective of this program was to provide a fundamental understanding of the processing science and technology necessary to fabricate ceramic-matrix, intermetallic-matrix, and metal-matrix composites with superior mechanical properties in high temperature and oxidizing environments. The composites are intended for use as structural materials for advanced aerospace applications at temperatures exceeding 1200°C (2200°F).

In order to accomplish the program objective, interactive research groups were established in three key areas of (a) Fiber Fabrication, (b) Coatings and Infiltration, and (c) Composite Fabrication. The objective of the fiber fabrication group was to develop new fibers which have superior strength and toughness at high temperatures and in oxidizing environments. The research effort focused on the development of two types of fibers: (1) glass-free mullite-based fibers, and (2) oxygen-free silicon carbide fibers. The coatings program had two primary objectives: (1) to control the characteristics of matrix/reinforcing phase interfaces (e.g., to control chemical reactions and bonding at a matrix/fiber interface) and (2) to develop coatings that will improve the oxidation resistance of metal-matrix and intermetallic-matrix composites. Coatings methods utilized included chemical vapor deposition, sol-gel processing, and solution coating with polymeric precursors to ceramics.

The composite fabrication group investigated various methods to incorporate reinforcing phases (i.e., fibers, whiskers, and particulates) into ceramic-, metal-, and intermetallic-matrices. Processing methods investigated included colloidal processing, chemical vapor infiltration, reactive hot-compaction and *in situ* coating, and microwave sintering. The objectives were not only to utilize innovative processing techniques, but also to develop and improved scientific understanding of processing-microstructure relationships in composites fabrication.

This annual report consists of seven sections compiled in four books as described below:

BOOK I

Section 1	Processing and Properties of Silicon Carbide Fibers
	Principal Investigators: C.D. Batich
	M.D. Sacks
Section 2	Processing of Mullite Composite Fibers
	Principal Investigators: J.H. Simmons
	M.D. Sacks
	A.B. Brennan
Section 3	Chemical Vapor Deposition (CVD) and Chemical Vapor Infiltration (CVI)
	Principal Investigator: T.J. Anderson

BOOK II

BOOK III

BOOK IV

BOOK II

Section 1

Processing and Properties

of

Intermetallic Matrix Composites

Principal Investigator: **R. Abbaschian**

Development of Intermetallic Matrix Composites

Principal Investigator: Reza Abbaschian

Objectives

The overall objectives of this program are:

(1)   To develop processing techniques for *in-situ* formation of intermetallic-matrix composites and various reinforcement coating formation methods for the stability of the composites.

(2)   To develop intermetallic-matrix composites with properties suitable for structural applications above 1200°C.

These objectives were pursued through the investigation on three classes of intermetallics, (1) molybdenum disilicide ($MoSi_2$), (2) Nb-base aluminides with the major focus on $NbAl_3$, and (3) Ni-base aluminides with the major focus on NiAl.

Background and Approach

The development of intermetallic-matrix composites is motivated by their inherent useful properties such as excellent oxidation resistance, high melting points and relatively low densities. It is expected that their inherent advantages can be effectively utilized via artificial compositing, targeted specifically to overcome their disadvantages, i.e., poor fracture toughness (~ 1 - 3 $MPa,m^{1/2}$) at ambient temperature and low creep resistance and strength at high temperatures. The approaches used are to improve fracture toughness via ductile phase toughening, and to increase the creep resistance and strength via high strength reinforcements such as alumina.

The present investigation has been carried out in four stages: (1) Developing a coating technique to prevent the deleterious interactions between ductile reinforcements and the brittle matrices and to maintain the integrity of the reinforcements. Different coating techniques have been used for different matrices because of their different chemical properties; (2) *In-situ* formation of intermetallic-matrix composites through reactive hot compaction (RHC), as exemplified using Nb-base aluminide composites; (3) Evaluating the effects of size,

morphology and orientation of ductile phases, and the matrix/ductile reinforcement interface on the toughness of the composites, modeling these effects, and providing guidelines for the design of ductile-phase-reinforced composites. The evaluation of ductile-phase-toughening is only carried out in $MoSi_2$ matrix composites but it is believed that the general rules disclosed would also be suitable for other ductile-phase-toughened brittle matrix composites; (4) Developing a reactive processing technique to form nickel aluminide microcomposites containing *in-situ* alumina reinforcements.

The specific results are summarized below, with additional information provided in the listed references and/or the attached publications.

Research Summary

1. MoSi₂ Matrix Composites

1.1 Owing to the projected use temperatures, the suitable ductile reinforcements are limited to the refractory metals, notably W, Ta, Mo and Nb. Niobium has been chosen as a ductile reinforcement in the present study because its thermal expansion coefficient is closest to that of $MoSi_2$, and it also has a relatively low density. For controlling the matrix/reinforcement interaction, chemical compatibilities of various potential coating materials (mullite, Al_2O_3, and ZrO_2) with $MoSi_2$ and Nb were studied via microstructural and compositional analyses [1,2]. Based on these analyses, Al_2O_3 was chosen as the final diffusion barrier coating because it is chemically compatible with both $MoSi_2$ and Nb, and it also has a thermal expansion coefficient close to those of both the matrix and reinforcement.

1.2 The techniques investigated to produce Al_2O_3 coating on Nb surface included (1) sol-gel processing; (2) physical vapor deposition; (3) hot dipping the reinforcement in molten aluminum, followed by anodizing Al to form Al_2O_3. The process control parameters for the techniques and the effectiveness of the coatings as a diffusion barrier were evaluated [3]. The results indicated that a thick and dense Al_2O_3 coating is necessary and effective in eliminating the interactions between Nb and the matrix of commercially pure $MoSi_2$. The results also showed that the best coating is provided with physical vapor deposition, followed by sol-gel technique. The main drawback of the latter technique was shrinkage of the coating during

drying and sintering of the gel.

1.3   A coating technique has been developed which is the combination of sol-gel coating with solid particle addition to co-deposit sol-derived colloids and fine particles to form a dense and continuous diffusion barrier for matrix/reinforcement interfaces [4]. In this process the gel derived from the sol acts as binder for the fine particles, while the fine particles reduce the shrinkage of the sol-gel and promote the formation of dense coatings. The technique has been applied to $MoSi_2$/Nb, $MoSi_2$/Ta, NiAl/Nb, and NiAl/Ta composite systems with a substantial improvement over the sol-gel coating technique. The developed coating technique also has a potential to be a continuous process.

1.4   A sandwich-type chevron-notched specimen was used to characterize the fracture energy of the interfaces in composites [5]. The specimen of this kind combines the advantages from both sandwich test specimens and chevron-notched specimens, and therefore, provides an easy and accurate test for the measurement of interfacial fracture energy. The specimen geometry has been successfully used in Al_2O_3/Nb and $MoSi_2$/Nb systems with coatings and without coatings to explore the effects of chemistry on the bond strength at the interfaces [5-8]. The main conclusions from these tests are: (1) A strong bond can be formed between two chemically compatible materials, such as the Al_2O_3/Nb interface; (2) The bond strength between chemically compatible materials is usually weaker than that between two reactive materials, such as Al_2O_3/Nb interface vs Al_2O_3/NbO interface; (3) The order of the bond strength between Al_2O_3 and intermetallics or metals might be predicted by the reactivities of the elements involved with Al_2O_3; and (4) The bond strength between a metal and an intermetallic is higher than that between an oxide and an intermetallic.

1.5   Effects of the matrix/reinforcement interface, the mechanical properties and size of the ductile phase on the flow behavior of constrained ductile phase were evaluated [9-12]. Based on the observations from the tensile tests, an approximate model was proposed which gave insight into the influence of yield strength, work hardening, matrix/reinforcement interfacial bonding strength and size of the ductile reinforcement on the flow behavior. The flow behavior of the constrained ductile phases was related to the fracture toughness of

composites via small-scale-bridging model. The major conclusions are: toughness of the composites is enhanced by a relatively weak bond at the matrix/reinforcement interface, by large size of ductile reinforcements, and by a ductile phase with a high yield strength and high work hardening rate [10-12]. The stress-displacement function has also been generated to calculate the bridging stress across the crack surface in a large-scale-bridging model proposed in the present study [13].

1.6   The role of the matrix/reinforcement interface in the fracture toughness of $MoSi_2/Nb$ composites has been assessed via four-point bend tests on chevron notched specimens [7]. Variation of the interfacial bonding was obtained by depositing different oxide coatings (Al_2O_3 and ZrO_2) or by the development of a reaction product layer between the matrix and reinforcement. Measurement of fracture energy (bond toughness) of the interfaces was carried out using the newly-developed sandwich-type chevron notched specimens [5-7]. It has been established that whether or not a strong interfacial bonding is conducive to toughness depends on the criterion used to describe the toughness of the composites [7], a finding which is in agreement with the prediction of the large-scale-bridging model developed in the present study [13].

1.7   Four-point bend test has also been used to evaluate the effects of the size, morphology and orientation of ductile laminae on the toughness of the composites [14,15]. The tests revealed that (1) toughness of the composites increased with increasing size of Nb laminae [14]; (2) both Nb fibers and laminae offer similar toughening capabilities, i.e., fracture toughness has been increased to about 14 MPa,m$^{1/2}$ from 3 MPa,m$^{1/2}$ for unreinforced matrix [15], suggesting that the bridging contribution of the ductile fibers and laminae are very similar; and (3) ductile laminae offered two dimensional toughening, while fibers only provided one-dimensional toughening [14]. The similar toughness of the fiber- and lamina-reinforced composites has a bearing on the design of ductile-phase-toughened composites, that is, ductile laminae can provide better toughening characteristics than ductile fibers.

1.8   The toughness evaluations and examination of the interaction of cracks with ductile reinforcements indicated that (1) ductile phase toughening involved large-scale bridging,

i.e., the bridging-length was at the same magnitude as the crack length, the specimen size or the distance from the crack to the specimen boundaries [2,16]; and (2) the toughening of brittle matrix with ductile phase could be described by the equilibrium stress distribution across the crack surface [14]. A general approach has been proposed to compute the ductile phase toughening in the case of large-scale-bridging [13]. The approach, which allowed for the prediction of the typical R-curve behaviors of ductile-phase-toughened composites, encompassed the effects of the bonding strength of the matrix/reinforcement interface, the size of ductile phases, and the intrinsic mechanical properties of the reinforcement and matrix. The main conclusions from this model are as follows: (1) A weak interface would be desirable if cracks concerned are long, whereas a strong interface would be beneficial if the cracks are short; (2) Large sizes of ductile phases are more capable of toughening when cracks are large, while composites with small sizes of ductile phases have a higher fracture stress when the cracks are small; and (3) Toughness increases with increasing yield strength, elastic modulus and work hardening rate of ductile phases. However, yield strength and elastic modulus are more effective in enhancing toughness than work hardening rate when cracks are small, while the work hardening rate provides a larger toughening after extensive crack propagation.

1.9   Incorporation of SiC whiskers into MoSi2 matrix has been accomplished via tape casting technique. The motivation of using this technique was that the orientation of SiC whiskers could be controlled by the stacking orientation of the tapes with different compositions and thickness.   Thus, laminates could be custom designed to yield desired properties. A slip formulation (organic solvent, dispersants and binders) for tape casting $MoSi_2/SiC$ suspension has been developed [17]. The formulation not only enhanced the uniform distribution of SiC-whiskers in $MoSi_2$ matrix, but also had a very low binder burnout temperature (< 300°C).   The latter was greatly helpful, in reducing oxygen contamination during processing.   Composites containing 30 vol.% SiCw made from these tapes have exhibited a substantial improvement in the strength and toughness. The flexural strength and toughness of $MoSi_2$ composites increased from 328 ± 65 to 650 ± 44 MPa and from 3.3 ± 0.2 to 5.0 ± 0.4 MPa,m$^{1/2}$, respectively [18].

1.10   Effects of ductile reinforcements on the stiffness and strength of the composites

have been evaluated using MoSi2/Nb laminates [19]. The results suggested that toughening by a ductile phase with a lower elastic modulus than that of the matrix would cause a decrease in the strength of the composites [19]. To overcome this drawback, a dual compositing approach to improve the strength and toughness of simultaneously has been proposed and confirmed with $MoSi_2$/SiC/Nb system [20]. For example, $MoSi_2$ reinforced with 20 vol.% Nb laminae exhibited a decrease in flexural strength from 328 ± 65 MPa for monolithic $MoSi_2$ to 286 ± 53 MPa for the composite, while the toughness had been increased from 3.3 ± 0.2 to ~ 14 MPa,m$^{1/2}$. Using the dual-reinforcement approach, the flexural strength of $MoSi_2$ composites with 30 vol.% SiCp and 20 vol.% Nb laminae had been improved to 480 ± 46 MPa, while still maintaining toughness at 14 MPa,m$^{1/2}$. The underlying principles for such simultaneous improvements in both strength and toughness are the control of the thermal expansion coefficient of the matrix and at the same time the improvement of the strength with SiCp addition. It is expected that if SiC whiskers are used, the strength would be further improved while still maintaining the high toughness of the composites.

1.11   To further improve the properties of $MoSi_2$ composites, especially the high temperature properties, the source of SiO_2 contamination in $MoSi_2$ has been investigated. [21]. The results showed that the exposure of clean molybdenum disilicide to the air at ambient temperatures for just a few minutes led to the formation of SiO_2 and MoO_2, and this oxidation would continue until the entire surface of $MoSi_2$ was covered by a duplex oxide layer of SiO_2 + MoO_3. This result clearly indicates that the oxidation of $MoSi_2$ occurs even at room temperatures, thus imposing a challenge for eliminating SiO_2 in $MoSi_2$ composites.

2. NbAl$_3$ Matrix Composites

2.1   Reactive hot compaction (RHC) has been successfully utilized to produce NbAl$_3$ matrix with close to 100% theoretical density at relatively low processing temperatures of around 1300°C. The effects of process control parameters such as ratio of the elemental Nb and Al powders, particle size, and heating rate, on the microstructure of NbAl$_3$ matrix have been evaluated [22,23]. By controlling the initial stoichiometry, NbAl$_3$ matrix composites containing a dispersion of Nb$_2$Al or Nb$_3$Al particles with a niobium core has been produced via RHC. The fracture toughness of the composites has been determined to be 3.5 MPa,m$^{1/2}$,

compared with 1.9 MPa,m$^{1/2}$ for the monolithic matrix [22,23]. The improvement can be attributed to crack deflection and crack bridging.

2.2   In order to further improve the fracture toughness of NbAl$_3$, refractory metal reinforcement, Nb, has been incorporated into the matrix during RHC process. To prevent the interactions between the ductile reinforcement and the matrix, an alumina coating is produced *in-situ* during RHC process. The detailed procedures for producing in situ alumina coating is provided in Patent 1. Briefly, it involved pre-oxidizing Nb filaments to form Nb$_2$O$_5$ scale, and converting the Nb$_2$O$_5$ scale into Al$_2$O$_3$ layer at the matrix/reinforcement interface via an interface reaction during the subsequent RHC process. The coating thickness was varied from 3 to 8 μm by changing the oxidation time of the Nb filaments. Long term annealing at 1200°C indicated that the *in-situ* Al$_2$O$_3$ coating was stable and effective in suppressing the interactions between the matrix and ductile reinforcement [24].

2.3   Fracture toughness of 20 vol.% Nb-reinforced NbAl$_3$ composites was measured to be 9.4 MPa,m$^{1/2}$, five times higher than the matrix. Fracture surface analysis indicated that partial decohesion had occurred at the matrix/filament interface allowing the Nb filaments to fail in a ductile manner. The *in-situ* Al$_2$O$_3$ coating, therefore, not only acts as an effective diffusion barrier, but also imparts a desirable interfacial strength to allow for a limited debonding at the interface [24].

3. NiAl Matrix Microcomposites

A process has been developed to produce (Al$_2$O$_3$) reinforcements *in-situ* in nickel aluminide [25,26]. The process involved reactively hot pressing of pretreated elemental nickel and aluminum powders to form an interconnected network of Al$_2$O$_3$ and an interpenetrating NiAl matrix.   Four-point bend tests of chevron-notched specimens indicate a substantial increase in room temperature fracture toughness with volume fraction of alumina up to a peek of 14 MPa√m at 18 volume percent, followed by a slight drop-off at 25 volume percent, the highest level in the study.

The reaction sequence was studied via differential thermal analysis (DTA) and by

interrupting the process at various points throughout the cycle. The elemental powders were found to form NiAl at temperatures will below the melting temperature of aluminum. However, when oxidized powders were reacted, the aluminum melted prior to the initiation of intermetallic-formation reaction which was delayed until 880°C. It was found that reacting the oxidized powders under pressure reverted the initiation of the intermetallic-formation reaction to below the melting temperature of aluminum.

The low-temperature reaction was found to result in the development of a three dimensional network of interconnected Al_2O_3 reinforcements in a NiAl matrix. Oxidizing the Al powders prior to hot pressing resulted in the formation of a rod-like network of alumina, while oxidizing the Ni powders produced a tubular alumina network. The oxidation of aluminum was determined to be the critical step for the development of the proper alumina morphology and interfacial properties necessary to improve the fracture toughness. Specifically, the relative humidity in the oxidizing atmosphere controlled spallation from the Al powders, reducing the occurrence of isolate alumina inclusions in the matrix, especially with weak $NiAl-Al_2O_3$ interfaces, which were found to severely degrade fracture toughness.

A physical model is presented which describes the effect of oxidation pretreatment on the reaction and the resultant alumina morphology. In addition, the role of pretreatment in controlling bonding at the $NiAl-Al_2O_3$ interface was shown to result in composites with improved room temperature fracture toughness.

Publications

1.   L. Xiao, Y. S. Kim and R. Abbaschian, "Ductile Phase Toughening of $MoSi_2$ - Chemical Compatibility and Fracture Toughness," in Intermetallic Matrix Composites, edited by D. L. Anton, P. L. Martin, D. B. Miracle and R. McMeeking, Proc. MRS Meeting, 1990, vol. 194, pp. 399-404.

2.   L. Xiao, Y. S. Kim, R. Abbaschian and R. J. Hecht, "Processing and Mechanical Properties of Nb Reinforced $MoSi_2$ Composites", Mater. Sci. Eng., 1991, vol. A144, pp. 277-85.

3.   L. Shaw and R. Abbaschian, "Control of the Interfacial Reactions in Nb Reinforced $MoSi_2$ Composites", J. Am. Ceram. Soc., 1993, vol. 76, pp. 2305-11.

4. L. Shaw and R. Abbaschian, Solid Particle Addition in Sol-Gel Coatings --- The Formation of Al_2O_3 Coatings as Diffusion Barriers between Ductile Reinforcements and Brittle Matrices, submitted to J. Am. Ceram. Soc.

5. L. Shaw and R. Abbaschian, A Test Specimen for Characterizing the Fracture Energy of Interfaces in Composites, in Control of Interfaces in Metal and Ceramic Composites, edited by R. Y. Lin and S. G. Fishman, 1993, pp. 211-223.

6. L. Shaw and R. Abbaschian, "Microstructure and Mechanical Properties of Metal/Oxide and Metal/Siliside Interfaces", submitted to Acta Metall. Mater.

7. L. Xiao and R. Abbaschian, "The Role of Matrix/Reinforcement Interfaces in the Fracture Toughness of Ductile Phase Reinforced $MoSi_2$ Composites", Metall. Trans., 1992, vol. 23A(10).

8. L. Xiao and R. Abbaschian, "Micorstructure and Properties of $MoSi_2$/Nb Interfaces with and without Alumina Coating", in Structure and Properties of Interfaces in Materials, MRS Symp. Proc., 1992, vol. 238, pp. 567-573.

9. L. Xiao and R. Abbaschian, "Evaluating a Technique for Determining the Toughening of Brittle Matrix by Ductile Reinforcements", in Advanced Metal-Matrix Composites for Elevated Temperatures, edited by M. N. Gungor, E. J. Lavernia and S. G. Fishman, (ASM International, 1991), pp. 33-40.

10. L. Xiao and R. Abbaschian, "On the Flow Behavior of Constrained Ductile Phases", winner of the 1992 ASM International Graduate Student Paper Contest, Metall. Trans., 1993, vol. 24A, pp. 403-415.

11. L. Xiao, "Study of the Flow Behavior of Constrained Ductile Phases ----- I. Experiment", in Developments in Ceramic- and Metal-Matrix Composites, edited by K. Upadhya, (A Publication of TMS, 1992), pp. 115-124.

12. L. Xiao, "Study of the Flow Behavior of Constrained Ductile Phases ----- II. Modeling", in Developments in Ceramic- and Metal-Matrix Composites, edited by K. Upadhya, (A Publication of TMS, 1992), pp. 359-369.

13. L. Shaw and R. Abbaschian, "Ductile Phase Toughening ---- Large Scale Bridging", in preparation.

14. L. Shaw and R. Abbaschian, "Toughening $MoSi_2$ with Niobium Metal - Effects of Size and Orientation of Ductile Reinforcement", Acta Metall. Mater., 1994, vol. 42, pp. 213-223.

15. L. Shaw and R. Abbaschian, "Toughening $MoSi_2$ with Niobium Metal - Effects of Morphology of Ductile Reinforcement", submitted to J. Mater. Sci.

16. L. Xiao and R. Abbaschian, "Interfacial Modification in $Nb/MoSi_2$ Composites and its Effects on Fracture Toughness", Mater. Sci. Eng., 1992, vol. A155, pp.135-145.

17. L. Shaw and R. Abbaschian, Fabrication of SiC-Whisker-Reinforced $MoSi_2$ Composites by Tape Casting, submitted to J. Am. Ceram. Soc.

18. L. Shaw and R. Abbaschian, "Mechanical Properties of SiC-Reinforced $MoSi_2$ Composites", in preparation.

19. L. Xiao and R. Abbaschian, "On the Strength and Stiffness of Ductile Phase Reinforced $MoSi_2$ Composites", in Advanced Metal-Matrix Composites for Elevated Temperatures, edited by M. N. Gungor, E. J. Lavernia and S. G. Fishman, (ASM International, 1991), pp. 21-31.

20. L. Shaw and R. Abbaschian, "Toughening and Strengthening of $MoSi_2$ with Dual Reinforcements", in preparation.

21. L. Shaw and R. Abbaschian, "Chemical States of Molybdenum Disilicide ($MoSi_2$) Surfaces, submitted to J. Am. Ceram. Soc.

22. L. Lu, Y. S. Kim, A. B. Gokhale and R. Abbaschian, "Reactive Synthesis of $NbAl_3$ Matrix Composites", in Intermetallic Matrix Composites, edited by D. L. Anton, P. L. Martin, D. B. Miracle and R. McMeeking, Proc. MRS Meeting, 1990, vol. 194, pp. 79-87 .

23. L. Lu, A. B. Gokhale, M. J. Kaufman and R. Abbaschian, " Niobium Aluminide Matrix Composites Produced by the Reactive Hot Compaction of Elemental Powders", in Powder Metallurgy: Key to Advanced Materials Technology, edited by, ASM International, 1990, pp. 32-36.

24. L. Lu, A. B. Gokhale and R. Abbaschian, "*In-situ* Formation of an Alumina Interface Coating in Reactively Synthesized $NbAl_3$-Nb Composites", Mater. Sci. Eng., 1991, vol. A144, pp. 11-23.

25. H. Doty, "Reactive Processing to Form *In-Situ* Nickel Aluminide Microcomposites," PhD Dissertation, University of Florida, 1994.

26. H. Doty, M. Somerday and R. Abbaschian, "The Application of Reactive Hot Compaction and *In-Situ* Coating Techniques to Intermetallic Matrix Composites," MRS Symposium Proceedings, Vol. 322, 1994, pp. 87-105.

Patents
1. L. Lu, A. B. Gokhale and R. Abbaschian, "An 'In-Situ' Coating Process of Reinforcements Used in Reactively Synthesized Metal, Intermetallic, and Ceramic Matrix Composites", 1991, patent disclosure.

Copies of papers 2, 3, 5, 7, 8, 9, 10, 11, 12, 14, 16 and 24 are attached.

A TEST SPECIMEN FOR CHARACTERIZING THE FRACTURE ENERGY OF

INTERFACES IN COMPOSITES

Leon Shaw[1] and Reza Abbaschian[2]

[1] Systran Corporation, Dayton, OH 45432
[2] Department of Materials Science and Engineering, University of Florida, Gainesville, FL 32611

Abstract

A sandwich-type chevron-notched specimen, which has a phase angle of loading near zero, is proposed to measure interfacial fracture energy arising mainly from chemical bonding. With the specimen configuration of this kind, the advantages from both sandwich test specimens and chevron-notched specimens can be combined to provide an easy and accurate test for the measurement of interfacial fracture energy. The validity of the specimen has been analyzed in terms of the mechanics of sandwich-type specimens and chevron-notched specimens, and demonstrated using the Al_2O_3/Nb bimaterial system. The results shows that for a phase angle of loading around -7 degree the Al_2O_3/Nb interface has an fracture energy of 9.3 ± 0.2 J/m^2.

Introduction

To obtain a high transverse loading on composites, a high interface strength is required, while this is in conflict with the toughening through the interface debonding As such, optimal interface properties between dissimilar materials are desirable for an optimal performance of composites in structural applications [1] Interfacial properties are also important for glass/metal, ceramic/metal, ceramic/ceramic seals and microelectronic components [2] Therefore, the measurement of strength and crack growth resistance at the interface between dissimilar materials is crucial for the design and quality control of dissimilar material components.

Measurement of interfacial fracture energy is much more involved than measurement of fracture energy of homogeneous materials due to the different elastic properties of the two materials at the interface. Interface crack tips usually experience both shear and normal stresses even when the external loading is pure tension or shear [3,4]. For example, for a plane strain interface crack, the stress and displacement fields at the crack tips can be fully characterized by a complex stress intensity factor, K, in which tensile and shear effects near the crack tip are intrinsically coupled and cannot be separated into classical mode I and mode II conditions [4]. Analyses of the mechanics of an elastic interface crack have further indicated that (i) the mixed tension and shear fields at the crack tip are not only inherently coupled, but also are oscillating, leading to crack surface interpenetration [4-6], (ii) the relative proportion of shear to normal stresses on the interface directly ahead of the crack tip depends on elastic mismatch across the interface, crack length, distance of the interface from the tip, and even units used for the complex stress intensity factor [4], and (iii) the tip fields are governed by two bimaterial elastic parameters, i.e., the Dundurs' parameters [7]

$$\alpha = \frac{\mu_1 (1-\upsilon_2) - \mu_2 (1-\upsilon_1)}{\mu_1 (1-\upsilon_2) + \mu_2 (1-\upsilon_1)}$$

$$\beta = \frac{\mu_1 (1-2\upsilon_2) - \mu_2 (1-2\upsilon_1)}{2\{\mu_1 (1-\upsilon_2) + \mu_2 (1-\upsilon_1)\}} \tag{1}$$

where μ is the shear modulus, υ is Poisson's ratio and the subscripts 1 and 2 refer to the two materials. Roughly speaking, the absolute value of α is an indication of the degree of difference in stiffness between materials 1 and 2. The larger the absolute value of α, the bigger the difference in the stiffnesses of materials 1 and 2. The parameter β is responsible for the oscillatory stress and displacement fields at the crack tip. Another useful parameter is [3]

$$\varepsilon = \frac{1}{2} \pi \ln \left(\frac{1-\beta}{1+\beta} \right) \tag{2}$$

In many interface crack tip stress and displacement equations, ε is used instead of β for convenience. The foregoing three aspects bring out the differences of the interface fracture from ordinary fracture of homogeneous materials. The crack surface interpenetration presents obvious ambiguity in the interface fracture. However, non-zero values of β are small for many bimaterial interfaces of interest. Thus, it has been proposed that a zero-β is used to deal with interface fracture in many cases [8-10]. The inseparability of the complex stress intensity factor and the dependence of the ratio of the shear to normal components of the traction at the crack tips on crack length, distance from the tip and units introduce complexity into the interface fracture. However, ε, which approaches zero when $\beta \rightarrow 0$, is also small for many material combinations

of interest. As such, it is suggested that the change of the degree of mixity of shear to tension at the crack tips with crack length can be neglected for crack propagation within a very broad limit [4]. Furthermore, as a result of small ε, the crack fields at fixed distances away from the tip can be expressed by stress intensity factors of classical type K_I and K_{II} by substituting $K_I + iK_{II}$ for complex $Kr^{i\varepsilon}$ (r is the fixed distance at the interface ahead of the crack tip and can be chosen arbitrarily within very broad limits) [4]. With the above simplifying hypotheses, measurement of interfacial fracture energy can be conducted by neglecting the interpenetration of crack surfaces, and by taking the ratio of the shear to normal components of the traction near the crack tip as constant along the interface and also as constant as crack propagates.

The separation of complex K into K_I and K_{II} allows one to describe the degree of mixity of shear to tension at the tip with the classical stress intensity factors. Thus, the mixed tension and shear fields experienced by the interface crack tip are commonly characterized by the so-called phase angle of loading, ψ, which is the angle with a tangent given by the ratio of mode II to mode I stress intensity factors at the crack tip [4,8]. The calculation of the phase angle of loading on the interface at a fixed distance from the tip can be made with the aid of [10,11]

$$\psi = \tan^{-1}(K_{II}/K_I)$$
$$= \phi + \omega(\alpha,\beta) + \varepsilon \ln(L_2/L_1) \qquad (3)$$

where ϕ is the phase angle of external loading, ω, tabulated in [10], is the shift due to the elastic mismatch across the interface, L_2 and L_1 are two different crack lengths, and the last term in the right hand side of the equation is the shift due to the crack propagation. As mentioned before, β is normally taken as zero, so is ε. Thus, equation 3 is reduced to

$$\psi = \phi + \omega(\alpha, 0) \qquad (4)$$

Therefore, the phase angle of loading at the interface is the sum of the external loading phase and the shift due to the elastic mismatch across the interface. The phase angle is important because it is found that interfacial fracture energy usually increases with the increase of the phase angle ψ [11]. The fracture energy of interfaces at ψ = 0 comes mainly from the chemical bonding, while crack shielding and dissipation from non-linearity of the constituents and non-planarity of the interfaces contribute more and more to the fracture energy as ψ increases [8].

Due to the ψ dependence of interfacial fracture energy and the occurrence of interface fracture at a wide range of ψ in composites, thin films and seals, various test specimens have been devised for characterizing interfacial fracture energy. Each specimen geometry has usually a limited range of phase angles, and therefore is suitable for certain interface fracture measurements. For example, double cantilever beam specimens [12] have a phase angle from about -10^0 to 5^0. Four-point flexure delamination specimens [13] have a phase angle about 50^0. Composite cylinder specimens [14] have phase angles ranging from 70^0 to 90^0. Peel test [15], which measures the coating-substrate interfacial fracture energy and strength, has a negative phase angle (about -50^0). Bimaterial chevron-notched short bars [16], which consist of a joint of two bulk dissimilar materials and a chevron notch along the jointed plane, have phase angles extending from about -10^0 to 5^0. Fiber push-out tests [17], which can also be used to obtain fracture energy data, have a phase angle of about -90^0 for specimens with no residual clamping stresses. With residual clamping stresses, the phase angle would range from -90^0 to more negative angles depending on the clamping stresses. Brazil-nut-sandwich specimens [11], designed for generating the full interfacial toughness curves over a spectrum of phase angles, provide phase angles from about 0^0 to 90^0. A recent tensioned push-out test [18] also gives phase angles from about 0^0 to 90^0. Obviously, various tests have been designed to measure

interfacial fracture energy However, some of these (e g fiber pull-out and push-out tests) are limited to high phase angles of loading, while others (e g four-point flexure delamination specimen) are only capable of large degree of mixed mode loading. Pull-out, push-out and tensioned push-out specimens are also difficult to fabricate and sensitive to residual thermal stresses. Brazil-nut-sandwich specimens are hard to fabricate in composites which require high temperature processing while maintaining or introducing a sharp interface crack at the same time. Bimaterial chevron-notch short bars containing two bulk materials need calibration of the dimensions for each particular pair of the dissimilar materials. Nevertheless, these different tests provide indispensable means for examining interfacial fracture energy from a wide range of phase angles, and afford flexibility in choosing a most suitable test specimen for a particular interface problem.

The present paper is aimed to providing a test specimen which has a nearly-zero phase angle of loading, and therefore is suitable for measuring the toughness mainly from chemical bonding. The proposed geometry is a sandwich-type chevron-notched specimen. As such, the advantages from both sandwich test specimens and chevron-notched specimens are combined to provide an easy and accurate test for the measurement of interfacial fracture energy.

Test Specimen

The test specimen proposed, consisting of a thin sandwich layer (material 2) within an otherwise elastically homogeneous specimen (material 1) with a chevron notch along the sandwich plane, is shown in Figure 1. The groove introduced on the side of the chevron notch tip is for the application of an opening mode external loading via a pair of grips which are not shown in the figure. Instead, a pair of "P" is used to represent the external loading. The thickness of sandwiched layer, h, has to be very small compared with all other in-plane length scales. With a small h, the critical interfacial stress intensity factor, K, can be evaluated from the applied, or apparent, stress intensity factor, K^∞, which is calculated as if the specimen were homogeneous. As such, the previously developed compliance calibrations for chevron-notched specimens made of homogeneous materials can be utilized directly. Theoretical analysis of converting K^∞ into K for sandwich-type specimens has been conducted by Suo and Hutchinson [10]. Briefly, because of the conservation of the J-integral and because the introduction of the thin layer does not disturb the remote K field, the energy release rate at the interface crack tip should be equal to the energy release rate computed using the far field. Based on this argument, the complex stress intensity factor at the interface crack tip field can be shown to be related to the apparent stress intensity factor by [10]

$$K h^{i\varepsilon} = pK^\infty e^{i\omega} \tag{5}$$

where $p = \{(1 - \alpha)/(1 - \beta^2)\}^{1/2}$, and α, β, ε and ω have the same meanings as defined before. For interfaces with very small β and thus ε, β and ε can be taken as zero. Thus, equation 5 becomes [10]

$$K = (1 - \alpha)^{1/2} K^\infty e^{i\omega} \tag{6}$$

Equation 6 indicates that the measurement of the interfacial fracture toughness can be carried out in two steps. First, the applied stress intensity factor, K^∞, is calculated from the critical external loads as if the specimen were homogeneous. Second, equation 6 is used to convert K^∞ into the interfacial stress intensity factor, K. Note that the simplification of equation 5 into 6 also

requires h to be small because β is hardly equal to zero for most interface systems of interest. With small h, the conversion of $K^{x)}$ to K is actually independent of h (see equation 6)

Another quantity to describe the toughness of interface is the energy release rate of the interface, G, which is more straightforward to evaluate than K for sandwich-type specimens. As pointed out before, for a very thin sandwiched layer the energy release rate at the interface crack tip is equal to the energy release rate computed using the far field. Thus, the familiar relation between stress intensity factor and energy release rate,

$$ G = \frac{1 - v_1^2}{E_1} \cdot |K^*|^2 \tag{7} $$

could be used directly to calculate the interfacial fracture energy as if the specimen were made of homogeneous material. However, the phase angle of loading at the interface for the measured interfacial fracture energy is not the external loading phase, but is that calculated from equation 3 or 4.

Measurement of K^{∞} using chevron-notched specimens made of homogeneous material has been an extensive topic in many investigations [19-27]. The unique features of chevron-notched specimens over conventional fracture-toughness specimens are: (i) an extremely high stress concentration at the chevron tip, and (ii) the development of a minimum stress intensity factor as the crack propagates. The high stress concentration at the tip allows the crack to initiate at a low applied load, eliminating the need to fatigue precrack a specimen. The minimum stress intensity factor permits fracture toughness to be evaluated from the maximum load without monitoring the crack length. The basic equation for evaluating fracture toughness from chevron-notched specimens is [23]

$$ K' = \frac{P}{B\sqrt{W}} Y(\frac{a_0}{W}, \frac{a_1}{W}, \frac{a}{W}) \tag{8} $$

where K' is the stress intensity factor at the crack tip, Y is the stress intensity factor coefficient and is a function of crack length, dimension and compliance of the specimen, and P, B, W, a_0, a_1 and a have been defined in Fig. 1. During the early stage of the crack propagation, Y decreases with increasing crack length. Thus, more and more load has to be applied to extend the crack if K^{∞} of the material remains constant. When the crack length, a, reaches a critical value, the Y reaches a minimum Y_{min} and at the same time, the load P reaches a maximum P_{max}. Therefore, K^{∞} can be calculated from

$$ K^* = \frac{P_{max}}{B\sqrt{W}} Y_{min} \tag{9} $$

The minimum value of Y has been predetermined for particular chevron-notched configurations by various techniques including finite element analysis [24,25], boundary element analysis [25], boundary integral method [26], and analytical approaches such as straight-through-crack assumption analysis [19] and Bluhm's slice model [27]. With Y_{min} in hand, K^{∞} can be determined directly from the measurement of the peak load, P_{max}, of the load-displacement curve.

For the sandwich-type chevron-notched specimens, the test can be conducted as if the specimen were made of homogeneous material. Then, the applied stress intensity factor is calculated using equation 9, and the interfacial fracture energy using equation 7. In the following, the application of this type of specimen is demonstrated using the Al_2O_3/Nb system.

After passing through the maximum load, the load suddenly dropped because of rapid specimen fracture. Thus, the maximum loads detected were regarded as valid values for calculating the fracture energy of Al_2O_3 with the aid of equations 9 and 7. The fracture energy measured, G, was 23.1 ± 1.2 J/m^2 (from 6 specimens), or in terms of fracture toughness, K^∞ = 3 0 $MPa.m^{1/2}$. Note that the current results are for the Al_2O_3 with a mean grain diameter of 3 μm after the consolidation, and are comparable with the literature [33-35]. For example, working with different grain sizes of Al_2O_3, Rice et al. [33] found that fracture energies of Al_2O_3 with grain diameters smaller than 10 μm were about 18 J/m^2, whereas Davidge [34] reported a value of 23 J/m^2 for 3 μm grain diameter Al_2O_3. Shannon and Munz [35] found the fracture toughness, K^∞, of Al_2O_3 with a uniform mix of grains 2 to 30 μm in size to be between 3.5 and 4.5 $MPa.m^{1/2}$ depending on the specimen geometry of the chevron notched short bars.

Stable crack propagation at the chevron plane was also supported by the examination of the fracture surface of the Al_2O_3. Typical fracture surfaces of Al_2O_3 at the chevron crack are presented in Figure 3. Higher-magnification photographs shown in Figure 3(b) and (c) were taken from the positions b and c shown in Figure 3(a), respectively. As seen in the figures, intergranular fracture prevailed near the tip of the notch, while transgranular fracture dominated at the bottom of the notch. Between these two positions, a transition of fracture mode was observed. The position dependence of the fracture mode is believed to be related to the characteristics of the crack propagation on the chevron plane. Due to the V-notch geometry and control of the crack propagation by the crosshead speed of the testing machine [27,36], the crack propagates stably near the notch tip, unstably at the bottom of the notch and changing from stably to unstably at the intermediate position. As such, at the notch tip, crack propagation is the slowest and it chooses the low energy path which is the grain boundary for the present matrix, while at the bottom of the notch, crack propagation is too fast to allow for the low energy path, leading to transgranular fracture. Such position dependence of the fracture mode was also observed in chevron-notched $MoSi_2$ specimens [37]. The above discussion clearly indicates that the present testing procedures and specimen dimensions are appropriated for stable crack propagation, and therefore suitable for fracture energy measurement.

Al_2O_3/Nb Interface

A typical load-displacement curve of the Al_2O_3/polished Nb laminate is shown in Figure 4. Again, a stable crack propagation was achieved, as indicated by the fluctuation in the curve near the maximum load. Therefore, the maximum load was used to calculate G with the aid of equations 9 and 7, and a fracture energy of 9.3 ± 0.2 J/m^2 was obtained (for 3 specimens tested). The two corresponding fracture surfaces at the chevron crack are presented in Figure 5. As seen from the figure, the two opposite surfaces match each other with one being concave and the other convex. The composition analysis with energy dispersive spectrometer (EDS) indicated that the fracture surface on the convex side contained only Al_2O_3, while the concave side consisted of only Nb. Thus, it is clear that the crack had propagated right along the interface between Al_2O_3 and Nb.

The phase angle of loading at the crack tip, ψ, for the measured interfacial fracture energy was calculated using equation 4. The $\omega(\alpha, \beta)$ was found from Table 1 in reference [10] with the shear moduli and Poisson's ratios of Al_2O_3 and Nb being 162 GPa and 0.22 [38], and 36.72 GPa and 0.38 [39], respectively. The results showed that ψ = - 7^0 for non-zero β or ψ = - 8^0 for assuming β = 0.

It is interesting to compare the present fracture energy of Al_2O_3/Nb interface with other studies [8,30]. Using a laser spallation technique, Gupta et al [30] found that the fracture energy

of Al_2O_3/Nb interface was 0.0009 J/m^2, while a fracture energy of 80 J/m^2 was obtained by Evans *et al* [8], using a notch-bend test. Both of these interfacial fracture energies were obtained at the condition of a nearly-zero phase angle of loading. However, the low fracture energy value in the laser spallation test has been attributed to the presence of interface flaws [30]. The value obtained in the notch-bend test is much closer to the present result, although a difference exists. The difference may be due to the different processing conditions or due to the notches rather than a sharp pre-crack used in the notch-bend test. Finally, it is noted that the currently measured fracture energy of the Al_2O_3/Nb interface is larger than the work of adhesion for this interface (about 1 J/m^2). This is in agreement with the general observations that fracture energy of interfaces is typically larger than the work of adhesion [8].

Concluding Remarks

A sandwich-type chevron-notched specimen, which has a nearly-zero phase angle of loading, has been proposed to measure interfacial fracture energy arising mainly from chemical bonding. The specimen has been analyzed based on the mechanics of sandwich-type specimens and chevron-notched specimens, and demonstrated using the Al_2O_3/Nb bimaterial system. The main advantages of this specimen are:

(1) It is easy to fabricate (either diffusion or adhesive bonding), and easy to test with no need for fatigue precracking. Thus, the specimen allows the generation of the sizable amount of toughness data at low cost.

(2) No special compliance calibration of specimens is necessary because a large body of previously developed compliance calibrations for homogeneous materials can be utilized directly.

(3) Due to the above characteristics, the specimen provides a quick and accurate testing method for measuring the trend of "chemical bonding" as a function of other material parameters, such as composition, processing conditions, and microstructure at the interface.

References

1. D. Lewis, "Strength and Toughness of Fiber-Reinforce Ceramics and Related Interface Behavior", in Whisker- and Fiber-Toughened Ceramics, edited by R. A. Bradley, D. E. Clark, D. C. Larsen, and J. O. Stiegler, (ASM International, 1988), 265-73.
2. W. H. Kohl, Handbook of Materials and Techniques for Vacuum Devices, (Reinhold, New York, 1967).
3. J. R. Rice and G. C. Sih, "Plane Problems of Cracks in Dissimilar Media", J. Appl. Mech., Transaction ASME, 32 (1965), 418-23.
4. J. R. Rice, "Elastic Fracture Mechanics Concepts for Interfacial Cracks", J. Appl. Mech., 55 (1988), 98-103.
5. M. Comninou, "Interface Crack with Friction in the Contact Zone", J. Appl. Mech., 44 (1977), 780-1.
6. M. Comninou and D. Schmueser, "The Interface Crack in a Combined Tension-Compression and Shear Field", J. Appl. Mech., 46 (1979), 345-8.

7 J Dundurs, "Mathematical Theory of Dislocation", (American Society of Mechanical Engineers, New York, 1969), 70

8 A G Evans, M Ruhle, B J Dalgleish and P G Charalambides, "The Fracture Energy of Bimaterial Interfaces", Mater. Sci. Eng., A126 (1990), 53-64

9 M -Y He and J W Hutchinson, "Kinking of a Crack out of an Interface", J. Appl. Mech., 56 (1989), 270-8

10 Z Suo and J W Hutchinson, "Sandwich Test Specimens for Measuring Interface Crack Toughness", Mater. Sci Eng., A107 (1989), 135-43

11 J -S Wang and Z Suo, "Experimental Determination of Interfacial Toughness Curves using Brazil-Nut-Sandwiches", Acta Metall. Mater., 38 (1990), 1279-90

12 T S Oh, R M Cannon and R O Ritchie, "Subcritical Crack Growth along Ceramic-Metal Interfaces", J. Am. Ceram. Soc., 70 (1987), C-352-C-355.

13 P G Charalambides, J Lund, A G Evans and R. M. McMeeking, "A Test Specimen for Determining the Fracture Resistance of Bimaterial Interfaces", J. Appl. Mech., 56 (1989), 77-82.

14 P. G. Charalambides and A. G. Evans, "Debonding Properties of Residually Stressed Brittle-Matrix Composites", J. Am. Ceram. Soc., 72 (1989), 746-53.

15. N. Aravas, K.-S. Kim and M. J Loukis, "On the Mechanics of Adhesion Testing of Flexible Films", Mater. Sci. Eng., A107 (1989), 159-68.

16. J. J. Mecholsky and L. M. Barker, "A Chevron-Notched Specimen for Fracture Toughness Measurements of Ceramic-Metal Interfaces", in Chevron-Notched Specimens: Testing and Stress Analysis, ASTM STP 855, edited by J H. Underwood, S. W. Freiman and F. I. Baratta, (America Society for Testing and Materials, 1984), 324-36.

17. R. J. Kerans and T. A. Parthasarathy, "Theoretical Analysis of the Fiber Pullout and Pushout Tests", J. Am. Ceram. Soc., 74 (1991), 1585-96.

18. M. C. Watson and T. W. Clyne, "The Tensioned Push-Out Test for Fiber-Matrix Interface Characterization under Mixed Mode Loading", Mater. Sci. Eng., A160 (1993), 1-5.

19. D. G. Munz, J. L. Shannon, Jr., and R. T. Bucey, "Fracture Toughness Calculation from Maximum Load in Four Point Bend Tests of Chevron Notch Specimens", Int. J. Fract., 16 (1980), R137-41.

20. J. C. Newman, Jr., "A Review of Chevron-Notched Fracture Specimens", in Chevron-Notched Specimens: Testing and Stress Analysis, ASTM STP 855, edited by J. H. Underwood, S. W. Freiman and F. I. Baratta, (America Society for Testing and Materials, 1984), 5-31.

21. L. M. Barker and F. I. Baratta, "Comparisons of Fracture Toughness Measurements by the Short Rod and ASTM Standard Method of Test for Plane-Strain Fracture Toughness of Metallic Materials (E 399-78)", J. Testing and Evaluation, 8 (1980), 97-102.

22. D. Munz, "Determination of Fracture Toughness of High Strength Aluminum Alloys with Chevron-Notched Short Rod and Short Bar Specimens", Eng. Fract. Mech., 15 (1981), 231-6.

23. S.-X. Wu, "Compliance and Stress-Intensity Factor of Chevron-Notched Three-Point Bend Specimen" in Chevron-Notched Specimens: Testing and Stress Analysis, ASTM STP 855, edited by J. H. Underwood, S. W. Freiman and F. I. Baratta, (America Society for Testing and Materials, 1984), 176-92.

24. I. S. Raju and J. C. Newman, Jr., "Three-Dimensional Finite-Element Analysis of Chevron-Notched Fracture Specimens" in Chevron-Notched Specimens: Testing and Stress Analysis, ASTM STP 855, edited by J. H. Underwood, S. W. Freiman and

F. I. Baratta, (America Society for Testing and Materials, 1984), 32-48

25. A. R. Ingraffea, R. Perucchio, T. Y. Han, W. H. Gerstle and Y.-P. Huang, "Three-Dimensional Finite and Boundary Element Calibration of the Short-Rod Specimen" in Chevron-Notched Specimens Testing and Stress Analysis, ASTM STP 855, edited by J. H. Underwood, S. W. Freiman and F. I. Baratta, (America Society for Testing and Materials, 1984), 49-68

26. A. Mendelson and L. J. Ghosn, "Three-Dimensional Analysis of Short-Bar Chevron-Notched Specimens by the Boundary Integral Method", in Chevron-Notched Specimens, Testing and Stress Analysis, ASTM STP 855, edited by J. H. Underwood, S. W. Freiman and F. I. Baratta, (America Society for Testing and Materials, 1984), 69-80

27. J. I. Bluhm, "Slice Synthesis of a Three Dimensional 'Work of Fracture' Specimen", Eng. Fract. Mech., 7 (1975), 593-604

28. W. Mader and M. Ruhle, "Electron Microscopy Studies of Defects at Diffusion-Bonded Nb/Al_2O_3 Interfaces", Acta Metall., 37 (1989), 853-66

29. A. G. Evans, M. C. Lu, S. Schmauder and M. Ruhle, "Some Aspects of the Mechanical Strength of Ceramic/Metal Bonded Systems", Acta Metall., 34 (1986), 1643-55.

30. V. Gupta, J. Yuan and D. Martinez, "Calculation, Measurement, and Control of Interface Strength in Composites", J. Am. Ceram. Soc., 76 (1993), 305-15

31. C. Wang, M. Yuan and T. Chen, "An Investigation of on the Method for Determination of Fracture Toughness K_{IC} of Metallic Materials with Chevron-Notched Short-Rod and Short-Bar Specimens", in Chevron-Notched Specimens: Testing and Stress Analysis, ASTM STP 855, edited by J. H. Underwood, S. W. Freiman and F. I. Baratta, (America Society for Testing and Materials, 1984), 193-204.

32. L. Chuck, E. R. Fuller, Jr. and S. W. Freiman, "Chevron-Notch Bend Testing in Glass: Some Experimental Problems" in Chevron-Notched Specimens: Testing and Stress Analysis, ASTM STP 855, edited by J. H. Underwood, S. W. Freiman and F. I. Baratta, (America Society for Testing and Materials, 1984), 167-75.

33. R. W. Rice, S. W. Freiman and P. F. Becher, "Grain Size Dependence of Fracture Energy in Ceramics: I, Experiment", J. Am. Ceram. Soc., 64 (1981), 345-9.

34. R. W. Davidge, "Effects of Microstructure on Mechanical Properties of Ceramics" in Fracture Mechanics of Ceramics, vol. 2, edited by R. C. Bradt, D. P. H. Hasselman and F. F. Lange, (Plenum Press, New York, 1974), 447-68.

35. J. L. Shannon, Jr. and D. G. Munz, "Specimen Size and Geometry Effects on Fracture Toughness of Aluminum Oxide Measured with Short-Rod and Short-Bar Chevron-Notched Specimens" in Chevron-Notched Specimens: Testing and Stress Analysis, ASTM STP 855, edited by J. H. Underwood, S. W. Freiman and F. I. Baratta, (American Society for Testing and Materials, 1984), 270-80.

36. T. T. Shih, "Chevron V-Notched Bend Specimen for K_{IC} Measurement of Brittle Materials", J. Testing and Evaluation, 9 (1981), 50-5.

37. L. Shaw and R. Abbaschian, "Toughening $MoSi_2$ with Niobium Metal --- Effects of Size and Orientation of Ductile Laminate", to appear in Acta Metall. Mater., 1993.

38. M. Miyayama, K. Koumoto and H. Yanagida, "Engineering Properties of Single Oxides", in Engineered Materials Handbook: Ceramics and Glasses, vol. 4, (ASM International, 1987), 748-57.

39. Metals Handbook, 8th ed., vol. 1, (American Society for Metals, 1961), 1202.
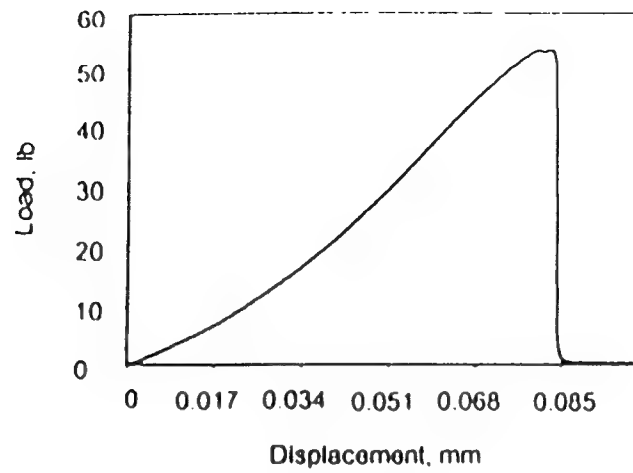
Fig. 2 A typical load-displacement curve of sandwich-type chevron-notched monolithic Al$_2$O$_3$.
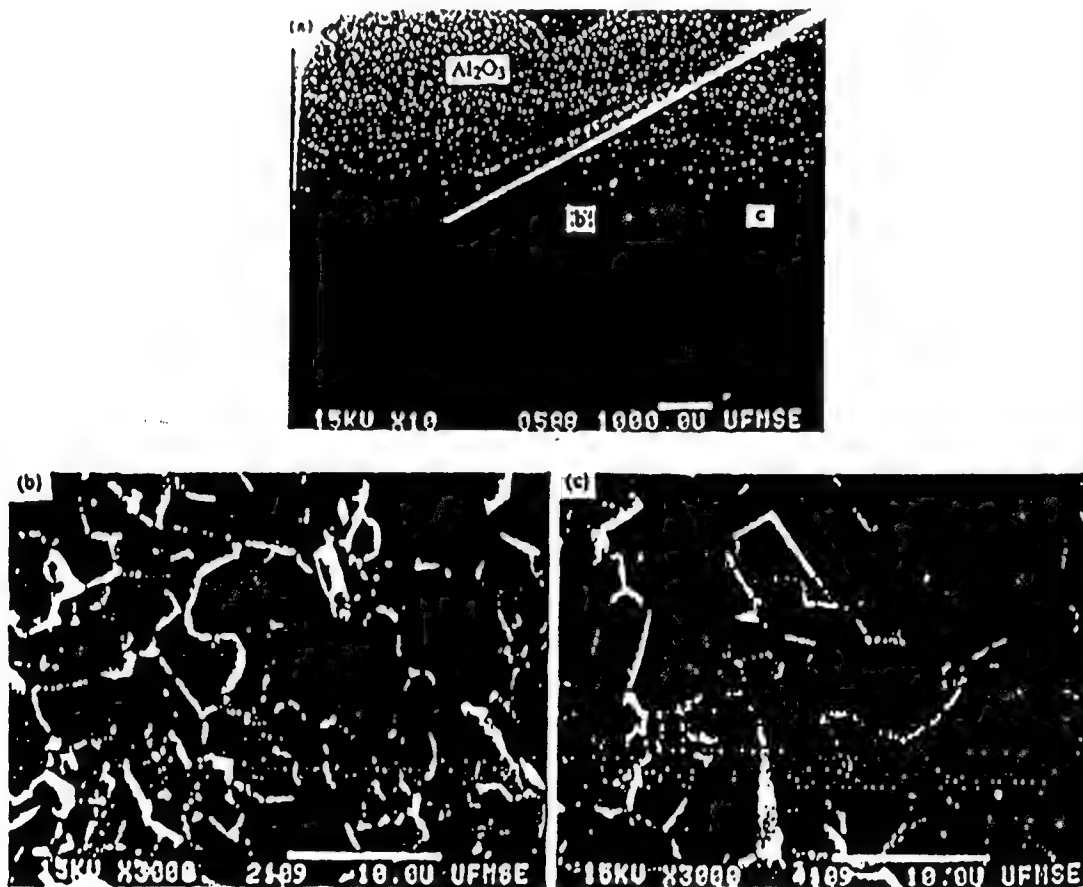

Fig. 3 (a) Fracture surface of Al$_2$O$_3$ at the chevron crack; (b) high magnification view of position b shown in figure (a); and (c) high magnification view of position c shown in figure (a).
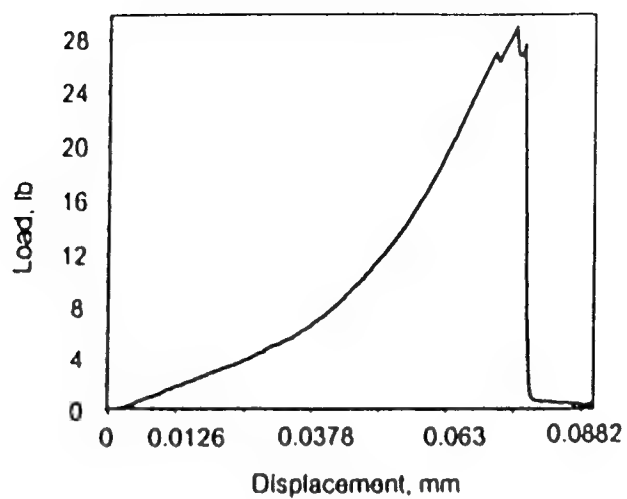
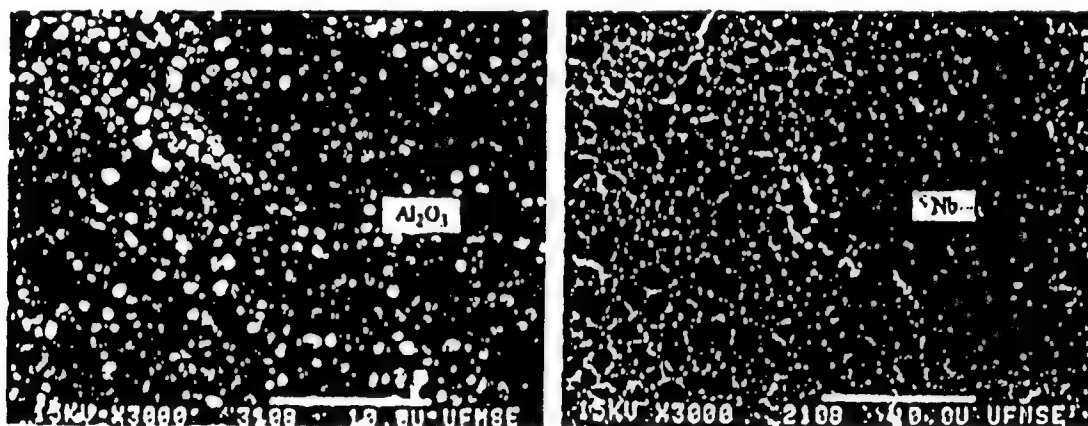Fig. 4 A typical load-displacement curve of the Al_2O_3/Nb sandwich-type chevron-notched specimens.

Fig. 5 The two corresponding fracture surfaces of an Al_2O_3/Nb specimen at the chevron plane.

Role of Matrix/Reinforcement Interfaces in the Fracture Toughness of Brittle Materials Toughened by Ductile Reinforcements

L. XIAO and R. ABBASCHIAN

Crack interactions with ductile reinforcements, especially behavior of a crack tip at the interface, have been studied using $MoSi_2$ composites reinforced with Nb foils. Effects of fracture energy of interfaces on toughness of the composites have also been investigated. Variation of interfacial bonding was achieved by depositing an oxide coating or by the development of a reaction product layer between the reinforcement and matrix. Toughness was measured using bend tests on chevron-notched specimens. It has been established that as a crack interacts with a ductile reinforcement, three mechanisms compete: interfacial debonding, multiple matrix fracture, and direct crack propagation through the reinforcement. Decohesion length at the matrix/reinforcement interface depends on the predominant mechanism. Furthermore, the results add to the evidence that the extent to which interfacial bonding is conducive to toughness of the composites depends on the criterion used to describe the toughness and that ductility of the ductile reinforcement is also an important factor in controlling toughness of the composites. Loss of ductility of the ductile reinforcement due to inappropriate processing could result in little improvement in toughness of the composites.

I. INTRODUCTION

THE interface between matrix and reinforcements plays an important role in the mechanical performance of composites. It is commonly accepted that a relatively weak interface is desirable for improving fracture toughness of brittle materials reinforced by ceramic fibers.[1-4] The reason for this is that such an interface when present in the path of an advancing crack would fail locally and blunt the crack. Otherwise, if the interface is strong, the propagating crack is unlikely to "see" the fiber and little improvement in toughness will be realized. This toughening concept has become a dogma in design of brittle materials to be reinforced by ceramic fibers. However, when the reinforcement is a ductile fiber with a high strain to failure, the requirement for the interfacial bonding may be different. This is because occurrence of fracture for the two different fibers is based on different criteria. For a brittle fiber, the occurrence of fracture is simply based on the magnitudes of the maximum tensile stresses which are enhanced by the presence of stress concentration. In contrast, since ductile fibers can yield locally by dislocation slip and thus blunt the crack, the fracture occurs only after exhaustion of ductility of the fiber in the presence of triaxial stresses at the crack tip (particularly in plane strain). As such, there may be different requirements for the interfaces in ductile-fiber-reinforced brittle matrix composites.

The responsibility for the ductile phase toughening has been attributed to bridging of intact ligaments of the ductile phase behind the advancing crack tip.[5-12] Based on this mechanism, the increased toughness of the composites in the case of small-scale bridging can be related to the work of stretching and fracturing the ductile phases, ΔG, by the following equation:[6,9]

$$\Delta G = V_f \int_0^{u^*} \sigma(u)\, du \qquad [1]$$

where u is the crack opening, $\sigma(u)$ the nominal stress on the ligament, u^* the crack opening at the end of the traction zone, and V_f the area fraction of reinforcements on the crack plane. It is clear that the increased toughness depends on the stress-displacement function of the ductile ligament, $\sigma(u)$, which in turn relies on the extent of decohesion at the matrix/reinforcement interface and can be determined independently using a simple tensile test on a single constrained ductile reinforcement.[7,13-16] These experiments indicated that a high work of rupture of ductile reinforcements was encouraged by a partial decohesion at the interface.[7,13-15] Deve et al.,[16] however, found that whether or not extensive decohesion was desirable for a high work of rupture depended on the work-hardening capability of the reinforcements, suggesting that contributions of decohesion were complicated and interdependent with other material properties. Theoretical analysis of stress-displacement function, $\sigma(u)$, has also been attempted. Numerical models[5,6] showed that partial decohesion was beneficial to a high work of rupture, and therefore, a high toughness. Similar conclusions have also been drawn from analytical models.[6,7,17]

In the present work, effects of interfacial coating and decohesion on the toughness of ductile-phase-reinforced brittle matrix composites were measured directly using a four-point bend test on chevron-notched specimens rather than measuring the stress-displacement function and deducing the toughness increment via Eq. [1]. The composite system selected for the investigation was laminated $MoSi_2$ matrix reinforced with coated or uncoated Nb foils. The composite system was selected, because $MoSi_2$ is

among the most promising candidates for high-temperature structural applications. In addition, the two components used have similar coefficients of thermal expansion, thus minimizing the residual thermal stresses and simplifying the fracture toughness analysis. The use of Nb foil rather than filaments allowed for the ease of producing the composites with controlled properties, but it still served the main purpose of the present study.

II. EXPERIMENTAL

A. Measurement of Fracture Toughness

Disc-shaped laminated composites were produced by hot pressing $MoSi_2$ powder (-325 mesh) with 20 vol pct of coated or uncoated Nb foils at 1400 °C for 1 hour or 1700 °C for 40 minutes under a pressure of 40 MPa. In order to minimize residual thermal stresses, the hot-pressed discs were held in the hot-pressing chamber at 800 °C for 1 hour before cooling down to room temperature. The thickness of the Nb foils was 0.25 mm. The interface coatings were produced by depositing Al_2O_3 or ZrO_2 to the Nb surface prior to the hot pressing or by the development of a reaction product layer between the matrix and reinforcement. Details of the coating procedures can be found in Reference 18.

One way to evaluate the ductile phase toughening is to generate a resistance curve (R-curve) of the composites, as done by Elliott et al.[19] and Venkateswara Rao et al.[20] To generate this curve, however, the dimensions of the specimens should be at least as large as the bridging length. For the present model composites, based on the equilibrium stress distribution across the crack face, the bridging length has been estimated to be at least 50 mm.[21] To avoid using such a large specimen, the toughness of the present composites was measured by four-point bending of chevron-notched specimens.[22,23] The samples had inner and outer spans of 10 and 20 mm, respectively, and were tested using a hydro-servo-controlled MTS with a crosshead speed of 4×10^{-4} mm/s. In order to prepare the chevron-notched bending specimens, the hot-pressed discs were cut into rectangular bars with dimensions of $3.81 \times 5.08 \times 25.4$ mm. The notch on each sample was cut perpendicular to the foil plane using a diamond wafering blade. To investigate interactions between cracks and reinforcements, some specimens were unloaded at various levels of load during the bending tests. A cross section perpendicular to the chevron notch of the unloaded specimens was cut, polished, and examined using scanning electron microscopy (SEM) to measure decohesion length and the crack geometry and position.

The peak load of the bending tests was used to calculate fracture toughness with the aid of the following equation:[22]

$$K_{max} = \frac{P_{max}}{B\sqrt{W}} Y^*_{min} \qquad [2]$$

where P_{max} is the maximum test load, B and W the width and height of the bending bar, respectively, and Y^*_{min} the minimum value of the dimensionless stress intensity fac-

tor coefficient as a function of relative crack length for the particular specimen used. The present experiments revealed that P_{max} was reached when the crack was inside the chevron. However, because of the rising crack-growth resistance for ductile-phase-toughened composites, P_{max} and Y^*_{min} do not occur coincidentally at the same crack length, and therefore, P_{max} does not exactly correspond to the stress-intensity factor at failure but is a good approximation to it.[23,24,25] Thus, the value calculated using Eq. [2] is called "damage tolerance" in this article and is designated as K_{max} rather than K_{Ic}.

B. Interface Fracture Energy Measurement

The measurement of the fracture energy of matrix/reinforcement interfaces was conducted on chevron-notched short bars using the procedures recommended in Reference 26. The technique involves determining the critical stress intensity factor from the peak load of the notched bars and then converting the critical stress intensity factor to the fracture energy of the interface (bond toughness of the interface). In the present study, however, a modified specimen geometry, as shown in Figure 1, was used. An advantage of the present geometry is that there is no need for compliance calibration due to symmetry of compliance of the specimen with respect to the interface.

The short bar specimens were produced by hot pressing. The hot-pressing temperature and coating procedures were the same as for preparing the composite laminates mentioned in Section A. The Nb foils used for the short bar specimens were 0.127 mm thick, and the notch was cut parallel to the foil using a diamond wafering blade with a thickness of 0.4 mm. The thickness of the notch was chosen to be slightly larger than that of the foil to insure that the initiation and propagation of the crack were at the weakest positions among various interfaces between matrix/coating/reinforcement.
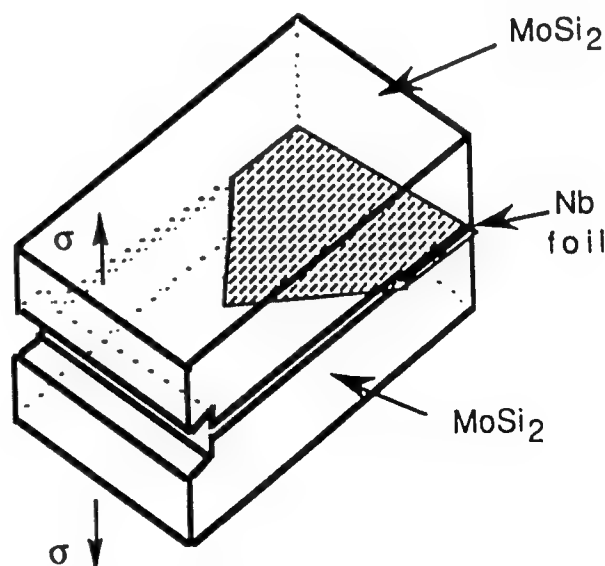

Fig. 1 — Short bar specimen geometry.

The fracture energy of the interface, G_{max}, was calculated using the following equation:[26]

$$G_{max} = \frac{K_{Icsr}^2}{E} \qquad [3]$$

where E is the elastic modulus of MoSi$_2$ and K_{Icsr} is the critical stress intensity factor determined from the peak load of the short bar bending test.

C. Tensile Tests on a Single Constrained Reinforcement

A schematic of a tensile test specimen used to determine the crack behavior near the reinforcement is shown in Figure 2. The specimens, consisting of a single Nb foil sandwiched between two MoSi$_2$ layers, were produced by hot pressing with the same processing conditions as for the composite laminates and short bar specimens. The straight-through notches on the MoSi$_2$ matrix were introduced using a diamond wafering blade with a thickness of 0.15 mm. The tensile specimens were polished on both sides perpendicular to the Nb foil before testing. The specimens were unloaded at various levels of load during testing and examined with SEM to observe the interactions and behavior of ductile reinforcement at the near-tip region.

III. RESULTS AND DISCUSSION

A. Fracture Energy of Interfaces

Microstructures of the matrix/reinforcement interfaces for the coated and uncoated foils are shown in Figure 3. The thicknesses of Al$_2$O$_3$ and ZrO$_2$ coatings produced are about 5 and 25 μm, respectively. For the uncoated foils, as shown in Figure 3(a), the interaction between the matrix and reinforcement causes formation of (Mo, Nb)$_5$Si$_3$, the thickness of which depends on the compositing and annealing conditions.[18] For the coated foils, no interaction between the composite constituents
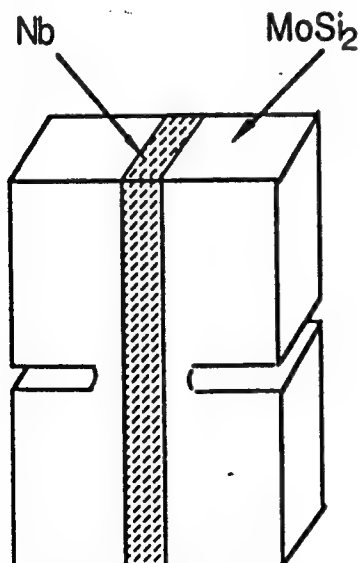
Fig. 2 — Schematic of a composite laminate tensile test specimen.

was observed. However, because of the diffusion of Si through the coatings, a Nb$_5$Si$_3$ layer was produced near the surface of the foil. Therefore, as can be seen in the figure, the coated foils contain three interfaces between the matrix and reinforcement: MoSi$_2$/coating/Nb$_5$Si$_3$/Nb; whereas, the uncoated foils contain two interfaces: MoSi$_2$/(Mo, Nb)$_5$Si$_3$/Nb.

When the hot-pressing temperature was 1400 °C, the interfaces between the uncoated Nb and MoSi$_2$ became MoSi$_2$/(Nb, Mo)Si$_2$/Nb$_5$Si$_3$/Nb. Detailed mechanisms of the interphase formation for the uncoated Nb/MoSi$_2$ system at different temperatures are described in Reference 27. Despite the different interfacial microstructures, mechanical behavior was observed to be the same for the specimens hot-pressed at 1400 °C and 1700 °C. For the ZrO$_2$ coated Nb, the same interfacial microstructure was produced at both hot-pressing temperatures. However, for the Al$_2$O$_3$ coated Nb, the coating became discontinuous when the hot-pressing temperature was 1700 °C. Such phenomenon has been attributed to the Kirkendal shift caused by the extensive Si diffusion across the coating.[18]

A typical load-displacement curve of the chevron-notched short bar for a ZrO$_2$ coated Nb/MoSi$_2$ laminate is shown in Figure 4. Some stable crack propagation has been achieved, as indicated by the fluctuation in the curve near the maximum load. Therefore, the maximum load was used to calculate G_{max} with the aid of Eq. [3]. The corresponding fracture surface at the chevron crack is also presented in Figure 4. By examining both fracture surfaces of a broken sample with SEM and an energy-dispersive spectrometer (EDS), the failure location at the interface was determined. The measured fracture energies of interfaces and failure locations for the uncoated and coated Nb/MoSi$_2$ composites are summarized in Table I. In the case of coated Nb systems, failure occurred along the oxide/Nb$_5$Si$_3$ interface or inside the oxide coating. For the uncoated system, on the other hand, the failure was observed to take place inside MoSi$_2$ rather than at the interfaces or inside the interphases formed, indicating that the interfacial region has a higher toughness than the matrix. Indeed, the value of G_{max} of MoSi$_2$ measured in the present study is 33.7 J/m^2, and all the measurements conducted on MoSi$_2$/uncoated Nb system showed that fracture energies for failure of the notched short bars were about 36.4 J/m^2 because the crack in MoSi$_2$ failed to follow the chevron-notched plane strictly. The data in Table I also show that the fracture energy of the interface has been reduced by the oxide coatings. Furthermore, the zirconia coating exhibits a lower fracture energy of the interface than the alumina. This is attributed to the existence of residual tensile stresses in the zirconia coating caused by the thicker coating layer and a higher coefficient of thermal expansion of the zirconia than that of the matrix and reinforcement.

B. Behavior of Cracks at the Interface

Details of cracks impinging on Nb foils for uncoated and coated composite systems are shown in Figure 5. The micrographs were taken from the cross sections of laminated composites unloaded at about 20 pct of the peak load of the composites during the four-point bend-
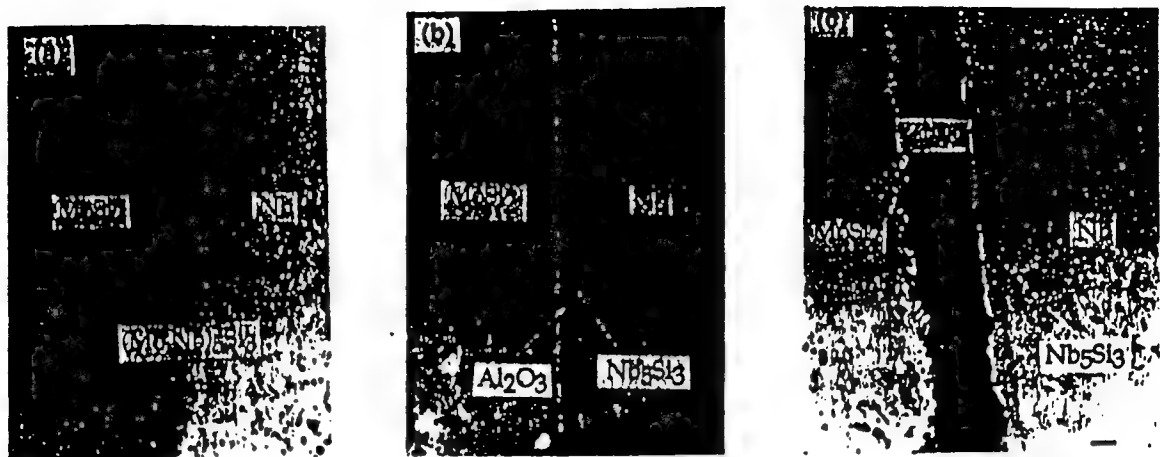
Fig. 3—Interfacial microstructures of the laminated composites reinforced by (a) uncoated Nb, hot-pressed at 1700 °C; (b) Al₂O₃ coated Nb, hot-pressed at 1400 °C; and (c) ZrO₂ coated Nb, hot-pressed at 1700 °C.
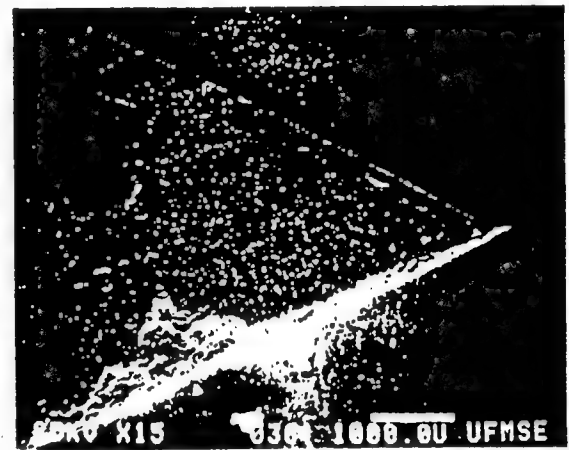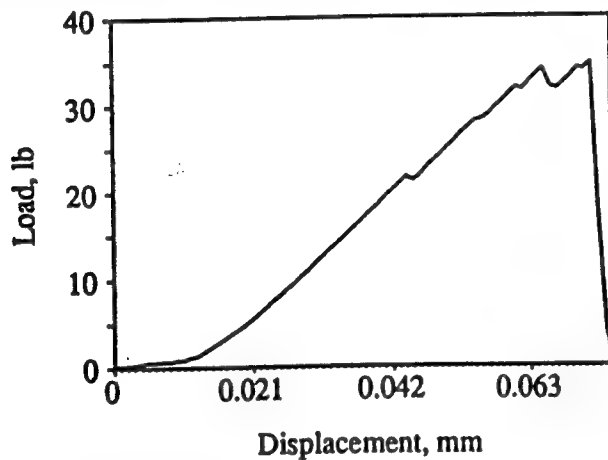

Fig. 4—A typical load-displacement curve of the chevron notched short bar for a ZrO₂ coated Nb/MoSi₂ laminate and the corresponding fracture surface at the chevron crack.

ing tests. It is noted from the figures that debonding at the interface does not occur when a crack approaches the interface or just impinges on it for both uncoated and coated reinforcement systems. Similar observations were made from tensile tests on a single constrained Nb foil. This is not surprising, since all the fracture energies of the interfaces measured in the present study are higher than 1/5 of the matrix fracture energy. The observation is consistent with an estimation made by Cook and Gordon.[28] They found that for an elliptical crack, an interfacial fracture energy of 1/5 or less of the matrix

fracture energy would cause interfacial debonding in advance of the crack.

Figure 6 shows a typical microstructure of an uncoated Nb tensile test specimen. A notch tip can be seen at the left side of Figure 6(a), which shows that a crack initiates at the notch tip and ends at the Nb foil. Figure 6(b) is a close-up of one of the crack tips in Figure 6(a). As seen in the figure, the impingement of the crack on the interface causes local dislocation slip of the reinforcement instead of interfacial failure, leading to the release of the stress concentration. In addition, there are also

Table I. Fracture Energy of Interfaces in Coated and Uncoated Nb/MoSi₂ Systems*

System	Processing Conditions	Failure Location	Fracture Energy of Interface $(G_{max}, J/m^2)$
MoSi₂/uncoated Nb	1400 °C and 1700 °C	inside the MoSi₂	>33.7 ± 1.4
MoSi₂/Al₂O₃ coated Nb	1400 °C	Al₂O₃/Nb₅Si₃ interface	16.1 ± 1.3
MoSi₂/ZrO₂ coated Nb	1400 °C and 1700 °C	ZrO₂/Nb₅Si₃ interface or inside the ZrO₂	12.8 ± 1.0

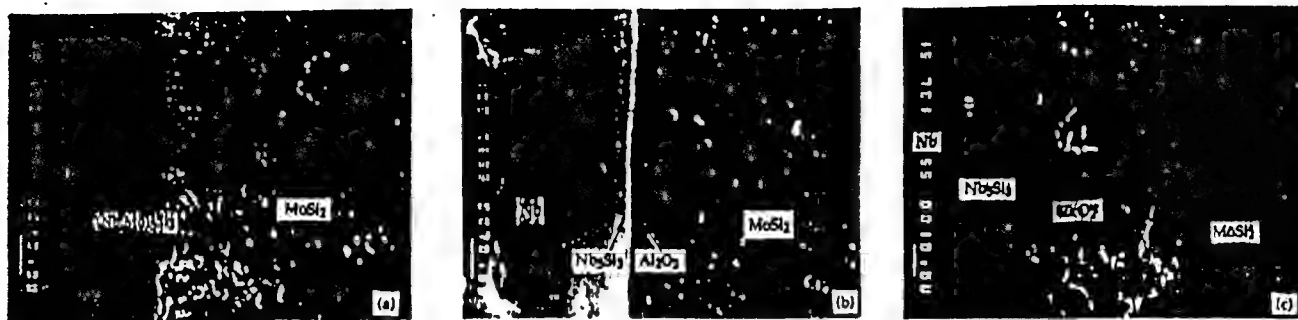*Four specimens for each condition were tested.

Fig. 5—Optical microstructures of composite laminates showing that cracks end at the front of the reinforcement without causing interfacial debonding. (a) Uncoated Nb, (b) Al$_2$O$_3$ coated Nb, and (c) ZrO$_2$ coated Nb reinforced composites.

multiple cracks at the interface which add to relaxation of tip stress intensity and effectively enlarge the initial plastic zone in the ductile phase. The result shows that interfacial failure is not the only mechanism of blunting cracks in the case of ductile reinforcements. The slip capability of ductile reinforcement can play an important role, as will be discussed further in the following sections.

A general view of the cross section of a composite laminate reinforced with 20 vol pct of uncoated Nb laminae unloaded at about 20 pct of the peak load is shown in Figure 7. As seen in the figure, the crack propagation is discontinuous in nature, i.e., after a crack stops at one side of a Nb lamina in the laminated composites, its propagation is accomplished by renucleation of another crack at the other side. Also, around a load level of 20 pct of the peak load, the crack has already propagated throughout the entire thickness of the matrix. Beyond this level, the load is carried exclusively by Nb laminae. Owing to the extensive cracking of the matrix at a load level considerably below the peak load of the composite, the value calculated from the peak load of a bending test on the chevron-notched specimen using Eq. [2] was actually a reflection of the bridging capability of the ductile phases and was interpreted as an indicator of the damage tolerance of the composite.[29]

C. *Debonding, Multiple Matrix Fracture, and Direct Crack Propagation through the Reinforcement*

As load continues to increase during the tensile tests after the cracks have impinged on the Nb foil, debonding at the interfaces and/or multiple fracture of the matrix near the interfaces occur due to a relatively large lateral deformation of the Nb reinforcement compared to the matrix and load transfer from the matrix to the reinforcement. Typical features of debonding at the interface and multiple fracture of the matrix near the interface for the coated and uncoated specimens are shown in Figure 8. It is noted that interfacial debonding has occurred at the oxide coated systems (Figure 8(a)) as contrasted with multiple matrix fracture near the interface for the uncoated systems (Figure 8(b)). This is in agreement with the interface fracture energy measurement, since the interfaces in the uncoated composites have a higher fracture energy than the matrix; as such, the matrix is expected to fail more easily than the interfaces in these composites. On the other hand, for the oxide coated

composites, the fracture energy of the interfaces is lower than the fracture energy of the matrix. Thus, interfacial debonding prevailed in these composites. Similar results were also observed in a related study on bending tests of chevron-notched composite laminates,[29] which showed that debonding at the interfaces prevailed in the Al$_2$O$_3$ coated Nb composites while multiple matrix fracture dominated in the uncoated Nb composites.

Both interfacial debonding and multiple matrix fracture create a "gage length" at the matrix/reinforcement interface which is a region virtually free from constraints of the matrix and is called "decohesion length" in the text. Measurement of the decohesion length was conducted for laminated composites, and the results are shown in Table II. Since the decohesion length of the laminated composites varies with load and position of the reinforcement, the values reported in Table II are measured at the peak load and for the second foil from the notch tip. Microhardness of the Nb reinforcements after hot pressing is also included in Table II to show how hardness of the Nb foils was effected by the processing conditions. Little change in microhardness across the whole Nb foil was observed so that the microhardness was taken as a constant for each specific condition. The results for the specimens hot-pressed at 1400 °C show that the lower the fracture energy of the interface, the longer the decohesion length. This is the result we would expect, since lower interfacial fracture energy means lower resistance to interfacial decohesion. However, in the case of ZrO$_2$ coated systems, when hot-pressing temperature is increased to 1700 °C, the decohesion length becomes negligible in contrast with the general trend exhibited by the composites processed at lower temperatures. Figure 9 shows two typical load-displacement curves of bending tests on ZrO$_2$ coated Nb/MoSi$_2$ laminated composites hot-pressed at 1400 °C and 1700 °C. It is noted that fracture toughness of the composites is reduced and the failure becomes catastrophic when hot-pressing temperature changes from 1400 °C to 1700 °C. Observation of fracture surfaces also shows a change of fracture modes from quasi-cleavage to cleavage, as shown in Figure 10. As indicated in Table II, microhardness of the Nb foils increases from 131 to 236 as the processing temperature is increased, indicating an increase in the slip resistance of the Nb foils. The embrittlement of Nb is probably due to the diffusion of interstitial oxygen into the foils at higher processing temperatures from the decomposition of ZrO$_2$.
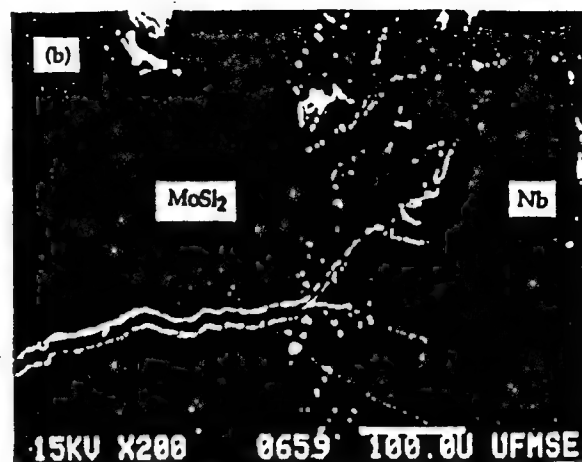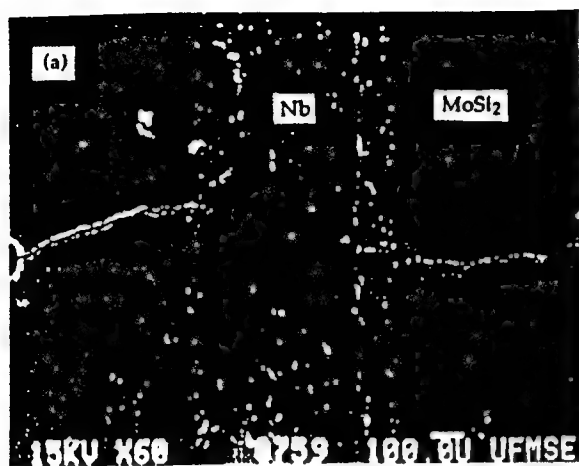
Fig. 6—An edge view of a unloaded tensile test specimen. (a) A general view of the cracks and (b) a close-up of the crack tips showing dislocation slip of the Nb at the crack tips.
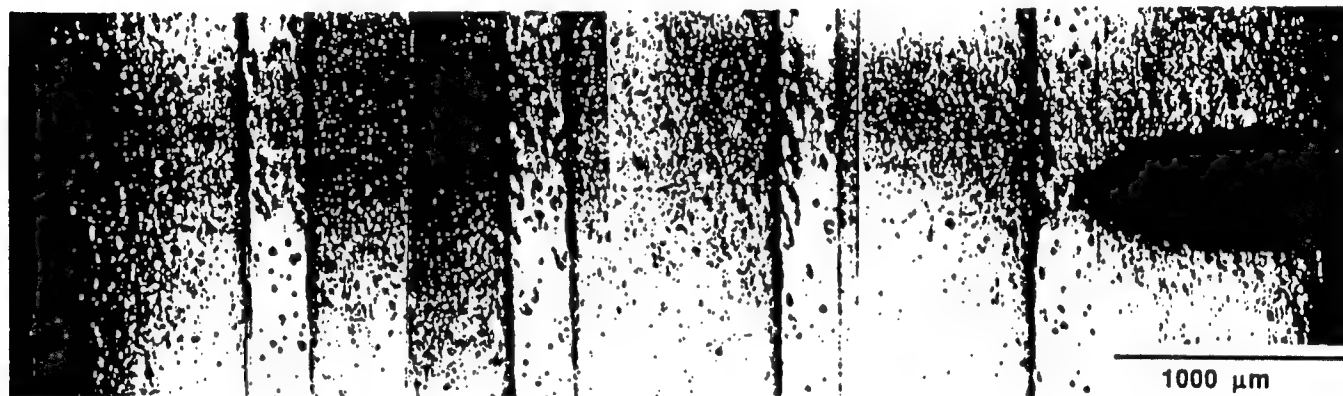

Fig. 7—A cross section of a laminated composite reinforced by 20 vol pct of uncoated Nb foils showing the characteristics of crack propagation in the composites.

Fig. 8—An edge view of tensile tested specimens. (a) Debonding at the interface in a specimen with Al₂O₃ coated Nb. (b) Multiple matrix fracture near the interface in a specimen with uncoated Nb.

Composite System	Uncoated Nb		Al₂O₃ Coated Nb	ZrO₂ Coated Nb	
Hot-pressing temperature	1700 °C	1400 °C	1400 °C	1400 °C	1700 °C
Decohesion length (mm)	0.75 ± 0.08	0.76 ± 0.06	0.80 ± 0.12	1.06 ± 0.23	0
Vickers hardness (kg/mm²)	145	131	134	131	236

*Four specimens for each condition were tested except for Al₂O₃ coated Nb system for which eight specimens were tested.
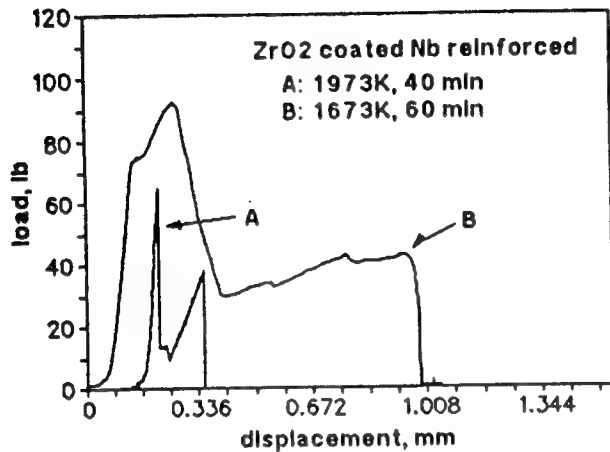
Fig. 9—Typical load-displacement curves of bending tests on chevron-notched composite laminates reinforced by ZrO₂ coated Nb foils.

Loss of ductility of the foil leads to little lateral deformation of the Nb and resultant transverse stresses and, therefore, results in negligible decohesion length. To support this inference, tensile tests on single constrained reinforcement specimens were conducted and the results showed that whenever Vickers hardness of uncoated Nb foils increased to about 200 by controlling hot-pressing conditions, fracture mode was always by cleavage even if the notches were cut directly into the Nb foils. This result shows clearly that brittle fracture of the Nb foils is due to embrittlement of the foils.

From the previous discussion, it can be summarized

that as a crack approaches the ductile reinforcements in these systems, there exist three competitive mechanisms: interfacial debonding, multiple matrix fracture, and direct crack propagation through the ductile reinforcement. Figure 11 shows schematically these interactions. In the case of high ductility of the reinforcement, the crack is blunted by local dislocation slip of the ductile phase. The present experiments showed that extensive debonding did not occur at the early stage of the crack/ductile phase interaction, so that the interaction could be approximated as the case of no debonding at this stage. Thus, to fail the ductile reinforcement, a much higher tensile stress has to be applied which increases shear stresses at the interface due to load transfer and transverse stresses caused by the difference between lateral displacements of the matrix and reinforcement. Both shear and transverse stresses enhance interfacial debonding and/or multiple matrix fracture. Thus, whether interfacial debonding or multiple matrix fracture predominates depends on the values of the fracture energies of the matrix and interface. On the other hand, for the case of low ductility of the reinforcements, the crack can relatively easily propagate through the reinforcement before occurrence of the interfacial debonding or multiple matrix fracture. The decohesion length, which results from the competition of the three above-mentioned mechanisms, is controlled by a combination of three material properties: interface fracture energy, toughness of the matrix, and slip capability of the reinforcement.

D. Fracture Toughness of the Laminated Composites

Typical load-displacement curves of bending tests on chevron-notched composite laminates hot-pressed at
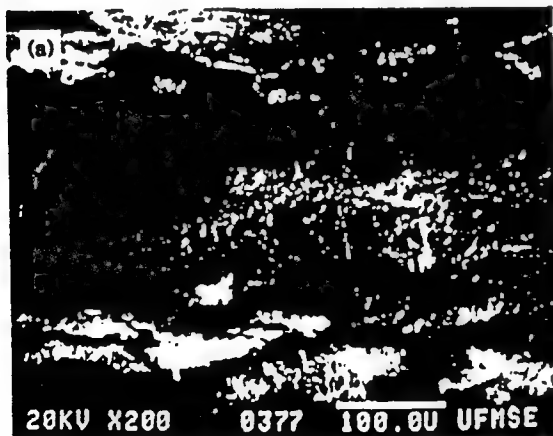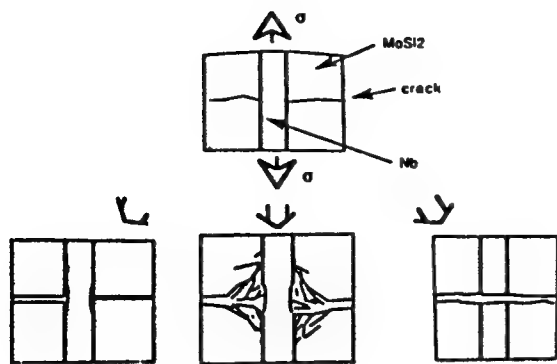

Fig. 10—Fracture surfaces of the Nb foils in composite laminates reinforced by ZrO₂ coated Nb: (a) hot-pressed at 1400 °C for 1 hour and (b) hot-pressed at 1700 °C for 40 min.

Fig. 11 — Schematic of the three competitive mechanisms at the interface. Conditions for the process to dominate shown in (a) are high toughness reinforcement and weak interface, (b) are high toughness reinforcement and strong interface, (c) are low toughness reinforcement and strong or weak interface.

1400 °C are shown in Figure 12. There are two prominent features in the figure: (1) uncoated Nb reinforced composites exhibit the highest peak load and (2) mechanical behaviors of ZrO_2 and Al_2O_3 coated systems are similar, both of them showing an increase in the carried load in the last part of the displacement curves. The latter observation is caused by the extensive delamination at the interface, and correspondingly, more niobium participates in deformation and deforms under much less constrained condition. Because of this feature, the total energy consumed to break a specimen (area under the curve) for the coated composites is larger than that to break the uncoated ones. The work of fracture, defined as the total energy normalized with respect to the generated crack area,[30] for the various composites is presented in Table III. As seen in the table, the coated composites show the higher work of fracture, indicating that the low interfacial fracture energy and, thus, long decohesion length are beneficial to improving the toughness of the composite. This result is consistent with
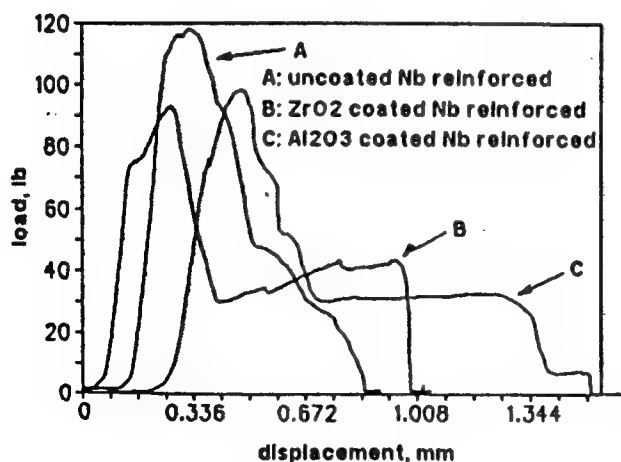

Fig. 12 — Typical load-displacement curves of bending tests on chevron notched laminates reinforced by 20 vol pct of coated and uncoated Nb foils, hot-pressed at 1400 °C for 1 hour.

predictions based on the numerical and analytical studies.[5-7,9,17]

However, damage tolerance determined from the peak load of the chevron-notched specimens shows an opposite trend. The damage tolerance determined in this way is also included in Table III. The data show that uncoated Nb reinforced composites exhibit the highest damage tolerance, followed by Al_2O_3 coated and then ZrO_2 coated composites. This sequence is parallel to the decrease in the interfacial fracture energy of the composites; that is, the higher the interfacial fracture energy, the higher the damage tolerance of the composites.

The data in Table III also indicate that loss of ductility of the ZrO_2-coated Nb foils hot-pressed at 1700 °C results in a large drop of toughness of the laminated composites. Therefore, the damage tolerance data suggest that a high degree of constraints is conducive to toughness as long as the ductile reinforcement has a high slip capability. When the reinforcement does not have the slip capability, as in the case of ZrO_2 coated composites processed at 1700 °C, decreasing the constraint (i.e., increasing the gage length by decreasing the interfacial bonding) is more beneficial to improving the toughness.

In summary, the results from the bend test of chevron-notched specimens indicate that the role of the interface for ductile reinforcement and debonding in the toughness depends on the criterion used to describe the toughness of the composites. If the peak load of the chevron-notched specimen is used as an indicator of the toughness, a strong bonding and, therefore, a high degree of constraints, would be desirable. On the other hand, if the total energy consumed to break a specimen is used as indicative of that specimen's toughness, then a relatively weak bonding is required.

The aforementioned dual effects of interfacial properties on the toughness of the composites are further supported using the data obtained from the simple tensile test on a single constrained Nb foil. Representative stress-displacement curves for 0.5-mm-thick Nb lamina are shown in Figure 13, and the corresponding decohesion lengths with different coating conditions for different sizes of Nb laminae are summarized in Table IV. It is noted that the area under the stress-displacement curve, called "work of rupture of the constrained ductile phase," increases with increasing decohesion length. As given by Eq. [11], the steady state toughness of the composites is proportional to the work of rupture of the constrained ductile phase. Thus, increasing decohesion length is conducive to improving steady state toughness of the composites, a trend also shown by the work of fracture measured from chevron-notched specimens (Table III). Figure 13, at the same time, also reveals that the maximum stress reached by the constrained Nb decreases with increasing decohesion length, a trend similar to that exhibited by the damage tolerance measured from the chevron-notched specimens. These apparently different roles of the interface can be explained by relating the maximum stress reached by the constrained ductile phases to the crack propagation resistance in the case of large-scale bridging (i.e., crack length is at the same order of magnitude as bridging length), as observed in the present composites (Figure 7). A recent calculation based on the equilibrium stress distributions across the crack face[21]

Material	Monolithic MoSi₂	Uncoated Nb Reinforced	Al₂O₃ Coated Nb Reinforced	ZrO₂ Coated Nb Reinforced	ZrO₂ Coated Nb Reinforced
Hot-pressing temperature	1700 °C	1700 °C and 1400 °C	1400 °C	1400 °C	1700 °C
Damage tolerance ($MPa \cdot m^{1/2}$)	3.3 ± 0.3	15.2 ± 1.3	14.0 ± 1.5	12.8 ± 1.5	8.6 ± 1.3
Work of fracture (J/m^2)	690 ± 30	21,600 ± 3000	28,700 ± 1900	28,700 ± 4600	2800 ± 300
Interfacial fracture energy**	—	high	medium	low	low
Ductility of the reinforcement**	—	high	high	high	low

*Four specimens for each condition were tested except for Al₂O₃ coated Nb system for which eight specimens were tested.
**For details, see Tables I and II.
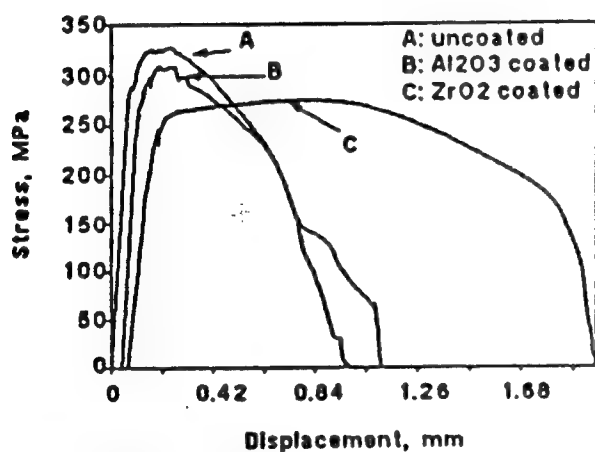
Fig. 13—Effect of the coatings on the stress-displacement curves, measured from tensile test on the single constrained Nb lamina (thickness of the Nb laminae = 0.5 mm).

indicates that the maximum crack propagation resistance of the composites increases with increasing decohesion length. However, the maximum crack propagation resistance is achieved only after the crack has propagated extensively. At the small crack size, the composites with less decohesion show a higher crack propagation resistance than their counterparts with more decohesion. Therefore, it seems that the choice of weak or strong interface in describing fracture behavior of ductile-phase-toughened composites depends on the criterion used to describe the toughness of the composites.

VI. SUMMARY AND CONCLUSIONS

The present set of experiments clarifies the role a matrix/reinforcement interface plays in brittle materials toughened by ductile reinforcements. It has been disclosed that influence of interfaces on fracture toughness of brittle matrix/ductile reinforcement composites is not as crucial as in brittle matrix/ceramic fiber composites due to the local dislocation slip of ductile phase at the crack tip. Furthermore, it has been established that as a crack impinges a reinforcement, there exist three competitive mechanisms: interfacial debonding, multiple matrix fracture, and direct crack propagation through the reinforcement. The mechanism that prevails is decided not only by fracture energies of the interface and toughness of the matrix but also by the slip capability of the ductile reinforcement. Decohesion length at the matrix/reinforcement interface is a result of the competition. In the case of high slip capability of the reinforcements, the higher the fracture energy of interfaces, the shorter the decohesion length.

The toughness measurement has revealed that whether or not a strong interfacial bonding is conducive to toughness depends on the criterion used to describe the toughness of the composites. If the peak load of the chevron-notched specimen is used as an indicator of the toughness, a strong bonding would be desirable. On the other hand, if the work of fracture is used as indicative of its toughness, then a relatively weak bonding is required. Ductility of the ductile reinforcement is also an important factor in controlling toughness of the composites. It has been demonstrated that loss of ductility of

Thickness of Nb Foil (mm)	1.0			0.5			0.25		
Processing condition	uncoated	Al₂O₃ coated	ZrO₂ coated	uncoated	Al₂O₃ coated	ZrO₂ coated	uncoated	Al₂O₃ coated	ZrO₂ coated
Decohesion length (mm)	10 ± 5	decohesion all the way to the grips		2.9 ± 0.4	3.3 ± 0.4	decohesion all the way to the grips	0.86 ± 0.09	0.94 ± 0.23	1.30 ± 0.61

*Four specimens for each condition were tested except for 0.5-mm-thick Nb foils for which eight specimens were tested.

the ductile reinforcement during processing could result in little improvement in toughness of the composites.

ACKNOWLEDGMENTS

REFERENCES

1. K.M. Prewo: *Mater. Res. Soc. Symp. Proc.*, 1988, vol. 120, pp. 145-56.
2. R.J. Diefendorf and R.P. Boisvert: *Mater. Res. Soc. Symp. Proc.*, 1988, vol. 120, pp. 157-62.
3. A.G. Evans and D.B. Marshall: in *High Tech Ceramics*, P. Vincenzini, ed., Elsevier Science Publishers B.V., Amsterdam, 1987, pp. 213-46.
4. R.W. Davidge: in *High Tech Ceramics*, P. Vincenzini, ed., Elsevier Science Publishers B.V., Amsterdam, 1987, pp. 763-77.
5. P.A. Mataga: *Acta Metall.*, 1989, vol. 37, pp. 3349-59.
6. L.S. Sigl, P.A. Mataga, B.J. Dalgleish, R.M. McMeeking, and A.G. Evans: *Acta Metall.*, 1988, vol. 36, pp. 945-53.
7. M.F. Ashby, F.J. Blunt, and M. Bannister: *Acta Metall.*, 1989, vol. 37, pp. 1847-57.
8. L.R.F. Rose: *J. Mech. Phys. Solids*, 1987, vol. 35, pp. 383-405.
9. A.G. Evans and R.M. McMeeking: *Acta Metall.*, 1986, vol. 34, pp. 2435-41.
10. B. Budiansky, J.C. Amazigo, and A.G. Evans: *J. Mech. Phys. Solids*, 1988, vol. 36, pp. 167-87.
11. B.N. Cox: *Acta Metall. Mater.*, 1991, vol. 39, pp. 1189-1201.
12. B.N. Cox and C.S. Lo: *Acta Metall. Mater.*, 1992, vol. 40, pp. 69-80.
13. H.C. Cao, B.J. Salgleish, H.E. Deve, C. Elliott, A.G. Evans, R. Mehrabian, and G.R. Odette: *Acta Metall.*, 1989, vol. 37, pp. 2969-77.
14. L. Xiao and R. Abbaschian: in *Advanced Metal Matrix Composites for Elevated Temperatures*, M.N. Gungor, E.J. Lavernia, and S.G. Fishman, eds., ASM INTERNATIONAL, Metals Park, OH, 1991, pp. 33-40.
15. L. Xiao: in *Developments in Ceramic and Metal-Matrix Composites*, K. Upadhya, ed., TMS, Warrendale, PA, 1992, pp. 115-24.
16. H.E. Deve, A.G. Evans, G.R. Odette, R. Mehrabian, M.L. Emiliani, and R.J. Hecht: *Acta Metall.*, 1990, vol. 37, pp. 1491-1502.
17. L. Xiao: in *Developments in Ceramic and Metal-Matrix Composites*, K. Upadhya, ed., TMS, Warrendale, PA, 1992, pp. 359-69.
18. L. Xiao, Y.S. Kim, and R. Abbaschian: in *Intermetallic Matrix Composites*, Proc. MRS Meeting, D.L. Anton, P.L. Martin, D.B. Miracle, and R. McMeeking, eds., 1990, vol. 194, pp. 399-404.
19. C.K. Elliott, G.R. Odette, G.E. Lucas, and J.W. Sheckherd: in *High Temperature/High Performance Composite*, MRS Proc., F.D. Lemkey, A.G. Evans, S.G. Fishman, and J.R. Strife, eds., 1988, vol. 120, pp. 95-102.
20. K.T. Venkateswara Rao, G.R. Odette, and R.O. Ritchie: *Acta Metall. Mater.*, 1992, vol. 40, pp. 353-61.
21. L. Xiao and R. Abbaschian: University of Florida, Gainesville, FL, unpublished research, 1992.
22. D.G. Munz, J.L. Shannon, Jr., and R.T. Busey: *Int. J. Fract.*, 1980, vol. 16, pp. R137-R141.
23. J.C. Newman, Jr.: in *Chevron-Notched Specimens: Testing and Stress Analysis*, ASTM STP 855, J.H. Underwood, S.W. Freiman, and F.I. Baratta, eds., ASTM, Philadelphia, PA, 1984, pp. 5-31.
24. L.M. Barker and F.I. Baratta: *J. Test. Eval.*, 1980, vol. 8, pp. 97-102.
25. D. Munz: *Eng. Fract. Mech.*, 1981, vol. 15, pp. 231-36.
26. J.J. Mecholsky and L.M. Barker: in *Chevron-Notched Specimens: Testing and Stress Analysis*, ASTM STP 855, J.H. Underwood, S.W. Freiman, and F.I. Baratta, eds., ASTM, Philadelphia, PA, 1984, pp. 324-36.
27. L. Xiao and R. Abbaschian: *Mater. Sci. Eng.*, in press.
28. J. Cook and J.E. Gordon: *Proc. R. Soc. London A*, 1964, vol. 282, pp. 508-20.
29. L. Xiao, Y.S. Kim, R. Abbaschian, and R.J. Hecht: *Mater. Sci. Eng.*, 1991, vol. A144, pp. 277-85.
30. H.G. Tattersall and G. Tappin: *J. Mater. Sci.*, 1966, vol. 1, pp. 296-301.

MICROSTRUCTURE AND PROPERTIES OF MOSI2/NB INTERFACES WITH AND WITHOUT ALUMINA COATING

L. Xiao and R. Abbaschian
Department of Materials Science and Engineering, University of Florida, Gainesville,
FL 32611

ABSTRACT

This study explores the relations between processing routes, microstructures and mechanical properties of the matrix/reinforcement interfaces in MoSi2/Nb composites. It was found that the fracture energy of the interfacial region depended on the interfacial bond strength, roughness of interface, and the nature of the interfacial compounds. The fracture energy between the oxide coating and intermetallic interfacial compounds was found to be lower than that between two intermetallics or between Nb and an intermetallic. Processing routes were found to affect the fracture energy of the interfacial region by changing interphase formation, changing microstructure of materials adjacent to the interface, or changing roughness of interface.

INTRODUCTION

It is commonly accepted that a relatively weak interface is desirable for improving fracture toughness of ceramics and intermetallics reinforced by ceramic fibers [1-4]. The reason for this is that such an interface when present in the path of an advancing crack would fail locally and blunt the crack. A relatively weak interface is also beneficial to fracture toughness of polymer-matrix composites. An example is provided by Harris et al. [5], who used different fiber surface treatments to change the bond strength of the interface in carbon fiber-reinforced polyester composites, and demonstrated that higher fracture energy was achieved in the case of the weakest interface, resulting from greater pullout length of the carbon fibers. Similar results are found in carbon fiber-reinforced epoxies [6] and a boron epoxy composite [7]. Metal-matrix composites also exhibit a strong dependence of toughness on the fiber-matrix debonding, as exemplified by tungsten wire-reinforced aluminum composites [8]. In this case, the toughness is proportional to the energy to break the debonded fibers.

The above examples show that debonding at the interface play an important role in the mechanical performance of composites. A recent study [9] has shown that debonding length in the composites depends strongly on the fracture energy of the matrix/reinforcement interface. The latter is expected to be affected by various factors, such as the extent of chemical interaction at the interface, roughness of interface, dissipation of strain energy by ductile reinforcements, thermal expansion mismatch, and bond strength of the interface. Therefore, parameters affecting interfacial fracture energy must be evaluated and understood in order to control the mechanical behavior of interfaces in composites. In the present study, the relations between processing routes, microstructures and fracture energy of the matrix/reinforcement interfaces in MoSi2/Nb composites were explored. The composites were fabricated by hot pressing MoSi2 powder with Al2O3 coated or uncoated Nb reinforcement. Deposition of the oxide coating on Nb was achieved via different processing routes, i. e., sol-gel coating technique, physical vapor deposition and hot dipping Nb in a molten Al bath, followed by an anodizing process to form Al2O3. Interfacial fracture energy was evaluated using chevron-notched-short-bar specimens. Variation in the fracture energy of the interfacial region is discussed in terms of the microstructures and types of the interfacial bonding.

EXPERIMENTAL

Coating Techniques

The sol solution for the sol-gel coating was an aluminum-alkoxide-derived sol (using aluminum-sec-butoxide (ASB)), hydrolyzed in excess water and peptized with aluminum

nitrate, $Al(NO_3)_3$. The procedures for preparing the sol solution developed by Clark et al. [10] were used. The Al_2O_3 coating was produced by electrophoretic deposition on to the Nb foils. Once the coating was applied, the coated Nb foils were suspended vertically for 48 hrs at the ambient temperature, and then further dried in a furnace at 500^0C for 1 hr with a heating rate of $3^0C/min$ before the hot pressing.

Physical vapor deposition of Al_2O_3 on to Nb foils was conducted using Thermionics 100-0030 with a electron beam heated source. The emission current was 200 mA with a potential difference between the cathode and the anode being 3 KV. The resulting deposition rate was 10 λ/sec. The thickness of the Al_2O_3 deposit in the present study was 1 μm.

The hot dipping and anodizing technique for the formation of Al_2O_3 coating consisted of the following steps. First, Nb foils were hot dipped into a molten aluminum bath for 2 minutes which was kept at a temperature of 930^0C. Second, the hot dipped Nb foils was anodized in an electrolyte containing 5 wt.% of sulfuric acid to convert the aluminum into alumina. The anodizing was conducted at ambient temperature, and a constant DC voltage ranging from 10 to 20 volts was applied to produce current densities ranging from 5 to 25 mA/cm^2. Anodizing time was 30 minutes. More detailed description of the coating techniques can be found elsewhere [11].

Fabrication of Laminate Composites

The test specimens were three layer composites with the coated or uncoated Nb foil sandwiched in between two layers of $MoSi_2$. The thickness of the Nb foils used was 0.127 mm. The specimens were prepared by stacking the coated or uncoated Nb foil with two layers of commercially pure $MoSi_2$ powder of -325 mesh and then vacuum hot pressing at 1400^0C for 1 hr with a pressure of 40 MPa. In order to minimize residual thermal stresses, the hot pressed discs were held in the hot pressing chamber at 800^0C for 1 hour before cooling down to room temperature. The discs were then cut into rectangular short bar with dimensions of 8.28x9.25x14.29 mm to prepare the specimens for the measurement of interfacial fracture energy.

Measurement of Interfacial Fracture Energy

The measurement of the interfacial fracture energy was conducted on chevron notched short bars using the procedures recommended in reference [12]. The technique involves determining the critical stress intensity factor from the peak load of the notched bars and then converting the critical stress intensity factor to the fracture energy of the interface. The equation used to calculate the fracture energy of the interface, G_{IC}, is [12]

$$G_{IC} = \frac{K_{ICSR}^2}{E} \qquad \ldots\ldots\ldots \quad (1)$$

where E is the elastic modulus of $MoSi_2$ and K_{ICSR} is the critical stress intensity factor determined from the peak load of the short bar test.

In the present study, however, a modified specimen geometry, as shown in Fig. 1, was used. An advantage of the present geometry is that there is no need for compliance calibration due to symmetry of compliance of the specimen with respect to the interface. The notch in the short bar was cut parallel to the foil using a diamond wafering blade with a thickness of 0.4 mm. The thickness of the notch was chosen to be slightly larger than that of the foil to insure that the
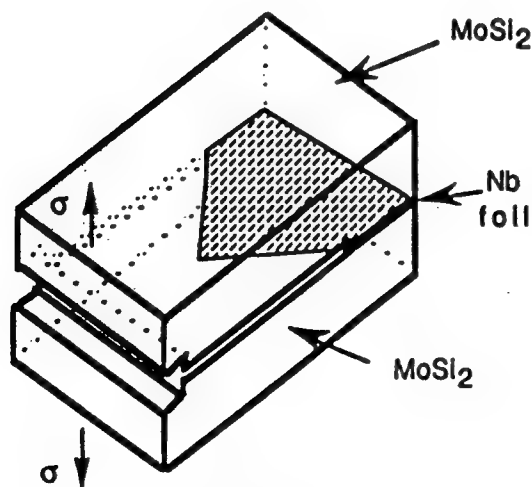

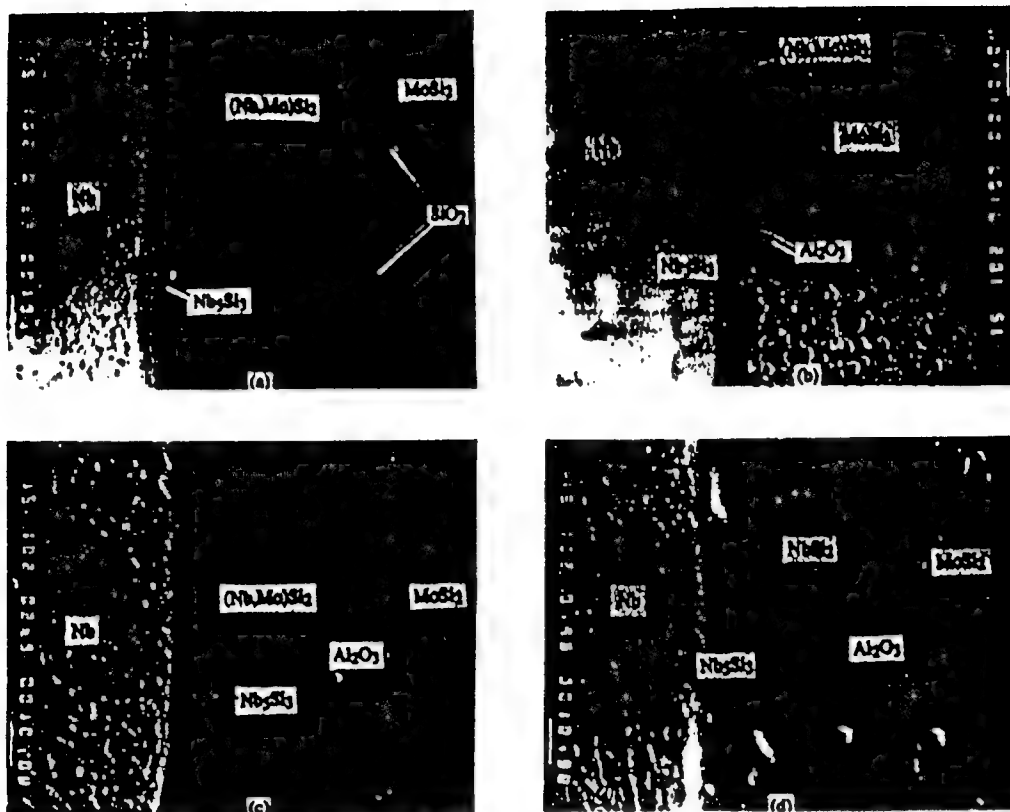Fig. 1 Short bar specimen geometry

Fig. 2 Interfacial Microstructures of MoSi2/Nb laminate composites with different processing conditions.
(a) uncoated Nb, (b) PVD coated Nb, (c) sol-gel coated Nb, and (d) hot-dipping-and-anodizing coated Nb.

initiation and propagation of the crack is at the weakest position among various interfaces between matrix/coating/reinforcement. The specimen was loaded at a constant test machine crosshead speed of 0.005 in/min using a hydro-servo controlled MTS. The load was recorded as a function of the crosshead displacement.

RESULTS

Interfacial microstructures of MoSi2/Nb laminate composites with different processing conditions are shown in Fig. 2. The detailed mechanism for the formation of the interfacial compounds (interphases) between MoSi2 and Nb and the effect of the coatings on the interphase formation can be found elsewhere [11,13,14]. Extensive interphase formation was observed in MoSi2/uncoated Nb composites, resulting in the formation of intermetallics of $(Nb,Mo)Si_2$ and Nb_5Si_3. When the Al_2O_3 coating was applied, either the thickness of the interphases was reduced or the composition of the interphase was changed (Fig. 2d). Such changes have been attributed to the the retardation of Si diffusion and the suppression of Mo and Nb interdiffusion across the coatings [14].

A typical load displacement curve of the hot-dipping-and-anodizing coated Nb/MoSi2 laminate and the corresponding fracture surface at the chevron crack are shown in Fig. 3. A stable crack propagation has been achieved, as indicated by the fluctuation in the curve near the maximum load. Therefore, the maximum load was used to calculate G_{IC} with the aid of eq. (1). By examining the two fracture surfaces of a broken short bar with SEM and EMP, the failure location at the interface could be determined. Depending on the processing conditions, the crack propagates along an interface in some cases, or by kinking between two interfaces, or only inside MoSi2 matrix in other cases. Owing to this feature, the measured fracture energy of interface using the notched short bar has been referred to as fracture energy of the interfacial region of the laminates. The measured fracture energies of the interfacial region and failure locations for laminate composites with different processing conditions are summarized in
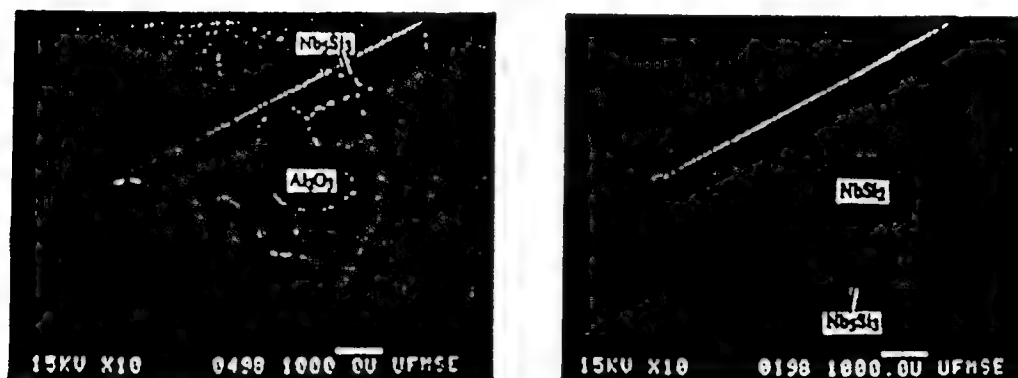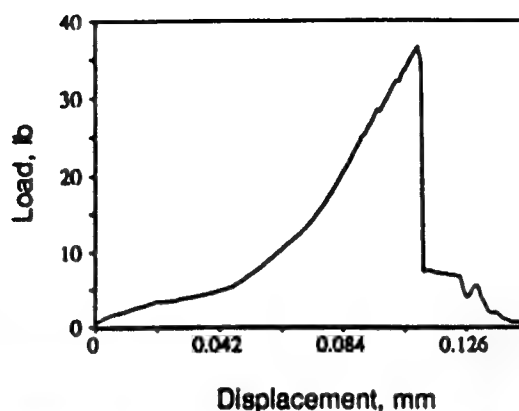
Fig. 3 A typical load displacement curve of the hot-dipping-and-anodizing coated Nb/MoSi$_2$ laminate and the corresponding fracture surfaces at the chevron crack.

Table 1. For comparison, fracture energy for MoSi$_2$ alone is also included in the table.

In the case of the hot-dipping-and-anodizing, the failure of the laminate occurred mainly along the Al$_2$O$_3$/NbSi$_2$ interface. A small portion of the failure also occurred in the Nb$_5$Si$_3$ phase, as shown in Fig. 3, which was probably due to the discontinuity of the oxide coating generated during the anodizing process and/or the roughness of the interface. Similar fracture surface was observed for the sol-gel coated Nb/MoSi$_2$ laminate. Correspondingly, the specimens using the two coating techniques mentioned above exhibited a similar fracture energy of the interfacial region. By changing the sol-gel processing control parameters, the interphase formed can be limited to be only one phase, i. e., Nb$_5$Si$_3$, instead of (Nb,Mo)Si$_2$ and Nb$_5$Si$_3$ [11,13]. However, the measured fracture energy of the interfacial region in this case is the same as Al$_2$O$_3$/(Nb,Mo)Si$_2$ interface, as shown in Table 1.

Quite different fracture surface was observed for the PVD coated specimens. As shown in Fig. 4, failure location in this case was partially in MoSi$_2$ and partially at the interface of

Table 1. Fracture energy and failure location of the interfacial region in the coated and uncoated Nb/MoSi$_2$ systems

System	Failure location	Toughness, G$_{IC}$, J/m^2
MoSi$_2$ alone		33.7 ± 1.4
MoSi$_2$/uncoated Nb	inside the MoSi$_2$	> 33.7
MoSi$_2$/sol-gel coated Nb	Al$_2$O$_3$/(Nb,Mo)Si$_2$ interface or Al$_2$O$_3$/Nb$_5$Si$_3$ interface	16.1 ± 1.3
MoSi$_2$/hot-dipping-and-anodizing coated Nb	Al$_2$O$_3$/NbSi$_2$ interface	15.5 ± 1.6
MoSi$_2$/PVD coated Nb	partially inside the MoSi$_2$ and partially at Al$_2$O$_3$/(Nb,Mo)Si$_2$ interface	31.7 ± 3.4

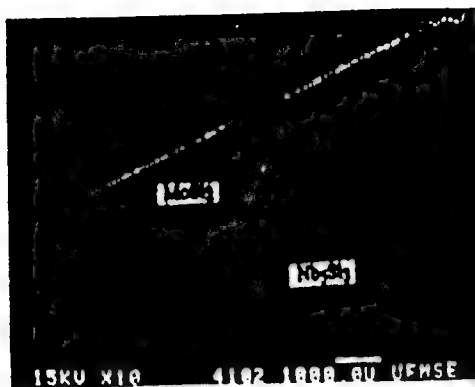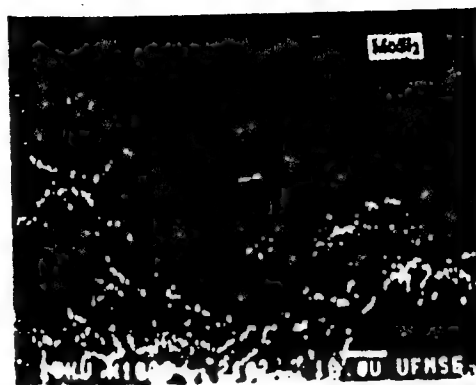Fig. 4 Fracture surface at the chevron crack of a PVD coated Nb/MoSi$_2$ specimen

Fig. 5 An enlarged fracture surface of the tip area in Fig. 4.

Al$_2$O$_3$/(Nb,Mo)Si$_2$. This is believed to be due to the small and frequent discontinuity of the oxide coating (Fig. 2b) caused by the presence of the SiO$_2$ and free Si in the commercially pure MoSi$_2$ powder, as shown in Fig. 2(a) and reported in elsewhere [15,16]. Because of such small and frequent discontinuity of the coating, the fracture resistance along the Al$_2$O$_3$/(Nb,Mo)Si$_2$ interface has been increased. Combining the effect of the roughness of the interface (Fig. 2b), crack is unable to propagate along the Al$_2$O$_3$/(Nb,Mo)Si$_2$ interface, but have to kink between the interface and MoSi$_2$ matrix to obtain crack propagation with minimum energy consumption.

For the uncoated Nb/MoSi$_2$ laminates, the failure was observed to take place inside MoSi$_2$ rather than at the interfaces, indicating that the interfacial region has a higher fracture energy than the matrix. The fracture energy of MoSi$_2$ measured in the present study is 33.7 J/m^2. Thus, the fracture energy of the interfacial region in uncoated Nb/MoSi$_2$ laminates must be higher than this value. Indeed, all the measurements conducted on uncoated Nb/MoSi$_2$ laminates were about 36.4 J/m^2 because the crack in MoSi$_2$ failed to follow the chevron notched plane strictly.

DISCUSSION

Various interphases were formed in the present study due to the diffusion of Si, Mo and/or Nb through the coating. The thickness and the nature of the interphases were found to depend on the processing temperature and time [13,14]. Because of the presence of the various interphases, the interfaces at the interfacial region have been divided into three categories, as shown in Table 2. Category I consists of an interface (bonding) between the oxide coating and intermetallics. Category II is composed of a bond between two intermetallics. Category III is the interfaces which have a bond between a metal and an intermetallic. Because of the interaction, no direct bonding between oxide and metal was observed. By examining the failure locations and fracture energy of the interfacial region measured, the fracture energy for the interfaces present in this study can be estimated and summarized in Table 2.

It is noted that fracture energy for the oxide bond, category I, is lower than the bonds between intermetallics or between a metal and an intermetallic (categories II and III). It is at a level of 16 J/m^2 in the present instance, which is even lower than the fracture energy of the alumina itself (~ 20-40 J/m^2). The low fracture energy of the oxide bond is attributed to the low bond strength between alumina and silicides involved. As concluded by Sutton and Feingold [17], the bond strength between oxide and other materials is directly related to the amount of interaction between the two materials, and the free energy of formation of the other materials' oxide is an important criterion in determining the interaction. Weak bonding will form when the conditions are unfavorable for the formation of other oxides. In the present case, elemental Mo, Nb and Si have a lower free energy of formation of their oxides in comparison with Al$_2$O$_3$ [18]. As such, formation of silica, niobium and molybdenum oxides,

Table 2. Fracture energy of the interfaces

System (category)		G_{IC}, J/m^2
MoSi$_2$		33.7
Al$_2$O$_3$/(Nb,Mo)Si$_2$	(I)	~ 16
Al$_2$O$_3$/NbSi$_2$	(I)	~ 16
Al$_2$O$_3$/Nb$_5$Si$_3$	(I)	~ 16
Al$_2$O$_3$/MoSi$_2$	(I)	> 16 ?
MoSi$_2$/(Nb,Mo)Si$_2$	(II)	≥ 33.7
Nb$_5$Si$_3$/(Nb, Mo)Si$_2$	(II)	≥ 33.7
Nb$_5$Si$_3$/Nb	(III)	≥ 33.7

directly or by decomposition of MoSi$_2$, is unfavorable in terms of free energy change. Therefore, it is expected that the reactivity of the silicides with alumina would be very low, resulting in a low bond strength. On the otherhand, if the free energy of formation is more favorable for forming other oxides instead of alumina, strong bond may form. An example is given by the work of Dalgleish et al. [19]. They found that crack always initiated in the alumina adjacent to the interface of a Al-Mg alloy bonded to an alumina. High bond strength in this case can be attributed to a much more negative free energy of formation for MgO than that of Al$_2$O$_3$.

Moreover, the fracture energy of category I interface was found to be insensitive to the change in the composition of the silicides, as shown in Table 2. This is probably due to the similarity of Nb and Mo in their atomic structures. If this is true, Al$_2$O$_3$/MoSi$_2$ interface should show similar fracture energy. However, no failure at Al$_2$O$_3$/MoSi$_2$ interface was observed in the present study. As shown in Fig. 2(c) and (d), one major difference of Al$_2$O$_3$/MoSi$_2$ interface from the Al$_2$O$_3$/NbSi$_2$ and Al$_2$O$_3$/(Nb,Mo)Si$_2$ interfaces is that the former is rougher than the latter. Such roughness of the interface can increase fracture resistance by the mechanism of interlocking and crack deflection. Thus, Al$_2$O$_3$/MoSi$_2$ interface shows a higher fracture resistance than Al$_2$O$_3$/NbSi$_2$ and Al$_2$O$_3$/(Nb,Mo)Si$_2$ interfaces, although their bond strengths may be similar.

Category II and III interfaces all exhibit higher fracture resistance than MoSi$_2$ matrix, indicating the bond strength between two intermetallics or between a metal and an intermetallic is high. In this case, crack was observed to propagate inside the MoSi$_2$ matrix instead of inside the interphases formed. However, this does not necessarily mean that MoSi$_2$ has a lower inherent fracture resistance than that of the interphases, (Nb,Mo)Si$_2$ and Nb$_5$Si$_3$. It is believed that the low apparent fracture resistance of MoSi$_2$ in the present instance is partially related to the high porosity and SiO$_2$ in MoSi$_2$ adjacent to the interface, as shown in Fig. 2(a). High porosity is due to the fast diffusion of Si into Nb and segregation of vacancy onto the opening channel of MoSi$_2$ powder compact. In contrast, the interphases formed are very dense, as shown in Fig. 2. Because the pores distribute along the grain boundary of MoSi$_2$, it is expected that crack would propagate along the grain boundary and an intergranular fracture results. Indeed, this is confirmed by SEM observation. Fig. 5 shows an enlarged fracture surface of the tip area in Fig. 4. Similar intergranular fracture was observed in MoSi$_2$ specimens, consistent with the report by Kaufman et al. [15]. Therefore, low apparent fracture resistance of MoSi$_2$ is partially caused by the presence of porosity and SiO$_2$.

Different processing routes have shown little effect on the fracture energy of the interfacial region as long as the oxide coating is thick enough to prevent the breakdown of the coating by the attack of SiO$_2$ and free Si. Fracture energies for the interfacial region generated by sol-gel technique and the hot-dipping-and-anodizing technique are similar because a thick and continuous coating has been formed in general by these two techniques. The results indicate that bond strength merely depends on chemical bonding rather than on a long range interaction force. For the PVD coated laminates, a frequent discontinuity in the coating results in a partial oxide bond and a partial intermetallic bond interface, leading to an increase in fracture resistance of the interfacial region.

CONCLUDING REMARKS

The present set of experiments have demonstrated that fracture energy of an interfacial region depends on the interfacial bond strength, roughness of interface and microstructure of the two component materials at the interface. Weak bond strength leads to a low interfacial fracture energy. Roughness of the interface increases the interfacial fracture energy. Porosity in one of the two component materials at the interface could lead to a low fracture energy of the interfacial region due to the crack propagation along the weak path in one of the component materials instead of along the interface. Processing routes can affect fracture energy of the

interfacial region by changing interphase formation, changing roughness of interface, or by changing microstructure of materials adjacent to the interface. However, if such changes have not been brought out during processing, there will be little effect of processing routes on fracture energy of the interfacial region.

REFERENCES

1. K. M. Prewo, in High Temperature/High Performance Composites, edited by F. D. Lemkey, et al. (Mater. Res. Soc. Symp. Proc., 120, Pittsburgh, PA, 1988), pp. 145-56.
2. R. J. Diefendorf and R. P. Boisvert, in High Temperature/High Performance Composites, edited by F. D. Lemkey, et al. (Mater. Res. Soc. Symp. Proc., 120, Pittsburgh, PA, 1988), pp. 157-62.
3. A. G. Evans and D. B. Marshall, in High Tech Ceramics, edited by P. Vincenzini, (Elsevier Science Publishers B. V., Amsterdam, 1987), pp. 213-46.
4. R. W. Davidge, in High Tech Ceramics, edited by P. Vincenzini, (Elsevier science Publishers B. V., Amsterdam, 1987), pp. 763-77.
5. B. Harris, P. W. R. Beaumont and E. Moncunill de Ferran, J. Mater. Sci., 6, 238(1971).
6. G. R. Sidey and F. J. Brandshaw, presented at Int. Conf. Carbon Fibers: Their Composites Appl., London, (1971).
7. J. Fitz-Randolph, D. D. Phillips, P. W. R. Beaumont and A. S. Tetelman, presented at St. Louis Symp. Advan. Fiber Composites, 5th, St. Louis, Missouri, (1971).
8. E. F. Olster and R. C. Jones, Massachusetts Inst. of Technol. Tech. Rep., R70-75, (Nov. 1970).
9. L. Xiao and R. Abbaschian, submitted to Metall. Trans., (1991).
10. D. E. Clark, W. J. Dalzell and D. C. Folz, Ceram. Eng. Sci. Proc., 9, 1111(1988).
11. L. Xiao and R. Abbaschian, to be published.
12. J. J. Mecholsky and L. M. Barker, in Chevron-Notched Specimens: Testing and Stress Analysis, ASTM STP 855, edited by J. H. Underwood, S. W. Freiman and F. I. Baratta, (ASTM 1916 Race Street, Philadelphia, PA, 1984), pp. 324-36.
13. L. Xiao, Y. S. Kim and R. Abbaschian, in Intermetallic Matrix Composites, edited by D. L. Anton, P. L. Martin, D. B. Miracle and R. McMeeking, MRS Proc., 194, 399(1990).
14. L. Xiao and R. Abbaschian, submitted to Mater. Sci. Eng., (1991).
15. J. D. Cotton, Y. S. Kim and M. J. Kaufman, Mater. Sci. Eng., A144, 287(1991).
16. J. D. A. Lofvander, J. Y. Yang, C. G. Levi and R. Mehrabian, in Advanced Metal Matrix Composites for Elevated Temperatures, edited by M. N. Gungor, E. J. Lavernia and S. G. Fishman, (ASM International, 1991), pp. 1-10.
17. W. H. Sutton and E. Feingold, Mater. Sci. Res., 3, 577(1966).
18. C. T. Lynch and H. M. Burte, in Metal Matrix Composites, ASTM STP 438, (Amer. Soc. Test. Mater., Philadelphia, PA, 1968), pp. 3-25.
19. B. J. Dalgleish, K. P. Trumble and A. G. Evans, Acta Metall., 37, 1923(1989).

Evaluating a Technique for Determining the Toughening of Brittle Matrix by Ductile Reinforcements

L. Xiao and R. Abbaschian
University of Florida
Gainesville, FL, USA

Lingang Xiao and Reza Abbaschian
Department of Materials Science and Engineering, University of Florida,
Gainesville, FL 32611

ABSTRACT

Substantial toughening of intermetallics and ceramics by ductile reinforcements has been established. To evaluate the toughening by ductile reinforcements, it is necessary to know the stress-displacement curve of the ductile phase constrained by the brittle matrix. In the present study, tensile tests involving the specimen with a ductile reinforcement imbedded in the notched brittle matrix have been used. Effects of experimental variables, notch geometry in the vicinity of the ductile phase, depth of the notches and size of ductile reinforcement, on the measured stress-displacement curves have been evaluated. The experimental results showed that these variables played important roles in the stress-displacement curves. The results are analyzed using theory of notch stresses and finite element method. A formula to estimate these effects of the variables has been put forward.

I. INTRODUCTION

It has been established that substantial toughening of brittle matrices can be achieved by incorporating ductile reinforcements [1-9]. The primary mechanism responsible for the enhanced toughness has been attributed to be bridging by intact ligaments of the ductile phase behind the advancing crack tip [10-14]. The physical mechanism of toughening by intact ligaments of the ductile phase is straightforward. If ductile ligaments span the advancing crack, they must stretch as the crack opens until they fracture or decohere. The work of stretching contributes to the toughness of the composite and the increased fracture toughness of the composite can be obtained directly from the J-integral around the traction zone as [11,12]

$$\Delta G = V_f \int_0^{u^*} \sigma(u)\, du \qquad \ldots\ldots\ldots \quad (1)$$

where u is the crack opening, $\sigma(u)$ the nominal stress on the ligament, u^* the crack opening at the end of the traction zone and V_f is the area fraction of reinforcements on the crack plane. Once $\sigma(u)$ as a function of crack opening is known, the increase in toughness of the composite can be evaluated through eq. (1).

Recognizing that $\sigma(u)$ is different from that measured in a simple tensile test, several investigators [15-17] have used a test procedure to
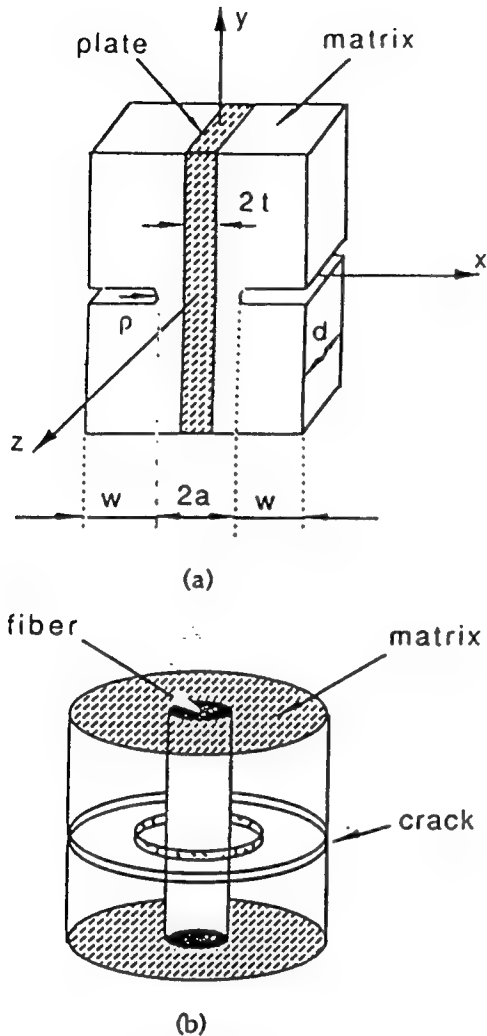
(a)

(b)

Fig. 1 (a) Schematic of a composite laminate test specimen;
(b) Schematic of a composite cylinder test specimen.

evaluate σ(u). The test procedure is based on the concept that the stress-displacement relationship obtained from one ductile reinforcement imbedded in a brittle matrix can be used to describe the mechanical characteristics of the reinforcements in the composites. The basic test specimen consists of one ductile filament or foil imbedded in a precracked brittle matrix, as shown in Fig. 1, and a tensile test is conducted to evaluate the σ(u). Clearly, in order to accurately simulate constrained condition of the reinforcements in the matrix, it is necessary to be aware of effects of experimental variables, such as depth of the notch and geometry of the notch tip, on the measured stress-

displacement relation. In the present study, effects of these two variables are evaluated and appropriate combination of these two variables with size of ductile reinforcement is also evaluated. The experimental results are analyzed using theory of notch stresses and finite element method. A formula to estimate the effects of the variables is established and will provide guideline for the future design of proper test specimens to obtain the intrinsic properties of the reinforcements.

II. EXPERIMENTAL

2.1 THE TEST SPECIMEN - The test specimens used in this study were laminated composites with pure Nb foil sandwiched between $MoSi_2$ matrices, as shown in Fig. 1(a). The specimens were prepared by stacking a Nb foil with two layers of $MoSi_2$ powder of -325 mesh at an appropriate ratio, and then vacuum hot pressing at 1400^0C for 1 hour under a pressure of 40 MPa to get the composite discs. Three different thicknesses of Nb foils (0.25, 0.5 and 1.0 mm) were used to prepare the composite discs. The discs were then cut into rectangular tensile test bars with dimensions of 5.0x3.8x30.0 mm. In order to obtain the relation between crack propagation and stresses, surfaces of the tensile test bars perpendicular to the plane of the Nb foil were polished before notching. The notches in the $MoSi_2$ matrix were introduced using diamond wafering blades. The variation in radius of the notch tip was obtained by using different sizes of diamond wafering blades. Three different radii of notch tips used in the present study were 0.075, 0.165 and 0.270 mm. Fig. 2 shows typical precracks in a test specimen and a close-up image of one of the notch tips with a radius of 0.075 mm. The notches on the both sides were symmetrical with respect to the central Nb foil. Depth of the notches was measured in terms of the width of the narrowest cross section, 2a, as shown in Fig. 1(a). The reason for that will become obvious in Section 3.

2.2 TEST PROCEDURE - Displacement controlled tensile tests were conducted with INSTRON. Wedge-type grips were used to clamp the specimens and load train alignment was achieved by coupling the top grip to a universal joint. Strictly speaking, to simulate the interaction between ductile reinforcements and cracks, very sharp precracks should be introduced in the matrix. However, this is difficult to do or very tedious procedure has to be
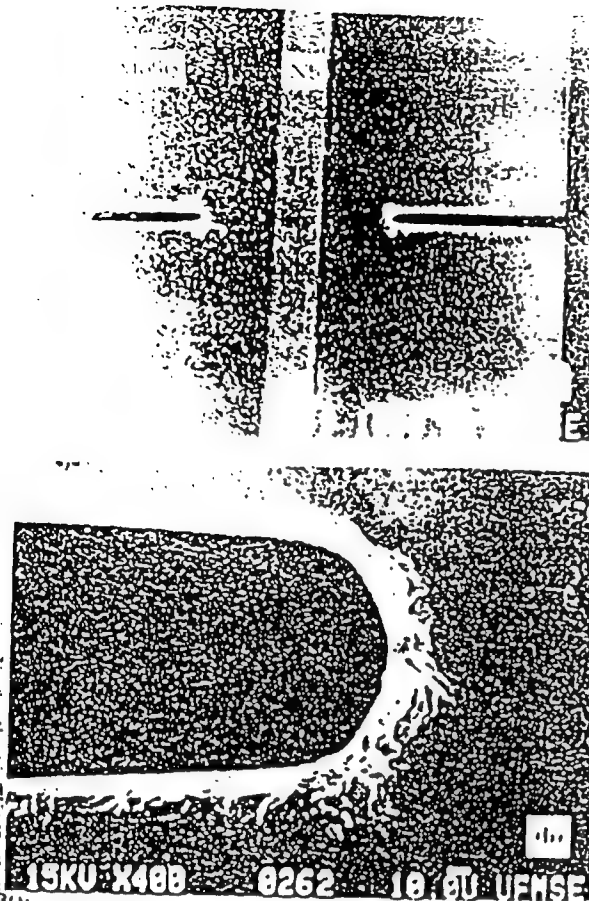
Fig. 2 (a) A general view of precracks in a composite laminate test specimen with a 0.5 mm thick Nb lamina and 0.075 mm notch tip radius; (b) A close-up image of one of the notch tips in (a).

taken, such as initiating cracks by fatigue or by introducing a chevron form of notch. In the present study, a very slow displacement speed, 0.005 in/min, was used to alleviate this conflict. With such low speed, it was easy to unload the specimens at the load level desired for examining the specimens with SEM to identify the critical stress for initiating a crack at the notch tip and to observe sharpness of cracks and crack propagation.

For comparison, the critical stress for initiating a crack at the notch tip was also detected by conducting tensile tests on some notched monolithic $MoSi_2$ specimens.

III RESULTS AND DISCUSSION

3.1 STRESS DISTRIBUTION IN A MONOLITHIC MATERIAL SPECIMEN

Because of geometry of the specimens in the present study, stress distribution in the specimens consisting of a monolithic material can be approximately treated as a problem of a flat bar with a deep notch on each side. H. Neuber [18] has already derived a formula to calculate stress distribution over the narrowest cross section of such specimen under a tensile loading (Fig.3). The stress distribution in question is only a function of a/ρ and not affected by depth of the notch, w (Fig.1). The formula proposed is

$$\sigma_v = \frac{\Lambda}{h^2} \cosh v \cos v \, (2 + \frac{\cos^2 v_0 - \cos^2 v}{h^2}) \quad \ldots\ldots\ldots \quad (2)$$

where Λ and h are defined as

$$\Lambda = \frac{F}{2ad} \frac{\sin v_0}{v_0 + \sin v_0 \cos v_0} \quad \ldots\ldots\ldots \quad (3)$$

$$h^2 = \sinh^2 v + \cos^2 v \quad \ldots\ldots\ldots \quad (4)$$

Meanings of the symbols used in eqs. (2)-(4) are as follows. v and v are elliptical coordinates and the relations between elliptical coordinates and Cartesian coordinates are

$$y = \sinh v \cos v$$
$$x = \cosh v \sin v$$

σ_v is stress in v direction at any position in the plane of the narrowest cross section, F the tensile loading, F/2ad the nominal stress in y direction over the narrowest cross section, v_0 a constant which defines contour of the notches with a formula of $v = v_0$ (a hyperbola contour). The reason the contour of the notches was assumed as a hyperbola in the derivation of eq. (2) was because curvature of the notch tip had much more considerable effect on the stress distribution than the additional contour of the notch and the assumption of a hyperbola contour permitted the simplest possible calculation. Due to such an assumption, the contour of the notch is related to the width of the narrowest cross section and curvature of the notch tip with a formula of $v_0 = \arccos(1/\sqrt{(a/\rho+1)})$. The stress component, σ_y, over the narrowest cross section can be obtained from eq. (2) when setting v=0.

The tensile tests on the notched monolithic $MoSi_2$ specimens showed that the nominal stress over the narrowest cross section for initiating cracks at the notch tips, $\sigma_{crack(nom)}$, was 66.2 ± 13.6 MPa for
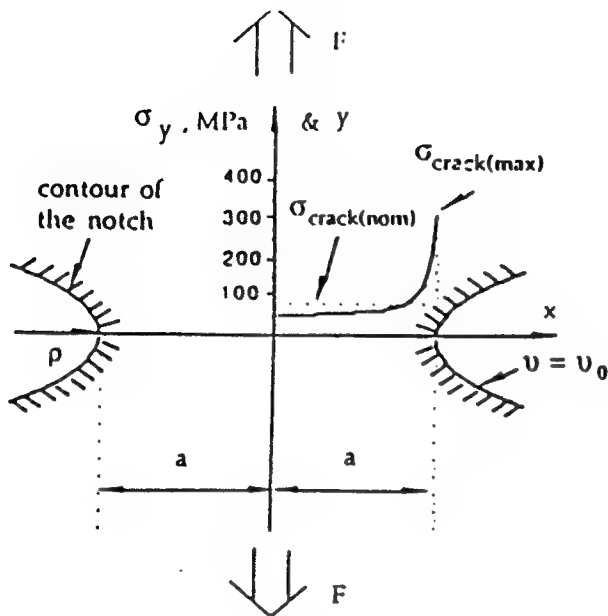
Fig. 3 Stress distribution over the narrowest cross section and the corresponding contour of the notches in a notched bar consisting of a monolithic MoSi$_2$

specimens with a width of 2.0 mm at the narrowest cross section and a notch tip radius of 0.075 mm. Inserting the $\sigma_{crack(nom)}$ measured and the specimen's dimensions into eq. (2) and setting $v = 0$, it was found that the stress at the notch tip at the point of crack initiation, $\sigma_{crack(max)}$, was 310.4 ± 60.6 MPa, as shown in Fig. 3. It is noteworthy that $\sigma_{crack(max)}$ calculated in the present study is very close to the flexural strength (319MPa) of monolithic MoSi$_2$ measured using four-point bend tests in a related study [19]. The physical meanings of these two quantities are the same, i.e., both of them are the maximum tensile stress the MoSi$_2$ can sustains before a crack is initiated. The results suggest that with a proper design of the notched specimen, tensile strength of brittle materials can be evaluated with such precracked specimen geometry.

3.2 STRESS ANALYSIS OF THE SANDWICHED SPECIMEN - In the case of sandwiched specimens, eq. (2) can still be utilized provided some assumptions are made. It is noted that there is a deformation continuity across the matrix/reinforcement interface before the debonding at the interface occurs. Therefore, it is assumed that the stress σ_y in the Nb side at the interface is 3.6 times less than that in the MoSi$_2$ side during the elastic stage because the elastic modulus of MoSi$_2$ (379GPa) is 3.6 times larger than that of Nb (105GPa). It is also assumed that the stress distribution described by eq. (2) is still valid even inside the Nb reinforcement but with all the stresses being only 1/3.6 of the stresses calculated using eq. (2). With the above assumptions, the stress distribution in the sandwiched specimens can be calculated using eq. (2). Errors introduced with the assumptions are estimated using finite element analysis and the results are presented in the Appendix.

Measured $\sigma_{crack(nom)}$ for laminated composites with 0.5 mm thick Nb lamina as a function of width of the narrowest cross section is shown in Fig. 4. If $\sigma_{crack(max)}$ of 310.4 MPa measured from the monolithic MoSi$_2$ is taken as the stress to initiate cracks at the notch tips in the laminated composite specimens, $\sigma_{crack(nom)}$ for the laminated specimens can be calculated using eq. (2) with the aforementioned assumptions. The calculated $\sigma_{crack(nom)}$ is also included in Fig. 4 for comparison. As seen in the figure, the theory of notch stresses predicts that $\sigma_{crack(nom)}$ increases with decreasing width of the narrowest cross section and such trend is confirmed by the measurement when the narrowest cross section is wide. However, the predicted value deviates from the experimental data when width of the narrowest cross section is small. Such deviation is caused by the residual thermal stresses, as discussed below. Using eq. (2) and the aforementioned assumptions,
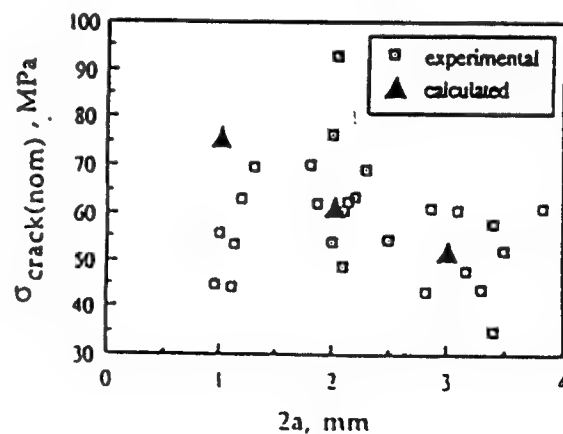

Fig. 4 A plot of $\sigma_{crack(nom)}$ vs width of the narrowest cross section for composite laminates with 0.5 mm thick Nb lamina and 0.075 mm notch tip radius.
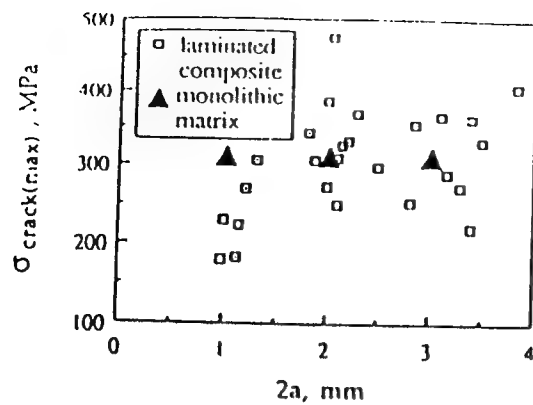
Fig. 5 A plot of $\sigma_{crack(max)}$ vs width of the narrowest cross section. The data for the laminated composites are calculated from the data in Fig. 4.

Fig. 6 Effect of notch size on the nominal stress for initiating cracks in the matrix.

the measured $\sigma_{crack(nom)}$ in Fig. 4 can be used to calculate $\sigma_{crack(max)}$ for the laminated specimens. The calculated $\sigma_{crack(max)}$ are presented in Fig. 5 as a function of width of the narrowest cross section. In principle, the stress to initiate cracks at notch tips for all the specimens should be the same in spite of different notch depths. However, Fig. 5 shows that the measured $\sigma_{crack(max)}$ is lower for deeply notched specimens than other specimens. It is believed that this conflict is caused by the residual thermal stresses which contribute a tensile stress in y-direction (Fig.1) of about 19 MPa to the $MoSi_2$ adjacent to the interfaces [19]. Superposition of the residual stresses to the external stress results in a drop of $\sigma_{crack(max)}$ when width of the narrowest cross section is small.

Effect of notch size on the measured $\sigma_{crack(nom)}$ is shown in Fig. 6. Taking 310.4 MPa as the stress to initiate cracks at the notch tips in the laminated specimens, $\sigma_{crack(nom)}$ has been calculated using eq. (2) as a function of notch size and the results are also presented in Fig. 6. As expected, the theory of notch stresses predicts increase of $\sigma_{crack(nom)}$ with increasing radius of notch tip. However, the measured $\sigma_{crack(nom)}$ shows no increase or a very small increase from 65.86 ± 12.48 to 71.15 ± 16.32 and then to 69.62 ± 10.14 MPa as radius of the notch tip increases from 0.075 to 0.165 and then to 0.27 mm. The results suggest that when radius of the notch tip is large, such as 0.165 and 0.27 mm, the stress to initiate cracks at the notch tips is no longer controlled by radius of the notch tips, but by intrinsic defects such as porosity
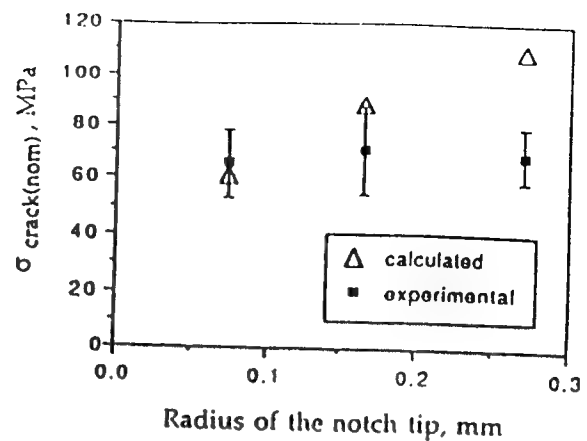
in the matrix or the defects introduced during the notching. Close examination of Fig. 2(b) reveals that some defects are indeed introduced at the notch tip. Such defects could become decisive factors when radius of the notch tip is large. The results indicate that a small radius of notch tip should be used if the stress to initiate cracks at the notch tips is to be controlled.

3.3 LOAD-DISPLACEMENT CURVES - Fig. 7 shows effect of notch depth (0.075 mm tip radius) on the load-displacement curves of laminated composites with 0.5 mm thick Nb lamina. Sudden load drops in curves A and B correspond to the load for initiating cracks at the notch tips. The load for initiating cracks in curve C is about 40 lbs and it is hard to ascertain from the curve because of small load drop. The reason the load drop in curve C is
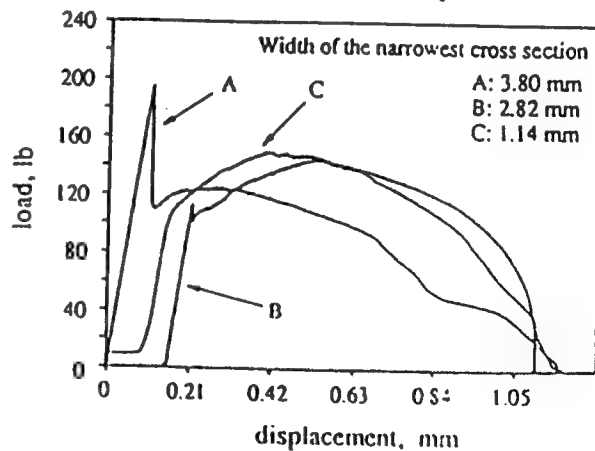

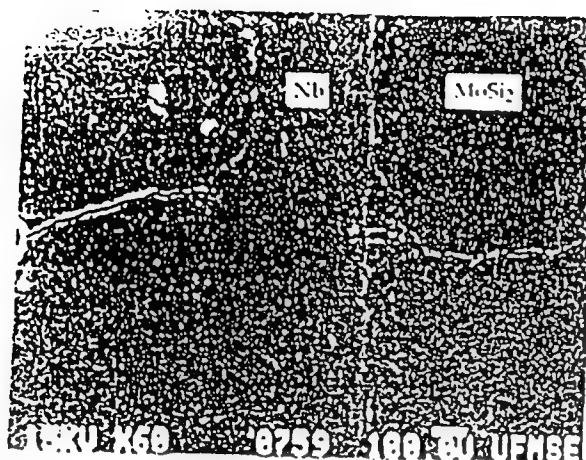Fig. 7 Effect of notch depth on the load-displacement curves of constrained Nb

Fig. 8 A SEM micrograph of a laminated specimen unloaded after the specimen has passed the sudden load drop in the load-displacement curve.

notch depth and the area under curve C is regarded as a truly representative of the contribution of the ductile reinforcements to the toughness of a brittle matrix composite.

The present experiments showed that cracks propagated through the whole matrix as soon as the cracks were initiated at the notch tips, and from that point on the load was carried only by the central Nb lamina. Fig. 8 shows such a typical crack propagation. Nominal stress carried by the central Nb lamina right after the crack propagation through the whole matrix, $\sigma^*_{Nb(nom)}$, is calculated using eq. (2) by assuming that 310.4 MPa is the stress to initiate cracks at the crack tips and the load reached at the point of initiating cracks is carried totally by the Nb lamina. The calculated results for different thicknesses of Nb laminae are plotted as a function of width of the narrowest cross section in Fig. 9. The maximum stress reached by the constrained Nb measured from the load-displacement curves are 351.3 ± 25.7, 320.4 ± 14.6 and 259.9 ± 22.9 MPa for Nb laminae with a thickness of 0.25, 0.5 and 1.0 mm, respectively. The present experiments showed that if $\sigma^*_{Nb(nom)}$ was below about half of the maximum stress reached by the constrained Nb lamina, then the stress to initiate cracks was not high enough to distort the intrinsic load-displacement curves of the constrained ductile phase. Half of the maximum stress reached by each size of constrained Nb lamina is indicated by arrows in Fig. 9. Thus, a proper combination of size of ductile reinforcement and depth of notch can be found in Fig. 9.

small is because the matrix only carries a small portion of the tensile loading when the width of the narrowest cross section is small. It is noteworthy that when width of the narrowest cross section is large, the stress to initiate cracks could be high enough to distort intrinsic load-displacement curves of the constrained ductile reinforcement, as in the cases of curves A and B.

A proper design of notch depth should remain an appropriate degree of elastic constraints on the ductile phase, and on the other hand it should prevent distortion of the load-displacement curves of the constrained ductile phase. Based on this guideline, the width of the narrowest cross section for curve C is deemed as an appropriate

Fig. 9 A plot of notch depth vs the nominal stress carried by different sizes of constrained Nb laminae right after the crack propagation through the whole matrix
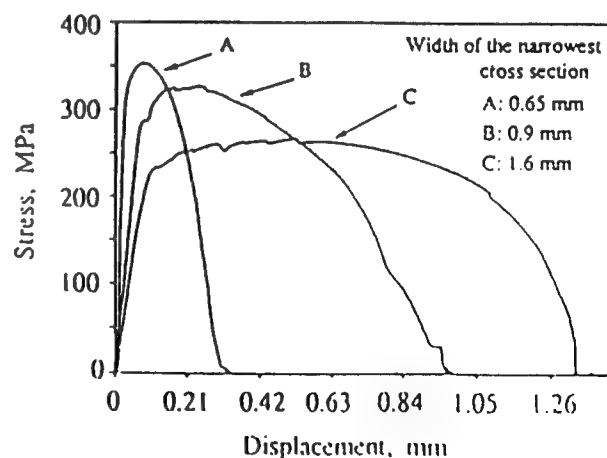

Fig. 10 Stress-displacement curves for different sizes of constrained Nb laminae. The thickness of the Nb laminae is 0.25, 0.5 and 1.0 mm for curves A, B and C, respectively

Examples of stress-displacement curves resulted from a proper combination of reinforcement size and notch depth are showed in Fig. 10. The widths of the narrowest cross section in the figure are 0.65, 0.9 and 1.6 mm for 0.25, 0.5 and 1.0 mm thick Nb laminae, respectively. It can be seen that with such combinations the load drop in the curves is at the lower stress level and very hard to ascertain. Thus, the area under the curves can be regarded as the contribution of Nb to the toughness of $MoSi_2$ matrix composites. From Fig. 10 and eq. (1), it is concluded that toughness of ductile-phase-reinforced brittle matrix composites increases with increasing size of ductile phases.

IV. CONCLUDING REMARKS

The present set of experiments demonstrate that the formula proposed by H. Neuber to describe the stress distribution of a flat bar with a deep notch on each side can be used to estimate the stress distribution for both notched monolithic and composite laminate tensile specimens. The stress to initiate cracks at the notch tips in the brittle matrix can be predicted using the formula and such stress has been found to be equal to the flexural strength of the basic matrix.

Evaluation of notch size effect indicates that a small radius of notch tip should be used for a better control of the stress to initiate cracks in the matrix. It is shown that in order to remain an appropriate degree of elastic constraints on the ductile phase and at the same time prevent the distortion of the stress-displacement curve of the constrained ductile phase, the nominal stress on the ductile phase at the point of crack initiation in the matrix should be below about half of the maximum stress reached by the constrained ductile phase. Thus, to avoid the distortion of the stress-displacement curve, notch depth should increase with decreasing size of constrained ductile reinforcement.

Although no experiment on composite cylinder specimens has been conducted, it is recommended that the formula proposed by H. Neuber to describe the stress distribution for a tensile rod with a deep circumferential notch could be used to analyze the notched composite cylinder specimen using an approach analogous to the present analysis of composite laminate specimens.

REFERENCES

1. J. L. Chermant and F. Osterstock, J. Mater. Sci., 11, 1939-51(1976).
2. J. Gurland, Trans. ASM, 50, 1063-71(1958).
3. A. V. Virkar and D. L. Jognson, J. Am. Ceram. Soc., 60, 514-19(1977).
4. D. T. Rankin, J. Am. Ceram. Soc., 54, 277-81(1971).
5. P. Hing and G. W. Groves, J. Mater. Sci., 7, 427-34 (1972).
6. V. V. Kristie and P. S. Nicholsin, J. Am. Ceram. Soc., 64, 499-504(1981).
7. C. K. Elliott, G. R. Odette, G. E. Lucas and J. W. Sheckherd, "High Temperature, High Performance Composites", edtied by F. D. Lemkey et al., MRS Proc., 120, 95-102(1988).
8. E. Fitzer, "Whisker- and Fiber-Toughened Ceramics", edited by R. A. Bradley, D. E. Clark, D. C. Larsen and J. O. Stiegler, pp. 165-83, ASM International TM (1988).
9. L. Xiao, Y. S. Kim and R. Abbaschian, "Intermetallic Matrix Composites", edited by D. L. Anton, P. L. Martin, D. B. Miracle and R. McMeeking, MRS Proc., 194, 399-404(1990).
10. L. R. F. Rose, J. Mech. Phys. Solids, 35, 383-405 (1987).
11. L. S. Sigl, P. A. Mataga, B. J. Dalgleish, R. M. McMeeking and A. G. Evans, Acta Metall., 36, 945-53(1988).
12. A. G. Evans and R. M. McKeeking, Acta Metall., 34, 2435-41(1986).
13. P. A. Mataga, Acta Metall., 37, 3349-59(1989).
14. B. Budiansky, J. C. Amazigo and A. G. Evans, J. Mech. Phys. Solids, 36, 167-87(1988).
15. M. F. Ashby, F. J. Blunt and M. Bannister, Acta Metall., 37, 1847-57(1989).
16. H. C. Cao, B. J. Salgleish, H. E. Deve, C. Elliott, A. G. Evans, R. Mehrabian and G. R. Odette, Acta Metall., 37, 2969-77(1989).
17. H. E. Deve, A. G. Evans, G. R. Odette, R. Mehrabian, M. L. Emiliani and R. J. Hecht, Acta Metall., 38, 1491-1502(1990).
18. H. Neuber, "Theory of Notch Stresses - Principles for Exact Stress Calculation", pp. 38-42, Edwards Brothers, Inc., Ann Arbor, Michigan (1946).
19. L. Xiao and R. Abbaschian, "On the Strength and

Stiffness of Ductile Phase Reinforced MoSi$_2$ Composites", to be presented in TMS Fall Meeting, Cincinnati, OH, Oct. 1991.

APPENDIX

Finite element analysis (FEA) of the stress distribution in the notched composite laminates during the elastic deformation was implemented using the finite element software package ANSYS. Due to the symmetry, only one quarter of the specimen was analyzed using both two-dimensional 4-node isoparametric and 6-node triangular elements with an assumption of plane stress deformation. Fig. 11 shows the mesh used in the analysis. A total of 184 elements were used. The displacement at the central plane along y-axis was allowed only in the y-direction, and the plane of the narrowest cross section was allowed to displace only in x-direction.

Stress distributions over the narrowest cross section from analysis of the theory of notch stresses and FEA are shown in Fig. 12 . The input data for the analysis are as follows: the Nb lamina is 0.5 mm thick, width of the narrowest cross section is 1.0 mm, radius of notch tips is 0.075 mm and the nominal stress over the narrowest cross section is 66.75 MPa. It is noted that the stress distributions analyzed using both methods are very similar with
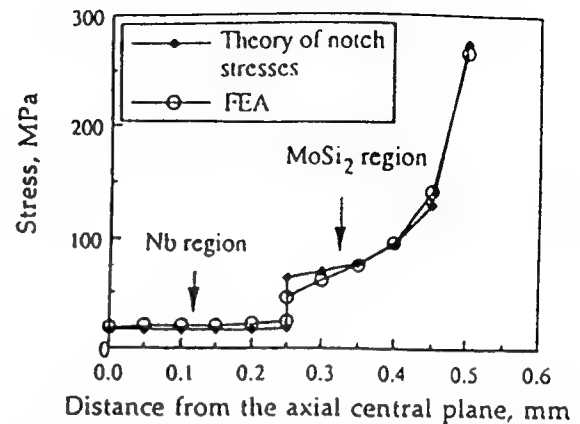
Fig. 12 Comparison between FEA and the theory of notch stresses on the stress distribution over the narrowest cross section.

the maximum stress at the notch tip predicted from the theory of notch stresses 3% higher than that predicted from FEA. The results indicate that the assumptions mentioned in Section 3.2 only introduce 3% error either to the calculation of the maximum stress at the notch tips or to the calculation of the nominal stress over the narrowest cross section.

It is also noted that ratio of the stress in the MoSi$_2$ side to that in the Nb side at the interface is not 3.6 (ratio of the Poisson's ratios of MoSi$_2$ to Nb) but equals to 2.01 for FEA. It is believed that the deviation of the stress ratio from 3.6 is due to the presence of the precracks because if there are no precracks in the FEA, the ratio of the stresses becomes 3.6.

Fig. 11 Mesh used in the FEA.

On the Flow Behavior of Constrained Ductile Phases

L. XIAO and R. ABBASCHIAN

Effects of the matrix/reinforcement interface and the mechanical properties and size of the ductile reinforcement on the flow behavior of the constrained ductile reinforcement have been evaluated using a tensile test on a single Nb lamina imbedded in MoSi$_2$ matrix. It was found that work of rupture of the ductile reinforcement increased with size of the ductile reinforcement and with decreasing fracture energy of the matrix/reinforcement interface. It was also found that the work of rupture normalized by size and yield strength of the reinforcement was dependent on the interfacial properties and size of the reinforcement. Based on the observation, an analytical model is developed which gives insight into the influence on the stress-displacement curve of yield strength, work hardening, fracture energy of matrix/reinforcement interface, and size of the reinforcement. A characteristic decohesion length, which is a function of size of the reinforcement, has been identified by the model and related to the measured decohesion length. The results allow the extrapolation of the work of rupture measured from the large size of constrained ductile phases to the small size of the ductile phases. As the reinforcements used in composites are usually smaller in size than those tested in such tensile tests, the extrapolation of the work of rupture allows the contribution of ductile reinforcements to the toughness of a brittle matrix composite to be calculated.

I. INTRODUCTION

NUMEROUS studies have shown that improved fracture toughness can be achieved by the incorporation of a ductile second phase into a brittle matrix. Examples of current or potential technological significance are tungsten carbide toughened with cobalt network,[1,2] zirconia toughened with zirconium network,[3] alumina toughened with dispersed molybdenum,[4] magnesia toughened with cobalt and nickel particles or fibers,[5] and glass-enamels toughened with dispersed aluminum and nickel particles.[6] Successful toughening has also been observed in titanium aluminide[7] and molybdenum disilicide[8,9] reinforced with niobium pancake or filament.

The primary toughening mechanism of ductile reinforcement has been attributed to the bridging of ductile ligaments.[10-14] When the size of the bridging zone in the wake of the crack tip is small relative to the crack length and the specimen dimension, the contribution to fracture toughness from bridging can be estimated by extending the cohesive force model[15] to the ligament bridging[11,12] and can be written as

$$\Delta G = V_f \int_0^{u^*} \sigma(u)\, du \qquad [1]$$

where $\sigma(u)$ is the nominal stress carried by the constrained ductile reinforcement for a given crack opening u, V_f is volume fraction of the reinforcement, u^* is the crack opening at the point when the ductile reinforcement fails, and the definite integral, designated as ξ in the text, is the work of rupture of the constrained ductile ligament. Thus, the key to predict the increased fracture toughness is to calculate $\sigma(u)$ as a function of crack opening. Recognizing that $\sigma(u)$ is different from that measured in a simple tensile test, several investigators have attempted to relate $\sigma(u)$ to the uniaxial stress-strain properties of the ductile phase. The methods used included a slip-line field analysis,[11,12] finite element methods,[11,13] spring models,[10,14] and geometric models.[11,13,16] Experimental determination of the $\sigma(u)$ has also been conducted with a tensile test on a single constrained ductile phase.[16,17,18] Ashby et al.[16] found that the work of rupture was enhanced by limited decohesion at the interface. Deve et al.[18] however, revealed a more complicated situation; i.e., whether or not a limited decohesion was beneficial to a high work of rupture depended on the work-hardening capability of the ductile phase. Furthermore, Ashby et al.[16] also found that the work of rupture normalized with both the yield strength and the size of the ductile phase (lead metal in their study) was independent on the size of the lead in the matrix. Thus, the work of rupture measured from one size of ductile phase can be extended to other sizes of ductile phase. These results indicate that more experiments are necessary to identify the effects of the interface, and the extrapolation of the work of rupture measured from one size of constrained ductile phase to other sizes of ductile phase also needs to be further investigated in other systems.

The primary objective of the present study is to experimentally examine the effects of properties of the matrix/reinforcement interface and of the size of ductile phase on its flow behavior and, therefore, on the enhanced fracture toughness of the composite. The second goal of this study is to model the stress-displacement relation and to examine the feasibility of extrapolation of the work of rupture measured from a large size of constrained ductile phases to a small size of ductile phases. The system selected for investigation was MoSi$_2$ matrix reinforced with Nb. Since the two components used have similar coefficients of thermal expansion, the residual thermal stresses were minimized, thus simplifying the present stress analysis. Specimens with laminated form

have been used because of the ease of producing the composites with controlled properties, but they still serve the purpose of the present study. The symbols used in the text are defined in Table I.

II. EXPERIMENTAL

Disc-shaped laminated specimens were prepared by stacking a Nb foil with two layers of $MoSi_2$ powder (−325 mesh) at an appropriate ratio and then vacuum hot-pressing at 1400 °C for 1 hour under a pressure of 40 MPa. In order to minimize residual thermal stresses, the hot-pressed discs were held in the hot-pressing chamber at 800 °C for 1 hour before cooling down to room temperature. The residual thermal stresses induced with such processing have been estimated to be small with a tensile stress of 19 MPa in the matrix and a compressive stress of 79 MPa in the Nb on the lamina plane.[19] Three different thicknesses of Nb foils (1.0, 0.5, and 0.25 mm) with a purity of 99.8 pct were used to prepare the laminated specimens. Variation in bonding conditions at the matrix/reinforcement interfaces was achieved by depositing different oxide coatings (Al_2O_3 or ZrO_2) to the Nb surface prior to the hot-pressing or by the development of a reaction product layer between the matrix and reinforcement. Details of the coating procedures can be found in Reference 9.

The hot-pressed discs were cut into rectangular tensile test bars with dimensions of 5.0 × 3.9 × 30.0 mm, as shown in Figure 1. Straight-through notches in the $MoSi_2$ matrix were introduced using a diamond wafering blade

Table I. Symbols and Definitions

$2a$	remaining thickness of reinforcement
d	decohesion length
d_c	characteristic decohesion length
d_m	measured decohesion length
E	Young's modulus
E_t	normalized work of rupture $\int_0^{u^*} \sigma(u)/\sigma_0 \, du/t$
ε_t	true strain
$\overline{\varepsilon_x}$	average elastic strain in the x-direction on the midplane of the neck
ε_x	elastic strain in the x-direction at the position of x on the midplane of the neck
ΔG	increment in toughness caused by ductile reinforcement
$2H$	length of reinforcement affected by necking
μ	Poisson's ratio
R	radius of contour of the neck
σ	stress
$\overline{\sigma}$	effective stress
σ_0	yield strength
σ_{max}	maximum stress reached by constrained reinforcement
σ_{za}	stress in z-direction at the free surface of the neck
$2t$	initial thickness of reinforcement
u	axial extension equal to crack-opening displacement
u^*	crack-opening displacement at failure of ductile reinforcement
V_f	volume fraction of ductile reinforcement
ξ	work of rupture, $\int_0^{u^*} \sigma(u) \, du$

with a thickness of 0.15 mm. Distance from the notch tip to the laminate interface is 300 μm for 1.0-mm-thick Nb lamina and 200 μm for 0.5- and 0.25-mm-thick Nb laminae. Such distances have been found to be small enough not to distort the stress-displacement curve of the constrained ductile reinforcement, and at the same time, they maintain an appropriate degree of elastic constraint from the matrix.[20]

Displacement controlled tensile tests were conducted using Instron with a displacement speed of 0.005 in./min. The wedge-type grips were used to clamp the specimens, and load train alignment was achieved by coupling the top grip to a universal joint. The load was recorded as a function of crosshead displacement.

To obtain the intrinsic mechanical properties of Nb used, tensile and hardness tests were conducted on the as-received and processed Nb foils. The processed Nb foils were obtained from hot-pressed ZrO_2-coated $Nb/MoSi_2$ composites by breaking all the $MoSi_2$ on both sides of the Nb foil. This is not very difficult to do due to a relative weak bonding between Nb and $MoSi_2$ at the presence of a ZrO_2 coating layer, as described in Section III–B.

III. EXPERIMENTAL RESULTS

A. Mechanical Properties of Unconstrained Niobium

Properties measured from the processed Nb and as-received Nb are summarized in Table II. The data show that strength of Nb increased after hot-pressing, except for the 1.0-mm Nb foils, but the rate of strain hardening increased for all the niobium. Such changes are believed to be due to a combination of two competitive processes during hot-pressing: (1) grain growth of Nb, as shown in Figure 2, and (2) solid solution strengthening because of the equilibrium of Nb with the silicides formed at the matrix/reinforcement interface. In related studies,[21,22] it has been shown that the coated $Nb/MoSi_2$ systems contain three interfaces between the matrix and reinforcement, $MoSi_2/coating/Nb_5Si_3/Nb$, whereas the uncoated
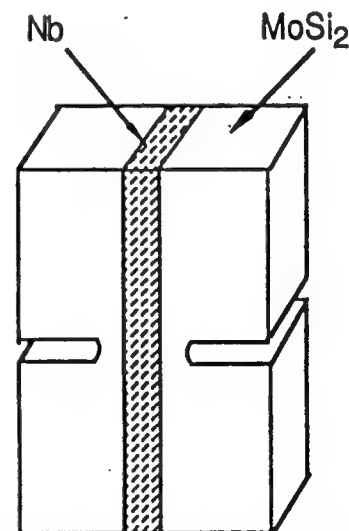

Fig. 1 — A schematic of a composite laminate test specimen.

Table II. Mechanical Properties of Niobium

Processing Condition	As-Received[*]			Processed[**] (ZrO$_2$ Coated, 1400 °C, 40 MPa for 1 hour)		
Thickness of Nb foil (mm)	1.0	0.5	0.25	1.0	0.5	0.25
Microhardness (HV, kg/mm^2)[*]	110	79.4	82.3	104	114	131
Yield strength (σ_0, MPa)	204	121	123	180 ± 6	211 ± 9	236 ± 11
Tensile strength (σ_u, MPa)	277	195	204	221 ± 8	260 ± 7	285 ± 10
Elongation (δ)	0.403	0.523	0.468	0.32 ± 0.03	0.18 ± 0.02	0.10 ± 0.02
Strength coefficient (MPa)	454	353	370	356 ± 11	363 ± 10	386 ± 12
Strength hardening coefficient	0.173	0.245	0.243	0.165 ± 0.032	0.085 ± 0.004	0.076 ± 0.007
σ_0/HV	1.85	1.52	1.49	1.73	1.85	1.80
σ_u/HV	2.52	2.45	2.48	2.12	2.28	2.1

[*]Only one sample for each condition was tested.
[**]Three samples for each condition were tested.

Nb/MoSi$_2$ systems contain the interfaces of MoSi$_2$/ (Mo, Nb)$_5$Si$_3$/Nb or MoSi$_2$/(Nb, Mo)Si$_2$/Nb$_5$Si$_3$/Nb depending on the processing temperatures. In short, for the present case, Nb always equilibrates with silicides, resulting in the solid solution strengthening of the Nb. For 1.0-mm Nb foil, grain size has changed from 15 to ~500 μm during hot-pressing, which leads to a large decrease in strength and overshadows the increase due to the solid solution hardening. For 0.5- and 0.25-mm Nb foils, grain size has changed from 50 to ~370 μm and from 48 to ~300 μm, respectively. However, shorter diffusion distance to the center of the niobium has made solid solution hardening dominant over softening due to grain growth. Therefore, 0.5- and 0.25-mm Nb foils show an increased strength after hot-pressing.

Examination of the true stress-strain data of the processed Nb reveals that after the true strain is larger than a certain value, the true stress-strain follows power law quite well. For example, the true strain at which the true stress-strain starts to follow a power law is ~0.34 pct for 0.25-mm processed Nb and ~1.0 pct for 1.0-mm processed Nb. Thus, the true stress-strain data after the previously mentioned strains (e.g., 0.34 pct for 0.25-mm Nb) have been used to calculate both the strength coefficient and the strength-hardening coefficient. The results are listed in Table II and also presented in Eq. [2] for convenience.

$$\sigma_t = 356\varepsilon_t^{0.165} \text{ (MPa)} \quad \text{for 1.0-mm Nb}$$

$$\sigma_t = 363\varepsilon_t^{0.085} \text{ (MPa)} \quad \text{for 0.5-mm Nb} \quad [2]$$

$$\sigma_t = 386\varepsilon_t^{0.076} \text{ (MPa)} \quad \text{for 0.25-mm Nb}$$

The above true stress-strain relations have been utilized to describe the intrinsic properties of the unconstrained ZrO$_2$-coated Nb and the unconstrained Al$_2$O$_3$-coated and uncoated Nb because of the following reasons. As shown in Table II, although the tensile strength of the niobium varies with the thickness, the tensile strength is proportional to its hardness (i.e., σ_u/HV equals to 2.48 ± 0.04 and 2.19 ± 0.08 for the as-received and processed Nb, respectively). Such a definite relationship has also been reported for other materials.[23] The ratio of the yield strength to the Vicker's hardness is also approximately a constant, as shown in Table II. The results indicate that it is reasonable to infer the strength of the niobium from the hardness measured. Hardnesses of Nb hot-pressed with different conditions are summarized in Table III. The table shows that the hardnesses are almost the same for each group of Nb based on the size. Due to such hardness results, the stress-strain relations for both the uncoated and the Al$_2$O$_3$-coated Nb under the unconstrained condition can be assumed to be the same as those of the processed Nb, which is the ZrO$_2$ uncoated Nb, before MoSi$_2$ on both sides of the Nb foils has been broken away.

It is clear from the previous discussion that the intrinsic mechanical properties of the Nb reinforcement in the composites are different from those of the Nb before the compositing. It is believed that such a change in properties due to hot-compaction processing is a common phenomenon for ductile-phase reinforced brittle matrix composites, because most of them have to be fabricated with high-temperature processing techniques. Even in chemically compatible composites, change of grain size will cause property change of the ductile reinforcements. Such change imposes difficulty on the prediction of the composite properties.

B. *Failure Mechanism and Related Observation on Constrained Niobium*

An edge view of the unconstrained and constrained uncoated Nb foils after the tensile test is shown in Figure 3. As seen in the figure, Nb foils fail by drawing down to a wedge for both the constrained and unconstrained conditions. All three sizes of Nb foils show the same failure mechanism. Furthermore, similar necking is also observed for all of the coated Nb. Close examination of Figure 3 reveals that the decohesion of Nb from the matrix is due to either multiple matrix fracture (Figures 3(b) and (d)) or partial matrix fracture and partial debonding at the interface (Figure 3(c)). For the Al$_2$O$_3$- and ZrO$_2$-coated Nb, the decohesion of the Nb was found to largely come from debonding at the interface, as shown in Figure 4. These results are in agreement with a related study,[22] which shows that the uncoated interface has a higher interfacial fracture energy than the fracture energy of the matrix, while the oxide-coated interfaces have a lower interfacial fracture energy than the matrix. Thus, it is expected that the matrix would fracture before the interface fails in the case of the uncoated Nb in contrast to the predominance of interfacial failure in the case of the coated Nb.
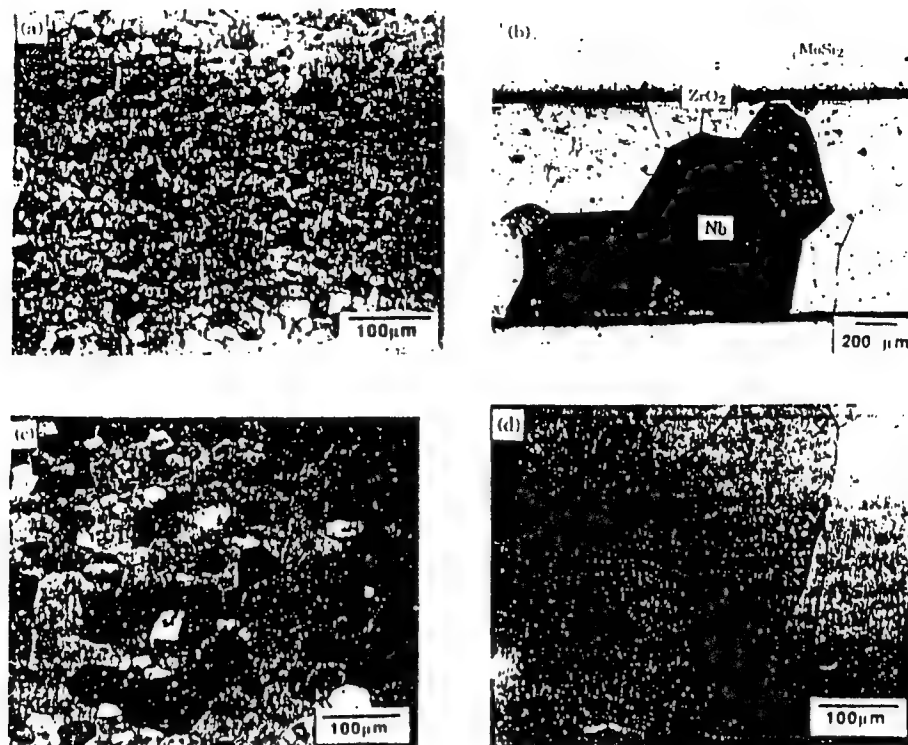
Fig. 2 — Optical microstructures of Nb foils: (*a*) as-received, 1.0-mm thick; (*b*) processed, 1.0-mm thick; (*c*) as-received, 0.5-mm-thick; and (*d*) processed, 0.5-mm thick. Note that different magnifications are used.

Table III. Microhardness of Nb with Different Processing Conditions (Hot-Pressed at 1400 °C, 40 MPa for 1 Hour)

Thickness of Nb Foil (mm)	1.0			0.5			0.25		
Processing condition	uncoated	Al_2O_3 coated	ZrO_2 coated	uncoated	Al_2O_3 coated	ZrO_2 coated	uncoated	Al_2O_3 coated	ZrO_2 coated
HV (kg/mm^2)	104	106	104	118	116	114	131	134	131

Both interfacial failure and matrix fracture create a "gage length" at the matrix/reinforcement interface, which is a region virtually free from constraints of the matrix and is called decohesion length in the text. The measured decohesion lengths are summarized in Table IV. The data show that within each size group, decohesion length increases from the uncoated to Al_2O_3-coated and then to ZrO_2-coated Nb/MoSi$_2$ composites. Such results are consistent with the measurement of the interfacial fracture energy,[22] which shows that the uncoated Nb/MoSi$_2$ has the highest interfacial fracture energy, followed by the Al_2O_3-coated and then ZrO_2-coated Nb/MoSi$_2$ composites.

Increase of the decohesion length with the thickness of Nb foils, as shown in Table IV, is believed to be mainly related to the necking of the Nb. Figure 5 shows schematically the effect of the necking on the decohesion length. The length of the Nb region affected by necking, 2H, is proportional to the thickness of the Nb, as shown in Figure 3. Approximately, H is 1.3 times the Nb thickness, a result measured from Figure 3. Large lateral displacement of Nb in the necking-affected region gives rise

to large transverse stresses that lead to the interfacial debonding and/or matrix fracture. Thus, the thicker the niobium, the longer the necking-affected region and, therefore, the longer the decohesion length. If the interface bonding is relatively weak, such as the Al_2O_3- and ZrO_2-coated interfaces, the transverse stresses aroused by lateral displacement of the Nb during uniform strain can be large enough to cause the interfacial debonding all the way to the test grips. During the uniform strain, the lateral displacement of Nb right at the interface is proportional to the thickness of the Nb. Therefore, decohesion by this mechanism can more easily occur in thick Nb composites than in thin Nb counterparts, as indicated in Table IV.

It has been shown[22,24] that the failure of the constrained Nb laminae in MoSi$_2$ matrix involves the following scenario. When an advancing crack just impinges a Nb reinforcement, no debonding at the matrix/reinforcement interface occurs. As external load continues to increase, debonding at the interface and/or multiple fracture of the matrix near the interface occur due to a relatively large lateral deformation of the Nb reinforcement compared to the matrix and load transfer from
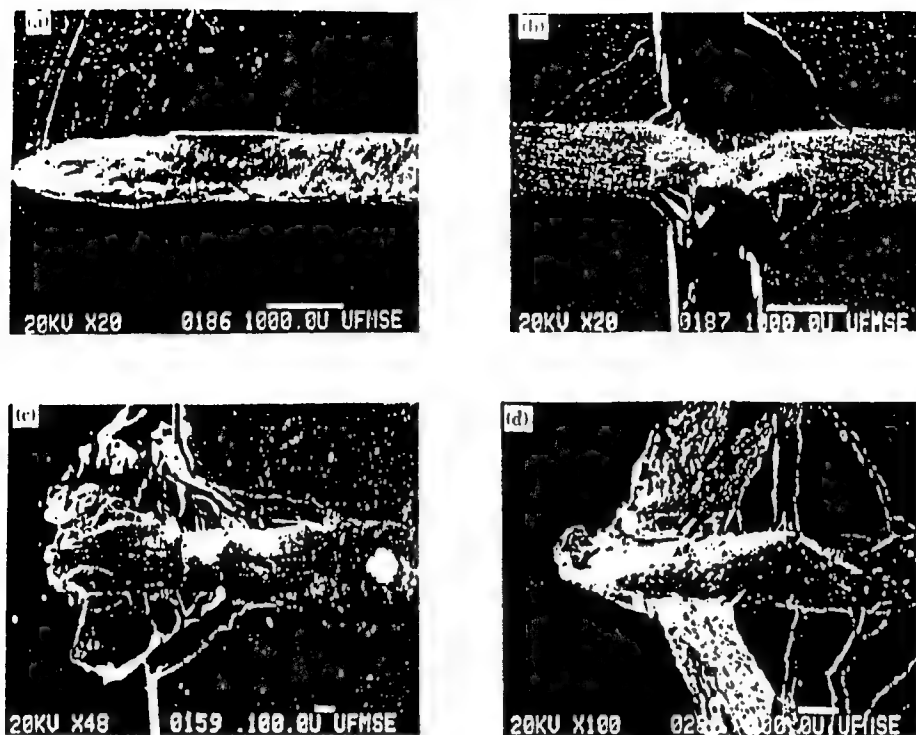
Fig. 3—An edge view of fractured specimens showing the contour of the neck: (a) an unconstrained, processed Nb foil with a thickness of 1.0 mm; and (b) through (d) constrained Nb with thicknesses of 1.0, 0.5, and 0.25 mm, respectively. Note that different magnifications are used.
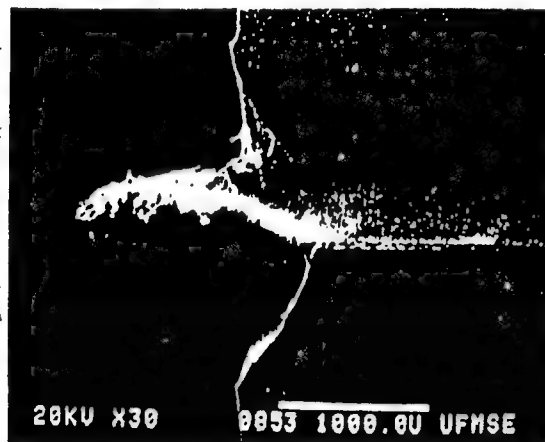

Fig. 4—An edge view of a fractured Al$_2$O$_3$-coated Nb/MoSi$_2$ composite laminate showing interfacial debonding.

the matrix to the reinforcement. Then the necking and fracture of the niobium occur as the load continues to increase. The aforementioned results[22,24] and the present observations suggest that flow behavior of the constrained Nb can be simplified into three stages: (1) elastic deformation; (2) plastic deformation within the decohesion region; and (3) localized plastic deformation within the necking region. Such processes are illustrated in Figure 6. The crack opening of the matrix can be directly related to the deformation of Nb in the decohesion zone. At the early stage of crack opening,

Nb only undergoes elastic deformation, as shown in Figure 6(a). As crack opening increases, Nb enters the stage of plastic deformation (Figure 6(b)). At last, when the work-hardening rate of the niobium at the central portion of the decohesion region is lower than the stress increase rate due to a decrease in the cross-sectional area of the reinforcement, the localized deformation begins (Figure 6(c)), which leads to the final failure of the Nb lamina. Such simplified deformation processes will be used to model stress-displacement behavior of the constrained Nb, as will be presented in Section IV.

C. Stress-Displacement Curves of Constrained Niobium

Figure 7 shows typical stress-displacement curves for the uncoated Nb foils with different thicknesses constrained in MoSi$_2$ matrix. The parameters measured are summarized in Table V. The work of rupture normalized by the yield strength, σ_0, and half-thickness of ductile phase, t,

$$\int_0^{u^*} \frac{\sigma(u)}{\sigma_0} \frac{du}{t}$$

in presented as E, in Table V and is called the normalized work of rupture in the text for convenience. As seen in Figure 7 and Table V, due to the different intrinsic properties, the maximum stresses reached by the constrained Nb, σ_{max}, are different for different sizes of Nb. However, if the σ_{max} is normalized by its own yield

Table IV. Decohesion Length in the MoSi₂/Nb Composites (Hot-Pressed at 1400 °C, 40 MPa for 1 Hour)*

Thickness of Nb foil (mm)	1.0			0.5			0.25		
Processing Condition	uncoated	Al_2O_3 coated	ZrO_2 coated	uncoated	Al_2O_3 coated	ZrO_2 coated	uncoated	Al_2O_3 coated	ZrO_2 coated
Decohesion length (mm)	10 ± 5	decohesion all the way to the grips		2.9 ± 0.4	3.3 ± 0.4	decohesion all the way to the grips	0.86 ± 0.09	0.94 ± 0.23	1.30 ± 0.61

*Four specimens for each condition were measured, except for 0.5-mm-thick Nb lamina, for which eight specimens were measured.
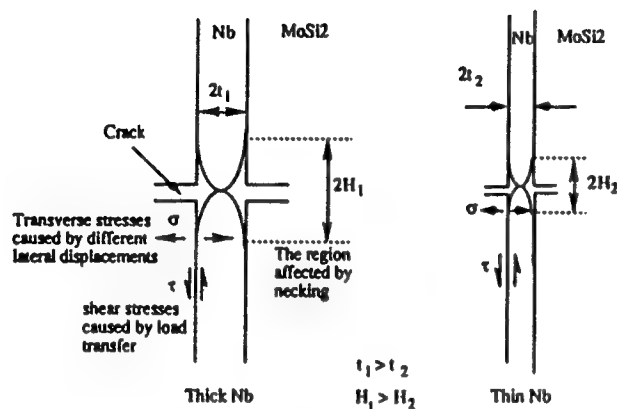

Fig. 5 — A schematic showing the effect of necking on the decohesion length.

Fig. 7 — Typical stress-displacement curves of constrained, uncoated Nb laminae with different thicknesses.

(a) Elastic deformation. (b) Plastic deformation. (c) Localized deformation.
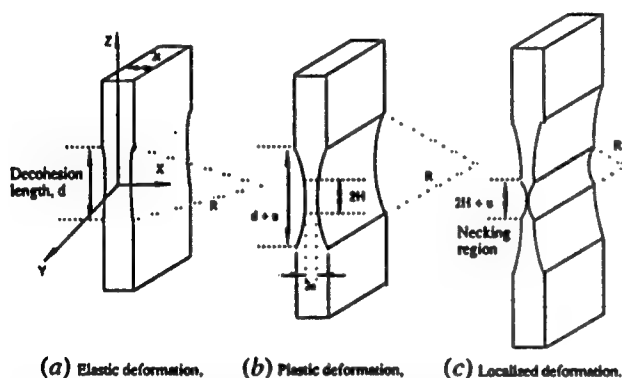
Fig. 6 — A schematic of three stages of deformation for constrained Nb. $2H$ is the length of the necking-affected region, $2a$ is the remaining thickness of the reinforcement, and u is displacement.

strength, the normalized maximum stress, σ_{max}/σ_0, exhibits an independence on the size of Nb. This result suggests that the maximum stress reached is not a function of size of the ductile phase. It is noted that the work of rupture increases with the size of Nb, indicating that the large size of ductile reinforcement is more effective in improving toughness of the brittle matrix composites. It is also noted that the normalized work of rupture shows a dependence on the size of Nb. The value of E_r increases with the increasing size of the niobium. The size dependence of the normalized work of rupture is attributed to the size dependence of the decohesion length, as will be discussed in Section V. This result suggests that the data of the normalized work of rupture obtained from the test on the large size of ductile reinforcements cannot
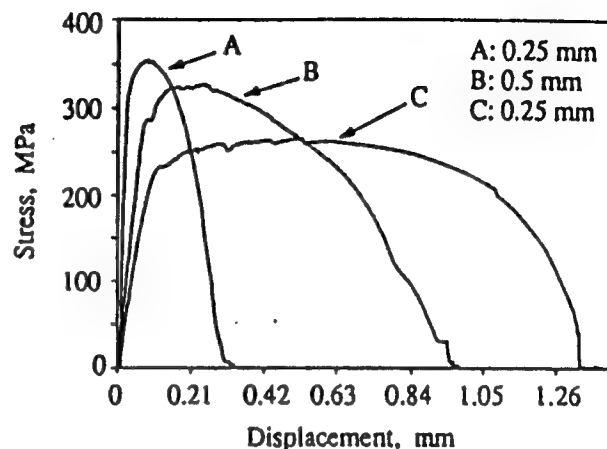
be extended to the small size of the reinforcements directly for the present composites.

The effect of coatings on the stress-displacement curves is shown in Figure 8. The parameters measured are summarized in Table VI. The data show that as the decohesion length increases, i.e., the constraints on the reinforcement decreases, the work of rupture increases. This is not surprising, since the longer the decohesion length, the more the ductile material participates in the plastic deformation and, therefore, the more energy is consumed before fracture occurs. It is noted that as the decohesion length increases, the normalized maximum stress decreases, indicating that increasing constraints on the ductile phase increase the σ_{max}. Table VI also shows that the normalized work of rupture is inversely dependent on the interfacial bonding strength. This is believed to be due to the increase of work of rupture with increasing decohesion length. The previous results indicate that limited decohesion enhances the energy consumed to fracture the constrained ductile reinforcement and, therefore, improve the toughness of the composites.

IV. MODELING

As discussed in Section III–B, the flow behavior of the constrained Nb in the present study can be simplified into three stages: (1) elastic deformation; (2) plastic deformation within the decohesion region; and (3) localized plastic deformation within the necking region. To model the stress-displacement relation of constrained ductile phase, σ-u, some assumptions are made.

Table V. Summary of the Parameters Calculated from the Model and Measured for the Uncoated Nb/MoSi₂ Laminates*

	Measured				Calculated				
$2t$ (mm)	σ_{max} (MPa)	σ_{max}/σ_0	ξ (J/m²)	E_t	σ_{max} (MPa)	σ_{max}/σ_0	ξ (J/m²)	E_t	$E_{\kappa cal)}/E_{\kappa exp)}$
1.0	259 ± 23	1.44	477,000 ± 35,900	5.3	292	1.62	400,000	4.4	0.838
0.5	325 ± 16	1.54	239,000 ± 24,000	4.5	329	1.56	196,000	3.7	0.814
0.25	351 ± 15	1.49	85,000 ± 7800	2.8	354	1.50	88,000	2.9	1.025

*Four specimens for each condition were tested, except for 0.5-mm-thick Nb lamina, for which eight specimens were tested.
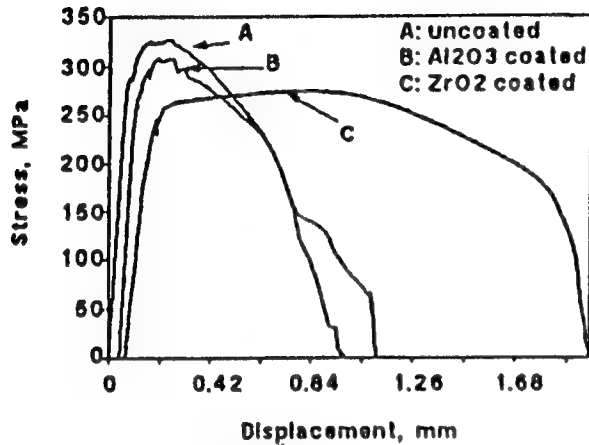
Fig. 8—The effect of the coatings on the stress-displacement curve measured from composite laminates with 0.5-mm-thick Nb lamina.

First, displacement of the stress-displacement curve is assumed to come only from the deformation of Nb lamina inside the decohesion region, because the Nb outside the decohesion region is bonded to the matrix and only undergoes elastic deformation. Second, the contour of the Nb lamina in the decohesion region is assumed to be part of the outside surface of a cylinder with a varied radius of R for all stages of deformation, as shown in Figure 6. Such an assumption is an approximation of the real contour of the Nb observed in the experiments and makes the calculation possible. Third, plane strain is assumed for the computation in all of the stages. In addition, in the calculation, the value of u is measured as the axial displacement of the matrix point at the boundary of the decohesion region while σ is computed from the total force exerted on the remaining cross section of the midplane at the neck normalized by the original midplane area.

A. Stage of Elastic Deformation

To compute σ-u data for elastic deformation, two more assumptions are made: (1) the volume-conserving nature of large-scale plastic deformation is also applicable to this stage; and (2) the effective stress across the midplane of the neck is constant.

Assumption (1) and the assumed contour relate the displacement, u, to the radius of the cylinder, R, by geometry as

$$R = \frac{(d + u)^3}{12tu} + \frac{4}{3}\frac{tu}{(d + u)} \qquad [3]$$

Assumption (2) renders the Bridgman formula for a necking plate,[25]

$$\left(\frac{x}{a}\right)\sigma_t = \left(\frac{x}{a}\right)\sigma_x - \left[R + \frac{a}{2}\left(1 - \frac{x^2}{a^2}\right)\right]\frac{\partial\sigma_x}{\partial x} \qquad [4]$$

computable even for elastic deformation. The terms x and a in Eq. [4] are defined in Figure 6, and σ_t and σ_x, which are functions of x, are the stresses on the midplane of the neck in the z- and x-directions, respectively. Although the assumed contour and constant effective stress do not represent the real situation of the decohesion region, they introduce negligible error to the work of rupture (see the Appendix).

With assumption (2), boundary conditions at the neck, and plane-strain assumption, the stress component σ_t can be related to the stress σ_{za}, which is σ_t at the free surface of the neck, as follows,

$$\sigma_{za}^2 = \sigma_x^2 + \sigma_t^2 - \frac{(1 + 2\mu - 2\mu^2)}{(1 - \mu + \mu^2)}\sigma_x\sigma_t \qquad [5]$$

where μ is the Poisson's ratio and is equal to 0.39 for

Table VI. Summary of the Parameters Calculated from the Model and Measured from the Composites with 0.5-mm-Thick Nb Lamina*

Processing Condition	Measured				Calculated				
	σ_{max} (MPa)	σ_{max}/σ_0	ξ (J/m²)	E_t	σ_{max} (MPa)	σ_{max}/σ_0	ξ (J/m²)	E_t	$E_{\kappa cal)}/E_{\kappa exp)}$
Uncoated	325 ± 16	1.54	239,000 ± 24,000	4.5	329.3	1.56	196,000	3.707	0.824
Al₂O₃ coated	310 ± 11	1.47	243,000 ± 21,000	4.6	328.4	1.55	203,000	3.860	0.839
ZrO₂ coated	275 ± 12	1.31	429,000 ± 26,000	8.1	328.2	1.55	339,000	6.435	0.794

*Eight specimens for each condition were tested.

Nb.[26] Introduction of the Poisson's ratio of Nb into Eq. [5] yields

$$\sigma_t \approx 0.968 \, \sigma_t \pm \sigma_{za} \qquad [6]$$

The negative sign in Eq. [6] is discarded in the following computation because of the boundary conditions at the neck (i.e., $\sigma_t = 0$ and $\sigma_t = \sigma_{za}$ when $x = a$). Substituting Eq. [6] into Eq. [4] and solving the linear first-order differential equation for σ_t yield

$$\sigma_x = \sigma_{za}\left[31.25 - 31.25 \frac{\left(\dfrac{R}{a}\right)^{0.032}}{\left(\dfrac{R}{a} + \dfrac{1}{2} - \dfrac{x^2}{2a^2}\right)^{0.032}}\right] \qquad [7]$$

where σ_{za} is related to the average elastic strain, $\overline{\varepsilon}_x$, which can be measured from the dimension of the neck using the relation of $\overline{\varepsilon}_x = \ln(a/t)$ and can be related to the elastic strain in the x-direction at the position of x on the midplane of the neck, $\varepsilon_x(\sigma_x, \sigma_y, \sigma_z)$, as follows:

$$\overline{\varepsilon}_x \frac{\displaystyle\int_0^a \varepsilon_x(\sigma_x, \sigma_y, \sigma_z)\,dx}{a}$$

$$= \frac{\sigma_{za}}{aE}\left\{9.56a - \int_0^a \frac{10.1\left(\dfrac{R}{a}\right)^{0.032}}{\left(\dfrac{R}{a} + \dfrac{1}{2} - \dfrac{x^2}{2a^2}\right)^{0.032}}\,dx\right\} \qquad [8]$$

where E is the Young's modulus of Nb. Thus, by numerical integration of Eq. [8], σ_{za} can be found for any specific R and a. Using Eqs. [3] and [6] through [8], σ-u data can be calculated for the elastic deformation.

B. Stage of Plastic Deformation

The von Mises yield criterion is used to monitor the initial yielding. Thus, when the effective stress reaches the yield strength of the Nb, plastic deformation begins. Now the Bridgman formula for a necking plate,[25]

$$\sigma_t = \sigma_{za}\left\{1 + \ln\left[1 + \frac{1}{2}\frac{a}{R}\left(1 - \frac{x^2}{a^2}\right)\right]\right\} \qquad [9]$$

can be used directly to compute the nominal axial stress. By applying boundary conditions at the neck, a relation between σ_{za} and the effective stress, $\overline{\sigma}$, can be found:

$$\sigma_{za} = 1.1547\overline{\sigma} \qquad [10]$$

where $\overline{\sigma}$ is determined by the effective strain.

In the computation, the effective strain at the initial yield is assigned as zero, while the effective stress has a value of the yield strength of the unconstrained Nb. After the initial yield, the niobium is assumed to be a perfect isotropy of strain hardening, and the power law, Eq. [2], is used to compute the effective stress.

C. Stage of Localized Plastic Deformation

The localized plastic deformation is assumed to begin when the nominal axial stress is about to decrease. The length of the region affected by necking, $2H$, shown in Figure 6, is chosen as $2t$. After necking down to a point at the neck, the region with such dimension gives two triangles with height equal to the base. The base is assumed to have no more deformation when the localized deformation begins. The assumptions give rise to a contour, as shown in Figure 6(c), and such contour is an approximation for the contour of Nb in the decohesion region, as shown in Figure 3. The displacement in the stage of the localized deformation is assumed to come only from the deformation of the necking-affected region, and the computation of the nominal axial stress is carried out using Eqs. [9] and [10].

In summary, in the preceding approximate model, the effect of bonding conditions at the interface on the calculated $\sigma(u) \sim u$ curve is introduced by properly selecting the decohesion length at the interface, since the decohesion length is dependent on the interfacial conditions, as revealed in the experiments (Section III–B). The effects of intrinsic mechanical properties of ductile phase are addressed by utilizing the elastic modulus, yield strength, and true stress-strain relation of the ductile phase throughout the computation of the $\sigma(u) \sim u$ curve. Finally, the size of the ductile phase comes into play through the selection of the decohesion length and the direct entry of the half-thickness of the ductile phase in the model.

V. COMPARISON BETWEEN THE MODEL AND EXPERIMENTS

A. Effect of the Decohesion Length

Dependence of the stress-displacement curve on the decohesion length is shown in Figure 9, which is generated using the true stress-strain data of 0.5-mm Nb. The results indicate that the maximum stress reached by the constrained Nb, σ_{max}, increases with increasing constraints on the ductile reinforcement, but increasing constraints decrease the work of rupture, a trend also exhibited
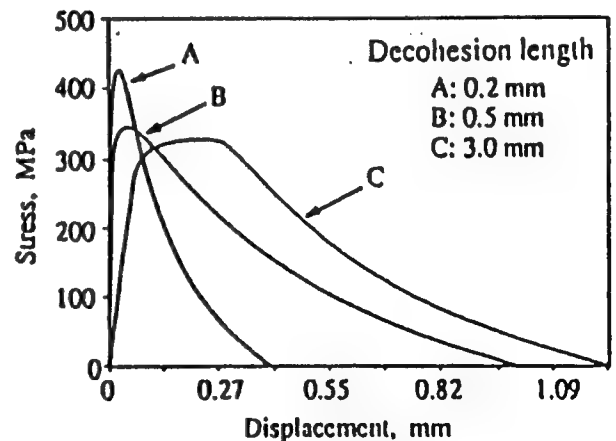

Fig. 9—The effect of decohesion length on the stress-displacement curve.

by the experiments. The results suggest that a relatively weak bond at the interface enhances the work of rupture and, therefore, is conducive to toughening brittle matrix composites. Similar results were obtained by other investigators using different models.[11,13,16]

The calculated parameters from the model, based on the experimental data of 0.5-mm-thick Nb lamina in Table IV, are presented in Table VI. Ratios of the calculated and measured normalized work of rupture, E_{ncal}/E_{nexp}, are also included in the table. A comparison between the calculated and measured data in Table VI reveals that the calculated work of rupture deviates from the measured counterparts by about 20 pct. However, the general trend that the work of rupture decreases with the increasing interfacial fracture energy observed in the experiments has been maintained in the prediction of the model. The discrepancy in the values between the calculated and measured work of rupture lies in the assumptions involved in the model, especially the assumption of the contour of the Nb lamina in the decohesion region. The assumed contour of the neck makes the computation feasible, but it does not exactly reflect the real contour of the Nb, which actually displays a convex shape at the region away from the neck, as shown in Figure 3. On one hand, the assumed contour (a concave shape) leads to a larger strain to failure when compared with the convex shape of the real contour; on the other hand, it also results in a larger radius of curvature at the neck than does the real contour. As such, a less severe state of triaxial stresses results, and a lower stress in the axial direction (z-direction) is predicted by the model. All of these contribute to the discrepancy in the work of rupture. Nevertheless, the predicted values are reasonable approximations to the measured counterparts.

It is also noted from Table VI that σ_{max}, predicted by the model, is insensitive to the interfacial bonding conditions in the range of the measured decohesion lengths. The result indicates that the model becomes less sensitive to the decohesion length when the decohesion length is large, because for short decohesion lengths, σ_{max} is very sensitive to the decohesion length, as shown in Figure 9. This phenomenon will be further discussed in Section V–B. An implication of the present result is that the present coated and uncoated Nb/MoSi$_2$ laminates are in the range of low constraints (i.e., long decohesion length). The experimental evidence for this is that the maximum stress reached by the laminate composites with 1.0-mm Nb lamina is almost the same for different decohesion lengths ranging from ~5 to ~15 mm.

B. Effect of Reinforcement Size

A comparison of the size effect between the model and experiments for the uncoated Nb/MoSi$_2$ laminates is shown in Figure 10. The input data for the model are from Eq. [2] and Tables II and IV, with each size of Nb having its own measured parameters and properties. The input of Young's modulus is from the slope of the stress-strain curve of the unconstrained Nb in a simple tensile test. As shown in Figure 10, the model fits the experimental data reasonably well, except the stage of the localized plastic deformation. The deviation in this stage
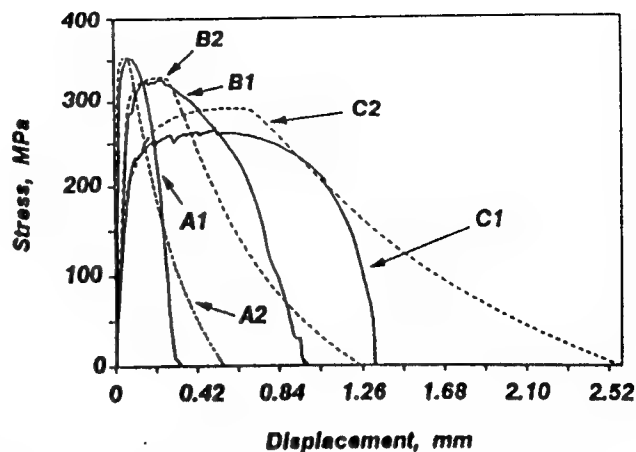
Fig. 10—The effect of reinforcement size on the stress-displacement curve. A1, B1, and C1 (solid lines) are experimental curves of the composites with 0.25-, 0.5-, and 1.0-mm-thick Nb laminae, respectively; A2, B2, and C2 (dashed lines) are results from the model for composites with 0.25-, 0.5-, and 1.0-mm-thick Nb laminae, respectively.

is largely due to the difference between the real and assumed contours of the neck, as discussed in Section V–A. The parameters calculated from the model are summarized in Table V. It is noted that the calculated maximum stress, the work of rupture, and the normalized work of rupture are all close to the measured counterparts. It is clear that the estimation of the maximum stress, the work of rupture, and the normalized work of rupture can be made from the model.

Reinforcements used in composites may be smaller in size than those tested in the present study. To predict the work of rupture for the small size of reinforcements, it is necessary to know the decohesion length in advance for use of the model. A plot of σ_{max} vs decohesion length, computed from the model for the composites with 0.25-mm Nb lamina, is shown in Figure 11. It is noted that there exists a characteristic decohesion length, d_c,
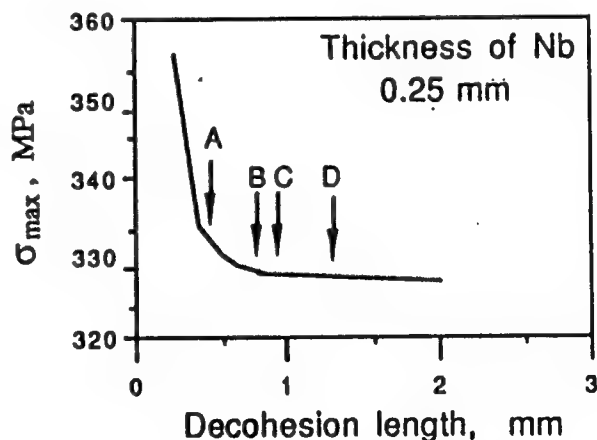

Fig. 11—A plot of σ_{max} vs decohesion length. Arrow A shows characteristic decohesion length, and arrows B, C, and D show the measured decohesion lengths of the composites containing uncoated, Al$_2$O$_3$-coated, and ZrO$_2$-coated Nb laminae, respectively.

below which σ_{max} becomes very sensitive to the decohesion length. Computation of the model shows that the characteristic decohesion length is equal to twice the thickness of the niobium and that the normalized work of rupture with the characteristic decohesion length, called the characteristic normalized work of rupture, is constant regardless of the size of the reinforcement.

The measured decohesion lengths, d_m, in the present study are all larger than d_c. However, the ratio of d_m to d_c is found to be a linear function of size of the reinforcement, as shown in Figure 12. The relations found are

$d_m/d_c = 0.66 + 10.72t$ (for Al_2O_3-coated laminates)

$d_m/d_c = 0.66 + 8.70t$ (for uncoated laminates)   [11]

It is noted that d_m becomes closer to d_c as the size of the reinforcement decreases, suggesting that the normalized work of rupture becomes smaller and closer to the characteristic normalized work of rupture. The oxide coating changes the slope of the line, indicating that the coating enhances decohesion, and the effect becomes larger as the size of the reinforcement increases. With Eq. [11], the decohesion length of the small size of the reinforcement can be predicted, and the work of rupture can be calculated from the model. A plot generated in this way is shown in Figure 13, which shows that E_t decreases with decreasing size of the reinforcement, a general trend found in the experiments. The discrepancy in the values between the predicted and measured work of ruptures is believed to be mainly related to the difference between the assumed and real contours of the neck, as discussed in Section V–A. Notwithstanding the discrepancy, the model deviates from the experiments by only about ±20 pct and is still capable of predicting the general trend of the change of the work of rupture with the size of ductile phase. Thus, as a first approximation, the model can be used to estimate the contribution of ductile reinforcements to the toughness of a brittle matrix composite.

C. *Effect of Yield Strength and Work Hardening*

Effects of yield strength and work hardening on the work of rupture are evaluated by substituting the properties of several different materials into the model. The properties are obtained from Reference 27, and the true stress-strain curves for some materials are shown in Figure 14. It is noted that both 4340 steel and 70/30 brass have a higher work-hardening rate than the Nb used in the present study. The computed stress-displacement curves are shown in Figure 15, and the input and output data are summarized in Table VII. It is clear that the work of rupture increases with increasing work-hardening rate. Although 70/30 brass has the lowest yield strength, its high work-hardening rate enables it to have a much higher work of rupture than both 4340 steel and Nb, both of which have a higher yield strength than the brass. The reason for such phenomena is that a high work-hardening rate reinforcement has a higher increase rate in the load-carrying ability, and instability (*i.e.*, the localized plastic deformation within the necking region), therefore, comes later than a low work-hardening rate reinforcement. Thus, high work-hardening rate reinforcements have a relatively longer stage of plastic deformation in the whole decohesion region, leading to more energy being dissipated and a higher work of rupture. It is noteworthy that the brass has a very high normalized work of rupture, which suggests that the normalized work of rupture could probably be used as an indicator of the efficiency with
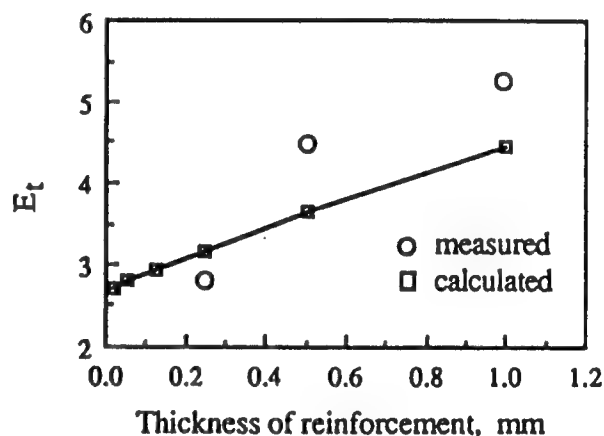

Fig. 13—The normalized work of rupture as a function of reinforcement size.

Fig. 12—A plot of ratio of the measured to characteristic decohesion lengths as a function of reinforcement size.
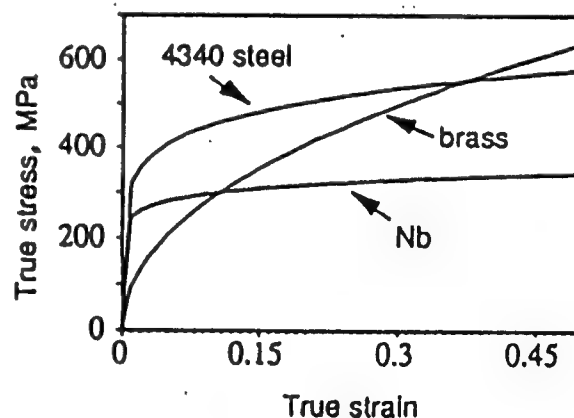

Fig. 14—The true stress-strain curves of some of the materials used for evaluating effects of yield strength and work hardening.
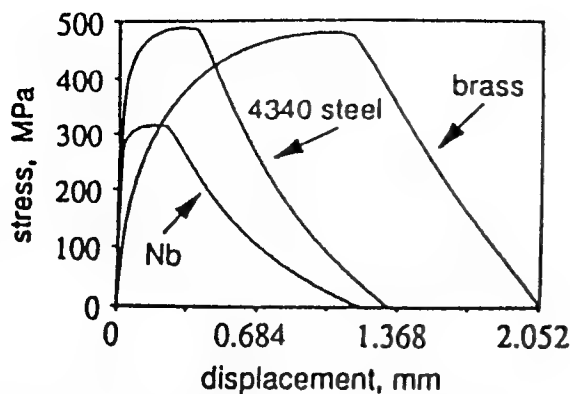
Fig. 15—Computed stress-displacement curves using the data in Fig. 14 and Table VII.

which the work hardening contributes to enhancing the work of rupture.

When yield strength is very high, such as 0.6 pct C steel in Table VII, the work of rupture is also very high. As shown in Table VII, 0.6 pct C steel has a much higher work of rupture than 70/30 brass, although it has a lower work-hardening rate than the brass. The contribution of yield strength to the work of rupture is mainly to increase the maximum stress reached by the constrained reinforcement. From the previous discussion, it is concluded that both the high work-hardening rate and yield strength are beneficial to the work of rupture. Work hardening, however, is more effective in enhancing the work of rupture than yield strength, because a high work-hardening rate delays the instability of deformation for constrained ductile reinforcements; therefore, more material of the reinforcements participates in plastic deformation, and more energy has to be consumed.

VI. CONCLUDING REMARKS

1. The present set of experiments demonstrates that flow behavior of constrained ductile reinforcement depends strongly on the intrinsic properties and size of the reinforcement and the properties of the matrix/reinforcement interface. The maximum stress reached by the constrained reinforcement increases as the strength of the reinforcement and constraints increases. Constraints, indicated by decohesion length, are found to be related to the interfacial properties and size of the reinforcement. Decohesion length increases from the uncoated to the oxide-coated laminates and increases with increasing size of the reinforcement. Dependence of the decohesion length on the size of the reinforcement is attributed to the dependence on the size of the reinforcement of the length of the necking-affected region and the lateral displacement difference between the matrix and reinforcement at the interface.

2. The normalized work of rupture, E_t, is found to be dependent on the size of the reinforcement. The E_t decreases with decreasing size of the reinforcement and increases with decohesion length. The results indicate that both the weak interface and the large size of reinforcement improve the toughness of the composites.

3. Based on the observation, the flow behavior of the constrained reinforcement has been divided into three stages: (1) elastic deformation; (2) plastic deformation within the decohesion region; and (3) localized plastic deformation within the necking region. An approximate model has been developed to describe these three stages. The model gives insight into the influence of decohesion, yield strength, work hardening, and size of the reinforcement on the stress-displacement curve. The overall shape of the σ-u curves generated by the model fits the measured curves reasonably well.

4. Computation of the model indicates that the work of rupture is enhanced by a relatively weak bond at the matrix/reinforcement interface, by a large size of reinforcement, and by a high yield strength and work-hardening rate. A high work-hardening rate is more effective in enhancing work of rupture than is a high yield strength.

5. Computation of the model suggests that there is a characteristic decohesion length, d_c, with which the normalized work of rupture, E_t, is constant regardless of the size of the reinforcement. It is found that the deviation of the measured decohesion length from d_c increases with increasing size of the reinforcement, which leads to E_t increasing with increasing size of the reinforcement. A relationship between d_m and d_c is found, which allows the prediction of the real decohesion length for the small size of the reinforcement and, therefore, the calculation of the work of rupture for the specific size of the reinforcement.

Table VII. The Input and Output Data for Computing the Stress-Displacement Curves Shown in Figure 16 (the Thickness of all Materials Is Assumed as 0.5 mm)

Material	Input Data				Output Data		
	$\sigma_t = K\varepsilon_t^n$ (MPa)	σ_0 (MPa)	E (GPa)	μ	σ_{max} (MPa)	ξ (J/m^2)	E_t
Nb	$363\varepsilon_t^{0.045}$	210	105	0.39	329	196,000	3.7
SAE 4340 steel	$642\varepsilon_t^{0.15}$	230	193	0.29	496	351,000	6.1
0.6 pct C steel	$1573\varepsilon_t^{0.10}$	500	199	0.29	1337	801,000	6.4
70/30 brass	$897\varepsilon_t^{0.49}$	80	111	0.30	483	662,000	33.1

APPENDIX

Finite element analysis (FEA) of the stress distribution across the neck and the contour of the decohesion region during the elastic deformation was implemented using the finite element software package ANSYS. Due to the symmetry, only one-quarter of the specimen was analyzed using two-dimensional four-node isoparametric elements with an assumption of plane-strain deformation. A typical finite element model for the constrained Nb is shown in Figure 16. The displacement at the midplane of the neck was allowed only in the x-direction, and the bonded boundaries of Nb to the matrix and to the axial central plane were allowed to displace only in the z-direction, as shown in Figure 16.

Results from the FEA for the case of a constrained 1.0-mm Nb lamina with a 2.28-mm decohesion length under a nominal axial stress of 150 MPa are presented in Figures 17 and 18. Figure 17 compares the assumed contour of the decohesion region with the FEA result. The data show that the assumed contour deviates from the FEA result, leading to a smaller crack-opening displacement compared to the finite element analysis. However, the difference is so small that it introduces negligible errors to the computation of the work of rupture.

Evaluation of the effective stress distribution across the midplane of the neck is shown in Figure 18. Clearly, the effective stress is not constant across the midplane but increases from the free surface to the center of the

Fig. 17—A comparison between the assumed contour and finite element analysis of the decohesion region. The values of X and Z are defined in Fig. 16.
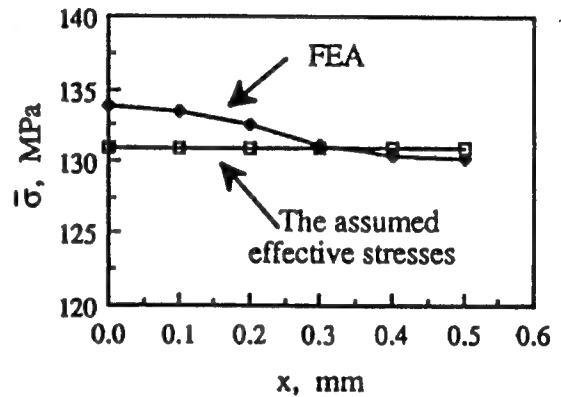
Fig. 18—The effective stress distribution at the midplane of the neck.

neck. Although the assumed constant effective stress does not represent the real stress distribution, the crack-opening displacement calculated according to the assumptions is not much different from the finite element analysis, as shown in Figure 17. Similar results were also obtained from the calculation of constrained 0.25- and 0.5-mm Nb laminae. Thus, it is concluded that the assumed constant effective stress and contour of the decohesion region impose negligible errors on the calculation of the σ-u curve and the work of rupture.

Fig. 16—The mesh and boundary conditions used for analysis of constrained Nb.

REFERENCES

1. J.L. Chermant and F. Osterstock: *J. Mater. Sci.*, 1976, vol. 11, pp. 1939-51.
2. J. Gurland: *Trans. ASM*, 1958, vol. 50, pp. 1063-71.
3. A.V. Virkar and D.L. Johnson: *J. Am. Ceram. Soc.*, 1977, vol. 60, pp. 514-19.
4. D.T. Rankin: *J. Am. Ceram. Soc.*, 1971, vol. 54, pp. 277-81.
5. P. Hing and G.W. Groves: *J. Mater. Sci.*, 1972, vol. 7, pp. 427-34.
6. V.V. Krstic, P.S. Nicholson, and R.G. Hoagland: *J. Am. Ceram. Soc.*, 1981, vol. 64, pp. 499-504.
7. C.K. Elliott, G.R. Odette, G.E. Lucas, and J.W. Sheckherd: *High Temperature, High Performance Composites*, Materials Research Society Proc., F.D. Lemkey, A.G. Evans, S.G. Fishman, and J.R. Strife, eds., Materials Research Society, Pittsburgh, PA, 1988, vol. 120, pp. 95-102.
8. E. Fitzer: *Whisker- and Fiber-Toughened Ceramics*, R.A. Bradley,

D.E. Clark, D.C. Larsen, and J.O. Stiegler, eds., ASM INTERNATIONAL., Metals Park, OH, 1988, pp. 165-83.

9. L. Xiao, Y.S. Kim, and R. Abbaschian: *Intermetallic Matrix Composites*, Materials Research Society Proc., D.L. Anton, P.L. Martin, D.B. Miracle, and R. McMeeking, eds., Materials Research Society, Pittsburgh, PA, 1990, vol. 194, pp. 399-404.

10. L.R.F. Rose: *J. Mech. Phys. Solids*, 1987, vol. 35, pp. 383-405.

11. L.S. Sigl, P.A. Mataga, B.J. Dalgleish, R.M. McMeeking, and A.G. Evans: *Acta Metall.*, 1988, vol. 36, pp. 945-53.

12. A.G. Evans and R.M. McMeeking: *Acta Metall.*, 1986, vol. 34, pp. 2435-41.

13. P.A. Mataga: *Acta Metall.*, 1989, vol. 37, pp. 3349-59.

14. B. Budiansky, J.C. Amazigo, and A.G. Evans: *J. Mech. Phys. Solids*, 1988, vol. 36, pp. 167-87.

15. J.R. Rice: *Fracture*, H. Liebowitz, ed., 1968, vol. 2, pp. 191-311.

16. M.F. Ashby, F.J. Blunt, and M. Bannister: *Acta Metall.*, 1989, vol. 37, pp. 1847-57.

17. H.C. Cao, B.J. Salgleish, H.E. Deve, C. Elliott, A.G. Evans, R. Mehrabian, and G.R. Odette: *Acta Metall.*, 1989, vol. 37, pp. 2969-77.

18. H.E. Deve, A.G. Evans, G.R. Odette, R. Mehrabian, M.L. Emiliani, and R.J. Hecht: *Acta Metall.*, 1990, vol. 38, pp. 1491-1502.

19. L. Xiao and R. Abbaschian: *Advanced Metal Matrix Composites for Elevated Temperatures*, M.N. Gungor, E.J. Lavernia, and S.G. Fishman, eds., ASM INTERNATIONAL, Metals Park, OH, 1991, pp. 21-31.

20. L. Xiao and R. Abbaschian: *Advanced Metal Matrix Composites for Elevated Temperatures*, M.N. Gungor, E.J. Lavernia, and S.G. Fishman, eds., ASM INTERNATIONAL, Metals Park, OH, 1991, pp. 33-40.

21. L. Xiao and R. Abbaschian: *Mater. Sci. Eng.*, 1992, vol. A155, pp. 135-45.

22. L. Xiao and R. Abbaschian: *Metall. Trans. A*, 1992, vol. 23A, pp. 2863-72.

23. F.C. Lea: *Hardness of Metals*, Charles Griffin and Company, Ltd., London, 1936, pp. 91-105.

24. L. Xiao, Y.S. Kim, R. Abbaschian, and R.J. Hecht: *Mater. Sci. Eng.*, 1991, vol. A144, pp. 277-85.

25. P.W. Bridgman: *Studies in Large Plastic Flow and Fracture*, 1st ed., McGraw-Hill, Inc., New York, NY, 1952, pp. 9-37.

26. M.E. Sibert, A.J. Kolk, Jr., and M.A. Steinberg: *Technology of Columbium (Niobium)*, B.W. Gonser and E.M. Sherwood, eds., John Wiley & Sons, Inc., New York, NY, 1958, pp. 20-34.

27. G.E. Dieter, Jr.: *Mechanical Metallurgy*, McGraw-Hill Kogakusha, Ltd., Tokyo, 1961, p. 248.

STUDY OF THE FLOW BEHAVIOR OF CONSTRAINED DUCTILE PHASES

.... I. EXPERIMENT

Lingang Xiao

Department of Materials Science and Engineering, University of Florida,
Gainesville, FL 32611

Abstract

Effects of the matrix/reinforcement interface, and the mechanical properties and size of the ductile reinforcement on the flow behavior of the constrained ductile reinforcement have been evaluated using a tensile test on a single Nb lamina imbedded in $MoSi_2$ matrix. Three different thicknesses of Nb foils (1.0, 0.5 and 0.25 mm) have been tested. Variation of interfacial bonding was achieved by depositing an oxide coating (Al_2O_3 or ZrO_2) or by the development of a reaction product layer between the reinforcement and matrix. It was found that work of rupture of the ductile reinforcement increased with size of the ductile reinforcement and with decreasing bonding strength at the matrix/reinforcement interface. Such results suggested that both of increasing size of ductile reinforcement and obtaining a relatively weak interface were conducive to toughness of the composites. It was also found that the work of rupture normalized by size and yield strength of the reinforcement was dependent on the interfacial properties and size of the reinforcement. The results were interpreted in terms of the dependence of the decohesion length on the interfacial properties and size of the reinforcement.

I. Introduction

Numerous studies have shown that improved fracture toughness can be achieved by the incorporation of a ductile second phase into a brittle matrix. Examples of current or potential technological significance are tungsten carbide toughened with cobalt network [1,2], zirconia toughened with zirconium network [3], alumina toughened with dispersed molybdenum [4], magnesia toughened with cobalt and nickel particles or fibers [5], and glass-enamels toughened with dispersed aluminum and nickel particles [6]. Successful toughening has also been observed in titanium aluminide [7] and molybdenum disilicide [8,9] reinforced with niobium pancake or filament.

The primary toughening mechanism of ductile reinforcement has been attributed to the bridging of ductile ligaments [10-14]. The contribution to fracture toughness from bridging can be estimated by extending cohesive force model [15] to ligament bridging [11,12] and can be written as

$$\Delta G = V_f \int_0^{U^*} \sigma(U) \, dU \qquad \text{(1)}$$

where $\sigma(U)$ is the nominal stress carried by the constrained ductile reinforcement for a given crack opening U, V_f is volume fraction of the ductile reinforcement, U^* is the crack opening at the point when the ductile reinforcement fails and the definite integral, designated as ξ, is the work of rupture of the constrained ductile ligament. Thus, the key to predict the increased fracture toughness is to calculate $\sigma(u)$ as a function of crack opening. Recognizing that $\sigma(u)$ is different from that measured in a simple tensile test, several investigators [16-18] have used a test procedure to evaluate $\sigma(u)$. The test procedure is based on the concept that the stress-displacement relationship obtained from one ductile reinforcement imbedded in a brittle matrix can be used to describe the mechanical characteristics of the reinforcements in the composites. Their results demonstrated that flow behavior of constrained ductile phases was governed by the yield strength, σ_0, work hardening coefficient, n, and the decohesion length, d, at the matrix/reinforcement interface. Clearly, more work needs to be done in this area to evaluate the effect on $\sigma(u)$ of the intrinsic properties of the ductile reinforcement (yield strength, work hardening and ductility), interfacial properties and size of the ductile phases.

The principle intent of the present study is to experimentally examine the effects of properties of the matrix/reinforcement interface and size of ductile phase on its flow behavior, and therefore on the enhanced fracture toughness of the composite. The system selected for investigation was $MoSi_2$ matrix reinforced with Nb. Since the two components used have similar coefficients of thermal expansion, the residual thermal stresses were minimized, thus simplifying the present stress analysis. Specimens with laminated form have been used, because of the ease of producing the composites with controlled properties, but it still serves the purpose of the present study. The results showed that work of rupture of the ductile reinforcement increased with size of the ductile reinforcement and with decreasing bonding strength at the matrix/reinforcement interface. Such results suggested that both of increasing size of ductile reinforcement and having a relatively weak interface are conducive to toughness of the composites.

II. Experimental

Disc shaped laminated specimens were prepared by stacking a Nb foil with two layers of $MoSi_2$ powder (-325 mesh) at an appropriate ratio, and then vacuum hot pressing at 1400°C for 1 hour under a pressure of 40 MPa. In order to minimize residual thermal stresses, the hot pressed discs were held in the hot pressing chamber at 800°C for 1 hour before cooling down to room temperature. The residual thermal stresses induced with such processing have been estimated to be small with a tensile stress of 19 MPa in the matrix and a compressive stress of 79 MPa in the Nb on the lamina plane [19]. Three different thicknesses of Nb foils (1.0, 0.5 and 0.25 mm) with a purity of 99.8% were used to prepare the laminated specimens. Variation of the
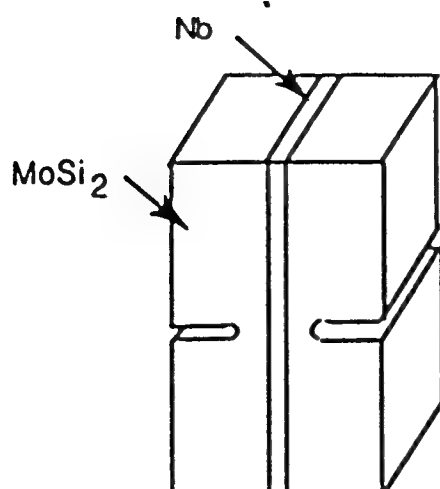
Fig. 1 Schematic of a composite laminate test specimen.

matrix/reinforcement interfaces was achieved by depositing different oxide coatings (Al_2O_3 or ZrO_2) to the Nb surface prior to the hot pressing or by the development of a reaction product layer between the matrix and reinforcement. Details of the coating procedures can be found in Reference [9].

The hot pressed discs were cut into rectangular tensile test bars with dimensions of 5.0x3.9x30.0 mm, as shown in Fig. 1. Straight-through notches in the $MoSi_2$ matrix were introduced using a diamond wafering blade with a thickness of 0.15 mm. Distance from the notch tip to the laminate interface is 300 μm for 1.0 mm thick Nb lamina and 200 μm for 0.5 and 0.25 mm thick Nb laminae. Such distances have been found to be small enough not to distort the stress-displacement curve of the constrained ductile reinforcement and at the same time remain an appropriate degree of elastic constraint from the matrix [20].

Displacement controlled tensile tests were conducted using INSTRON with a displacement speed of 0.005 in/min. The wedge type grips were used to clamp the specimens and load train alignment was achieved by coupling the top grip to a universal joint. The load was recorded as a function of cross head displacement.

To obtain the intrinsic mechanical properties of Nb used, tensile and hardness tests were conducted on the as-received and processed Nb foils. The processed Nb foils were obtained from hot pressed ZrO_2 coated $Nb/MoSi_2$ composites by breaking all the $MoSi_2$ on both sides of the Nb foil. This is not very difficult to do due to a relative weak bonding between Nb and $MoSi_2$ at the presence of a ZrO_2 coating layer (it is described in Section 3.2) .

III. Results and Discussion

3.1 Mechanical Properties of Unconstrained Niobium

Properties measured from the processed Nb and as-received Nb are summarized in Table 1. The data show that strength of Nb has increased after hot pressing except for the 1.0 mm Nb foils, but the rate of strain hardening increased for all the niobium. Such changes are believed to be due

Table 1. Mechanical properties of the niobium used

Processing condition	As received			Hot pressed (ZrO_2 coated, 1400^0C, 40 MPa for 1 hr)		
Thickness of Nb foil (mm)	1.0	0.5	0.25	1.0	0.5	0.25
Microhardness (HV)	110	79.4	82.3	104	114	131
Yield strength (σ_0, MPa)	204	121	123	180	211	236
Tensile strength (σ_u, MPa)	277	195	204	221	260	285
Elongation (δ)	0.403	0.523	0.468	0.317	0.175	0.103
Strength coefficient (MPa)	454	353	370	356	363	386
Strength hardening coefficient (n)	0.173	0.245	0.243	0.165	0.085	0.076
σ_0/HV	1.85	1.52	1.49	1.73	1.85	1.80
σ_u/HV	2.52	2.45	2.48	2.12	2.28	2.1
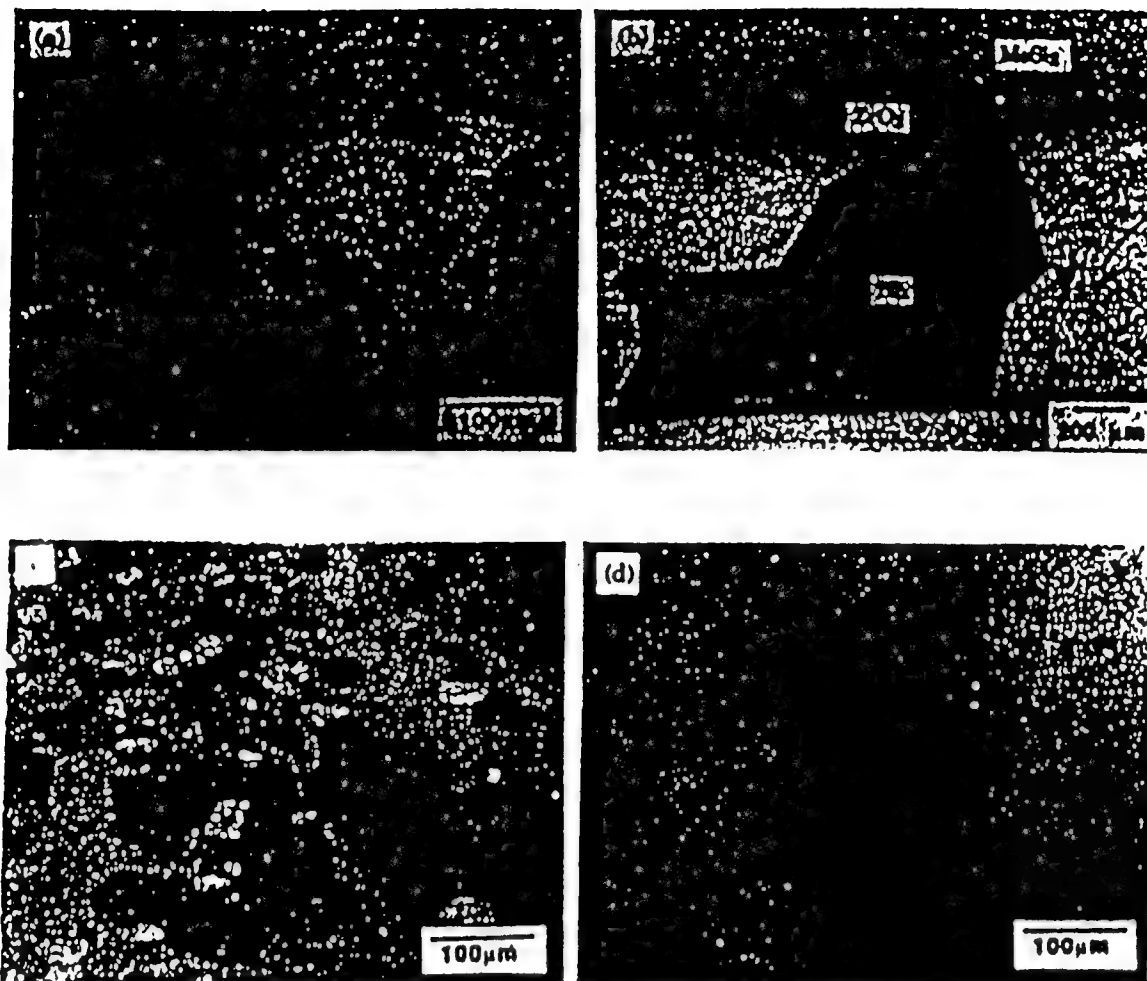
Fig. 2 Optical microstructures of Nb foils. (a) as-received, 1.0 mm thick; (b) processed , 1.0 mm thick; (c) as-received, 0.5 mm thick and (d) processed, 0.5 mm thick. Note that different magnifications are used.

to a combination of two competitive processes during hot pressing: (1) grain growth of Nb, as shown in Fig. 2; (2) solid solution strengthening because of the equilibrium of Nb with the silicides formed at the matrix/reinforcement interface, as shown in Fig. 3. For 1.0 mm Nb foils, grain size has changed from 15 to ~500 μm, which leads to a large decrease in strength and overshadows the increase due to the solid solution hardening. For 0.5 and 0.25 mm Nb foils, grain size has changed from 50 to ~370 μm and from 48 to ~300 μm, respectively. However, shorter diffusion distance to the center of the niobium has made solid solution hardening dominate over the softening due to the grain growth. Therefore, 0.5 and 0.25 mm Nb foils show an increased strength after hot pressing.

It is noted in Table 1 that the tensile strength and Vicker's hardness exhibit a definite relationship, i. e., σ_u/HV equals to 2.48 ± 0.04 and 2.19 ± 0.08 for the as-received and processed Nb, respectively. Such definite relation has also been reported for other materials [21]. Ratio of the yield strength to the Vicker's hardness is also approximately a constant, as shown in Table 1. The results indicate that it is reasonable to infer the strength of the niobium from the hardness measured. Hardnesses of Nb hot pressed with different conditions are summarized in Table 2. The table shows that the hardnesses are almost the same for each group of Nb based on the size. Due to such hardness results, the stress-strain relations for the unconstrained uncoated and Al_2O_3 coated Nb can be assumed to be the same as that of the processed Nb which is the ZrO_2 uncoated Nb before $MoSi_2$ on both sides of the Nb foils has been broken away.
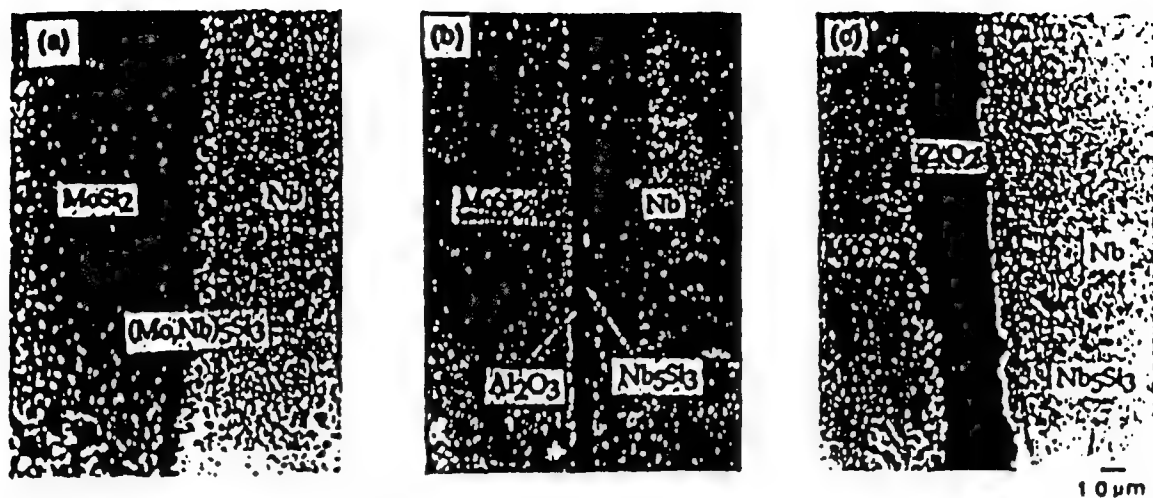
Fig. 3 Interfacial microstructures of (a) uncoated, (b) Al_2O_3 coated and (c) ZrO_2 coated Nb/MoSi$_2$ laminated composites.
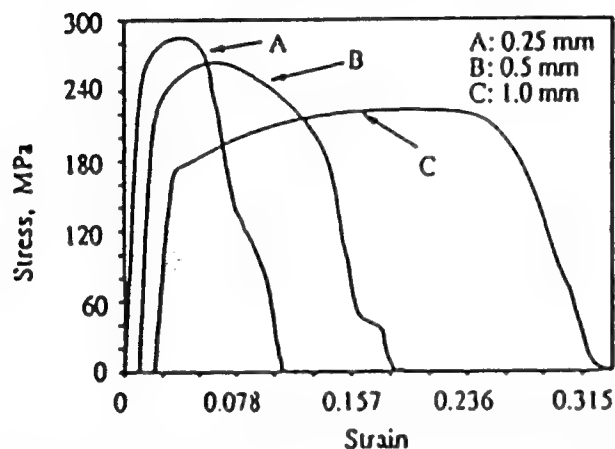
Fig. 4 Typical engineering stress-strain curves for three different thicknesses of the processed Nb foils.

Typical engineering stress-strain curves for different sizes of the processed Nb foils are shown in Fig. 4. As seen in the figure, strengths and rate of work hardening are different for different sizes of Nb. It is believed that such difference is mainly due to the differences in grain size and solid solution strengthening, as discussed above.

From the above discussion, it is clear that the intrinsic mechanical properties of the Nb reinforcement in the composites are different from those of the Nb before the compositing. It is believed that such change in properties due to hot compaction processing is a common phenomenon for ductile-phase-reinforced brittle matrix composites, because most of them have to be fabricated with high temperature processing techniques. Even in chemically compatible composites, change of grain size will cause property change of the ductile reinforcements. Such change imposes difficulty on the prediction and modeling of the composite properties.

3.2 Failure Mechanism and Related Observation on Constrained Niobium

An edge view of the unconstrained and constrained uncoated Nb foils after tensile test is shown in Fig. 5. As seen in the figure, Nb foils fail by drawing down to a wedge for both the constrained and unconstrained conditions. All three different sizes of Nb foils show the same failure mechanism, as shown in Fig. 5. Furthermore, such necking is also observed for all the coated Nb.

Details of the interfaces for the coated and uncoated foils are shown in Fig. 3. As seen in the figure, the coated foils contain three interfaces between the matrix and reinforcement:

Table 2. Microhardness of Nb with different processing conditions (hot pressed at 1400°C, 40MPa for 1 hr)

Thickness of Nb foil (mm)	1.0			0.5			0.25		
Processing condition	Uncoated	Al_2O_3 coated	ZrO_2 coated	Uncoated	Al_2O_3 coated	ZrO_2 coated	Uncoated	Al_2O_3 coated	ZrO_2 coated
HV	104	106	104	118	116	114	131	134	131
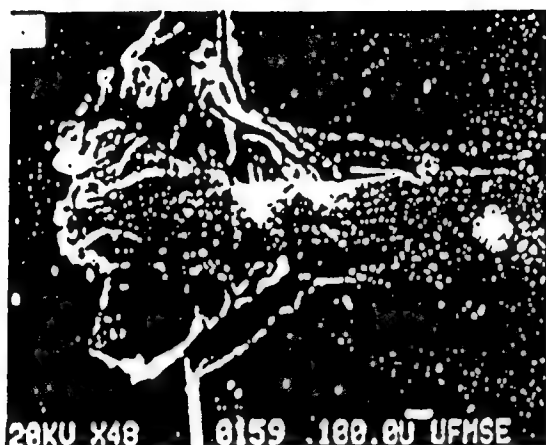
Fig. 5 An edge view of fractured specimens, showing contour of the neck. (a) is a unconstrained, processed Nb foil with a thickness of 1.0 mm, (b), (c) and (d) are constrained Nb with thicknesses of 1.0, 0.5 and 0.25 mm, respectively. Note that different magnifications are used.

$MoSi_2$/coating/Nb_5Si_3/Nb; whereas, the uncoated foils contain two interfaces : $MoSi_2$/$(Mo,Nb)_5Si_3$/Nb. Examination of the microstructures on the tested specimens show that decohesion of the Al_2O_3 and ZrO_2 coated Nb from the matrix was largely due to debonding at the interfaces, as shown in Fig. 6, while decohesion in the uncoated Nb came largely from the matrix fracture, as shown in Fig. 5. This is in agreement with a related study [22], which shows that the uncoated interface has a higher interfacial fracture energy than the fracture energy of the matrix, while the oxide coated interfaces have a lower interfacial fracture energy than the matrix. Thus, it is expected the matrix would fracture before the interface fails in the case of the uncoated Nb, as contrasted with predominance of interfacial failure in the case of the coated Nb.
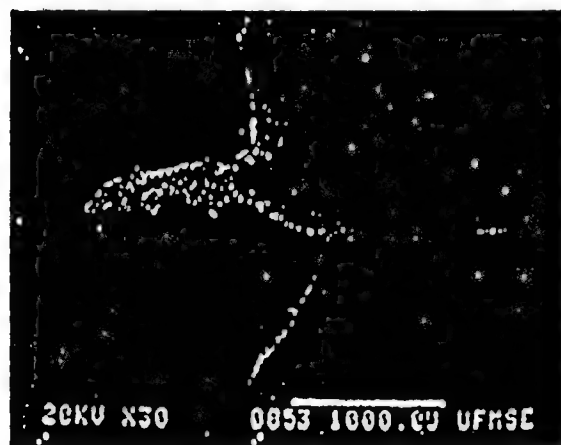
Fig. 6 An edge view of a fractured Al_2O_3 coated Nb/$MoSi_2$ composites laminate, showing interfacial debonding.

Both interfacial failure and matrix fracture create a "gauge length" at the matrix/reinforcement interface which is virtually a region free from constraints of the matrix and is called decohesion length in the text. The measured decohesion lengths are

Table 3. Decohesion length in the MoSi2/Nb composites
(hot pressed at 1400°C, 40MPa for 1 hour)

Thickness of Nb foil (mm)	1.0			0.5			0.25		
Processing condition	Uncoated	Al_2O_3 coated	ZrO_2 coated	Uncoated	Al_2O_3 coated	ZrO_2 coated	Uncoated	Al_2O_3 coated	ZrO_2 coated
Decohesion length (mm)	10 ± 5	Decohesion all the way to the grips.		2.9±0.4	3.3±0.4	Decohesion all the way to the grips.	0.86±0.09	0.94±0.23	1.30±0.61

summarized in Table 3. The data show that within each size group, decohesion length increases from the uncoated to Al_2O_3 coated and then to ZrO_2 coated Nb/MoSi2 composites. Such results are consistent with the measurement of the interfacial fracture energy [22], which shows that the uncoated Nb/MoSi2 has the highest interfacial fracture energy, followed by the Al_2O_3 coated and then ZrO_2 coated Nb/MoSi2 composites.

Increase of the decohesion length with the thickness of Nb foils, as shown in Table 3, is believed to be mainly related to the necking of the Nb. Fig. 7 shows schematically effect of the necking on the decohesion length. Length of the Nb region affected by necking, 2H, is proportional to the thickness of the Nb, as shown in Fig. 5. Approximately, H is 1.3 times of the thickness of Nb, measured from Fig. 5. Large lateral displacement of Nb in the necking affected region gives rise to large transverse stresses which lead to the interfacial debonding and/or matrix fracture. Thus, the thicker the niobium, the longer the necking affected region, and therefore the longer the decohesion length. If the interface bonding is relatively weak, such as the Al_2O_3 and ZrO_2 coated interfaces, the transverse stresses aroused by lateral displacement of the Nb during uniform strain can be large enough to cause the interfacial debonding all the way to the test grips. During the uniform strain, the lateral displacement of Nb right at the interface is proportional to thickness of the Nb. Therefore, decohesion by this mechanism is easier to occur in thick Nb composites than in thin Nb counterparts, as indicated in Table 3.

The failure mechanism observed in the present study suggests that flow behavior of the constrained Nb can be simplified into three stages: (1) elastic deformation; (2) plastic deformation within the decohesion region; (3) localized plastic deformation within the necking region. Such processes are illustrated in Fig. 8. The crack opening of the matrix can be directly related to the deformation of Nb in the decohesion zone. At the early stage of crack opening, Nb only
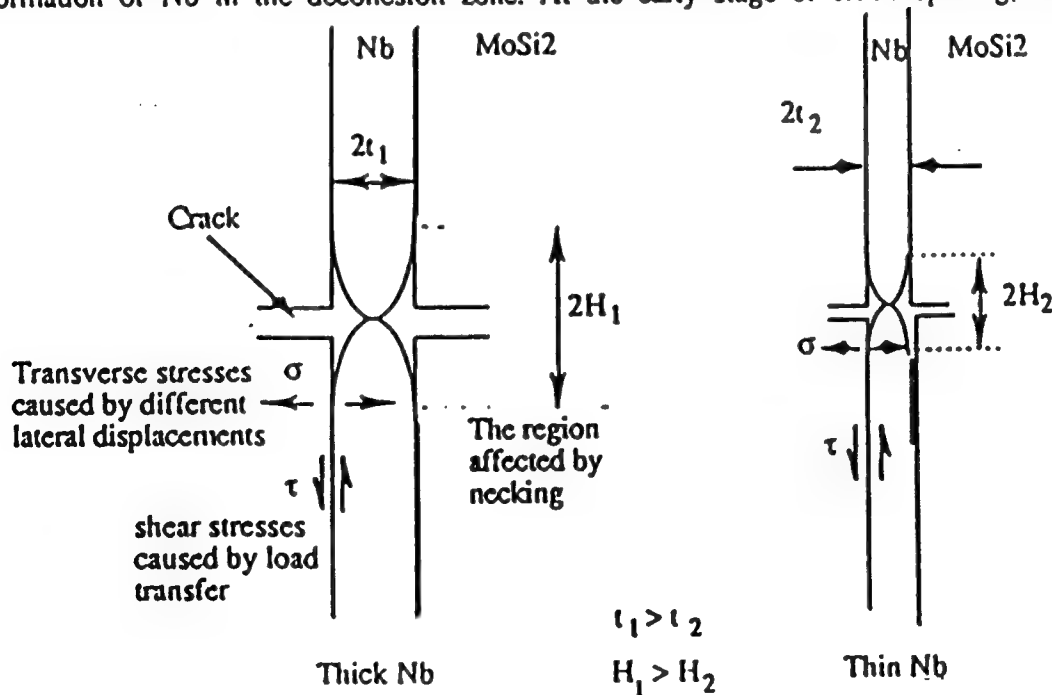
Fig. 7 A schematic showing effect of necking on the decohesion length.

a. Elastic deformation,   b. Plastic deformation,   c. Localized deformation.
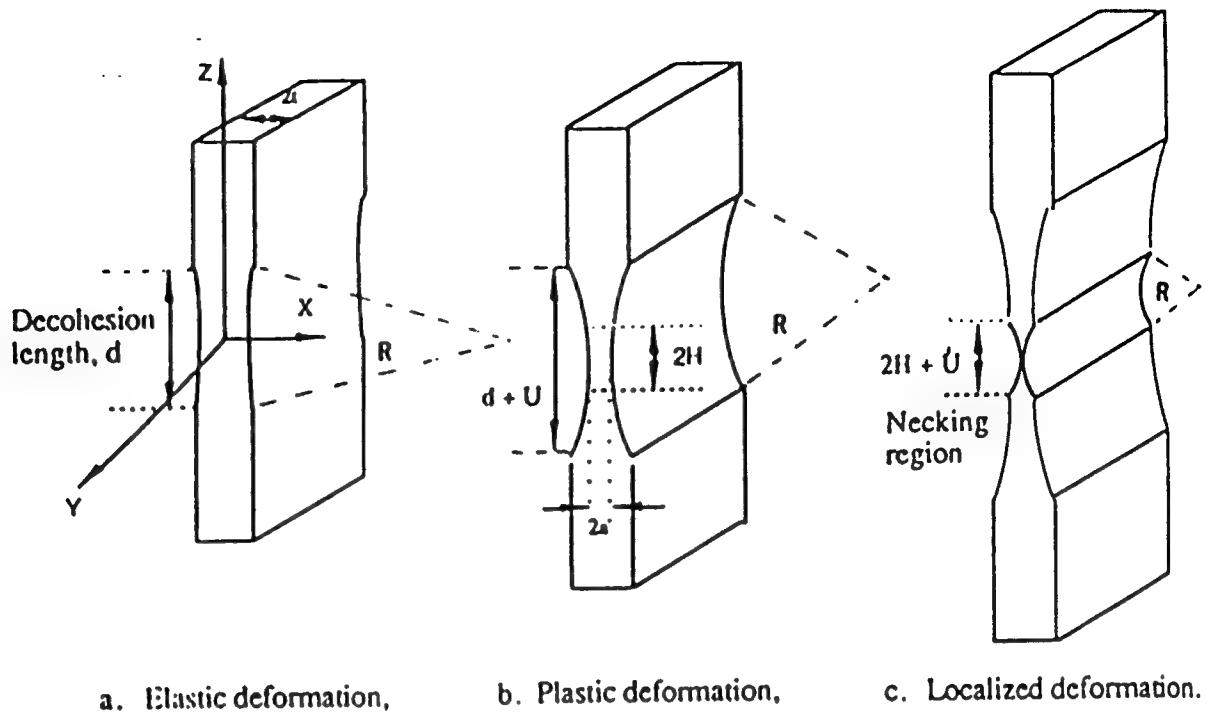
Fig. 8 A schematic of three stages of deformation for constrained Nb. 2H is the length of the necking affected region, 2a is remaining thickness of the reinforcement and U is displacement.

undergoes elastic deformation, as shown in Fig. 8a. As crack opening increases, Nb enters the stage of plastic deformation (Fig.8b). At last, the work hardening rate of the niobium at the central portion of the decohesion region is lower than stress increase rate due to decrease in the cross section area of the reinforcement, the localized deformation begins (Fig.8c), which lead to the final failure of the Nb lamina. Such simplified deformation processes can be used to model stress-displacement behavior of the constrained Nb, as presented in a related study [23].

3.3 Stress-Displacement Curves of Constrained Niobium

Fig. 9 shows typical stress-displacement curves for the uncoated Nb foils with different thicknesses constrained in MoSi$_2$ matrix. The parameters measured are summarized in Table 4. The work of rupture normalized by the yield strength, σ_0, and half thickness of ductile phase, t,

$$\int_0^{U^*} \frac{\sigma(U)}{\sigma_0} \frac{dU}{t}$$

is presented as E_t in the table and is called the normalized work of rupture in the text for convenience. As seen in the figure and table, due to the different intrinsic properties, the maximum stresses reached by the constrained Nb, σ_{max}, are different for different sizes of Nb. However, if the σ_{max} is normalized by its own yield strength, the normalized maximum stress, σ_{max}/σ_0, exhibits an independence on size of Nb. This result suggests that the maximum stress reached is not a function of size of the ductile phase. It is noted that the work of rupture increases with size of Nb, indicating that large size of ductile reinforcement is more effective in improving toughness of the brittle matrix composites. Such size dependence of work of rupture is believed to be due to the increase of decohesion length with increasing size of the ductile phase. It is also noted that the normalized work of rupture shows a dependence on size of Nb. E_t increases with increasing size of the niobium. The size dependence of the normalized work of rupture is again attributed to the size dependence of the decohesion length [23]. This result suggests that the data of the normalized work of rupture obtained from the test on large size of ductile reinforcements

Table 4. Parameters measured from the uncoated Nb/MoSi₂ laminates

2t (mm)	σ_{max} (MPa)	σ_{max}/σ_0	ξ (J/m²)	E_t
1.0	259	1.44	477,000	5.3
0.5	320	1.54	239,000	4.5
0.25	351	1.49	85,000	2.8

Table 5. Parameters measured from the composites with 0.5 mm thick Nb lamina

Processing condition	σ_{max} (MPa)	σ_{max}/σ_0	ξ (J/m²)	E_t
uncoated	320	1.54	239,000	4.5
Al₂O₃ coated	310	1.47	243,000	4.6
ZrO₂ coated	275	1.31	429,000	8.1
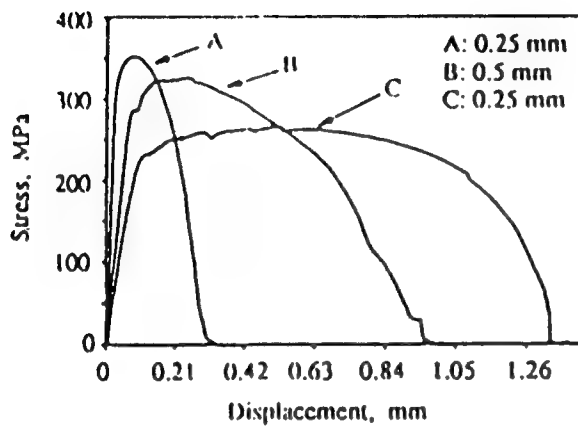
Fig. 9 Typical stress-displacement curves of constrained, uncoated Nb laminae with different thicknesses.
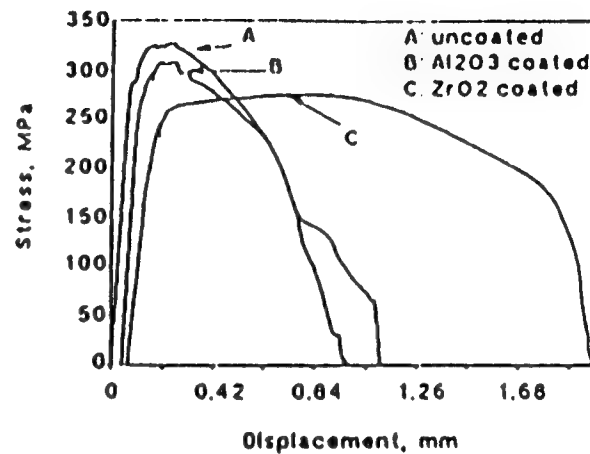
Fig. 10 Effect of the coatings on the stress-displacement curve, measured from composite laminates with 0.5 mm thick Nb lamina.

cannot be extended to small size of the reinforcements directly.

Effect of coatings on the stress-displacement curves is shown in Fig. 10. The parameters measured are summarized in Table 5. The data show that as the decohesion length increases, i.e., the constraints on the reinforcement decreases, the work of rupture increases. This is not surprising since the longer the decohesion length, the more ductile material participates in the plastic deformation, and therefore the more energy is consumed before fracture occurs. It is noted that as the decohesion length increases, the normalized maximum stress decreases, indicating that increasing constraints on the ductile phase increases the σ_{max}. This is consistent with theoretical analyses [11,13,16]. Table 5 also shows that the normalized work of rupture is dependent on the interfacial bonding strength. This is believed to be due to the increase of work of rupture with increasing decohesion length. The above results indicate that limited decohesion enhances the energy consumed to fracture the constrained ductile reinforcement, and therefore improves toughness of the composites.

IV. Concluding Remarks

The present set of experiments demonstrate that flow behavior of constrained ductile reinforcement depends strongly on the intrinsic properties and size of the reinforcement and the properties of the matrix/reinforcement interface. The maximum stress reached by the constrained reinforcement increases as the strength of the reinforcement and constraints increase. Constraints, indicated by decohesion length, are found to be related to the interfacial properties and size of the reinforcement. Decohesion length increases from the uncoated to the oxide coated laminates and increases with increasing size of the reinforcement. Dependence of decohesion length on size of the reinforcement is attributed to the dependence on size of the reinforcement of the length of the necking affected region and the lateral displacement difference between the matrix and reinforcement at the interface. The results indicate that both weak interface and large size of reinforcement improve toughness of the composites.

The normalized work of rupture, E_t, is found dependent on size of the reinforcement. E_t decreases with decreasing size of the reinforcement and increases with decohesion length. This result suggest that more work needs to be done before the data of the normalized work of rupture obtained from the test on large size of ductile reinforcements can be extended to small size of the the reinforcements.

Based on the observation, the flow behavior of the constrained reinforcement has been simplified into three stages: (1) elastic deformation; (2) plastic deformation within the decohesion region; (3) localized plastic deformation within the necking region. Such simplified deformation processes enable the modeling of the stress-displacement relation to be implemented.

References

1. J. L. Chermant and F. Osterstock, J. Mater. Sci., 1976, vol. 11, pp. 1939-51.
2. J. Gurland, Trans. ASM, 1958, vol. 50, pp. 1063-71.
3. A. V. Virkar and D. L. Jognson, J. Am. Ceram. Soc., 1977, vol. 60, pp. 514-19.
4. D. T. Rankin, J. Am. Ceram. Soc., 1971, vol. 54, pp. 277-81.
5. P. Hing and G. W. Groves, J. Mater. Sci., 1972, vol. 7, pp. 427-34.
6. V. V. Kristic and P. S. Nicholsin, J. Am. Ceram. Soc., 1981, vol. 64, pp. 499-504.
7. C. K. Elliott, G. R. Odette, G. E. Lucas and J. W. Sheckherd, High Temperature, High Performance Composites, edited by F. D. Lemkey et al., MRS Proc., 1988, vol. 120, pp. 95-102.
8. E. Fitzer, Whisker- and Fiber-Toughened Ceramics, edited by R. A. Bradley, D. E. Clark, D. C. Larsen and J. O. Stiegler, (ASM International TM, 1988), pp. 165-83.
9. L. Xiao, Y. S. Kim and R. Abbaschian, Intermetallic Matrix Composites, Edited by D. L. Anton, P. L. Martin, D. B. Miracle and R. McMeeking, MRS Proc., 1990, vol. 194, pp. 399-404.
10. L. R. F. Rose, J. Mech. Phys. Solids, 1987, vol.35, pp. 383-405.
11. L. S. Sigl, P. A. Mataga, B. J. Dalgleish, R. M. McMeeking and A. G. Evans, Acta Metall., 1988, vol.36, pp. 945-53.
12. A. G. Evans and R. M. McMeeking, Acta Metall., 1986, vol.34, pp. 2435-41.
13. P. A. Mataga, Acta Metall., 1989, vol.37, pp. 3349-59.
14. B. Budiansky, J. C. Amazigo and A. G. Evans, J. Mech. Phys. Solids, 1988, vol.36, pp. 167-87.
15. J. R. Rice, Fracture, edited by H. Liebowitz, 1968, vol. 2, pp.191-311.
16. M. F. Ashby, F. J. Blunt and M. Bannister, Acta Metall., 1989, vol. 37, pp. 1847-57.
17. H. C. Cao, B. J. Salgleish, H. E. Deve, C. Elliott, A. G. Evans, R. Mehrabien and G. R. Odette, Acta Metall., 1989, vol. 37, pp. 2969-77.
18. H. E. Deve, A. G. Evans, G. R. Odette, R. Mehrabien, M. L. Emiliani and R. J. Hecht, Acta Metall., 1990, vol. 38, pp. 1491-1502.
19. L. Xiao and R. Abbaschian, "On the Strength and Stiffness of Ductile Phase Reinforced MoSi$_2$ Composites", to be published in Advanced Metal Matrix Composites for Elevated Temperatures, Proc. in 1991 TMS Fall Meeting, Cincinnati, OH, Oct. 1991.
20. L. Xiao and R. Abbaschian, "Evaluating A Technique for Determining the Toughening of Brittle Matrix by Ductile Reenforcement", to be published in Advanced Metal Matrix Composites for Elevated Temperatures, Proc. in 1991 TMS Fall Meeting, Cincinnati, OH, Oct. 1991.
21. F. C. Lea, Hardness of Metals, charles Griffin and Company, Ltd, 42 Drury Lane, W. C. 2., London, 1936, pp. 91-105.
22. L. Xiao and R. Abbaschian, "Role of Matrix/Reinforcement Interfaces in the Fracture Toughness of Brittle Materials Toughened by Ductile Reinforcements", presented in TMS Fall Meeting, Cincinnati, OH, Oct. 22, 1991.
23. L. Xiao, "Study of the Flow Behavior of Constrained Ductile Phases ---- II. Modeling", published in this Proceedings.

STUDY OF THE FLOW BEHAVIOR OF CONSTRAINED DUCTILE PHASES

------------ II. MODELING

Lingang Xiao

Department of Materials Science and Engineering, University of Florida, Gainesville, FL 32611

Abstract

Brittle materials can be toughened by incorporating ductile reinforcements into them. To evaluate the toughening by ductile reinforcements, it is necessary to know the stress-displacement relation of the ductile phase constrained by the brittle matrix. In the present study, based on the observations from tensile tests on the specimens of a single Nb lamina imbedded in $MoSi_2$ matrix, an analytical model is developed which gives insight into the influence on the stress-displacement curve of yield strength, work hardening, matrix/reinforcement interfacial bonding strength and size of the reinforcement. A characteristic decohesion length, which is a function of size of the reinforcement, has been identified by the model and related to the measured decohesion length. The results allow the extrapolation of the work of rupture measured from large size of constrained ductile phases to small size of the ductile phases. As the reinforcements used in composites are usually smaller in size than those tested in such tensile tests, the extrapolation of the work of rupture allows the contribution of ductile reinforcements to the toughness of a brittle matrix composite to be calculated.

I. Introduction

It has been established that substantial toughening of brittle matrices can be achieved by incorporating ductile reinforcements [1-9]. The primary toughening mechanism of ductile reinforcement has been attributed to the bridging of ductile ligaments [10-14], although the ductile reinforcements may also increase toughness by crack deflection and by trapping mechanisms. The contribution to fracture toughness from bridging can be estimated by extending cohesive force model [15] to ligament bridging [11,12] and can be written as

$$\Delta G = V_f \int_0^{U^*} \sigma(U)\, dU \qquad \text{.. (1)}$$

where $\sigma(U)$ is the nominal stress carried by the constrained ductile reinforcement for a given crack opening U, V_f is volume fraction of the ductile reinforcement, U^* is the crack opening at the point when the ductile reinforcement fails, and the definite integral, designated as ξ in the text, is the work of rupture of the constrained ductile ligament. Thus, the key point to predict the increased fracture toughness is to calculate $\sigma(U)$ as a function of crack opening. Due to the difference between $\sigma(U)$ and that measured in a simple tensile test, several investigators have attempted to relate $\sigma(U)$ to the uniaxial stress-strain properties of the ductile phase. The methods used included a slip line field analysis [11,12], finite element methods [11,13], spring models [10,14] and geometric models [11,13,16]. Their results indicated that $\sigma(U)$ was dependent on the intrinsic properties of the ductile phase and the constraint conditions. However, direct comparison of stress-displacement curves between the models and experimental results is not very satisfying in magnitude, although the general trends are the same for the models and experiments. The extrapolation of the work of rupture measured from large size of constrained ductile phases to small size of the ductile phases also needs to be investigated.

The present study is aimed to model the stress-displacement relation and to examine the feasibility of extrapolation of the work of rupture measured from large size of constrained ductile phases to small size of the ductile phases. Based on the observations from tensile tests on the specimens of a single Nb lamina imbedded in $MoSi_2$ matrix, an analytical model is developed which gives insight into the influence on the stress-displacement curve of yield strength, work hardening, matrix/reinforcement interfacial bonding strength and size of the reinforcement . A characteristic decohesion length, which is a function of size of the reinforcement, has been identified by the model and related to the measured decohesion length. The results allow the extrapolation of the work of rupture measured from large size of constrained ductile phases to small size of the ductile phases and allows the contribution of ductile reinforcements to the toughness of a brittle matrix composite to be calculated.

The symbols used in the text are defined in Table 1.

II. Modeling

2.1 Experimental Observations

It has been shown [17,18] that the failure of the constrained Nb laminae in $MoSi_2$ matrix involves the following scenario. When an advancing crack just impinges a Nb reinforcement, no debonding at the matrix/reinforcement interface occurs. As external load continues to increase, debonding at the interface and/or multiple fracture of the matrix near the interface occur due to a relatively large lateral deformation of the Nb reinforcement compared to the matrix and load transfer from the matrix to the reinforcement. Then come the necking and fracture of the niobium as the load continues to increase. The observations [17] lead to a simplified flow behavior of the constrained Nb which can be divided into three stages: (1) elastic deformation; (2) plastic deformation within the decohesion region; (3) localized plastic deformation within the necking region. Such deformation processes are illustrated in Fig. 1. At the early stage of crack opening, Nb only undergoes elastic deformation, as shown in Fig. 1a. As crack opening increases, Nb enters the stage of plastic deformation (Fig.1b). At last, the work hardening rate of the niobium

at the central portion of the decohesion region is lower than stress increase rate due to decrease in the cross section area of the reinforcement, the localized deformation begins (Fig.1c), which lead to the final failure of the Nb lamina.

In the present study, displacement of the stress-displacement curve is assumed to only come from the deformation of Nb lamina inside the decohesion region because the Nb outside the decohesion region is bonded to the matrix and only undergoes elastic deformation. Contour of the Nb lamina in the decohesion region is assumed to be part of the outside surface of a cylinder with a varied radius of R for all the stages of the deformation, as shown in Fig. 1. Such assumption is a good approximation to the real contour of the Nb observed in the experiments [17] and makes the calculation possible. To generate data of the nominal axial stress-displacement curve (σ-U), U is measured as the axial displacement of the matrix point at the boundary of the decohesion region, while σ is computed from the total force exerted on the remaining cross section of the midplane at the neck, normalized by the original midplane area. Plane strain is assumed for the computation in all the stages.

Table 1. Symbols and definition

2a	remaining thickness of reinforcement
d	decohesion length
d_c	characteristic decohesion length
d_m	measured decohesion length
E	Young's modulus
E_t	normalized work of rupture

$$\int_{0}^{u^*} \frac{\sigma(U)\, dU}{\sigma_0\, t}$$

ε_t	true strain
$\bar{\varepsilon}_x$	mean strain in x-direction at the midplane of the neck during elastic deformation
ΔG	increment in toughness caused by ductile reinforcement
2H	length of reinforcement affected by necking
n	work hardening coefficient
μ	Poisson's ratio
R	radius of contour of the neck
σ	stress
$\bar{\sigma}$	effective stress
σ_0	yield strength
σ_{max}	maximum stress reached by constrained reinforcement
σ_y	yield stress of constrained reinforcement
σ_{za}	stress in z-direction at the free surface of neck
2t	initial thickness of reinforcement
U	axial extension equal to crack-opening displacement
U^*	crack opening displacement at failure of ductile reinforcement
V_f	volume fraction of ductile reinforcement
ξ	work of rupture, $\int_{0}^{u^*} \sigma(U)\, dU$

The true stress-strain relations of the Nb laminae used in the calculation are

$$\sigma_t = 356\, \varepsilon_t^{0.165}\ (MPa) \quad \text{for 1.0 mm Nb}$$
$$\sigma_t = 363\, \varepsilon_t^{0.085}\ (MPa) \quad \text{for 0.5 mm Nb}$$
$$\sigma_t = 386\, \varepsilon_t^{0.076}\ (MPa) \quad \text{for 0.25 mm Nb}$$

$$\ldots\ldots\ldots\ldots\ldots \quad (2)$$

The above equations are obtained from the direct measurement on the unconstrained hot pressed Nb which is different from the Nb prior to the compositing because of change of the properties of the Nb during hot compaction. Use of the above equations allow us to compare the model to the experiment directly. Details of the measurement of the true stress-strain relations for the unconstrained hot pressed Nb can be found in Reference [17]. The yield strengths, σ_0, of three different sizes of Nb laminae measured are also different due to different grain sizes and solid solution strengthening [17]. The yield strengths are 180, 211 and 236 MPa for Nb laminae with a thickness of 1.0, 0.5 and 0.25 mm, respectively.

2.2 Stage of Elastic Deformation

To compute σ-U data for elastic deformation, two more assumptions are made: (1) the volume-conserving nature of large scale plastic deformation is also applicable to this stage; (2) the effective stress across the midplane of the neck is constant.

Assumption (1) and the assumed contour relate the displacement, U, to the radius of the cylinder, R, as
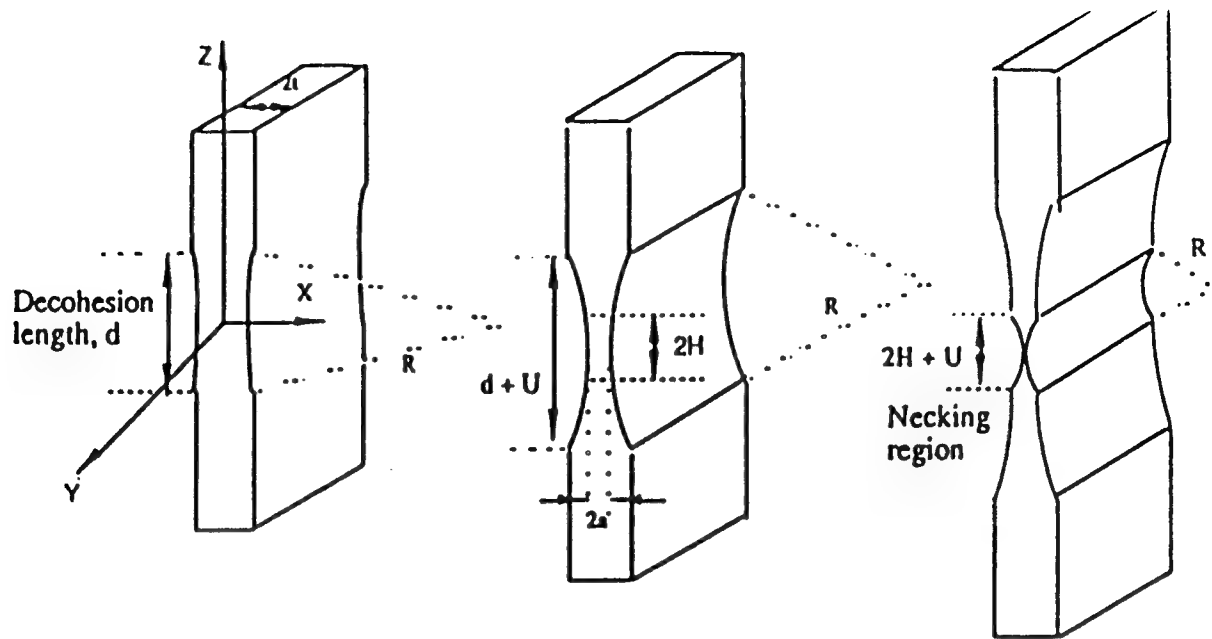
| a. Elastic deformation, | b. Plastic deformation, | c. Localized deformation. |

Fig. 1 A schematic of three stages of deformation for constrained Nb.

$$R = \frac{(d + U)^3}{12\, t\, U} + \frac{4}{3} \frac{t\, U}{(d + U)} \qquad \ldots\ldots\ldots\ldots \quad (3)$$

Assumption (2) renders Bridgman formula for a necking plate [19]

$$\sigma_z(\tfrac{x}{a}) = \sigma_x(\tfrac{x}{a}) \cdot [\, R + \tfrac{a}{2}(1 - \tfrac{x^2}{a^2})] \frac{\partial \sigma_x}{\partial x} \qquad \ldots\ldots\ldots\ldots\ldots \quad (4)$$

computable even for elastic deformation. x and a in the above equation are defined in Fig. 1. Although the assumed contour and constant effective stress do not represent the real situation of the decohesion region, they introduce negligible error to the work of rupture (see the Appendix).

With the assumption (2), boundary conditions at the neck and plane strain assumption, the stress component σ_z at the midplane of the neck can be related to the stress σ_{za}, which is σ_z at the free surface of the neck, as follows

$$\sigma_{za}^2 = \sigma_x^2 + \sigma_z^2 \cdot \frac{(1 + 2\mu - 2\mu^2)}{(1 - \mu + \mu^2)} \sigma_x \sigma_z \qquad \ldots\ldots\ldots\ldots\ldots \quad (5)$$

Introduction of the Poisson's ratio of Nb ($\mu = 0.39$) into eq. (5) yields

$$\sigma_z = 0.968\, \sigma_x + \sigma_{za} \qquad \ldots\ldots\ldots\ldots \quad (6)$$

Substituting eq. (6) into eq. (4) and solving for σ_x yield

$$\sigma_x = \sigma_{za}[\, 31.25 - 31.25 \frac{(\frac{R}{a})^{0.032}}{(\frac{R}{a} + \frac{1}{2} \cdot \frac{x^2}{2a^2})^{0.032}}] \qquad \ldots\ldots\ldots\ldots \quad (7)$$

where σ_{za} is related to the average strain, $\bar{\varepsilon}_x$, measured from the neck with the following

equation

$$\overline{\mathcal{E}}_x = \frac{\int_0^. \mathcal{E}_x(\sigma_x, \sigma_y, \sigma_z)\, dx}{a}$$

$$= \sigma_{za} \frac{1}{aE} \left[9.5579\, a - \int_0^. \frac{10.1\left(\frac{R}{a}\right)^{0.032}}{\left(\frac{R}{a} + \frac{1}{2} - \frac{x^2}{2a^2}\right)^{0.032}} \, dx \right] \qquad \ldots\ldots\ldots\ldots\ldots \qquad (8)$$

where E is Young's modulus of Nb, and $\overline{\mathcal{E}}_x$ can be measured from the dimension of the neck using the relation of $\overline{\mathcal{E}}_x = Ln(a/t)$. Thus, by numerical integration of eq. (8), σ_{za} can be found for any specific R and a. Using eqs. (3), (6), (7) and (8), σ-U data can be calculated for the elastic deformation.

2.3 Stage of Plastic Deformation

Von Mises yield criterion is used to monitor the initial yielding. Thus, when the effective stress reaches the yield strength of the Nb, plastic deformation begins. Now, Bridgman formula for a necking plate [19]

$$\sigma_z = \sigma_{za} \left\{ 1 + Ln \left[1 + \frac{1}{2} \frac{a}{R} \left(1 - \frac{x^2}{a^2} \right) \right] \right\} \qquad \ldots\ldots\ldots\ldots\ldots \qquad (9)$$

can be used directly to compute the nominal axial stress. By applying boundary conditions at the neck, a relation between σ_{za} and the effective stress, $\overline{\sigma}$, can be found, which is

$$\sigma_{za} = 1.1547\, \overline{\sigma} \qquad \ldots\ldots\ldots\ldots\ldots\ldots\ldots\ldots \qquad (10)$$

where $\overline{\sigma}$ is determined by the effective strain.

In the computation, the effective strain at the initial yield is assigned as zero, while the effective stress has a value of the yield strength of the unconstrained Nb. After the initial yield, the niobium is assumed to be perfect isotropy of strain hardening and the power law, eq. (2), is used to compute the effective stress.

2.4 Stage of Localized Plastic Deformation

The localized plastic deformation is assumed to begin when the nominal axial stress is about to decrease. The length of the region affected by necking, 2H, shown in Fig.1, is chosen as 2t. After necking down to a point at the neck, the region with such dimension gives two triangles with the height equal to the base. The base is assumed to have no more deformation when the localized deformation begins. The assumptions give rise to a contour as shown in Fig. 1c, and such contour is an approximation for the contour of Nb in the decohesion region observed in the experiments [17]. The displacement in the stage of the localized deformation is assumed to come only from the deformation of the necking affected region and the computation of the nominal axial stress is carried out using eqs. (9) and (10).

III. Results of the Model

3.1 Effect of the Decohesion Length

Dependence of the stress-displacement curve on the decohesion length is shown in Fig. 2 which

Table 2. Decohesion length in the MoSi$_2$/Nb composites (hot pressed at 1400°C, 40MPa for 1 hour)

Thickness of Nb foil (mm)	1.0			0.5			0.25		
Processing condition	Uncoated	Al$_2$O$_3$ coated	ZrO$_2$ coated	Uncoated	Al$_2$O$_3$ coated	ZrO$_2$ coated	Uncoated	Al$_2$O$_3$ coated	ZrO$_2$ coated
Decohesion length (mm)	10 ± 5	Decohesion all the way to the grips.		2.9±0.4	3.3±0.4	Decohesion all the way to the grips.	0.86±0.09	0.94±0.23	1.30±0.61

is generated using the true stress-strain data of 0.5 mm Nb. The results indicate that the maximum stress reached by the constrained Nb, σ_{max}, increases with increasing constraints on the ductile reinforcement; but increasing constraints decreases the work of rupture. Such results suggest that a relatively weak bond at the interface enhances the work of rupture and therefore is conducive to toughness of the brittle matrix composites. Similar results are obtained by other investigators using different models [11,13,16].

When the data measured in the experiment [17], as shown in Table 2, are put into the model, the results show that the maximum stresses are nearly constant for each size of Nb, although the work of rupture increases with increasing decohesion length. The work of rupture normalized by the yield strength, σ_0, and half thickness of ductile phase, t,

$$\int_{0}^{v^*} \frac{\sigma(U)}{\sigma_0} \frac{dU}{t}$$

called as the normalized work of rupture, E_t, in the text, also exhibit an increase with increasing decohesion length. The computed parameters for the constrained Nb lamina with a thickness of 0.5 mm are summarized in Table 3. The results suggest that the present coated and uncoated Nb/MoSi$_2$ laminates are in the range of low constraints because in the high constraint range (i.e., short decohesion length), σ_{max} is very sensitive to the decohesion length, as shown in Fig. 2. An experimental evidence indicating that the present laminates are in the range of low constraints is that the maximum stress reached by the laminate composites with 1.0 mm Nb lamina are almost the same for different decohesion lengths ranging from ~ 5 to ~ 15 mm.

3.2 Effect of Reinforcement Size

A comparison on the size effect between the model and experiments for the uncoated Nb/MoSi$_2$ laminates is showed in Fig. 3. The input data for the model are from eq. (2) and Table 2 with each size of Nb having its own measured parameters and properties. The input of Young's

Table 3. Calculated parameters for the composite laminates with 0.5 mm thick Nb lamina

Processing condition	σ_{max} (MPa)	σ_{max}/σ_0	ξ (J/m^2)	E_t
uncoated	329.3	1.56	196,000	3.707
Al$_2$O$_3$ coated	328.4	1.55	203,000	3.860
ZrO$_2$ coated	328.2	1.55	339,000	6.435
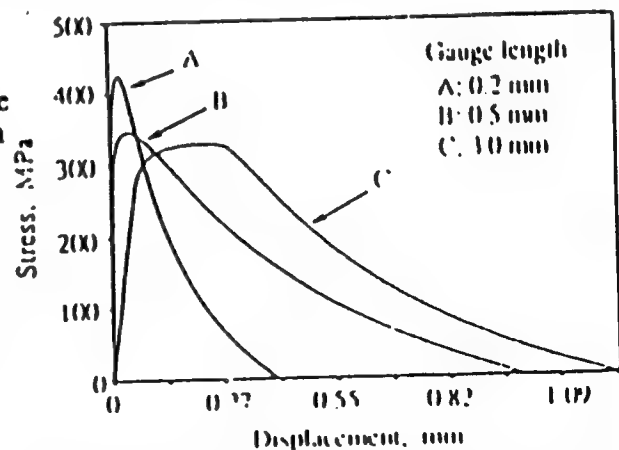
Fig. 2 Effect of decohesion length on the stress displacement curves

Table 4. Summary of parameters calculated from the model and measured for the uncoated Nb/MoSi$_2$ laminates

2t (mm)	Calculated				Measured				$E_{t(cal)}/E_{t(exp)}$
	σ_{max} (MPa)	σ_{max}/σ_o	ξ (J/m^2)	E_t	σ_{max} (MPa)	σ_{max}/σ_o	ξ (J/m^2)	E_t	
1.0	292	1.62	400,000	4.4	259	1.44	477,000	5.3	0.838
0.5	329	1.56	196,000	3.7	320	1.54	239,000	4.5	0.814
0.25	354	1.50	88,000	2.9	351	1.49	85,000	2.8	1.025

modulus is from the slope of the stress-strain curve of the unconstrained Nb in a simple tensile test. As shown in Fig. 3, the model fits the experimental data reasonably well except the stage of the localized plastic deformation. The deviation in this stage is believed to be due to the difference between the real and assumed contours of the neck. The parameters calculated from the model are summarized in Table 4. For comparison the measured parameters [17] are also included in the table. Ratios of the calculated and measured normalized work of rupture, $E_{t(cal)}/E_{t(exp)}$, is also included in the table. It is noted that the calculated maximum stress, the work of rupture and the normalized work of rupture are all close to the measured counterparts. It is quite clear that the maximum stress, the work of rupture and the normalized work of rupture can be estimated from the model.

Reinforcements used in composites are usually smaller in size than those tested in the present study. To predict the work of rupture for small size of reinforcements, it is necessary to know the decohesion length in advance for computation of the model. A plot of σ_{max} vs decohesion length computed from the model for the composites with 0.25 mm Nb lamina is shown in Fig. 4. It is noted that there exists a characteristic decohesion length, d_c, below which σ_{max} becomes very sensitive to the decohesion length. Computation of the model shows that the characteristic decohesion length is equal to twice of the thickness of the niobium and the normalized work of rupture with the characteristic decohesion length, called as the characteristic normalized work of rupture, is constant regardless of size of the reinforcement.

The measured decohesion lengths, d_m, in the present study are all larger than d_c. However, ratio of d_m to d_c is found to be a linear function of size of the reinforcement, as shown in Fig. 5. The relations found are
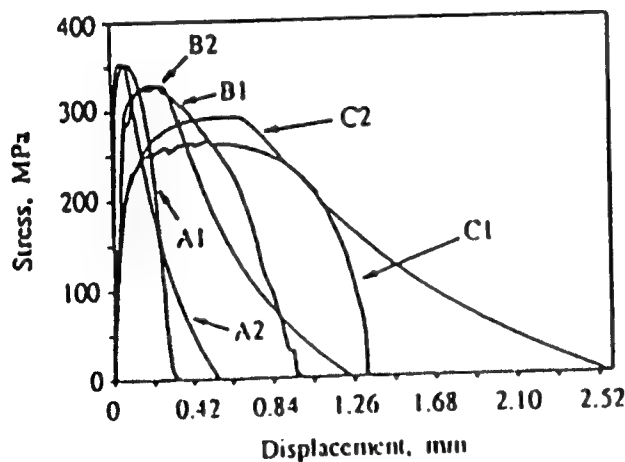
Fig. 3 Effect of reinforcement size on the stress displacement curve. A1, B1 and C1 are experimental curves of the composites with 0.25, 0.5 and 1.0 mm thick Nb laminae, respectively; A2, B2 and C2 are results from the model for composites with 0.25, 0.5 and 1.0 mm thick Nb laminae, respectively.
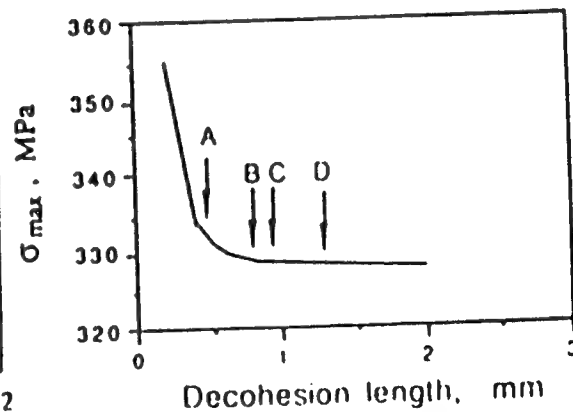
Fig. 4 A plot of σ_{max} vs decohesion length. Arrow A shows characteristic decohesion length, and arrows B, C and D show the measured decohesion lengths of the composites containing uncoated, Al$_2$O$_3$ coated and ZrO$_2$ coated Nb laminae, respectively.
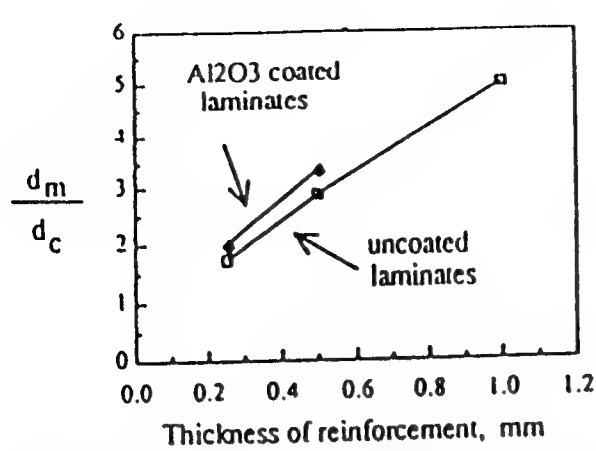
Fig. 5 A plot of ratio of the measured to characteristic decohesion length as a function of reinforcement size.
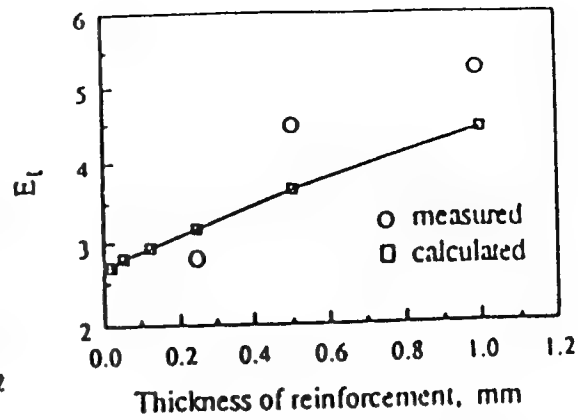
Fig. 6 Normalized work of rupture as a function of reinforcement size.

$$d_m/d_c = 0.66 + 10.72 \, t \quad \text{(for } Al_2O_3 \text{ coated laminates)}$$
$$d_m/d_c = 0.66 + 8.70 \, t \quad \text{(for uncoated laminates)} \quad \ldots\ldots\ldots\ldots \quad (11)$$

It is noted that d_m becomes closer to d_c as size of the reinforcement decreases, suggesting that the normalized work of rupture becomes smaller and closer to the characteristic normalized work of rupture. The oxide coating changes the slope of the line, indicating that the coating enhances decohesion and such effect becomes larger as size of the reinforcement increases. With eq. (11), the decohesion length of small size of the reinforcement can be predicted and the work of rupture be calculated from the model. A plot generated in this way is shown in Fig. 6 which shows that E_t decreases with decreasing size of the reinforcement, as found in the experiments [17]. Thus, to estimate the contribution of ductile reinforcements to the toughness of a brittle matrix composite, the model can be used.

3.3 Effect of Yield Strength and Work Hardening

Effects of yield strength and work hardening on the work of rupture are evaluated by putting the properties of several different materials into the model. The properties are obtained from Reference [20] and the true stress-strain curves for some materials are shown in Fig. 7. It is noted that both 4340 steel and 70/30 brass have a higher work hardening rate than the Nb used in the present study. The computed stress-displacement curves are shown in Fig. 8, and the input and output data are summarized in Table 5. It is clear that work of rupture increases with increasing work hardening rate. Although 70/30 brass has the lowest yield strength, its high work hardening rate enables it to have a much higher work of rupture than both 4340 steel and Nb both of which have a higher yield strength than the brass. Reason for such phenomenon is that a high work hardening rate reinforcement have a higher increase rate in the load-carrying ability, and instability (i.e., the localized plastic deformation within the necking region), therefore, comes relatively later than a low work hardening rate reinforcement, when the two

Table 5. The input and output data for computing the stress-dsiplacement curves shown in Fig. 8 (the thickness of all materials is assumed as 0.5 mm)

Material	Input Data				Output Data		
	$\sigma_t = Kc_t^n$ (MPa)	σ_0 (MPa)	E (GPa)	μ	σ_{max} (MPa)	ξ (J/m^2)	E_t
Nb	$363c_t^{0.085}$	210	105	0.39	329	196,000	3.7
SAE 4340 steel	$642c_t^{0.15}$	230	193	0.29	496	351,000	6.1
0.6% C steel	$1573c_t^{0.10}$	500	199	0.29	1337	801,000	6.4
70/30 brass	$897c_t^{0.49}$	80	111	0.30	483	662,000	33.1
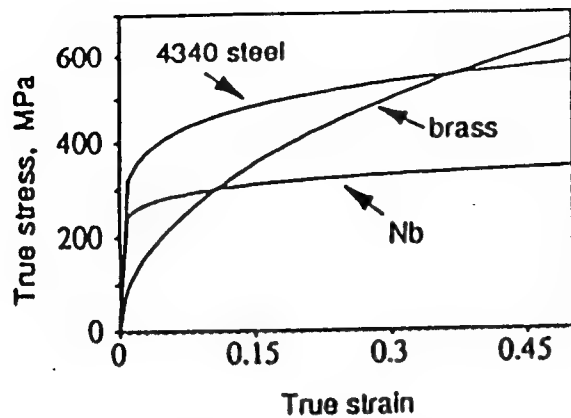
Fig. 7 The true stress-strain curves of the some materials used for evaluating effects of yield strength and work hardening.
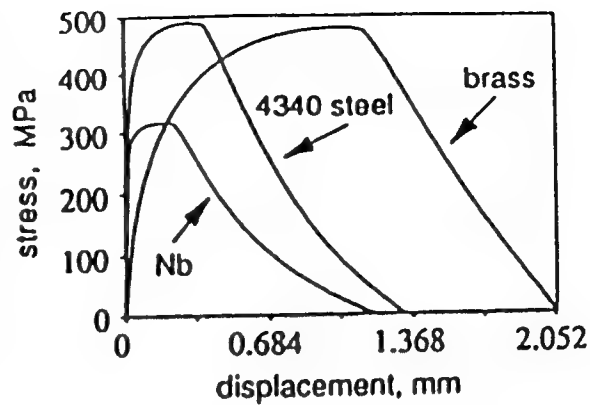
Fig. 8 Computed stress-displacement curves using the data in Fig. 7 and Table 5.

reinforcements have the same increase rate in stress due to decrease in the cross-sectional area of the reinforcements. Thus, high work hardening rate reinforcements have a relatively longer stage of plastic deformation in the whole decohesion region, leading to more energy to be dissipated and higher work of rupture. It is noteworthy that the brass has a very high normalized work of rupture, which suggests that the normalized work of rupture could probably be used as an indicator of the efficiency with which the work hardening contributes to enhancing the work of rupture.

When yield strength is very high, such as 0.6 % C steel in Table 5, work of rupture would be also very high. As shown in Table 5, 0.6% C steel has a much higher work of rupture than 70/30 brass although it has a lower work hardening rate than the brass. Contribution of yield strength to work of rupture is mainly to increase the maximum stress reached by the constrained reinforcement. From the above discussion, it is concluded that both high work hardening rate and yield strength are beneficial to work of rupture. Work hardening is more effective in enhancing the work of rupture than yield strength because high work hardening rate delays the instability of deformation for constrained ductile reinforcements, therefore more material of the reinforcements participates in plastic deformation and more energy has to be consumed.

IV. Concluding Remarks

Based on the observation, the flow behavior of the constrained reinforcement has been divided into three stages: (1) elastic deformation; (2) plastic deformation within the decohesion region; (3) localized plastic deformation within the necking region. An analytical model has been developed to describe these three stages. The model gives insight into the influence of decohesion, yield strength, work hardening and size of the reinforcement on the stress-displacement curve. The overall shape of the σ-U curves generated by the model fits the measured curves reasonably well.

Computation of the model indicates that work of rupture is enhanced by a relatively weak bond at the matrix/reinforcement interface, by large size of reinforcement, and by a high yield strength and high work hardening rate. High work hardening rate is more effective in enhancing work of rupture than high yield strength.

Computation of the model suggests that there is a characteristic decohesion length, d_c, with which the normalized work of rupture, E_t is constant regardless of size of the reinforcement. It is found that the deviation of the measured decohesion length from d_c increases with increasing size of the reinforcement, which leads to E_t increases with increasing size of the reinforcement. A relation between d_m and d_c is found which allows the prediction of the real decohesion length for small size of the reinforcement and therefore the calculation of the work of rupture for

specific size of the reinforcement.

References

1. J. L. Chermant and F. Osterstock, J. Mater. Sci., 1976, vol. 11, pp. 1939-51.
2. J. Gurland, Trans. ASM, 1958, vol. 50, pp. 1063-71.
3. A. V. Virkar and D. L. Jognson, J. Am. Ceram. Soc., 1977, vol. 60, pp. 514-19.
4. D. T. Rankin, J. Am. Ceram. Soc., 1971, vol. 54, pp. 277-81.
5. P. Hing and G. W. Groves, J. Mater. Sci., 1972, vol. 7, pp. 427-34.
6. V. V. Kristic and P. S. Nicholsin, J. Am. Ceram. Soc., 1981, vol. 64, pp. 499-504.
7. C. K. Elliott, G. R. Odette, G. E. Lucas and J. W. Sheckherd, High Temperature, High Performance Composites, edited by F. D. Lemkey et al., MRS Proc., 1988, vol. 120, pp. 95-102.
8. E. Fitzer, Whisker- and Fiber-Toughened Ceramics, edited by R. A. Bradley, D. E. Clark, D. C. Larsen and J. O. Stiegler, (ASM International TM, 1988), pp. 165-83.
9. L. Xiao, Y. S. Kim and R. Abbaschian, Intermetallic Matrix Composites, Edited by D. L. Anton, P. L. Martin, D. B. Miracle and R. McMeeking, MRS Proc., 1990, vol. 194, pp. 399-404.
10. L. R. F. Rose, J. Mech. Phys. Solids, 1987, vol.35, pp. 383-405.
11. L. S. Sigl, P. A. Mataga, B. J. Dalgleish, R. M. McMeeking and A. G. Evans, Acta Metall., 1988, vol.36, pp. 945-53.
12. A. G. Evans and R. M. McMeeking, Acta Metall., 1986, vol.34, pp. 2435-41.
13. P. A. Mataga, Acta Metall., 1989, vol.37, pp. 3349-59.
14. B. Budiansky, J. C. Amazigo and A. G. Evans, J. Mech. Phys. Solids, 1988, vol.36, pp. 167-87.
15. J. R. Rice, Fracture, edited by H. Liebowitz, 1968, vol. 2, pp.191-311.
16. C. A. Anderson and M. K. Aghajanian, Ceram. Eng. Sci. Proc., 1988, vol. 9, pp. 621-26.
17. L. Xiao, "Study of the Flow Behavior of Constrained Ductile Phases --- I. Experiment", published in this Proceedings.
18. L. Xiao and R. Abbaschian, "Role of Matrix/Reinforcement Interfaces in the Fracture Toughness of Brittle Materials Toughened by Ductile Reinforcements", presented in TMS Fall Meeting, Cincinnati, OH, Oct. 22, 1991.
19. P. W. Bridgman, Studies in Large Plastic Flow and Fracture, 1st ed., McGraw-Hill Book Comp., Inc., New York, NY, 1952, pp. 32-37.
20. G. E. Dieter, Jr., Mechanical Metallurgy, McGraw-Hill Kogakusha, Ltd., Tokyo, 1961, p. 248.

Appendix

Finite element analysis (FEA) of the stress distribution across the neck and the contour of the decohesion region during the elastic deformation was implemented using the finite element software package ANSYS. Due to the symmetry, only one quarter of the specimen was analyzed using two-dimensional 4-node isoparametric elements with an assumption of plane strain deformation. A typical finite element model for the constrained Nb is shown in Fig. 9. The displacement at the midplane of the neck was allowed only in the x-direction, and the bonded boundary of Nb to the matrix and the axial central plane were allowed to displace only in z-direction, as shown in Fig. 9.

Results from the FEA for the case of constrained 1.0 mm Nb lamina with 2.28 mm decohesion length under a nominal axial stress of 150 MPa are presented in Figures 10-12. Fig. 10 compares the assumed contour of the decohesion region with the FEA result. The data show that the assumed contour deviates from the FEA result, leading to a smaller crack opening displacement compared to the finite element analysis. However, the difference is so small that it introduces negligible errors to the computation of the work of rupture.

Evaluation of effective stress distribution across the midplane of the neck is shown in Fig. 11.
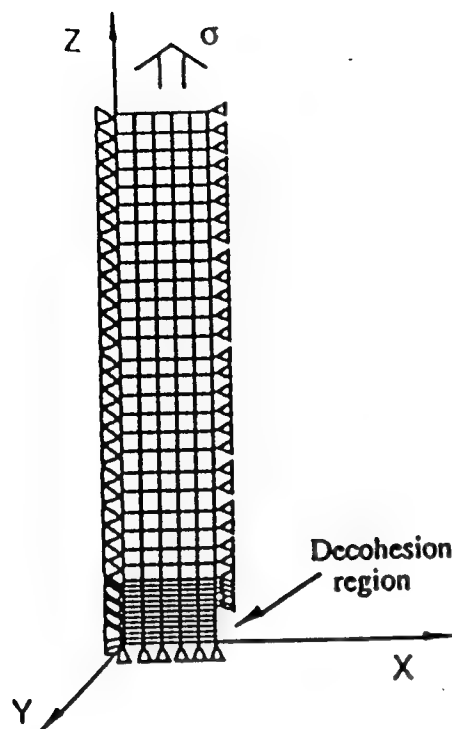
Fig. 9 Mesh and boundary conditions used for analysis of constrained Nb.
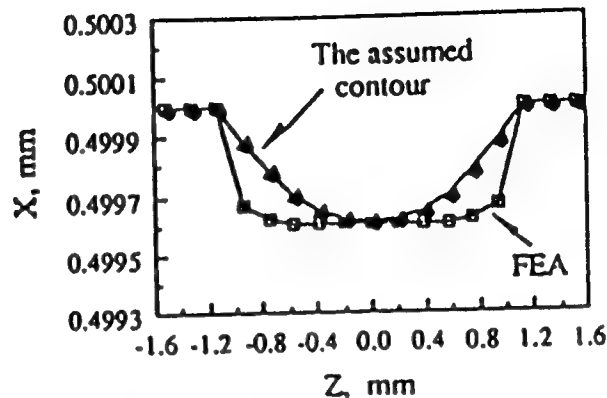
Fig. 10 A comparison between the assumed contour and finite element analysis of decohesion region during the stage of elastic deformation. X and Z are defined in Fig. 17.
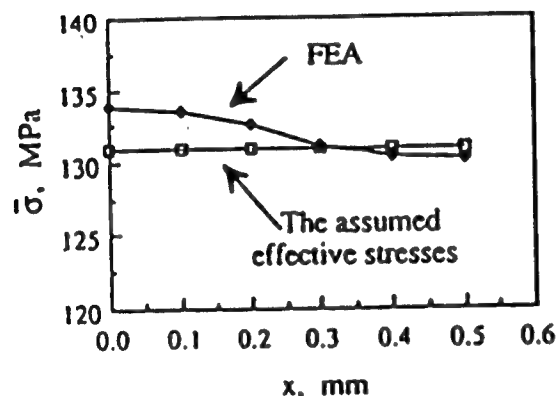
Fig. 11 Effective stress distribution at the midplane of neck.
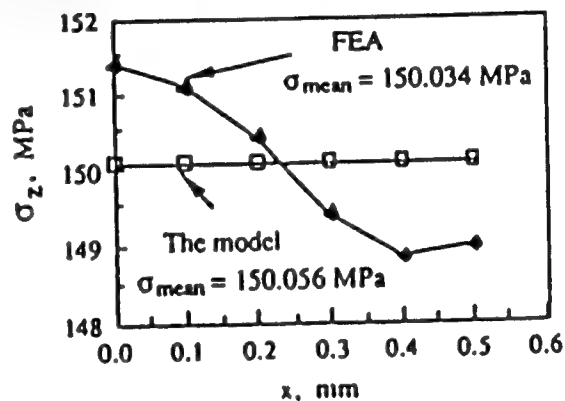
Fig. 12 A comparison of the axial stresses at the midplane of neck between the model and FEA. Note that mean axial stresses, σ_{mean}, are almost the same.

Clearly, the effective stress is not constant across the midplane, but increases from the free surface to the center of the neck. Although the assumed constant effective stress does not represent the real stress distribution, the mean axial stresses across the midplane are almost the same for the model and FEA, as shown in Fig. 12. The axial stress calculated from the model increases monotonously from the free surface to the center, which is hard to tell from Fig. 12 because of the scale used. Similar results were also obtained from calculation of constrained 0.25 and 0.5 mm Nb laminae. Thus, it is concluded that the assumed constant effective stress and contour of the decohesion region impose negligible errors on the calculation of σ-U curve and the work of rupture.

TOUGHENING MoSi$_2$ WITH NIOBIUM METAL—EFFECTS OF SIZE AND ORIENTATION OF DUCTILE LAMINAE

L. SHAW and R. ABBASCHIAN

Department of Materials Science and Engineering, University of Florida, Gainesville, FL 32611, U.S.A.

Abstract—Effects of size and orientation of ductile laminae on the toughness of brittle matrix composites have been evaluated using MoSi$_2$ composites reinforced with Nb laminae. Nb laminae with thicknesses ranging from 0.127 to 1.0 mm were hot pressed with MoSi$_2$ powder to prepare the composites. Toughness of the composites was measured using four-point bend test on chevron-notched specimens. It was found that the toughness of the composites increased with increasing size of the niobium laminae. Furthermore, toughening was observed at crack propagation directions perpendicular to the lamina plane, indicating that ductile laminae offer two dimensional toughening. A model based on the bridging contribution of the ductile phase has been proposed to analyze the chevron-notched specimens of the ductile-phase-reinforced brittle matrix composites. The analysis showed that the dependence of the toughness of the composites on the size and orientation of the ductile laminae could be interpreted in terms of their bridging capability and bending contributions.

1. INTRODUCTION

The need to increase operating temperature of heat engines to improve their fuel efficiency has provided a large impetus in recent years for the development of high temperature materials such as carbides, nitrides, aluminides and silicides. These ceramics and intermetallics have high melting temperatures, high elastic moduli, low densities, and can withstand hostile environments. Their structural application, however, is currently limited by their low room-temperature ductility and toughness. Accordingly, much effort has been made to improve the toughness of these materials by composite toughening.

Among various composite toughening approaches, ductile phase toughening has been shown to be an effective way to improve toughness of ceramics and intermetallics. Examples of such systems which have current or potential applications at high temperatures are WC/Co [1, 2], TiAl/Nb [3-5], TiAl/TiNb [4, 5], MoSi$_2$/Nb [6-10] and Nb$_5$Si$_3$/Nb [11]. The primary mechanism responsible for the enhanced toughness has been ascribed to the bridging of ductile ligaments behind the advancing crack tip, although other effects such as crack deflection, crack trapping, crack shielding and decohesion at the matrix/reinforcement interface also contribute [12-17]. When the size of the bridging zone in the wake of the crack tip is small relative to the crack length and the specimen dimension (i.e. small-scale bridging), the increased fracture energy of the composite can be related to the work of stretching and fracturing of the ductile phase bridging ligaments with the aid of the following equation [12, 14]

$$\Delta G = V_f \int_0^{u^*} \sigma(u) \, d(u) \qquad (1)$$

where u is the crack opening, $\sigma(u)$ the nominal stress on the ligament, u^* the crack opening at the end of the traction zone, and V_f is the area fraction of reinforcements on the crack plane. Equation (1) indicates that the increased toughness depends on the stress–displacement function of the ductile ligament, $\sigma(u)$, which in turn depends on the extent of decohesion at the matrix/reinforcement interface, intrinsic properties and size of the ductile phase. Ashby *et al.* [17] initiated a test technique to evaluate the stress–displacement function of constrained ductile phases. The technique consisted of tensile testing of a specimen with one ductile filament imbedded in a precracked brittle matrix. The composite system tested was Pb imbedded in a glass matrix. They found that the fracture energy was enhanced by limited decohesion at the interface or by matrix fracture, and that the fracture energy normalized with the yield strength and size of the ductile phase depended on the strength of the matrix/reinforcement interface only. Based on the observation, equation (1) could be rewritten as [17]

$$\Delta G = V_f C \sigma_0 a_0 \qquad (2)$$

where σ_0 and a_0 are the yield strength and representative cross-sectional radius of the ductile phase, respectively, and C is a dimensionless function representing the work of rupture. The latter is defined as

$$C = \int_0^{u^*} \frac{\sigma(u) \, d(u)}{\sigma_0 a_0} \qquad (3)$$

which was constant for different sizes of lead in glass. Other investigators have also conducted similar tests on other systems such as Nb in TiAl and TiNb in TiAl [4, 5], and Nb in MoSi$_2$ [10, 18–21] to study toughening mechanisms in ductile-phase-reinforced composites. Working with TiAl/TiNb systems, Deve *et al.* [5] found that whether or not extensive decohesion was desirable for a high work of rupture depended on the work hardening capability of the ductile phase. For MoSi$_2$/Nb system [19–21], it was found that the dimensionless function C in equation (2) depended on the size of the niobium, rather than being a constant, and varied from 5.3 to 2.8 when a_0 of the niobium changed from 0.25 to 0.063 mm. The results further indicated that the effects of the decohesion length and the reinforcement size on the toughness were complicated and interdependent with other material properties.

To fully evaluate the effect of the reinforcement size on the toughness of ductile-phase-reinforced composites, the present study dealt with four-point bend test of chevron-notched composite laminates to determine the toughness of the composites directly, instead of measuring the stress–displacement function, and then deducing the toughness via equation (1). In addition, the effect of orientation of laminae on the toughness of the composites was also evaluated. The composite system investigated was molybdenum disilicide (MoSi$_2$) reinforced with niobium. MoSi$_2$ has excellent oxidation resistance, high melting temperature (2010°C) and fairly low density (6.26 g/cm^3), and therefore a promising candidate as a matrix material for high temperature structural applications. Niobium has a high ductility, high melting temperature and a similar thermal expansion coefficient to MoSi$_2$, and therefore is one of the most promising candidates as a ductile reinforcement for MoSi$_2$. The use of Nb foils rather than filaments allowed for the ease of producing the composites with controlled properties, but it still served the main purpose of the present study.

2. EXPERIMENTAL

2.1. Preparation of composite laminates

Disc-shaped laminated composites were produced by hot pressing commercially pure MoSi$_2$ powder of −325 mesh (supplied by Johnson Mathey Inc.) with 20 vol.% of Nb foils at 1400°C for 1 h under a pressure of 40 MPa. In order to minimize residual thermal stresses, the hot pressed discs were held in the hot pressing chamber at 800°C for 1 h before cooling down to room temperature. Four different thicknesses of Nb foils, i.e. 1.0, 0.5, 0.25 and 0.127 mm, were used, giving 3, 5, 9 and 17 plies in the final composites, respectively. The laminates were arranged symmetrical with the outer layers being MoSi$_2$.

2.2. Mechanical testing

The toughnesses of the MoSi$_2$ matrix and the laminated composites were measured by four-point bending of chevron-notched specimens, with an inner and outer span of 10 and 20 mm, respectively, using a hydro-servo controlled MTS with a cross head speed of 4×10^{-4} mm/s. To prepare the chevron notched specimens, the hot pressed discs were cut into rectangular bars with dimensions of $3.81 \times 5.08 \times 25.4$ mm. A schematic of the bend test setup is shown in Fig. 1(a). For the evaluation of the size effect of the ductile phase, the notch on each sample was cut perpendicular to the laminar plane using a diamond wafering blade with a thickness of 0.15 mm. The remaining V-shape cross section of the notch plane relative to the orientation of the niobium laminae is shown in Fig. 1(b). For this case the crack propagation in the matrix is *normal* to the niobium laminae. Correspondingly, this notch orientation is called N-orientation in the text. To evaluate the orientation effect of the ductile laminae, another chevron notch orientation was tested which is shown in Fig. 1(c) and is called T-orientation because the crack propagation in the matrix is *transverse* to the niobium laminae.

(a)

(b)   (c)
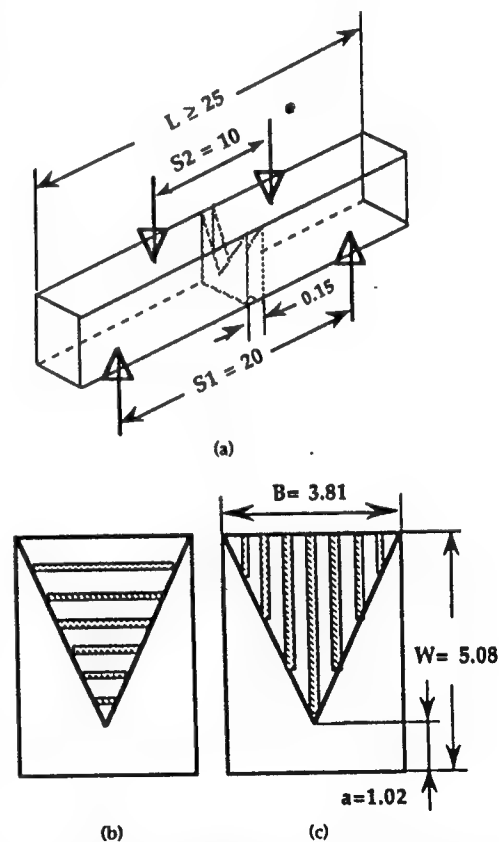
Fig. 1. (a) Configuration of four point bend test on chevron-notched specimens (all dimensions in mm); (b) the notched plane of N-orientation where crack propagates normal to the lamina plane; (c) the notched plane of T-orientation where crack propagates transverse to the lamina plane.

The peak load of the bending tests was used to calculate the toughness of the composites with the aid of the following equation [22]

$$K_{max} = \frac{P_{max}}{B\sqrt{W}} Y^*_{min} \qquad (4)$$

where P_{max} is the maximum test load, B and W are the width and height of the bending bar, respectively, and Y^*_{min} is the minimum value of the dimensionless stress intensity factor coefficient as a function of relative crack length for the particular specimen used. Because of the rising crack-growth resistance for ductile-phase-toughened composites, the maximum load and the minimum value of the dimensionless stress intensity factor coefficient do not occur coincidentally at the same crack length, and therefore P_{max} does not exactly correspond to the stress-intensity factor at failure, but a good approximation to it [23–26]. The fact that P_{max} and Y^*_{min} do not occur coincidentally at the same crack length also induce a specimen size effect [23, 26]. Thus, the dimensions of the specimens in the present study were kept constant, and the value calculated using equation (4) is called "damage tolerance" and designated as K_{max} in the paper, rather than K_{IC}.

3. EXPERIMENTAL RESULTS

3.1. Fractographic observations on MoSi₂ matrix

An overall view of fracture surface of a chevron-notched monolithic MoSi₂ is presented in Fig. 2. Higher-magnification photographs shown in Fig. 3(a–c) are taken from the positions a–c shown in Fig. 2, respectively. As seen in the figures, intergranular fracture prevails near the tip of the notch, while transgranular fracture dominates at the bottom of the notch. Between these two positions, a transition of fracture mode is observed. This position dependency of the fracture mode has also been observed in the chevron-notched monolithic Al₂O₃ [27]. Most of the visible second phases on the intergranular fracture surface [Fig. 3(a)] have been identified as amorphous silica, and the rest as carbon-stabilized Mo₅Si₃

Fig. 3. High magnification views of the fracture surfaces of MoSi₂. Figures (a), (b) and (c) are taken from the positions a, b and c shown in Fig. 2, respectively.

particles [28]. There also exist some pores along the grain boundary, as seen on the intergranular fracture surface, which together with the silica weaken the grain boundary. The change in fracture mode with the position is ascribed to the stable propagation of the crack near the notch tip, unstable at the bottom of the notch and changing from stable to unstable at the intermediate position. This is due to the V-notch geometry and control of the crack propagation by the crosshead speed of the testing machine [29, 30]. Thus, at the notch tip, crack propagation is the slowest and it has more time to choose the low energy path which is grain boundary for the present matrix, while at the

Fig. 2. Fracture surface of a MoSi₂ chevron-notched specimen.
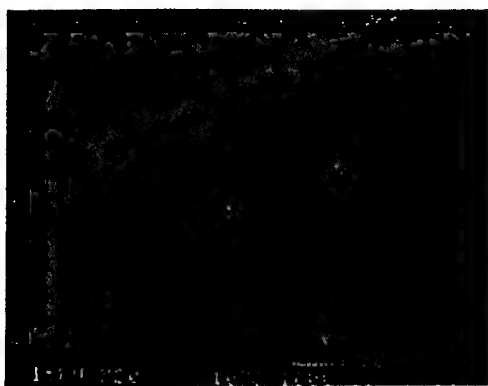
Fig. 4. An overall view of fracture surface of a laminated composite containing 20 vol.% of Nb laminae with a thickness of 0.25 mm. The a, b, c and d denote the positions where the fractographs of Fig. 5(a), (b), (c) and (d) are taken, respectively.
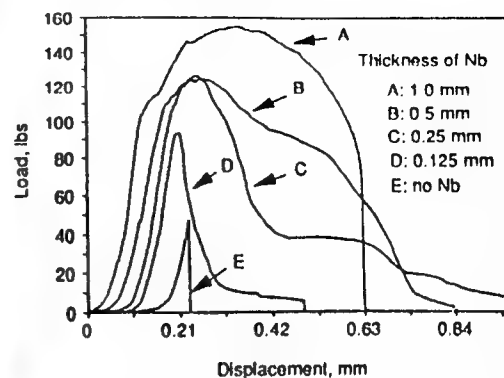
Fig. 6. Typical load displacement curves of chevron-notched specimens for monolithic MoSi₂ and laminated composites containing different thicknesses of Nb laminae. The origin for each curve has been shifted for the convenience of observation.

bottom of the notch, crack propagation is too fast to allow for the low energy path, leading to transgranular fracture.

A general view of a typical fracture surface at the notch plane of a laminate containing 20 vol.% of Nb laminae with a thickness of 0.25 mm is presented in Fig. 4. The a–d in Fig. 4 denote the positions where the fractographs of Fig. 5(a–d) are taken, respect-. ively. Note that intergranular fracture again domi-nates at the notch tip, while transgranular fracture

prevails at the bottom of the notch, a general trend also observed in the monolithic MoSi₂. However, the presence of ductile laminae makes the crack propa-gation in the matrix discontinuous, i.e. crack has to stop at one side of Nb lamina and reinitiates on the other side to continue the propagation. Nevertheless, the position dependency of the fracture mode of MoSi₂ in the composites shows little difference from that of the monolithic MoSi₂. Such phenomena could be explained in terms of the observations made in a
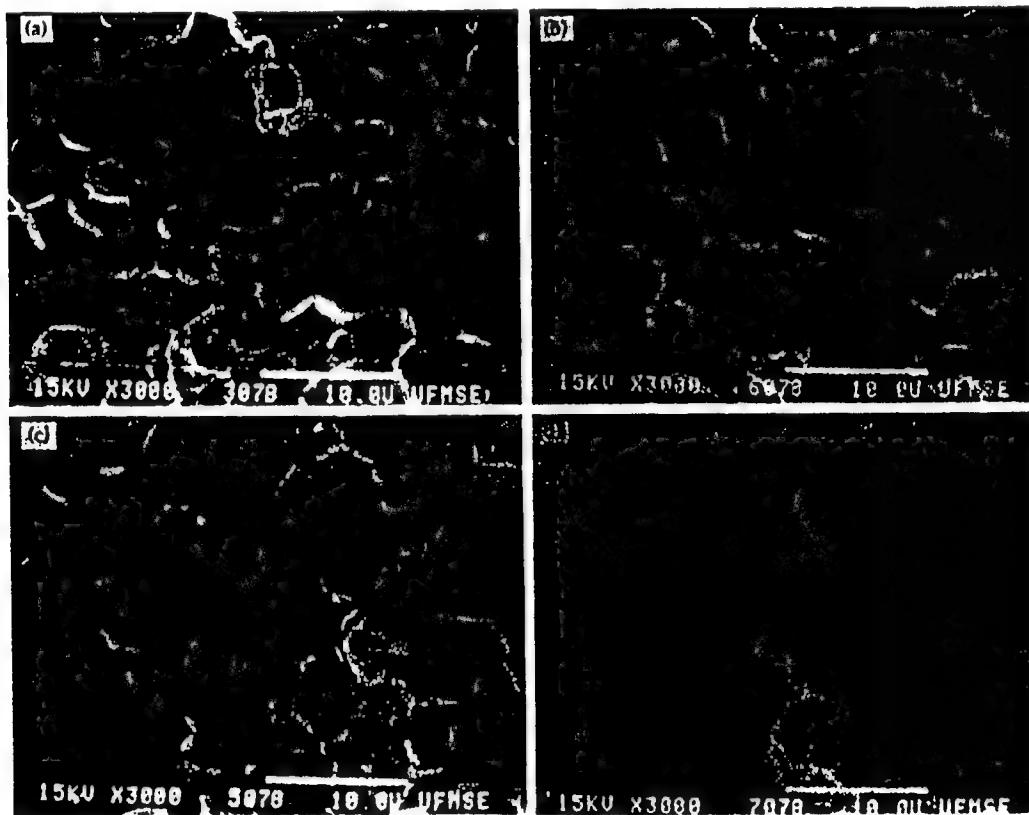
Fig. 5. Fracture surfaces of MoSi₂ matrix shown in Fig. 4.

related study [8] which shows that a primary crack has already propagated through the entire MoSi₂ matrix at a load level of about 20% of the peak load in the bend test of chevron-notched specimens. Beyond this level the load is mainly carried by the Nb reinforcement, whereas at the early stage of the bending, the load is mainly carried by MoSi₂. The Nb laminae with relatively lower elastic modulus, therefore, does not have much influence on the fracture mode of MoSi₂. The presence of Nb laminae, however, improves the damage tolerance of the composites, as will be shown in the following sections.

3.2. Effects of niobium size on the toughness

Representative load–displacement curves of chevron-notched specimens for monolithic MoSi₂ and laminated composites containing different thicknesses of Nb laminae are shown in Fig. 6. The origin for each curve in this figure has been shifted for the convenience of observation. It is noted that the catastrophic failure of MoSi₂ has changed to graceful failure, and the area under the load–displacement curve as well as the peak load have increased by the incorporation of Nb laminae. A comparison between laminated composites reveals that the area under the load–displacement curve increases with increasing thickness of Nb laminae. The peak load reached by the composites also exhibits a similar trend, i.e. as thickness of Nb laminae increases, the peak load increases, with the exception of 0.5 mm Nb laminae which show a peak load similar to 0.25 mm Nb laminae.

The area under the load–displacement curve normalized with the generated fracture area, called as work of fracture [31], are summarized in Table 1 for all the specimens tested. Included in Table 1 are also the damage tolerance data calculated from the peak load of the load–displacement curve using equation (4). It is clear that the work of fracture of the composites increases with increasing thickness of Nb laminae. Similar size effects have also been observed in Al₂O₃/Ni [32], WC–Co/Mo [33] and NiAl/Nb [34] composite systems. The damage tolerance of the present composites, however, does not exhibit a monotonic variation with the Nb lamina thickness. It is believed that this is due to a combined effect of the size as well as the intrinsic properties of the Nb laminae. As mentioned in Section 3.1, the peak load

of the bend test is mainly carried by Nb laminae. The damage tolerance, therefore, is actually an indicator of the bridging capability of the ductile phase and should be related to the combined effects of size, intrinsic properties and fracture behavior of the Nb laminae. An attempt has been made to separate this combined effect, and the results will be discussed in Section 4.2.

Overall views of representative fracture surfaces for composites containing different thicknesses of Nb laminae are provided in Fig. 7. Higher-magnification fractographs of the Nb laminae with different thicknesses are presented in Fig. 8. The crack propagation is from top to bottom in Fig. 8, and the positions from where the fractographs (a)–(d) are taken are indicated in Fig. 7 with the a–d, respectively. It is noted that fracture mode of Nb laminae changes from elongated dimples [Fig. 8(a)] to quasi-cleavage [Fig. 8(c, d)] as the thickness of Nb laminae decreases. In fact, cleavage fracture has also been observed for 0.25 and 0.127 mm Nb laminae [35]. The change in fracture mode of the reinforcement with its thickness can be related to the change in the ductility of the niobium laminae. The microhardness and yield strength of the hot pressed Nb laminae are presented in Table 1. Details on the measurement of the yield strength of the hot pressed Nb laminae have been described in Ref. [21]. As shown in Table 1, the microhardness and yield strength of Nb laminae increases with decreasing size. Thus, the thinner the Nb lamina, the less ductile it is.

Close examination of Fig. 7 reveals that some debonding at the matrix/reinforcement interface and/or multiple matrix fracture near the interface have occurred in all the composites. Both debonding at the interface and multiple matrix fracture near the interface will create a region, called decohesion region [21, 36], in which a Nb lamina can deform under much less constraints from the matrix. The length of the decohesion region has an influence on the deformation behavior of constrained ductile phases and has been found to increase with increasing the size of ductile phases [21]. A cross section of a composite reinforced with 20 vol.% of 0.25 mm thick Nb laminae unloaded after the peak load is shown in Fig. 9. The chevron notch tip is at the right side of the figure and the cracks propagate from right to left. As can be seen from the figure, the deformation in the

Table 1. Mechanical properties measured from MoSi₂/Nb composite laminates

Thickness of Nb lamina (mm)	0.125	0.125	0.25	0.5	1.0
Orientation	T	N	N	N	N
K_{max}[a] (MPa·m$^{1/2}$)	14.9 ± 1.4	12.2 ± 0.5	15.2 ± 1.1	15.4 ± 0.6	17.6 ± 0.1
Work of fracture[a] (J/m²)	6960 ± 350	5490 ± 200	21,600 ± 3000	30,900 ± 1700	35,900 ± 3500
HV (kg/mm²)	155	155	130	114	104
σ_0 (MPa)[b]	279[c]	279[c]	236 ± 5	210 ± 11	180 ± 9
σ_0/HV	1.80[c]	1.80[c]	1.80	1.85	1.73

[a] 3, 3, 9, 5 and 3 specimens have been tested for laminates containing 0.125 (T-orientation), 0.125 (N-orientation), 0.25, 0.5 and 1.0 mm Nb laminae, respectively.

[b] Three specimens for each size of Nb lamina have been tested.

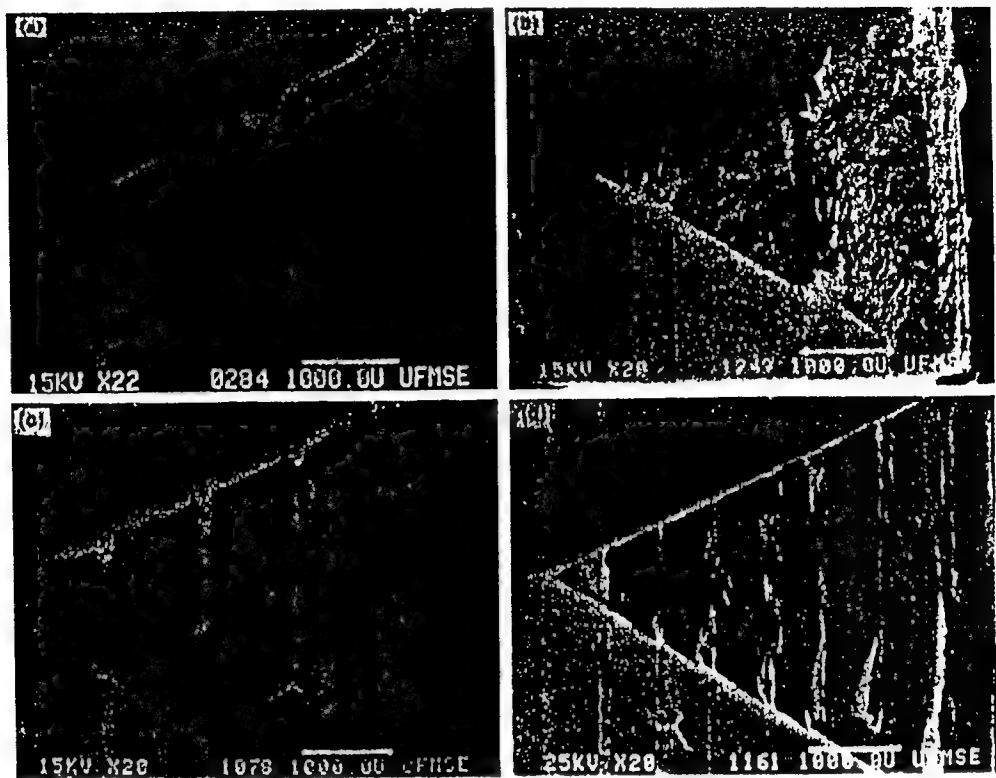[c] σ_0 is not measured directly, but obtained by assuming $\sigma_0/HV = 1.80$.

Fig. 7. Overall views of typical fracture surfaces of the laminated composites, reinforced with (a) 1.0 mm; (b) 0.5 mm; (c) 0.25 mm; (d) 0.127 mm thick Nb laminae. The a, b, c and d in the figures indicate the positions where Fig. 8 has been taken.
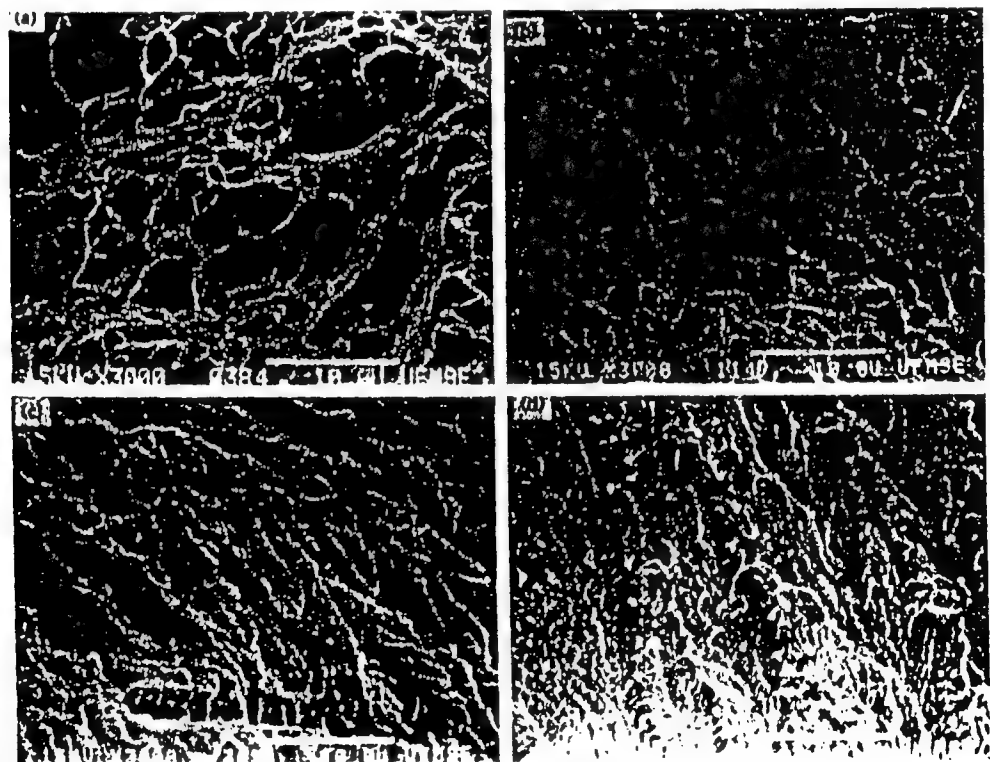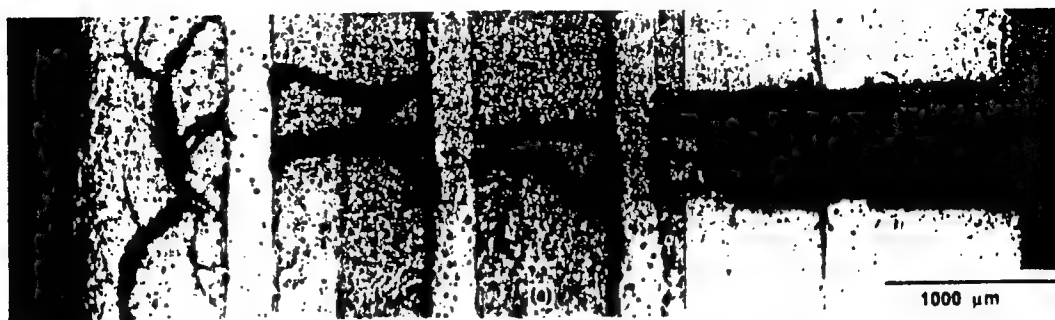

Fig. 8 Fracture surfaces of Nb laminae shown in Fig. 7

Fig. 9. A cross section of a laminated composite containing 20 vol.% of Nb laminae with a thickness of 0.25 mm. The sample is unloaded after the peak load of the load displacement curve [8].

direction perpendicular to the crack plane comes mainly from the niobium inside the decohesion region, as the rest of the niobium is still bonded to the matrix and deforms elastically only. This observation will be utilized in Section 4.1 to facilitate the stress analysis of the chevron-notched specimens.

3.3. Effects of the orientation of niobium laminae on the toughness

Typical load–displacement curves of chevron-notched specimens for two different orientations of the composites containing 0.127 mm thick Nb laminae are shown in Fig. 10. The corresponding damage tolerance and work of fracture have been summarized in Table 1 which shows that the T-orientation not only has a larger work of fracture but also has a larger damage tolerance than the N-orientation.

A general view of the fracture surfaces of chevron-notched specimens for the two different orientations is presented in Fig. 11. For the N-orientation, the crack propagation in the matrix is discontinuous in nature, as mentioned before. In contrast, for the T-orientation, crack propagates continuously in the matrix once initiated, leading to less tortuosity on the fracture surface of the matrix (Fig. 11). It is expected that the discontinuous crack propagation is more energy consuming process than the continuous crack

propagation. However, the T-orientation (continuous crack propagation) actually exhibits a higher damage tolerance and work of fracture than the N-orientation, as shown in Table 1. The apparent contradiction could be explained in terms of the observation that the matrix cracking actually occurs at a low level of load, and the peak load and the area after the peak load are controlled by the deformation and fracture of the Nb reinforcements. Thus, the crack propagation characteristics of the matrix is not a dominant factor in determining the toughness of the present composites. Moreover, the fracture surfaces of the
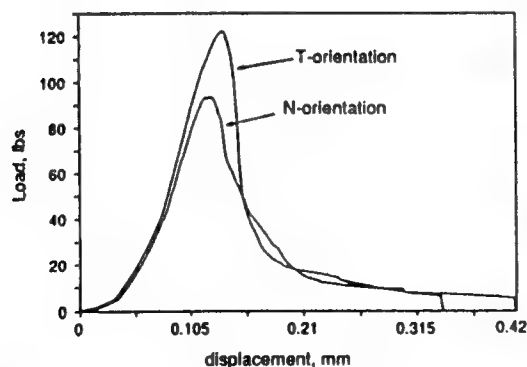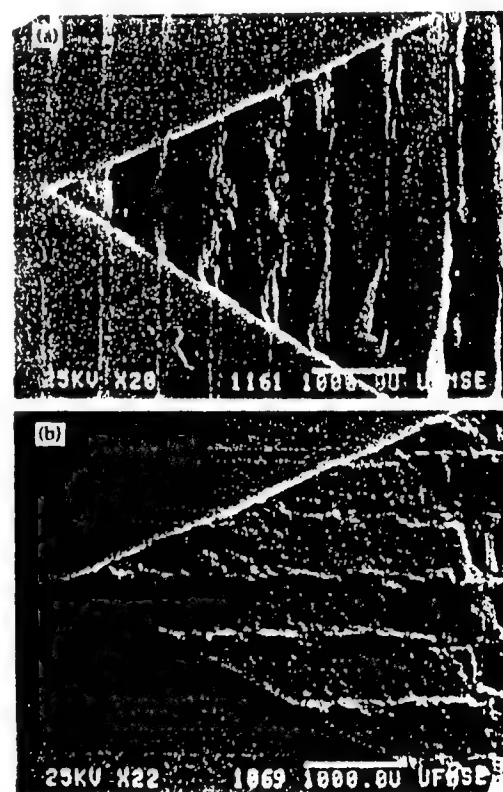
Fig. 11. Fracture surfaces of the laminated composites. (a) Crack propagation normal to the lamina plane (N-orientation); (b) crack propagation transverse to the lamina plane (T-orientation).

Fig. 10. Representative load displacement curves of chevron-notched specimens for two different orientations of the composites containing 0.127 mm thick Nb laminae.

Nb laminae (Fig. 12) reveals that fracture modes for the two orientations are very similar, both exhibiting quasi-cleavage fracture. The dependence of the toughness on the lamina orientation, therefore, might lie on the differences in the bending contributions of the Nb laminae at the different orientations, which will be further discussed in the following section.

4. BRIDGING TOUGHENING

4.1. Stress analysis of the chevron-notched specimens of the MoSi₂/Nb laminated composites

It has been previously shown that extensive matrix cracking occurs at load levels considerably lower than the peak load, and the latter is mainly carried by Nb laminae in the bend test. Based on this observation, an approximate model is proposed to relate the bridging capability of the Nb laminae to the peak load of the bend test. Figure 13 shows the relevant parameters used in the model. The hatched area in the tensile portion of the beam denotes the bridging region. The dashed line indicates the real neutral axis (N.A.) of the beam that changes gradually near the notch plane from the midplane of the beam to the position close to the bottom of the notch. Assumptions involved in the model are: (1) one-dimensional stress is assumed for chevron-notched bend bar; (2) all planar sections far from the notch plane and perpendicular to the axis of the beam remain planar and perpendicular to the axis after bending; (3) all longitudinal elements bend into concentric circular arcs; (4) near the peak load, the load in the tensile portion is carried solely by the bridging ductile phases; and (5) the deformation in this portion only comes from the ductile phases that are inside the "decohesion region" because other ductile phases are
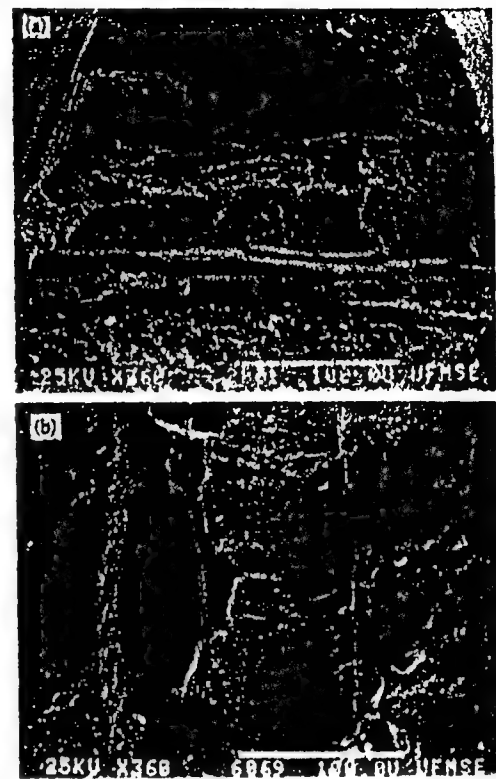
Fig. 12. Fracture surfaces of Nb laminae in laminated composites. The direction of the crack propagation is from top to bottom. (a) N-orientation; (b) T-orientation.

bonded to the matrix and only undergo elastic deformation.

As mentioned in the previous sections, near the peak load the load in the tensile portion of the notch plane is carried only by the Nb ligaments all or some of which may have entered the stage of plastic
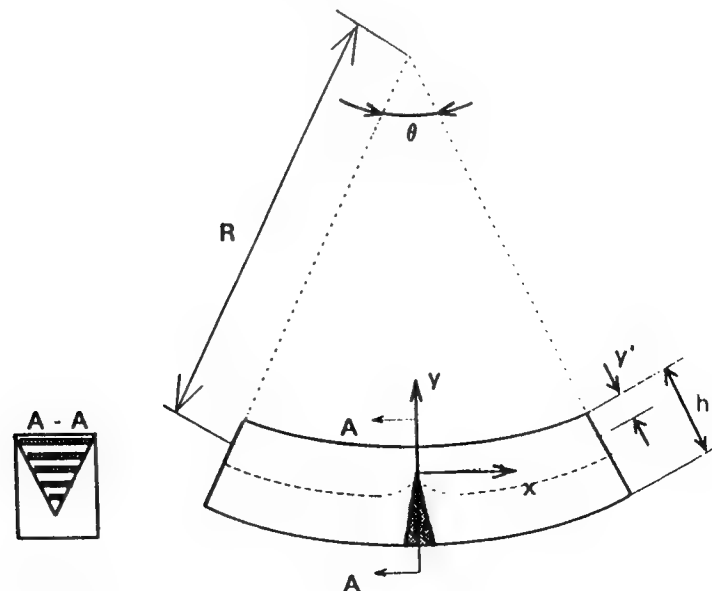
Fig. 13. Schematic of deformed bend bar, showing the relevant parameters used in the analysis

deformation, while in the compressive portion MoSi$_2$ matrix and Nb laminae still undergo elastic deformation. As such, the position of the neutral axis at the notch plane shifts toward the bottom of the notch as bending progresses. In order to simplify the calculation, the neutral axis right at the notch plane has been chosen as the neutral axis for the beam. This is a reasonable approximation since the moment and force balance are calculated right at the notch plane. Thus, the position of the neutral axis is determined from force balance at the x-axis right at the notch place, i.e.

$$\iint_0^{y'} \sigma_{x(com)} \, dy \, dz + \iint_{-(h-y')}^0 \sigma_{x(ten)} \, dy \, dz = 0 \quad (5)$$

where $\sigma_{x(com)}$ is the stress component in the x-direction in the compressive portion, $\sigma_{x(ten)}$ is the nominal stress on the bridging ductile phases in the tensile portion, h and y' are defined in Fig. 13, and z direction is perpendicular to the $x-y$ plane.

Based on the geometry and the assumptions mentioned above, it can be shown that the engineering strain in the compressive portion, ϵ_c, is

$$\epsilon_c = -\frac{y}{R} \quad (6)$$

and the nominal strain inside the decohesion region in the tensile portion, ϵ_t, is

$$\epsilon_t = -\frac{yL}{Rd_0} \quad (7)$$

where R is the radius of curvature of the neutral axis, L is the outer span of the bend test setup, and d_0 is the decohesion length at the matrix/reinforcement interface. $\sigma_{x(com)}$ in equation (5) is determined from the corresponding compressive strain in equation (6) according to the elastic stress–strain relations for MoSi$_2$ and Nb, whereas $\sigma_{x(ten)}$ is calculated from the corresponding strain in equation (7). It should be noted that the relation between $\sigma_{x(ten)}$ and ϵ_t is not an elastic stress–strain relation nor a relation from a simple tensile test. $\sigma_{x(ten)}$ is the nominal stress on the bridging ductile phases which deform under the

constraints from the matrix. It has been shown [19–21] that $\sigma_{x(ten)}$ as a function of crack opening can be simplified into three stages: elastic deformation, plastic deformation within the decohesion region, and localized plastic deformation within the necking region. Based on this, $\sigma_{x(ten)}$ as a function of crack opening has been calculated using Bridgman formula for a necking plate. For the present analysis, the equations derived in Ref. [21] have been utilized to relate $\sigma_{x(ten)}$ to ϵ_t. Since at the beginning of the calculation the position of the neutral axis is not known for a specific value of R, the values of y in equations (6) and (7) are unknown. An iteration approach has been used to calculate the position of the neutral axis by first assuming the midplane of the beam as the neutral axis, then calculating the corresponding ϵ_c and ϵ_t, and substituting them into equation (5) to check whether or not equation (5) is satisfied. If equation (5) is not satisfied, a new neutral axis closer to the bottom of the notch than the former neutral axis is assumed, and the new ϵ_c and ϵ_t are calculated, and equation (5) checked again. The procedure is repeated until the absolute values of the two terms on the left hand side of equation (5) are within $\pm 5\%$ of each other.

Once the neutral axis for one specific value of R has been found, then it is straightforward to find the bending force, P, using the following equation

$$\frac{LP}{8} = -\int_0^{y'} y\sigma_{x(com)} \, dy \, dz + \int_{-(h-y')}^0 y\sigma_{x(ten)} \, dy \, dz. \quad (8)$$

For each R value there is only one corresponding bending force. By decreasing R gradually, therefore, a maximum bending force can be found which is regarded to correspond to the peak load of the load–displacement curve of chevron-notched specimens. A comparison between this approximate model and experiments is made in the following section.

4.2. Comparison between the experiments and analytical results

Table 2 compares the measured and calculated damage tolerances for the N-orientation laminated

Table 2. Comparison between the measured and calculated damage tolerances for laminated composites with N-orientation

Thickness of Nb laminae (mm)	Designation of specimens	$K_{max(meas)}$ (MPa·m$^{1/2}$)	$K_{max(cal)}$ (MPa·m$^{1/2}$)	$\dfrac{K_{max(meas)} - K_{max(cal)}}{K_{max(meas)}}$
0.5	HP051	15.7	12.5	−20.4%
0.5	HP052	14.8	13.1	−11.5%
0.5	HP053	16.1	12.8	−20.5%
0.5	HP054	15.6	12.7	−18.6%
0.5	HP055	14.7	12.5	−15.0%
0.25	HP0251	15.0	11.9	−20.7%
0.25	HP0252	15.2	12.4	−18.4%
0.25	HP0253	14.9	12.6	−15.4%
0.25	HP0254	14.9	12.0	−19.5%
0.25	HP0255	16.4	12.5	−23.8%
0.25	HP0256	14.8	12.2	−17.6%
0.25	HP0257	16.9	12.6	−25.4%
0.25	HP0258	15.7	12.1	−22.9%
0.25	HP0259	13.2	11.9	− 9.8%

composites reinforced with 0.5 or 0.25 mm thick Nb laminae. The calculation is carried out on the basis of the actual dimensions of each specimen, and the relations between $\sigma_{x(\text{ten})}$ and r_i for 0.5 and 0.25 mm Nb laminae are taken from Ref. [21]. As can be seen from the table, the model reflects the main feature of the ductile-phase-reinforced composites, i.e. the peak load of the composites is related to the bridging capability and the size of the ductile ligaments. However, the calculated damage tolerance are about 15% lower than the measured values. The discrepancy probably comes from the assumption (1) because the state of stress near the notch plane is three-dimensional. The position dependence of the decohesion length at the interface may also contribute to the deviation of the calculated damage tolerance from the measured counterparts.

The model can be directly extended to predict the thickness effect of ductile laminae on the toughness of the composites, provided that the mechanical properties of the ductile laminae are independent of their thickness. One such calculation has been presented in Fig. 14 in which it is assumed that all Nb laminae with different thicknesses have the same properties as that measured from 0.25 mm Nb laminae. It is clear from Fig. 14 that the damage tolerance of the composites increases with increasing the thickness of Nb laminae. Thus, it can be concluded that in the size range studied (from 100 to 1000 μm), as Nb lamina thickness increases, both the damage tolerance and the work of fracture of the composites increase.

Since the nominal stress on the bridging niobium as a function of the crack opening in the T-orientation is not known, the present model cannot be used directly to compare with the experiments at the T-orientation. However, as discussed above, the damage tolerance of the composites is related to the bridging capability of the ductile laminae. Therefore, it is believed that the observed orientation dependence of the damage tolerance is due to the differences in the bending contributions of the Nb laminae. In fact, the moment of inertia of Nb cross section about the neutral axis at the notch plane reflects the contribution of the Nb laminae to resisting the external bending moment at the stage of elastic deformation. As given in Table 3, the ratios of the damage tolerances and work of fracture in the N-orientation to the T-orientation are very close to
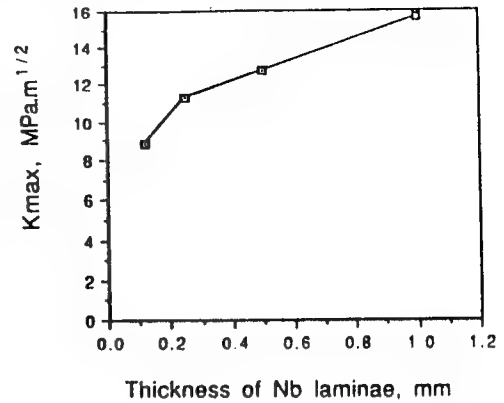
Fig. 14. Size effect of Nb laminae on toughness of the composites, calculated by assuming that different sizes Nb laminae have the same intrinsic properties.

the ratio of the moment of inertia of Nb cross section for these orientations, indicating that the orientation dependence of damage tolerance is mostly due to the different bending contributions of Nb laminae.

5. SUMMARY AND CONCLUSIONS

The effects of size and orientation of ductile laminae on the toughness of the ductile-phase-toughened composites have been evaluated in the MoSi$_2$/Nb laminated composites. It is found that as Nb lamina thickness increases at constant volume fraction, the work of fracture of the composites increases. It is also found that the damage tolerance of the composites determined from the peak load of the chevron-notched specimens is determined by the thickness and the intrinsic properties of the niobium laminae. A simple and approximate model has been proposed to analyze the chevron-notched specimens of the ductile-phase-toughened brittle matrix composites. The analysis indicates that as Nb lamina thickness increases, the damage tolerance of the composites also increases as well.

The damage tolerance and work of fracture of the composites have been shown to depend on the orientation of the Nb laminae. When the crack propagates normal to Nb laminae (N-orientation), the damage tolerance as well as the work of fracture of the composites exhibit a lower value than when the crack propagates transverse to Nb laminae (T-orientation).

Table 3. Measured toughness of the composites containing Nb laminae with a thickness of 0.127 mm and moment of inertia of Nb cross section about the neutral axis at the notch plane

	Damage tolerance[a] K_{max} (MPa m$^{1/2}$)	Work of fracture (J/m^2)	Moment of inertia of Nb cross-section I_{Nb} (mm^4)	$K_{max(N)}$ ── $K_{max(T)}$	Work of fracture$_{(N)}$ ── Work of fracture$_{(T)}$	$I_{Nb(N)}$ ── $I_{Nb(T)}$
Laminates with N-orientation	12.2 ± 0.5	5490 ± 200	1.261			
				0.80	0.79	0.84
Laminates with T-orientation	14.9 ± 1.4	6960 ± 350	1.507			

[a]Calculated from the peak load of the bending test.

The orientation dependence of the damage tolerance and work of fracture of the composites can be interpreted in terms of the bending contribution of the ductile Nb laminae. Despite the different toughnesses in the two orientations of Nb laminae, both orientations exhibit a large increase in toughness over the unreinforced matrix. The results indicate that ductile laminae offer two dimensional toughening.

REFERENCES

1. J. L. Chermant and F. Osterstock, *J. Mater. Sci.* **11**, 1939 (1976).
2. J. Gurland, *Trans. Am. Soc. Metals* **50**, 1063 (1958).
3. C. K. Elliott, G. R. Odette, G. E. Lucas and J. W. Sheckherd, in *High Temperature, High Performance Composites* (edited by F. D. Lemkey, S. G. Fishman, A. G. Evans and J. R. Strife), MRS Proc., Vol. 120, pp. 95 (1988).
4. H. C. Cao, B. J. Dalgleish, H. Deve, C. Elliott, A. G. Evans, R. Mehrabian and G. R. Odette, *Acta metall.* **37**, 2969 (1989).
5. H. E. Deve, A. G. Evans, G. R. Odette, R. Mehrabian, M. L. Emiliani and R. J. Hecht, *Acta metall. mater.* **38**, 1491 (1990).
6. E. Fitzer, in *Whisker- and Fiber-Toughened Ceramics* (edited by R. A. Bradley, D. E. Clark, D. C. Larsen and J. O. Stiegler), pp. 165–192. ASM International, Metals Park, Ohio (1988).
7. L. Xiao, Y. S. Kim and R. Abbaschian, in *Intermetallic Matrix Composites* (edited by D. L. Anton, P. L. Martin, D. B. Miracle and R. McMeeking), MRS Proc., Vol. 194, pp. 399–404 (1990).
8. L. Xiao, Y. S. Kim, R. Abbaschian and R. J. Hecht, *Mater. Sci. Engng* **A144**, 277 (1991).
9. L. Xiao nd R. Abbaschian, *J. Am. Ceram. Soc.* To be published.
10. T. C. Lu, A. G. Evans, R. J. Hecht and R. Mehrabian, *Acta metall. mater.* **39**, 1853 (1991).
11. J. J. Lewandowski, D. Dimiduk, W. Kerr and M. G. Mendiratta, in *High Temperature/High Performance Composites* (edited by F. D. Lemkey, S. G. Fishman, A. G. Evans and J. R. Strife), MRS Proc., Vol. 120, pp. 103–109 (1988).
12. A. G. Evans and R. M. McMeeking, *Acta metall.* **34**, 2435 (1986).
13. L. R. F. Rose, *J. Mech. Phys. Solids* **35**, 383 (1987)
14. L. S. Sigl, P. A. Mataga, B. J. Dalgleish, R. M. McMeeking and A. G. Evans, *Acta metall.* **36**, 945 (1988).
15. P. A. Mataga, *Acta metall.* **37**, 3349 (1989).
16. B. Budiansky, J. C. Amazigo and A. G. Evans, *J. Mech. Phys. Solids* **36**, 167 (1988).
17. M. F. Ashby, F. J. Blunt and M. Bannister, *Acta metall.* **37**, 1847 (1989).
18. L. Xiao and R. Abbaschian, in *Advanced Metal Matrix Composites for Elevated Temperatures* (edited by M. N. Gungor, E. J. Lavernia and S. G. Fishman), pp. 21–31. ASM International, Metals Park, Ohio (1991).
19. L. Xiao, in *Developments in Ceramic and Metal-Matrix Composites* (edited by K. Upadhya), pp. 115–124. TMS (1992).
20. L. Xiao, in *Developments in Ceramic and Metal-Matrix Composites* (edited by K. Upadhya), pp. 359–369. TMS (1992).
21. L. Xiao and R. Abbaschian, *Metall. Trans.* **24A**, 403 (1993).
22. D. G. Munx, J. L. Shannon Jr and R. T. Busey, *Int. J. Fract.* **16**, R137 (1980).
23. J. C. Newman Jr, in *Chevron-Notched Specimens: Testing and Stress Analysis*, ASTM STP 855 (edited by J. H. Underwood, S. W. Freiman and F. I. Baratta), pp. 5–31. Am. Soc. for Testing and Materials (1984).
24. L. M. Barker and F. I. Baratta, *J. Test. Eval.* **8**, 97 (1980).
25. D. Munz, *Engng Fract. Mech.* **15**, 231 (1981).
26. J. L. Shannon Jr and D. G. Munz, in *Chevron-Notched Specimens: Testing and Stress Analysis*, ASTM STP 855 (edited by J. H. Underwood, S. W. Freiman and F. I. Baratta), pp. 270–280. Am. Soc. for Testing and Materials (1984).
27. L. Xiao and R. Abbaschian, unpublished work.
28. J. D. Cotton, Y. S. Kim and M. J. Kaufman, *Mater. Sci. Engng* **A144**, 287 (1991).
29. J. I. Bluhm, *Engng Fract. Mech.* **7**, 593 (1975).
30. T. T. Shih, *J. Test. Eval.* **9**, 50 (1981).
31. H. G. Tattersall and G. Tappin, *J. Mater. Sci.* **1**, 296 (1966).
32. Z. Chen, Master's thesis, Univ. of Florida (1992).
33. D. Han and J. J. Mecholsky Jr, *Mater. Sci. Engng* **A144**, 293 (1991).
34. H. Doty and R. Abbaschian, unpublished work.
35. L. Xiao and R. Abbaschian, *Mater. Sci. Engng* **A155**, 135 (1992).
36. L. Xiao and R. Abbaschian, *Metall. Trans.* **23A**, 2863 (1992).

Interfacial modification in Nb/MoSi$_2$ composites and its effects on fracture toughness

L. Xiao and R. Abbaschian

Department of Materials Science and Engineering, University of Florida, Gainesville, FL 32611 (USA)

Abstract

Niobium-reinforced MoSi$_2$ composites have shown a large improvement in fracture toughness over the MoSi$_2$ matrix. However, the chemical incompatibility of niobium with MoSi$_2$ has to be solved for high-temperature structural applications of the composite. In addition, the effects of interfacial coatings on the fracture toughness of ductile-phase-reinforced composites need to be investigated to find the optimum toughening effect of niobium reinforcement. In the present study different oxide coatings, Al$_2$O$_3$ and ZrO$_2$, were applied to niobium reinforcement and effectiveness of the coatings as diffusion barriers was evaluated. The mechanical behavior and the fractographic characteristics of constrained niobium were also examined. Finally, the effect of the coatings on fracture toughness of the composites was studied and compared with predictions based upon tensile tests on a single constrained niobium reinforcement. The results are discussed in terms of the interfacial fracture energy and micromechanical models of ductile-phase-reinforced composites.

1. Introduction

Molybdenum disilicide is an attractive candidate material for elevated-temperature structure applications because of its high melting temperature (2030 °C), and excellent oxidation resistance at elevated temperatures. However, it has a low fracture toughness at ambient temperatures and a high creep rate at high temperatures. Toughening of the material can be achieved by the incorporation of a ductile second phase [1–6]. Previous studies [7, 8] have shown that incorporating niobium filaments or foils into the MoSi$_2$ matrix is a feasible approach to improving the toughness. For example, it has been shown [8] that the fracture toughness of MoSi$_2$ can be increased to around 12 MPa m$^{1/2}$ by the incorporation of 20 vol.% of niobium filaments. However, the resulting composites are unstable at elevated temperatures because niobium reacts with MoSi$_2$, forming other brittle inter-metallic compounds such as (Mo,Nb)$_5$Si$_3$ at the interface. The formation of the interfacial compounds at the expense of the ductile reinforcement not only degrades the toughening effect of the ductile phase, but also causes a notch effect on the ductile phase [9]. Therefore, the use of an inert diffusion barrier coating on the reinforcement is essential to decrease the interface interactions during processing, and also to maintain the integrity of the ductile phase at elevated service temperatures.

In the present study, oxide coatings (Al$_2$O$_3$ and ZrO$_2$) were applied to the surface of the niobium reinforcement prior to compositing. The effectiveness of the coatings as a diffusion barrier was evaluated. Effects of the coatings on the diffusion path of the composites and the fractographic characteristics of the ductile reinforcement were also examined. Furthermore, effects of the coatings on the toughness of the composites were studied and compared with predictions based upon tensile tests on a single constrained niobium reinforcement.

2. Experimental details

Al$_2$O$_3$ coating on niobium foils was produced by a sol–gel technique and ZrO$_2$ coating was obtained by dipping the foils into a ZrO$_2$ coating solution. Details of the coating procedures can be found elsewhere [7]. Model composites of MoSi$_2$ reinforced by 20 vol.% of uncoated or coated niobium foils were produced by hot pressing at 1400 °C for 1 h under a pressure of 40 MPa. The thickness of niobium foils used was 0.25 mm and the volume fraction of niobium reinforcements was controlled by stacking niobium foils with MoSi$_2$ powders in an appropriate thickness ratio.

The fracture toughness of the composites was measured by four-point bending on 3.81 × 5.08 × 25.4 mm^3 chevron notched specimens with an inner and outer span of 10 and 20 mm, using a hydro-servo controlled MTS with a cross-head speed of 4 × 10^{-4} mm s^{-1}. The chevron notch on the laminated composites was cut perpendicular to the foil plane using a diamond wafering blade.

The investigation of the effect of the coatings on the mechanical behavior of the constrained ductile phase was achieved by tensile tests on precracked specimens, as shown in Fig. 1. The test specimens were prepared by stacking a niobium foil with two layers of MoSi₂ powder at an appropriate ratio to form niobium foil sandwiched discs and then hot pressing under the same conditions as described for the laminated composites. The discs were then cut into rectangular tensile test bars with dimensions of 5.0 × 3.9 × 30.0 mm³. Niobium foils with thicknesses of 0.25 and 0.5 mm were used in this study. The notches in the MoSi₂ matrix were introduced using a diamond wafering blade. The distance from the notch tip to the laminate interface was 200 μm. This distance has been found to be small enough not to distort the stress–displacement curve of the constrained ductile reinforcement and at the same time maintain an appropriate degree of elastic constraint from the matrix [10]. The radius of the notch tip was 0.075 mm. The tensile tests were conducted using MTS with a displacement speed of 2.1 × 10⁻³ mm s⁻¹. The fracture surfaces of both chevron notched and precracked specimens were examined with scanning electron microscopy (SEM) to find the relationship between constraining conditions and fracture surfaces of ductile phases.

3. Results and discussion

3.1. Interactions between Nb and MoSi₂

The microstructure and compositional profiles of an MoSi₂–uncoated-niobium interface hot pressed at 1400 °C are shown in Fig. 2. As seen in the figure, niobium and MoSi₂ reacted extensively during the processing, forming three new intermetallic compounds at

the interface. The resulting interaction region consisted of

$$Nb\|Nb_5Si_3\|(Nb,Mo)Si_2\|(Mo,Nb)_5Si_3\|MoSi_2$$
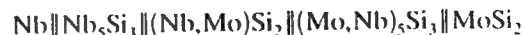
However, it was found that $(Mo,Nb)_5Si_3$ existed in a discrete form rather than a continuous layer. Most $(Mo,Nb)_5Si_3$ was formed around the dark areas in Fig. 2 which were porosities or SiO₂. A high magnification of the $(Mo,Nb)_5Si_3$ microstructure at the MoSi₂-$(Nb,Mo)Si_2$ interface is shown in Fig. 3. The thickness of the interaction zone formed was measured to be about 30 μm for hot pressing at 1400 °C for 1 h. In addition, the nature of the reaction products was found to depend on the processing temperature and time. For example, Fig. 4 shows the interfacial microstructure and the corresponding composition profiles of an MoSi₂/Nb sample which was hot pressed at 1700 °C for 30 min. As seen in the figure, at this processing temperature only one $(Nb,Mo)_5Si_3$ interphase
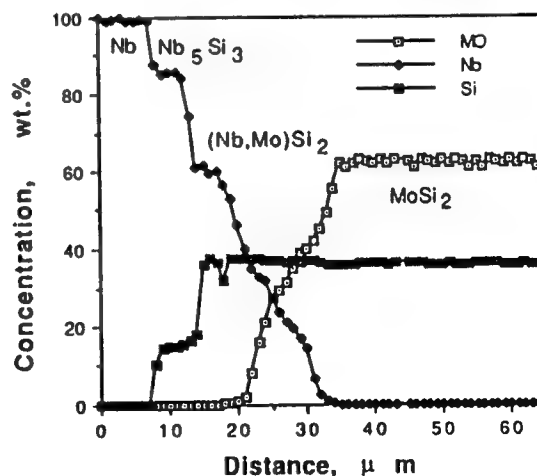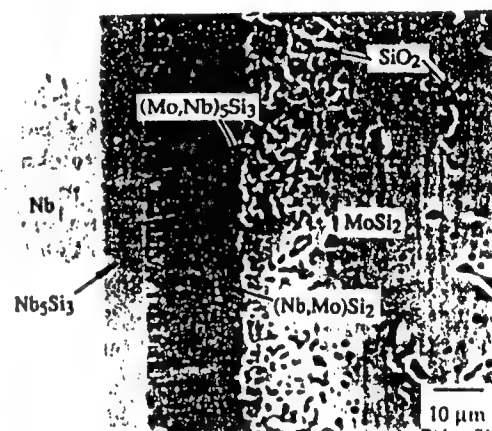
Fig. 2. Microstructure and composition profile across the interface in the MoSi₂/uncoated Nb composite, hot pressed at 1400 °C.

Fig. 1. Schematic diagram of a composite laminate tensile test specimen.
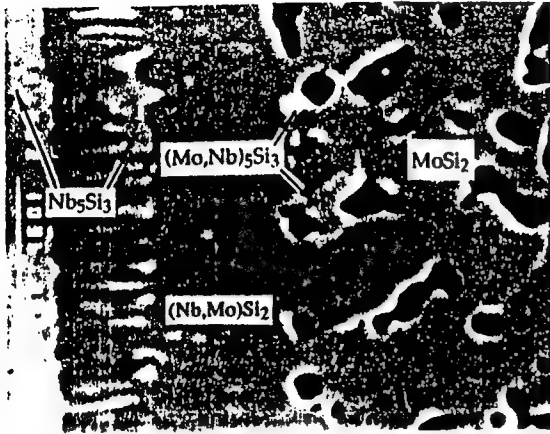
Fig. 3. Microstructure of $(Mo,Nb)_5Si_3$ at the $MoSi_2$-$(Nb,Mo)Si_2$ interface in the $MoSi_2$/uncoated-niobium composite, hot pressed at 1400 °C.
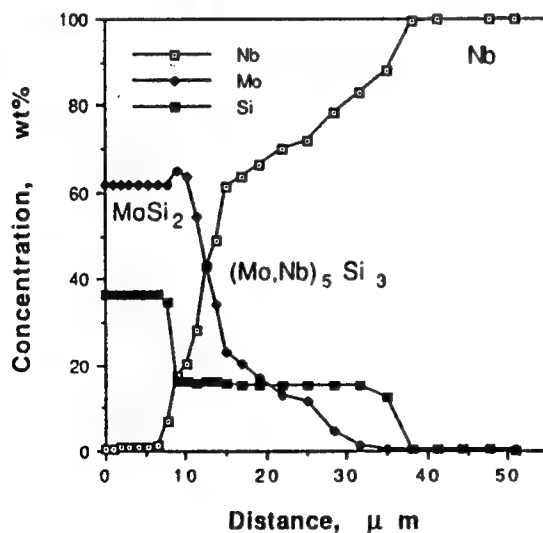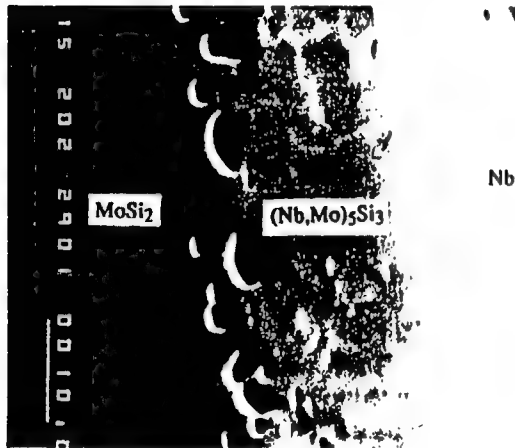
Fig. 4. Microstructure and composition profile across the interface in the $MoSi_2$/uncoated-niobium composite, hot pressed at 1700 °C.

was formed instead of the three intermetallics, Nb_5Si_3, $(Nb,Mo)Si_2$ and $(Mo,Nb)_5Si_3$, formed at 1400 °C.

Such temperature dependence of interphase formation can be explained in terms of the Mo–Si–Nb ternary phase diagram and temperature dependence of the diffusivity of each elemental species. The available isopleth through $MoSi_2$/Nb [11] shows that there are two four-phase equilibria, at 1730 and 1740 °C, associated with the $MoSi_2$/Nb vertical section. The isopleth [11] also shows that the relevant phase fields remain essentially unchanged below the two four-phase equilibria. Therefore, the composition path in the present study can be analyzed on the basis of the 800 °C isothermal section [12], which has been slightly modified by Lu et al. [13] to eliminate the Nb_4Si phase [14] and is shown in Fig. 5. The composition paths for hot pressing at 1400 °C and 1700 °C are also shown in Fig. 5 by lines A and B respectively. The non-planar interface of Nb_5Si_3-$(Mo,Mo)Si_2$ in Fig. 2 (hot pressed at 1400 °C) suggests that the composition path crosses the corresponding two-phase region by cutting across the tie lines. However, the sharp interface of Nb–Nb_5Si_3 indicates that the composition path runs along the tie line in the corresponding two-phase region. Therefore, the composition path for 1400 °C is shown in the following route:

$MoSi_2 \longrightarrow (Mo,Nb)Si_2 + (Mo,Nb)_5Si_3$ (discrete form)

$\longrightarrow (Mo,Nb)Si_2 + (Nb,Mo)Si_2 \longrightarrow (Nb,Mo)Si_2$

$\longrightarrow (Nb,Mo)Si_2 + (Nb,Mo)_5Si_3$ (cutting across the tie lines)

$\longrightarrow Nb_5Si_3 + Nb$ (along the tie line of the binary system)

$\longrightarrow Nb$
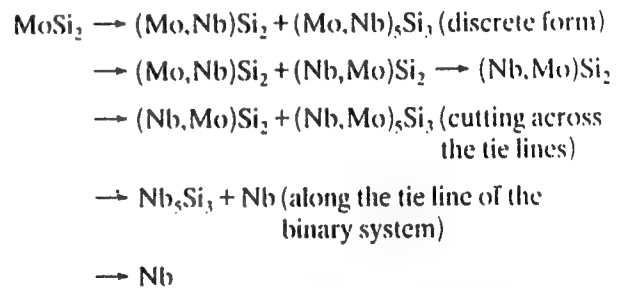
Similarly, based on the microstructure examination and composition analysis, the composition path for hot pressing at 1700 °C (Fig. 4) is
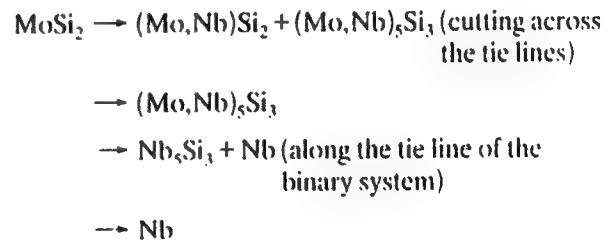
$MoSi_2 \longrightarrow (Mo,Nb)Si_2 + (Mo,Nb)_5Si_3$ (cutting across the tie lines)

$\longrightarrow (Mo,Nb)_5Si_3$

$\longrightarrow Nb_5Si_3 + Nb$ (along the tie line of the binary system)

$\longrightarrow Nb$

Since the isopleth of the Mo–Nb–Si system [11] shows that the relevant phase fields remain essentially unchanged below 1730 °C, the difference in the microstructures at different processing temperatures below 1730 °C might be due to the changes in the interface reaction rate which is proportional to the free energy of formation of these compounds or due to changes in diffusion kinetics of the elemental species to the reaction

Fig. 5. Isothermal section of the Mo–Si–Nb ternary diagram [12] at 800 °C, showing the composition path of Nb/MoSi₂ systems. Line A is for 1400 °C and line B for 1700 °C.

TABLE 1. The standard free energy of formation for some possible reactions in the MoSi₂/Nb diffusion couple

Reaction	ΔG_{1400} (kcal mol^{-1})	ΔG_{1700} (kcal mol^{-1})
3	-44.46	-49.76
6	-37.45	-38.20

and

$$(1-z)Nb_5Si_3 + zMo_5Si_3 = (Mo_z,Nb_{1-z})_5Si_3 \qquad (7)$$

Reactions (4), (5) and (7) correspond to the formation of the solid solutions from mixing of the pure components. Based on the available thermodynamic data [15], free energies of formation for consuming 1 mol of MoSi₂ in reactions (3) and (6) were calculated for two different temperatures, 1400 °C and 1700 °C, and the results are listed in Table 1. As seen in the table, free energies of formation for reactions (3) and (6) do not change much as the hot pressing temperature increases from 1400 °C to 1700 °C. It should be noted that depending on the amounts of MoSi₂ and niobium participating in reaction (3), the ratio of the products NbSi₂ to Nb₅Si₃ may not be fixed as indicated in the equation. Other possibilities such as the formation of much more Nb₅Si₃ than NbSi₂ or a similar amount have also been considered. However, the calculations show that the same conclusion mentioned above (for the case of more NbSi₂ than Nb₅Si₃) still holds for these cases. Since no data on the free energy of mixing for reactions (4) and (7) are available, the free energy of mixing can be assumed to be ideal. This may not be an unreasonable approximation since $(Mo_x,Nb_{1-x})_5Si_3$ is a continuous solid solution as shown in Fig. 5. For this case, the free energy of mixing is proportional to temperature for a fixed composition. Thus, the change in the free energy of mixing for reactions (4) and (7) from 1400 °C to 1700 °C should not change the order of the free energy of formation for reactions (1) and (2). A similar argument may apply to reaction (5), since the isopleth of the Mo–Nb–Si system [11] shows that the relevant phase fields remain essentially unchanged below 1730 °C, i.e. the phase relations between (Nb,Mo)Si₂, (Mo,Nb)Si₂ and (Nb,Mo)₅Si₃ remain unchanged (Fig. 5), implying that $(Nb_{1-v},Mo_v)Si_2$ behaves more or less like an ideal solid solution. Thus, although the free energies of formation for reactions (1) and (2) change with temperature, the order of the free energy of formation for reactions (1) and (2) does not vary with temperature in the range of interest. Therefore, the effect of the free energy of formation of these compounds on the reaction kinetics may not explain the observed microstructural changes from 1400 °C to 1700 °C.

sites. According to the phase diagram shown in Fig. 5, the compounds formed in the MoSi₂/Nb diffusion couple may be described, depending on whether or not (Nb,Mo)Si₂ forms, by the following formulae:

$$MoSi_2 + aNb \rightarrow b(Mo_x,Nb_{1-x})_5Si_3$$
$$+ c(Nb_{1-y},Mo_y)Si_2 \qquad (1)$$

or

$$MoSi_2 + [(1-z)/z]Nb \rightarrow (1/5z)(Mo_z,Nb_{1-z})_5Si_3 \qquad (2)$$

where the coefficients a, b, c, x, y and z depend on the composition and relative amounts of the products. For the above equations, it is assumed that 1 mol of MoSi₂ reacts completely with the required amount of niobium to form the compounds listed on the right-hand side of the equations. The free energy for reaction (1) can be calculated by considering several intermediate steps, such as the following

$$MoSi_2 + Nb = (4/7)NbSi_2 + (1/5)Mo_5Si_3 + (3/35)Nb_5Si_3 \qquad (3)$$

$$xMo_5Si_3 + (1-x)Nb_5Si_3 = (Mo_x,Nb_{1-x})_5Si_3 \qquad (4)$$

and

$$yMoSi_2 + (1-y)NbSi_2 = (Nb_{1-y},Mo_y)Si_2 \qquad (5)$$

Similarly, reaction (2) can be broken down into

$$MoSi_2 + (7/3)Nb = (7/15)Nb_5Si_3 + (3/15)Mo_5Si_3 \qquad (6)$$

In contrast, the microstructural changes in the interaction zone at different processing temperatures could be due to the change in the diffusion kinetics of silicon, niobium and molybdenum, as will be discussed below. The composition profile in Fig. 2 (1400 °C) shows clearly that silicon diffuses far deeper into the niobium-rich region than molybdenum, indicating that silicon has a higher mobility than molybdenum. This is consistent with the available literature data [16, 17], which show that diffusivities of silicon and molybdenum in niobium can be expressed as follows:

$$D_{Si} = 0.51 \times 10^{-2} \exp(-48000/RT) \quad 700-1500\,°C$$

$$D_{Mo} = 92 \exp(-122000/RT) \quad 1725-2182\,°C$$

The above equations indicate that the diffusion coefficients of silicon in niobium at 1400 °C and 1700 °C are 2.73×10^{-9} and 2.45×10^{-8} cm² s⁻¹ respectively. For molybdenum, the corresponding values are 1.56×10^{-14} and 2.81×10^{-12} cm² s⁻¹. Because of the low mobility of molybdenum relative to silicon, the interphase formation at 1400 °C is expected to be dominated by the diffusion of silicon into the niobium region. This is supported by the formation of Nb₅Si₃ adjacent to niobium instead of the formation of (Nb,Mo)₅Si₃. However, as the temperature increases, the diffusion of molybdenum becomes more pronounced relative to the diffusion of silicon because of its higher diffusion activation energy, and therefore a stronger temperature dependence of its diffusivity. Similarly, niobium diffusion becomes more competitive at high temperatures, which combined with the diffusion of molybdenum leads to the formation of (Nb,Mo)₅Si₃ at 1700 °C, as shown in Fig. 4. The limited growth of the (Mo,Nb)Si₂ interphase at 1700 °C is probably due to the faster growth of (Mo,Nb)₅Si₃ caused by the more pronounced diffusion of niobium relative to silicon at high temperatures. It should be noted that at ~1400 °C, growth of Nb₅Si₃ depends mainly on the transport of silicon through the (Nb,Mo)Si₂ layer. However, at 1700 °C, as niobium diffusion becomes more pronounced, the growth of (Mo,Nb)₅Si₃ is enhanced not only in the direction of the niobium-rich region but also in the direction of the (Nb,Mo)Si₂ interphase. Thus, when the diffusion of niobium becomes competitive with respect to the diffusion of silicon, the growth of (Mo,Nb)₅Si₃ will be enhanced and that of (Nb,Mo)Si₂ limited. In Section 3.2 where the hot pressing temperature is kept at 1400 °C, some more evidence will be provided that whenever diffusion of niobium becomes more competitive with respect to the diffusion of silicon, the growth of (Nb,Mo)Si₂ becomes limited.

Note that according to the conservation of mass, much more (Mo,Nb)₅Si₃ should exist in the diffusion couple. However, only a small amount of (Mo,Nb)₅Si₃ has been observed, as shown in Fig. 2. This is believed to be due to the presence of SiO₂ and free silicon in the commercially pure MoSi₂ powder as shown in Fig. 2 and reported in refs. 18 and 19. The presence of SiO₂ and free silicon shifts the actual composition of the starting MoSi₂ powder to the MoSi₂-Si two-phase field, instead of the single-phase MoSi₂ field. The presence of the extra silicon is also reflected in the composition profile. As shown in Fig. 2, Matano interfaces of three elements are not at the same position, with the silicon Matano interface far closer to the niobium-rich side than that of molybdenum. However, the difference in the position of the Matano interfaces becomes smaller at 1700 °C, as shown in Fig. 4. The results suggest that the presence of excess silicon and SiO₂ contributes more to the diffusion process at lower temperatures, whereas at high temperatures contributions from MoSi₂ and niobium became more pronounced.

3.2. Effect of the coatings on the diffusion path

Comparison of interfacial microstructures of MoSi₂ with coated and uncoated niobium is shown in Fig. 6. At 1700 °C the thickness of the interaction layer between niobium and MoSi₂ has been reduced from approximately 30 μm for the uncoated interface to about 6 μm for the ZrO₂ coated samples. In addition, the composition of the interphase formed was determined to be Nb₅Si₃, instead of (Mo,Nb)₅Si₃ for the uncoated samples, suggesting a substantial reduction in the diffusion of niobium and molybdenum across the coating. For 1400 °C the thickness of the interaction layer has also been reduced from approximately 30 μm to about 4 μm upon coating of niobium foils with Al₂O₃. Furthermore, only one interphase (Nb₅Si₃) was observed, instead of the three interphases Nb₅Si₃, (Nb,Mo)Si₂ and (Mo,Nb)₅Si₃ for the uncoated samples (Fig. 2). The reduction in the thickness and change in the composition of the interfacial compounds formed at 1700 and 1400 °C can again be attributed to the retardation of silicon diffusion and the suppression of niobium and molybdenum diffusion across the coatings. Note that the suppression of niobium diffusion across the coatings leads to the absence of interphase formation in the MoSi₂ side of the oxide coating, whereas suppression of molybdenum diffusion results in the formation of only the binary compound, instead of the ternary compound, in the niobium side. In addition, retardation of silicon diffusion in the coated samples favors the formation of niobium-rich compounds, such as Nb₅Si₃, instead of NbSi₂.

The effectiveness of the coatings as a diffusion barrier was found to be affected not only by the quality and integrity of the coating itself, but also by the presence of SiO₂ and free silicon near the coating. A typical

microstructure of MoSi₂ hot pressed with sol-gel-coated niobium is shown in Fig. 7. As can be seen, the coating is discontinuous. This is believed to be due to the interaction of the coating with SiO₂ and free silicon

[20]. This coating degradation can be eliminated by improvements in the matrix chemistry. As has been shown by Kaufman and coworkers [21, 22], one promising approach is to convert SiO₂ and silicon into SiC by mechanically mixing elemental molybdenum and silicon powders with excess carbon. The formation of SiC by this method not only eliminates the detrimental effect of SiO₂ and free silicon, but also provides *in situ* compositing of MoSi₂ with SiC. Optimization of this processing technique is currently under development [22].

The extent of the retardation of silicon diffusion has been found to depend also on the quality of the coatings. For example, the apparent diffusivity of silicon in the sol-gel derived Al_2O_3 coating has been estimated to be larger than 2.0×10^{-8} cm² s⁻¹ at 1400 °C [7]. Such high diffusivity has been attributed to the grain boundary diffusion and vapor phase diffusion through the pinholes which are characteristic defects associated with sol-gel processing. Therefore, in order to reduce further the silicon diffusion, grain boundary area and processing defects must be minimized in the coating. Figure 8 shows a microstructure and the corresponding composition profile of an MoSi₂ and sol-gel coated niobium interface which is obtained via electrophoresis with optimized processing parameters. As seen in the figure, the thickness of the interphase has been reduced from approximately 30 μm to less than 1 μm, compared with the uncoated samples. The reaction product in this case could not be determined because its thickness was close to the beam size of the electron microprobe (approximately 1 μm). Nevertheless, the result indicates that if the coating is dense enough, the diffusion of silicon can be effectively limited, and therefore the interaction between niobium and MoSi₂ can be prevented.
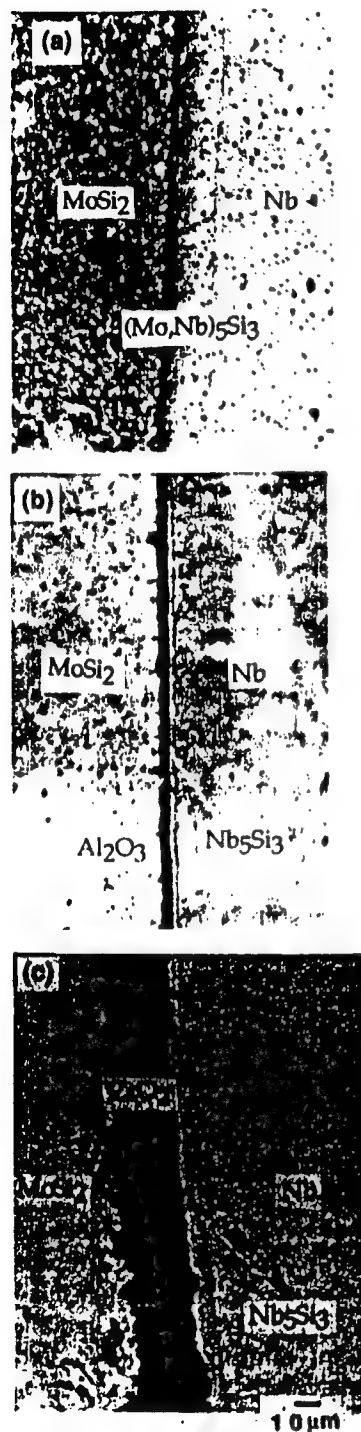
Fig. 6. Interfacial microstructures of MoSi₂ with (a) uncoated niobium, hot pressed at 1700 °C, (b) Al_2O_3-coated niobium, hot pressed at 1400 °C, (c) ZrO₂-coated niobium, hot pressed at 1700 °C.
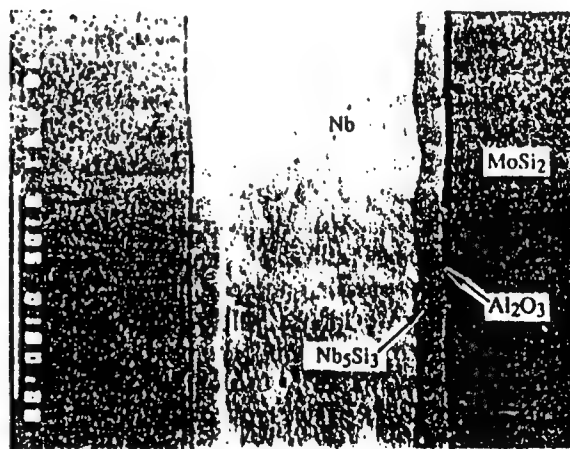
Fig. 7. A typical microstructure of MoSi₂, hot pressed with sol-gel-coated niobium.

Al₂O₃-coated and uncoated interfaces respectively. Moreover, the decohesion length at the matrix–reinforcement interface has been found to be inversely proportional to the interfacial fracture energy, *i.e.* the ZrO₂-coated interface exhibits the longest decohesion length, followed by the Al₂O₃-coated and then the uncoated interface [23]. The constraint from the matrix on the deformation of niobium is related to the decohesion length. The longer the decohesion length is, the lower the constraint from the matrix. Thus, the uncoated composites have a larger constraint from the matrix on the ductile phase, indicated by a shorter decohesion length [23]. The fracture surfaces shown in Fig. 9(a) and (c) show that as the constraint increases, the fracture mode niobium changes from dimple to quasi-cleavage. Similar to the Al₂O₃-coated samples, the ZrO₂-coated Nb/MoSi₂ system also has weak bonding at the interface. However, the fracture of ZrO₂-coated niobium does not strictly follow the constraint–fracture mode relation observed in the

uncoated and Al₂O₃-coated systems. One possible reason is the embrittlement of niobium by the interstitial oxygen in the ZrO₂-coated systems [23].

The fact that the fracture mode of the ductile phase depends on the constraint condition can be further illustrated by Fig. 10 which shows the fracture surfaces of uncoated niobium foils at different locations in the laminated composites. As seen in the figure, the fracture mode of niobium foils has changed from cleavage to dimple rupture as the location of the niobium foils changes from near the tip of the notch to the bottom of the notch. Between these two positions, a mixed mode of fracture is observed. Owing to the change in stress state during the bending test, a longer decohesion length was observed to occur at the bottom of the chevron notch than at the tip, which leads to a less constrained condition for the niobium foils at the bottom. Therefore, the fracture mode of the ductile phase changes from the total dimple to mixed mode, and even to cleavage, whenever the constraint increases either by
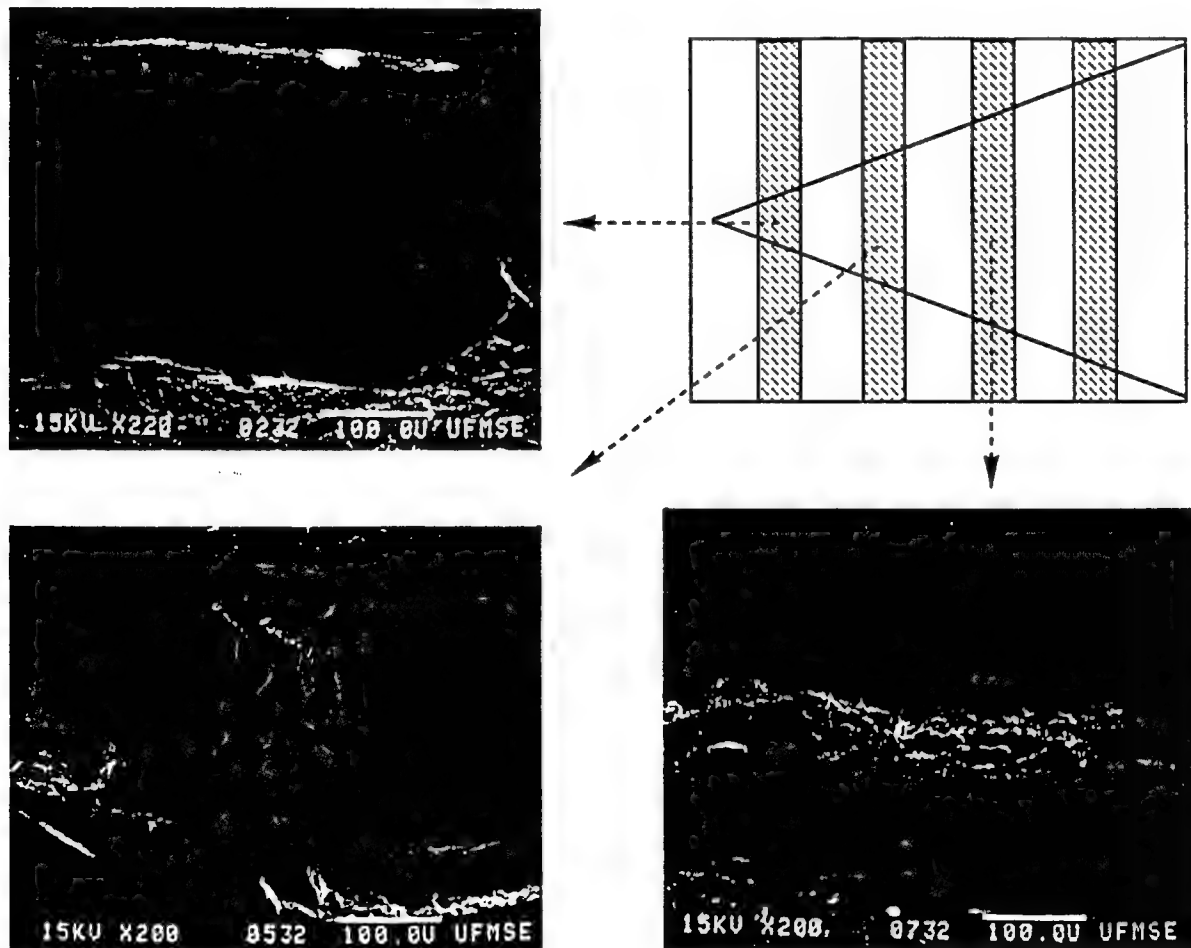
Fig. 10. Fracture surfaces of uncoated niobium foils in a chevron notched specimen, showing that the fracture mode of niobium foils changes with position.

changing the interfacial properties or by changing the stress state. Thus, fractographic analysis can be used to estimate the degree of constraint qualitatively.

3.4. Effect of the coatings on the mechanical behavior of constrained ductile phases

The effects of the coatings on the stress–displacement curves of the tensile test on precracked specimens (see Fig. 1) is shown in Fig. 11. It has been shown previously [10] that owing to the appropriate choice of notch depth in the precracked specimens, the cracks during tensile testing are initiated at the notch tips at very low stress levels. Thus, the curves in Fig. 11 are characteristic of the flow behavior of the constrained ductile phase. As shown in the figure, the uncoated niobium exhibits the highest peak stress, followed by the Al_2O_3-coated and then the ZrO_2-coated niobium. In contrast, the ZrO_2-coated niobium has the largest work of rupture (the area under the curve). The measured peak stress and work of rupture for 0.25 mm thick niobium lamina are summarized in Table 2. The decohesion length at the interface and the interfacial fracture energy-measured using chevron notched short
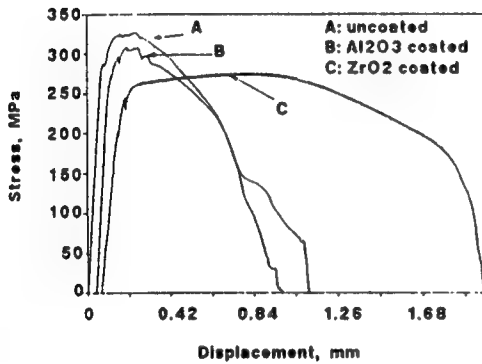
Fig. 11. Effect of the coatings on the stress–displacement curves, measured from precracked specimens with 0.5 mm thick niobium lamina.

bars of laminated composites [23] are also presented in Table 2 to illustrate the relation between the constraint condition and the mechanical characteristics. Also included in Table 2 is the microhardness of niobium in the precracked specimens, which shows the effect of the processing conditions on the hardness of the niobium foils.

Table 2 shows clearly that the degree of constraint on the ductile phase decreases with decreasing fracture energy of the interface, as indicated by the increase in decohesion length. In addition, as the degree of constraint decreases, the peak stress also decreases, but the work of rupture increases. These findings are consistent with theoretical analyses of Sigl et al. [24], Evans and McMeeking [25] and Ashby et al. [26].

Toughening of brittle materials by the bridging of ductile phases can be estimated with the aid of the following equation [24, 25]

$$\Delta G = V_f \int_0^{u^*} \sigma(u)\, du \qquad (8)$$

where $\sigma(u)$ is the nominal stress carried by the constrained ductile reinforcement for a given crack opening u, V_f is the volume fraction of the reinforcement and u^* is the crack opening at the point when the ductile reinforcement fails. The integral in eqn. (8) corresponds to the area under the stress–displacement curve from the tensile test on a single constrained ductile reinforcement. The steady-state toughness of the composite K_c can be related to the fracture energy increase ΔG by the use of the Rice J-integral [27], as follows:

$$\frac{(1 - v_c^2)K_c^2}{E_c} = \frac{(1 - v_m^2)K_m^2}{E_m} + \Delta G \qquad (9)$$

where v, E and K are Poisson's ratio, the elastic modulus and fracture toughness respectively. The subscripts

TABLE 2. Measured damage tolerance, steady-state toughness and other relevant parameters from the tensile tests and bend tests

Material	Uncoated Nb	Al_2O_3-coated Nb	ZrO_2-coated Nb
HV (kg/mm²)	131	134	131
Interfacial fracture energy[a] (J m⁻²)	> 33.7 ± 1.4	16.1 ± 1.3	12.8 ± 1.0
Decohesion length[b] (mm)	0.86 ± 0.09	0.94 ± 0.23	1.31 ± 0.61
Peak stress[b] (MPa)	350 ± 15	340 ± 30	330 ± 15
Work of rupture[b] (J m⁻²)	85400 ± 7800	92400 ± 9500	103200 ± 7300
Steady-state toughness[b] (MPa m^{1/2})	88	92	97
Damage tolerance[c] (MPa m^{1/2})	15.2 ± 1.3	14.0 ± 1.5	12.8 ± 1.5
Work of fracture[c] (J m⁻²)	21600 ± 3000	28700 ± 1900	28700 ± 4600

[a] From chevron notched short bars of laminated composites [23].
[b] From tensile tests on a single constrained niobium foil (0.25 mm thick).
[c] From bend tests on chevron notched composite laminates reinforced with 20 vol.% of niobium laminae (0.25 mm thick).

c and m refer to the composite and matrix respectively. Using the experimental data from the tensile tests on the precracked specimens, the fracture toughness of the Nb/MoSi₂ system has been calculated using eqns. (8) and (9) and the results are compared with the measured fracture toughness presented in the next section.

3.5. Effect of the coatings on the fracture toughness of the laminated composites

Typical load–displacement curves of four-point bending tests on the chevron notched specimens of uncoated and coated niobium reinforced composites are shown in Fig. 12. As can be seen, the maximum load P_{max} increases with increasing the degree of constraint, that is uncoated niobium-reinforced laminates exhibit the highest maximum load. The maximum load reached by the chevron notched specimen can be used to calculate the fracture toughness with the aid of the following equation [28]

$$K_{Ic} = \frac{P_{max}}{B\sqrt{W}} Y^* \qquad (10)$$

where P_{max} is the maximum test load, B and W are the width and height of the bending bar respectively, and Y^* is the dimensionless stress intensity factor coefficient. The latter is a function of the geometry of the specimen and bending test set-up. Substituting the measured P_{max} into eqn. (10), the calculated fracture toughness is obtained and listed as damage tolerance in Table 2. For comparison, the steady-state toughness calculated from the work of rupture of a single constrained ductile phase is also listed in the table.

It is noted that a very large discrepancy exists between the fracture toughnesses calculated from the two aforementioned methods. The discrepancy is believed to be due to the fact that the fracture toughness

Fig. 12. Typical load–displacement curves of bend tests on chevron notched laminates reinforced with 20 vol.% of coated and uncoated niobium foils, hot pressed at 1400 °C.

measured from the peak load of the bend test on the chevron notched specimens is not a steady-state fracture toughness, but merely an indicator of the damage tolerance of the composites. The previous study has shown [8] that a primary crack has already propagated through the entire MoSi₂ matrix at a load level of about 20% of the peak load in the bend test. Beyond this level, the load is mainly carried by the niobium reinforcement alone. Therefore, to measure the actual toughness using the bending test of chevron notched specimens, a very large size specimen has to be used. An alternative approach would be to reduce the size of the ductile phase, which would in turn lead to a decrease in the length of the bridging zone, making the ductile phase more effective in preventing the crack opening. Thus, the size of the crack will be much smaller than that of the specimen dimensions. Under these conditions, the damage tolerance measured from the bend test on chevron notched specimens may become a valid measurement of fracture toughness. In contrast, the fracture toughness calculated from the work of rupture is a steady-state fracture toughness. Therefore, only with an appropriate combination of sizes of test specimen and ductile reinforcement can the two testing methods exhibit a similar result. Calculation of the critical size of the ductile reinforcement for such a situation is currently under development.

Figure 12 also reveals another salient feature for ductile phase toughening, that is that the mechanical behaviors of ZrO₂- and Al₂O₃-coated systems are similar, and both show an increase in the carried load in the last part of the displacement curves which is caused by extensive delamination at the interface; this means that the niobium can deform under a much less constrained condition and much more niobium participates in deformation. Because of this feature, the total energy consumed to break a specimen (area under the curve) for the coated composites is larger than for the uncoated composites. To reflect this feature, the work of fracture, defined as the total energy normalized with respect to the generated crack area during the bend test [29], is calculated and included in Table 2. Comparing the values measured from these tests shows that the damage tolerance and the peak stress have the same trends as the interfacial fracture energy changes, whereas the steady-state fracture toughness and the work of fracture follow the opposite trend. These results indicate that whether or not strong interfacial bonding is conducive to improving the toughness depends on the criterion used to describe the toughness of the composite. If the damage tolerance measured from chevron notched specimens is used as an indicator of the toughness, strong bonding would be desirable. However, if the work of fracture and/or steady-state toughness are used as indicative of its
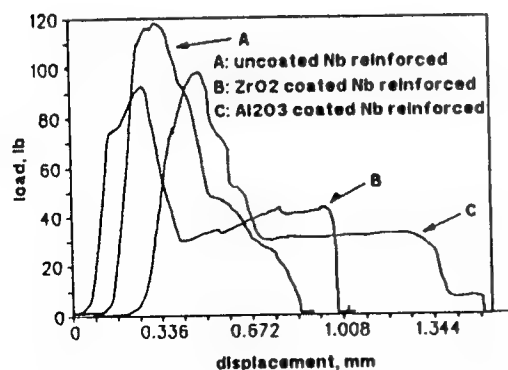
toughness, then a relatively weak bonding would be preferable.

4. Concluding remarks

The present set of experiments shows that niobium interacts with $MoSi_2$ extensively at high temperatures forming various interfacial compounds. The nature and composition of the compounds are found to depend on the processing temperature, and to depend on the diffusion kinetics of silicon, niobium and molybdenum. The oxide coatings (Al_2O_3 and ZrO_2) suppress the interdiffusion of niobium and molybdenum, and limit the diffusion of silicon, leading to the very limited interaction between niobium and $MoSi_2$.

It has been demonstrated that the degree of constraint on the ductile phase decreases with decreasing fracture energy of the interface. Fractographic analysis has been utilized to estimate the degree of constraint on the ductile phases and provide an alternative to analyzing the constraints when the stress states are complicated.

Toughness analyses indicate that whether or not a strong interfacial bonding is conducive to increasing toughness depends on the criterion used to describe the toughness of the composites. If the damage tolerance measured from chevron notched specimens is used as an indicator of the toughness, strong bonding would be desirable. However, if the work of fracture measured from chevron notched specimens and/or steady-state toughness measured from the tensile test on a single constrained ductile phase are used as indicative of the composite toughness, then a relatively weak bonding is preferable.

References

1 E. Fitzer, in R. A. Bradley, D. E. Clark, D. C. Larsen and J. O. Stiegler (eds.), *Whisker- and Fiber-Toughened Ceramics*, ASM International, Metals Park, OH, 1988, p. 165.

2 C. K. Elliott, G. R. Odette, G. E. Lucas and J. W. Sheckherd, *High Temperature, High Performance Composites*, MRS Proc. Vol. 120, Materials Research Society, Pittsburgh, PA, 1988, p. 95.

3 A. V. Virkar and D. L. Jognson, *J. Am. Ceram. Soc.*, 60 (1977) 514–519.

4 M. I. Mendelson and M. E. Fine, *J. Am. Ceram. Soc.*, 57 (1974) 154-159.

5 J. Gurland, *Trans. ASM*, 50 (1958) 1063–1071.

6 V. V. Kristic and P. S. Nicholsin, *J. Am. Ceram. Soc.*, 64 (1981) 499–504.

7 L. Xiao, Y. S. Kim and R. Abbaschian, *Intermetallic Matrix Composites*, MRS Proc. Vol. 194, Materials Research Society, Pittsburgh PA, 1990, pp. 399–404.

8 L. Xiao, Y. S. Kim, R. Abbaschian and R. J. Hecht, *Mater. Sci. Eng.*, A144 (1991) 277–285.

9 A. G. Metcalfe and M. J. Klein, in A. G. Metcalfe (ed.), *Interfaces in Metal Matrix Composites, Composite Materials*, Vol. 1, Academic Press, New York, 1974, pp. 125–168.

10 L. Xiao and R. Abbaschian, in M. N. Gungor, E. J. Lavernia and S. G. Fishman (eds.), *Advanced Metal Matrix Composites for Elevated Temperatures*, ASM International, Materials Park, OH, 1991, pp. 33–40.

11 E. M. Savitsky, V. V. Baron and M. I. Bychkova, *Trudy Inst. Met. Baikova, Acad. Nauk SSSR*, 12 (1963) 179–188.

12 E. M. Savitsky, V. V. Baron, M. I. Bychkova, S. A. Bakuta and E. I. Gladyshevskiy, *Russian Metall.*, 2 (1965) 91.

13 T. C. Lu, Y. G. Deng, C. G. Levi and R. Mehrabian, in M. N. Gungor, E. J. Lavernia and S. G. Fishman (eds.), *Advanced Metal Matrix Composites for Elevated Temperatures*, ASM International, Materials Park, OH, 1991, pp. 11–19.

14 H. Okamoto, A. B. Gokhale and R. Abbaschian, in T. B. Massalski (ed.), *Binary Alloy Phase Diagrams*, ASM International, Materials Park, OH, 1990, p. 2767 and p. 1632.

15 I. Barin, O. Knacke and O. Kubaschewski, *Thermochemical Properties of Inorganic Substances*, Springer, Berlin, 1977.

16 E. Fitzer and F. K. Schmidt, *High Temp. High Pressures*, 3 (1971) 445–460.

17 F. Roux and A. Vignes, *Rev. Phys. Appl.*, 5 (1970) 393.

18 J. D. Cotton, Y. S. Kim and M. J. Kaufman, *Mater. Sci. Eng.*, A144 (1991) 287–291.

19 J. P. A. Lofvander, J. Y. Yang, C. G. Levi and R. Mehrabian, in E. J. Lavernia and S. G. Fishman (eds.), *Advanced Metal Matrix Composites for Elevated Temperatures*, ASM International, Materials Park, OH, 1991, pp. 1–10.

20 L. Xiao and R. Abbaschian, to be published.

21 Y. S. Kim, M. R. Johnson, R. Abbaschian and M. J. Kaufman, *High-Temperature Ordered Intermetallic Alloys IV*, MRS Proc., Vol. 213, Materials Research Society, Pittsburgh, PA, 1990, pp. 839–845.

22 S. Jayashankar and M. J. Kaufman, *Scripta Metall.*, 26 (1992) 1245–1250.

23 L. Xiao and R. Abbaschian, submitted to *Metall. Trans.*

24 L. S. Sigl, P. A. Mataga, B. J. Dalgleish, R. M. McMeeking and A. G. Evans, *Acta Metall.*, 36 (1988) 945–953.

25 A. G. Evans and R. M. McMeeking, *Acta Metall.*, 34 (1986) 2435–2441.

26 M. F. Ashby, F. J. Blunt and M. Bannister, *Acta Metall.*, 37 (1989) 1847–1857.

27 J. R. Rice, *J. Appl. Mech.*, 35 (1968) 379–386.

28 D. G. Munz, J. L. Shannon, Jr., and R. T. Busey, *Int. J. Fracture*, 16 (1980) R137–141.

29 H. G. Tattersall and G. Tappin, *J. Mater. Sci.*, 1 (1966) 296–301.

rapid spreading of liquid aluminum throughout the powder mass. This is followed by the matrix synthesis reaction (initiated at approximately 980 °C), accompanied by a sharp temperature rise due to release of the heat of formation (-119 kJ mol^{-1}) of NbAl$_3$. Subsequent densification via pressurization then yields a sample of near-theoretical density, as shown in Fig. 2. In addition, it was found that, by controlling the initial stoichiometry of the Nb-Al powder mixture and selecting an appropriate niobium powder size, a uniform dispersion of Nb$_2$Al particles in an NbAl$_3$ matrix can be obtained. Such two-phase in situ composites are expected to possess better high temperature mechanical properties (owing to the higher melting temperature of Nb$_2$Al), without sacrificing the ambient mechanical properties. In fact, a slight increase in ambient fracture toughness has been observed previously [7].

The scope of RHC can be expanded to include the fabrication of niobium-filament-toughened NbAl$_3$ matrix composites with a diffusion barrier coating at the matrix-reinforcement interfaces. As discussed below, the synthesis reaction can be extended not only for producing the NbAl$_3$ matrix but also the simultaneous in situ formation of an Al$_2$O$_3$ layer at the Nb-NbAl$_3$ interfaces. Conceptually, the strategy for forming the Al$_2$O$_3$ layer in situ was based on initially providing a layer of niobium oxide on the surface of niobium filament reinforcements via a pre-oxidation treatment. Subsequent coupling with the reactive synthesis and consolidation of the aluminide matrix was utilized for the reactive conversion of the niobium oxide into an Al$_2$O$_3$ interfacial layer.

Thermodynamic data indicated that the niobium oxide(s) could be reduced by aluminum to produce Al$_2$O$_3$ during subsequent processing. This is illustrated by a plot of the Gibbs energy of formation of Al$_2$O$_3$ and the three possible niobium oxides (NbO, NbO$_2$ and Nb$_2$O$_5$) as a function of temperature (Fig. 3), indicating that Al$_2$O$_3$ is thermodynamically more stable than each of the three niobium oxides at all temperatures.

3.2. Pre-oxidation and its coupling with reactive hot compaction

The chopped niobium filaments (250 μm in diameter) were pre-oxidized at various temperatures and lengths of time. It was found that at temperatures above about 550 °C, a spontaneous uncontrollable self-propagating oxidation reaction occurred. Evidently, the high oxidation rate and the high heats of formation of the niobium oxides (ranging from -406 to -1990 kJ mol^{-1}) result in a rate of temperature rise which greatly exceeds the rate of heat removal from the specimen under the experimental conditions employed. Consequently, setting the upper limit of the treatment temperature at 500 °C, the thickening kinetics of the oxide layer were determined as described below. In addition, diffusion calculations indicated that, at 500 °C, the oxygen penetration depth in niobium was limited to about 4 μm if the treatment times were kept under 10 min, thus minimizing the potential embrittlement of the niobium filaments.

The thickening kinetics of the oxide layer at 500 °C are shown in Fig. 4 with a plot of the measured oxide layer thickness as a function of the square root of oxidation time. The linearity of

Fig. 2. NbAl$_3$ fabricated by the RHC process (polarized light illumination).
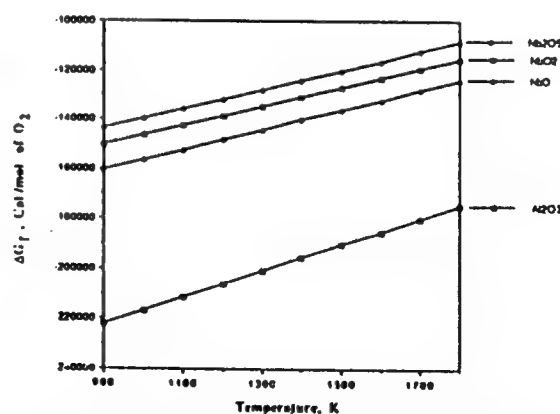
Fig. 3. The Gibbs free-energy data for niobium oxides and Al$_2$O$_3$.
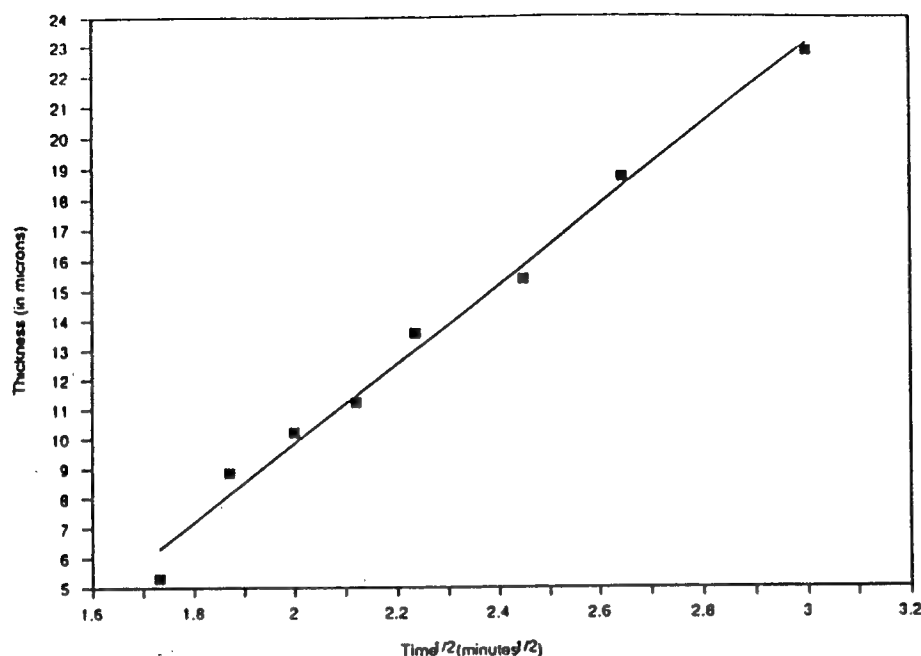
Fig. 4. Thickening of niobium oxide layer at 773 K under an oxygen pressure of 14.7 lbf in^{-2}.
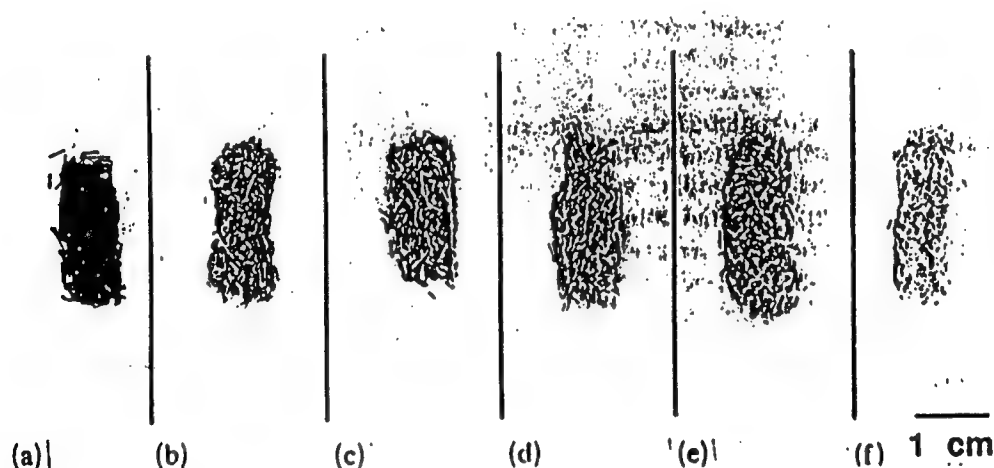
Fig. 5. Appearance of oxidized niobium filaments treated for various times: (a) 3 min; (b) 4 min; (c) 5 min; (d) 6 min; (e) 7 min; (f) 9 min.

the data indicates a parabolic oxidation rate during the short-term oxidation treatment and that the rate is most probably controlled by oxygen diffusion through the oxide layer.

The oxidized niobium filaments exhibited a continuous color change from blue through gray to white with increasing oxidation time, as shown in Fig. 5 (which shows the color change as gray shades), while XRD analysis of the oxidized filaments (Fig. 6) indicated that the major oxide formed on the niobium surface is Nb_2O_5. Neither

NbO nor NbO_2 were detected, in agreement with data in the literature [10], while according to the relative peak intensities the amount of Nb_2O_5 increased with increasing treatment time. Consequently, it may be concluded that the oxide layer thickening is solely a result of additional Nb_2O_5 formation and is not due to the formation of other oxides.

The morphology of the oxide scale was examined by scanning electron microscopy (SEM) of epoxy-mounted and metallographically prepared
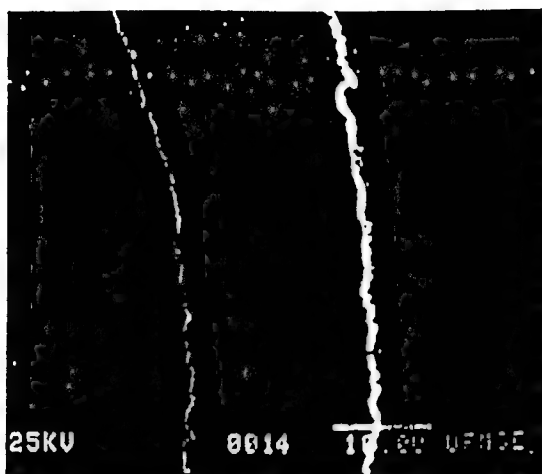
Fig. 8. Microstructure of the Nb_2O_5 scale on a typical oxidized niobium filament.

Fig. 9. Synthesis sequence for RHC of an Nb–NbAl$_3$ composite (schematic).

TABLE I

Summary of niobium oxidation time series at 500 °C under 14.7 lbf in^{-2} oxygen pressure

Oxidation time (min)	Average oxide thickness (μm)	Surface color	Layer stability
3.0	5.30	Dark blue	Stable
3.5	8.85	Light blue	Stable
4.0	10.20	Dark gray	Stable
4.5	11.20	Dark gray	Stable
5.0	13.55	Light gray	Stable
6.0	15.38	Light gray	Cracks
7.0	18.0	Light gray	Cracks
9.0	22.83	White	Spalling

described earlier. Differential thermal analysis and microstructural analysis of samples at various stages in the reaction sequence [11] indicate that the interfacial Al_2O_3 formation is triggered by the temperature rise which accompanies the matrix synthesis reaction. The interfacial microstructural morphology presented below revealed that the Al_2O_3 layer is surrounded by a layer of $Nb_2Al(\sigma)$ on the matrix side. This also suggests that the bulk of Al_2O_3 formation occurs via a solid state reaction with the matrix (i.e. in the post-matrix-synthesis stage), leading to an aluminum-poor region immediately adjacent to the interface. It should be noted that, although a similar local compositional change would be encountered during Al_2O_3 formation via reaction with liquid aluminum, rapid mass transport in the liquid would tend to level the compositional gradients.

The various reactions, their sequence and the related sequence of microstructural development of an RHC processed composite are shown schematically in Fig. 9 together with their location in relation to the processing cycle used.

It was found that the thickness of the subsequently formed Al_2O_3 layer was linearly related to the original thickness of the Nb_2O_5 layer, as illustrated in Fig. 10. The plot indicates a significant reduction in the thickness after reactive hot pressing, even though Al_2O_3 has a lower density than Nb_2O_5 (3.97 g cm^{-3} for Al_2O_3 compared with 4.47 g cm^{-3} for Nb_2O_5). Linear least-squares regression analysis of the experimental data ($R^2 = 0.98$) gave the following relation:

$$t_{Nb_2O_5} = 5.07 + 2.53 t_{Al_2O_3}.$$

One of the reasons for the observed thickness reduction is believed to be due to the 30–50% porosity in the initial Nb_2O_5 layer. In addition, it is likely that the higher temperature encountered during RHC (compared with that for the pre-oxidation treatment) may decrease the amount of Nb_2O_5 because of the increased oxygen solubility in niobium.

3.3. Microstructure of the composites

The microstructures of RHC-processed NbAl$_3$–Nb composites reinforced with bare (uncoated) and Al_2O_3-coated niobium filaments are shown in Figs. 11(a) and 11(b) respectively. It can be seen that, in the absence of an interfacial coating, there is an extensive matrix–filament interaction in the form of intermetallic formation
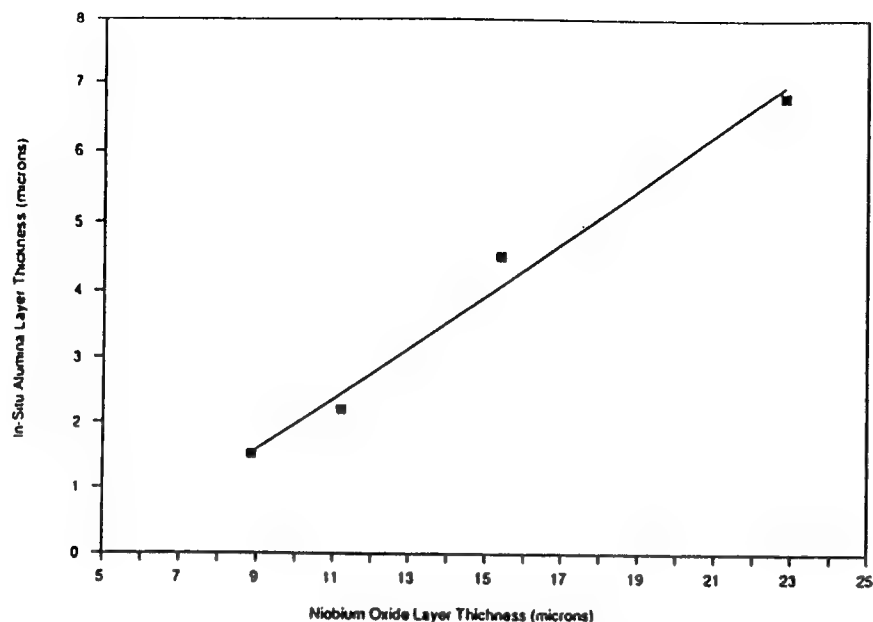
Fig. 10. Thickness relation between the initial Nb_2O_5 scale and the alumina layer formed *in situ*.

as well as the penetration of aluminum (with characteristics similar to grain boundary embrittlement) into the niobium filaments. By contrast, these interactions were significantly reduced upon formation of the Al_2O_3 layer at the interface (Fig. 11(b)). These uncoated and coated composites were further annealed at 1200 °C for 100 h. The microstructure of the two types of niobium filaments after annealing are shown in Figs. 12(a) and 12(b) respectively. It is clear that the interfacial reaction zone has thickened for the uncoated reinforcements. In addition, it was found that the microhardness of the reinforcement increased sharply towards the periphery for the uncoated filaments, which is clearly an undesirable situation. Furthermore, the interfacial layer continued to thicken with further annealing, leading to an unstable composite microstructure. By contrast, the microhardness across the coated filament was approximately constant. This is corroborated independently by compositional line scans across the coated reinforcement–matrix interfaces in the pre-annealed and post-annealed (1200 °C for 100 h) conditions (Figs. 13(a) and 13(b) respectively). It can be seen that after the annealing treatment there is only a limited amount of aluminum diffusion in the filaments coated *in situ*.

The above line scans and the interfacial microstructural morphology (Fig. 14) also reveal that a multilayer structure is formed at the interfacial region, with a sequence of $NbAl_3 \rightarrow Nb_2Al \rightarrow Al_2O_3 \rightarrow Nb$, upon traversing from the matrix to the reinforcement side. Also, it is noted that the aluminum profile in the Al_2O_3 layer decays towards the niobium side of the $Nb-Al_2O_3$ interface in both samples, suggesting that the aluminum diffusion could be one of the rate-controlling steps in the Al_2O_3 formation process. Furthermore, it should be noted that there is a slight increase in the niobium content of the Al_2O_3 scale toward the niobium filament side, indicating that the Al_2O_3 formation sequence must also be controlled by a niobium rejection and transport mechanism.

Transmission electron microscopy (TEM) analysis of the interfacial regions [12] also supported this morphological sequence, as shown by the bright field micrograph in Fig. 15(a). The analysis indicated that the Al_2O_3 was present in the stable α modification, while niobium precipitates were detected in the Al_2O_3 layer toward the niobium filament side of the interface (Fig. 15(b)), supporting the compositional analysis. The presence of niobium particles predominantly near the niobium side and their near-absence toward the matrix side reveal an interesting aspect of the Al_2O_3 formation reaction: it appears that the niobium released during Nb_2O_5 reduction by aluminum according to the reaction $3Nb_2O_5 +$
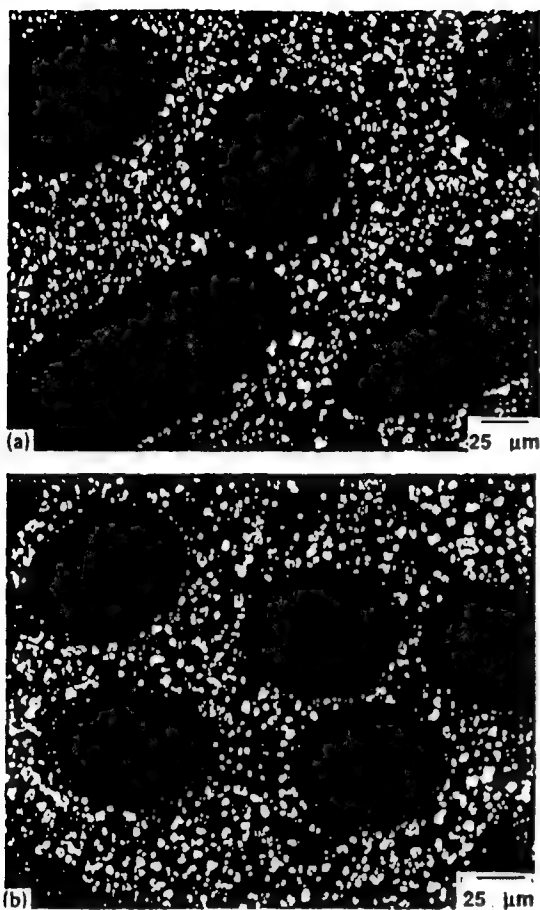
Fig. 11. Microstructures of niobium-filament-reinforced NbAl₃ composites (as processed): (a) uncoated filaments; (b) filaments coated in situ.

Fig. 12. Microstructures of niobium filaments embedded in an NbAl₃ matrix after long-term annealing: (a) uncoated filament; (b) filament coated in situ.

$10Al = 5Al_2O_3 + 6Nb$ may be accommodated by the unreacted Nb_2O_5 ahead of the Al_2O_3–Nb_2O_5 interface. Subsequently, the continued transformation of Nb_2O_5 to Al_2O_3 may lead to the observed precipitation of niobium. The interface morphology is summarized schematically in Fig. 15(c).

It was critical for the success of the *in situ* alumina coating technique that the niobium reinforcements themselves do not degrade because of the pre-oxidation treatment, since it is well known that interstitial elements such as oxygen can significantly embrittle niobium. The Vickers microhardness of the pre-oxidized niobium filaments embedded in the matrix was measured as a function of the pre-oxidation time. It was found that the Vickers microhardness ranged from a minimum of 70HV (for 4 min of oxidation treatment) to a maximum of 300 HV (for 9 min of oxidation treatment). On comparison of these values with the data of other investigators [13] (60 HV for pure niobium to a maximum of 325 HV for niobium containing 0.35 wt.% O), it is clear that the maximum oxygen content in the pre-oxidized niobium filaments may not exceed 0.35 wt.%. This is important, since Stoop and Shaninian [13] found that below 0.35 wt.%, the ductility of niobium was not degraded and all other mechanical properties were slightly improved at both ambient and elevated temperature owing to the dynamic-strain-aging effects [14].

3.4. Fracture toughness

The fracture toughness of the matrix and niobium filament-reinforced composites was measured via three-point bending tests on chevron-notched specimens. The tests indicated a significant increase in K_{Ic} upon reinforcing with the niobium filaments coated with Al_2O_3 *in situ*,
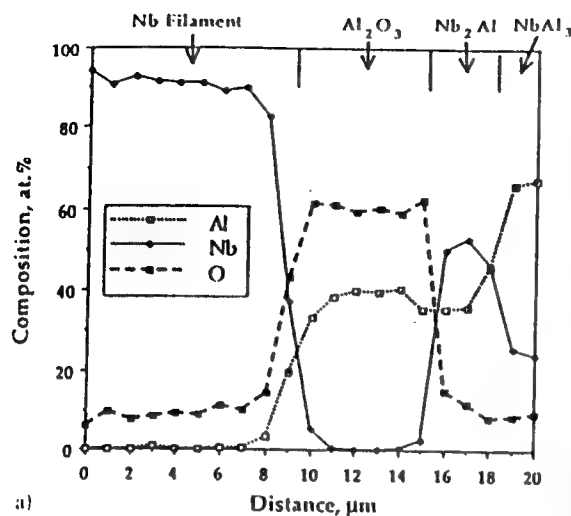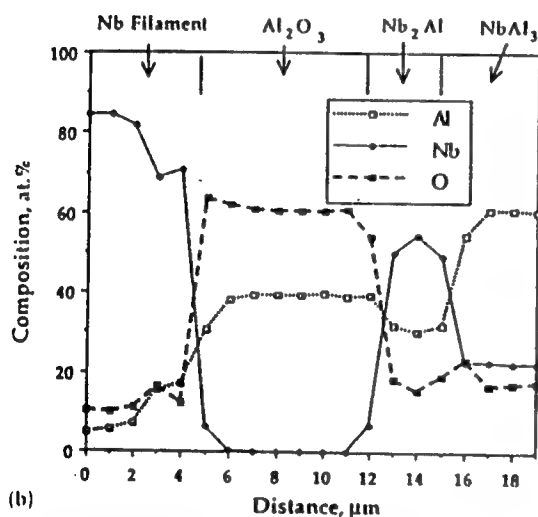
Fig. 13. Compositional profiles across the Al₂O₃ layer formed *in situ*: (a) as processed; (b) annealed.
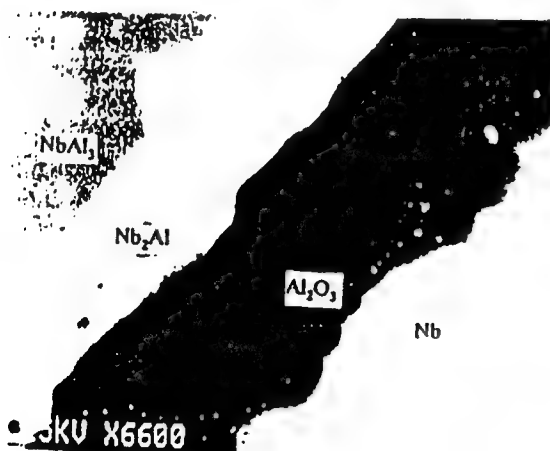
Fig. 14. Microstructure of the interface showing a multilayer structure.
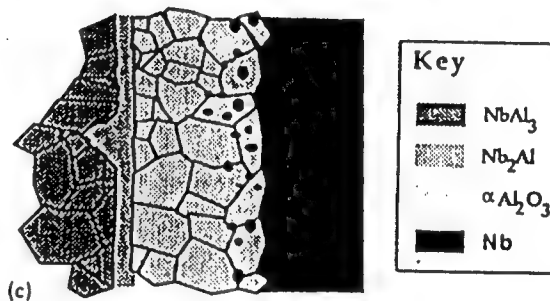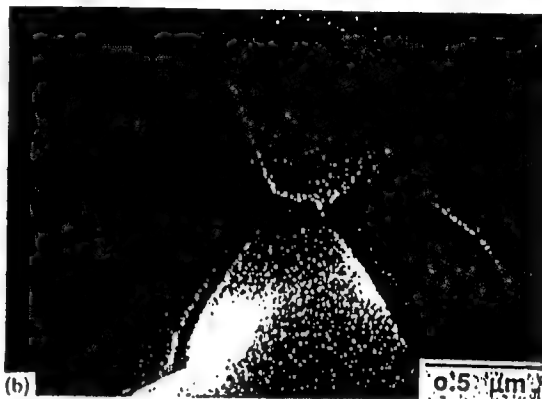
Fig. 15. The Al₂O₃ interfacial region formed *in situ*: (a) bright field TEM image, showing a dense fine-grained Al₂O₃ layer; (b) high magnification TEM micrograph, showing an Al₂O₃ layer containing a fine dispersion of niobium particles; (c) schematic illustration of the interface structure.

as illustrated by the load–displacement curves for the unreinforced matrix and a composite containing 20 vol.% Nb filaments (Fig. 16). The unreinforced matrix showed typical catastrophic brittle failure after the peak load, implying an insignificant damage tolerance. By contrast, the composite shows an initial linear elastic region, followed by a non-linear load increase with some fine perturbations caused most probably by microcrack generation in the matrix up to the maximum
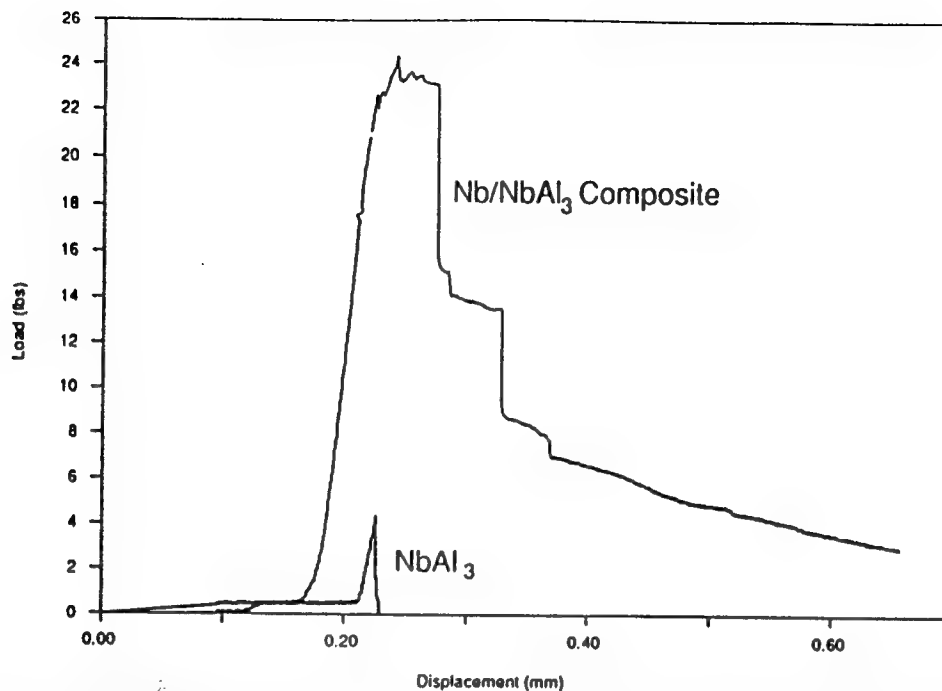
Fig. 16. Load–displacement curves of three-point bending tests with chevron-notched toughened composite specimens consisting of a monolithic matrix and 20 vol.% Nb (Al_2O_3 coated).

load, followed by a continuous and stepwise load decrease. It should be noted that both the higher fracture toughness and the higher damage tolerance of the composite arise because of an effective load transfer to the reinforcing phase.

Observation of the fracture surface of the tested samples provides an insight into the characteristics of the load–displacement curves. Figure 17(a) shows the general appearance of the fracture surface at a low magnification of an $NbAl_3$ composite reinforced with niobium filaments coated with Al_2O_3 in situ. The figure clearly demonstrates a significant degree of bridging by the niobium reinforcements. Furthermore, the fracture surface topography suggests that crack deflection occurred when the cracks intersected the niobium filaments. The niobium filament reinforcements failed typically in a highly ductile manner as shown in Fig. 17(b). Several observations may be illustrated from this micrograph; the filament fracture is a "knife edge", indicating extremely ductile behavior, while there is clear evidence of partial circumferential decohesion at the interface. A closer look at the interfaces on the fracture surfaces indicated that the decohesion occurs first on that side of the filament first encountered by the crack front and

subsequently on the other side, contributing to the knife-edge nature of the niobium filament fracture.

From physical considerations, it is apparent that a certain amount of ductility of the reinforcement is needed for any significant improvement in the toughness of brittle matrix composites. It has also been recognized that ductility of the reinforcing phase alone is not sufficient for achieving a significant improvement in the fracture toughness; equally as important is the matrix–reinforcement interfacial strength. For example, if the interface is very strong, a high degree of geometrical constraint can lead to a triaxial state of stress, resulting in a brittle failure of the ductile reinforcement [15]. Consequently, there would not be a significant increase in the composite toughness under these circumstances. On the contrary, for a very low reinforcement–matrix interface strength, the reinforcement would readily debond and there would be no crack surface bridging action, again resulting in a limited improvement in the toughness.

On the contrary, a significant improvement in the fracture toughness would be expected if a partial interfacial debonding (decohesion) can remove the geometrical constraints and allow the
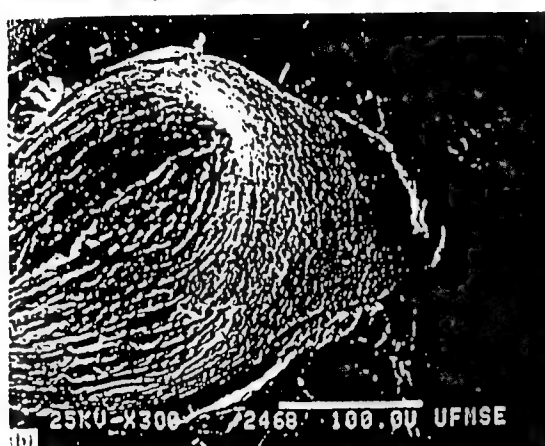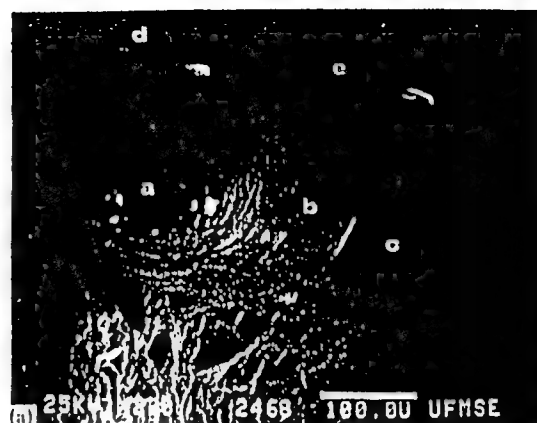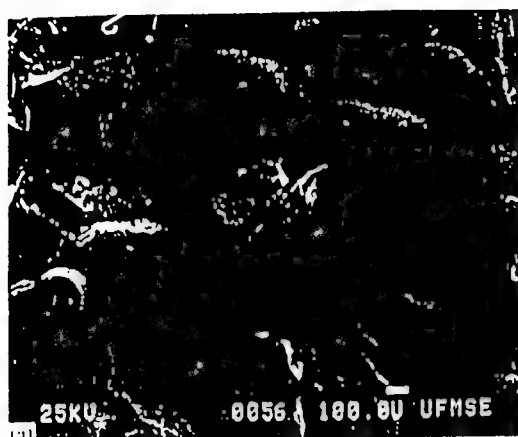
Fig. 17. Fractographs of Nb–NbAl₃ composite coated *in situ*: (a) general fracture surface; (b) fractured niobium filament showing knife-edge failure and partial interfacial bonding.

reinforcement to neck, while the remaining interface area in contact with the matrix (because of a combination of the interface bonding strength and mechanical interlock) allows an effective load transfer to the reinforcement.

The niobium filament–matrix interface in the present instance clearly shows evidence of partial decohesion along the fracture surface with associated filament necking and ductile fracture. This suggests that the interface of the composite fabricated by this processing technique possesses optimal interface properties. Since the interfacial regions exhibited a multiphase multilayered morphology, it was important to determine the exact location (within the layers) of interfacial decohesion. A closer look at the interface via SEM and energy-dispersive spectroscopy (EDS) analysis of the fracture surface revealed that the interface between the $Nb_2Al(\sigma)$ layer and the Al_2O_3 formed *in situ* had the weakest bond. This

Fig. 18. Surface geometry of the debonded interface: (A) general view; (B) surface geometry of the niobium filament corresponding to the area labeled b in (A); (C) surface geometry of the Al_2O_3 layer formed *in situ* corresponding to the area labeled c in (A), showing typical intergranular fracture surface

is illustrated in Fig. 18 with a set of micrographs: Fig. 18(A) is the general view of the debonded interface, Fig. 18(B) a magnified view of the area labeled b in Fig. 18(A), and Fig. 18(C) a magni-
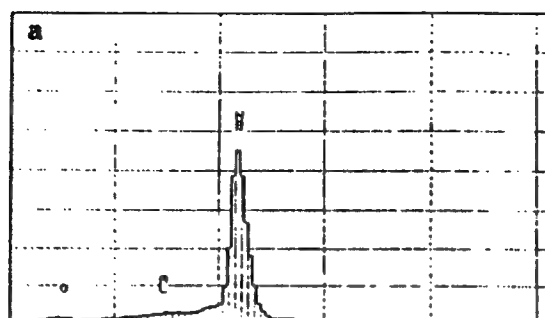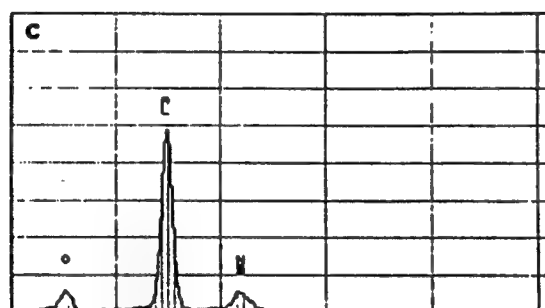
Fig. 19. EDS spectra of the areas shown in Fig. 18(A).

fied view of the area labeled c in Fig. 18(A). A series of EDS spectra is given in Fig. 19 (labeled a–e corresponding to a–e in Fig. 18(A)): a is the filament knife-edge, b is the niobium filament surface, c is the Al_2O_3 coating layer formed *in situ*, d is partially debonded matrix surface and e is the $NbAl_3$ matrix. The EDS analysis was carried out by directly focusing the electron beam on these individual areas. It is clear that the spectra for a and b correspond to the niobium filament with a surface morphology shown in Fig. 18(B), while the spectrum for c corresponds to the Al_2O_3 coating layer formed *in situ* with the morphology shown in Fig. 18(C); the spectra for d and e correspond to Nb_2Al and $NbAl_3$ (matrix) respectively. These observations clearly indicate

that the partial interfacial decohesion is initiated at the Al_2O_3–Nb_2Al interface. In addition, during necking of the niobium filaments, decohesion at the Nb–Al_2O_3 interface was observed. However, the Nb_2Al–$NbAl_3$ interface did not exhibit any decohesion, implying a strong interfacial bond, as supported independently by our previous work on Nb_2Al–$NbAl_3$ composites [7].

4. Summary and conclusions

With the unique coupling of RHC process with pre-oxidation treatment of the niobium filament reinforcements, Nb–$NbAl_3$ composites were obtained with an Al_2O_3 layer formed *in situ* at reinforcement–matrix interfaces during the synthesis and consolidation of the composites. Post-annealing microstructural analysis indicated that the Al_2O_3 layer formed *in situ* acts as an effective diffusion barrier, while the uncoated niobium filaments degraded to a significant extent. The fracture roughness of the composites showed a significant improvement over that of the unreinforced matrix. Fracture surface analysis suggested that a partial debonding (decohesion) occurs at the Al_2O_3–matrix interface during crack propagation. Thus the *in situ* coating appears to provide both an excellent and stable diffusion barrier and optimum properties for the operation of various toughening and strengthening mechanisms.

References

1 R. L. Fleischer, *J. Mater. Sci.*, 22 (1988) 2281–2288.
2 J. H. Schneibel, P. F. Becher and J. A. Horton, *J. Mater Res.*, 3 (6) (1988).
3 S. Ochiai and K. Osamura, in H. Ishida (ed.), *Interfaces in Polymer, Ceramic and Metal Matrix Composites*, Elsevier, Amsterdam, 1988, pp. 413–423
4 A. Bose, B. Moore, R. M. German and N. S. Stoloff, *J. Met.*, 14–17 (9) (1988).
5 *ASTM Stand. J92-87*, 1988.
6 S.-X. Wu, in J. H. Underwood, S. W. Freiman and F. I. Baratta (eds.), *Chevron-notched Specimens: Testing and Stress Analysis, ASTM Spec. Tech. Publ. 855*, 1984, pp. 176–192 (ASTM, Philadelphia, PA).
7 L. Lu, Y. S. Kim, A. B. Gokhale and R. Abbashian, *Proc. Conf. on Intermetallic Matrix Composites, Materials Research Society Spring Meeting, San Francisco, CA, April 16–21, 1990*, Materials Research Society, Pittsburgh, PA, 1990, pp. 79–87.
8 *Powder Diffraction File*, Joint Committee on Powder Diffraction Standards, International Center for Diffraction Data, Swarthmore, PA, 1989, Card 34-370.
9 *Powder Diffraction File*, Joint Committee on Powder Diffraction Standards, International Center for Diffraction Data, Swarthmore, PA, 1989, Card 27-1313.
10 E. A. Gulbransen and K. F. Andrew, *J. Electrochem. Soc.*, 105 (1) (1959) 4–9.
11 L. Lu, A. B. Gokhale and R. Abbaschian, *Masters Thesis*, 1991.
12 L. Lu, A. B. Gokhale, M. J. Kaufman and R. Abbaschian, *Extended Abstracts, in Conf. on Powder Metallurgy: Key To Advanced Technology, Vancouver, British Columbia, July 30–August 1, 1990*, Metals Park, OH, 1990.
13 J. Stoop and P. Shaninian, *Proc. Conf.*, Metallurgical Society of AIME, Warrendale, PA, 1960, Part II, Conf. Symp. 34, pp. 407–432.
14 J. F. Enrietto, G. M. Sinclair and C. A. Wert, *Proc. Conf. on Columbium*, Metallurgical Society of AIME, Warrendale, PA, 1960, pp. 503–521.
15 C. K. Elliott, G. R. Odette, G. E. Lucas and J. W. Shecherd, in F. D. Lemkey, S. G. Fishman, A. G. Evans and J. R. Strife (eds.), *High Temperature/High Performance Composites, Materials Research Society Symp. Proc.*, Vol. 120, Materials Research Society, Pittsburgh, PA, 1988, pp. 95–101.

Processing and mechanical properties of niobium-reinforced MoSi$_2$ composites

L. Xiao, Y. S. Kim and R. Abbaschian

Department of Materials Science and Engineering, University of Florida, Gainesville, FL 32611 (U.S.A.)

R. J. Hecht

Pratt and Whitney, West Palm Beach, FL 33410-9600 (U.S.A.)

Abstract

In this paper, we describe a framework for the processing of niobium-reinforced MoSi$_2$ composites. As a part of the program, composites containing coated and uncoated niobium reinforcements were produced. Chemical compatibility between the coatings and the matrix was studied and the effect of the interface modification by the coating on the fracture toughness of the composites was investigated via four-point bending tests on chevron-notched samples. The results indicated that the coatings have a significant effect on the debonding at the reinforcement–matrix interface, which in turn can affect the damage tolerance of the composite. Also observation of the crack propagation in the composites suggests that the matrix failed at the early stages of loading. The results are discussed in terms of the mismatch between the elastic constants of the composite constituents.

1. Introduction

MoSi$_2$ heating elements have been used since the early 1950s because of a combination of properties: proper electrical resistivity, high melting temperature (2030 °C) and excellent oxidation resistance up to 1700 °C in oxidizing environment. In addition, MoSi$_2$ has a relatively low density (6.4 g cm^{-3}) and can retain a significant part of its ambient temperature strength up to 1200 °C. These properties make MoSi$_2$ an excellent candidate as a structural material for high temperature applications. However, its poor room temperature fracture toughness imposes a severe limitation on its use in practical applications.

The toughness of MoSi$_2$ can be improved by the incorporation of ductile reinforcements such as refractory metal filaments or particles. Since the ductile reinforcements commonly have a lower elastic modulus than MoSi$_2$, the composite was termed an "inverse composite" [1, 2]. The principal mechanism of toughness improvements in these composites is attributed to crack shielding or crack bridging by the ductile reinforcements. Results of independent theoretical modeling also indicate that the ductile phase toughening can be an effective tool in improving the fracture toughness of brittle matrices [3, 4].

The major difficulty in using ductile reinforcements, especially pure refractory metals, is that they tend to react with the matrix at high temperatures, leading to the formation of brittle interfacial products. For example, when Nb-MoSi$_2$ composites were annealed at high temperatures, (Mo, Nb)$_5$Si$_3$, among other compounds, formed at the reinforcement–matrix interface at a relatively rapid rate [1, 5]. The formation of the interfacial compounds at the expense of the ductile reinforcement not only degrades the ductile phase toughening effect but also can cause a notch effect on the ductile phase as the compound grows thicker [6]. Therefore the use of an inert diffusion barrier coating on the reinforcements prior to processing of the composites is essential for minimizing the matrix–reinforcement interactions during processing and service at elevated temperatures.

In this study, the effect of various oxide coatings on the decohesion length at the reinforcement–matrix interface and consequently the fracture toughness of the composites were investigated. It will be shown not only that the coatings have a significant effect on the fracture toughness of the composites but also that the magnitude of the effect changes according to the reinforcement geometry. Furthermore, the crack propagation

and crack–reinforcement interactions at various stages of loading were explored to understand the role of ductile reinforcements which have an elastic modulus lower than that of the matrix in determining the fracture toughness of the composites.

2. Experimental details

· The chemical compatibility of various oxide coating materials (Al_2O_3, ZrO_2 and mullite) with $MoSi_2$ was investigated by compositional and microstructural analysis of vacuum hot-pressed $MoSi_2$ samples containing the oxide powders. The hot pressing was carried out 1700 °C for 30 min under 40 MPa pressure.

Laminated composites containing uncoated and coated niobium foils were produced by vacuum hot pressing. Details of coating niobium foils with Al_2O_3 or ZrO_2 via the sol–gel route can be found elsewhere [5]. In order to fabricate the laminated composites, niobium foils 0.25 mm thick and − 325 mesh $MoSi_2$ powder were stacked to produce 20 vol.% of niobium foils in the final composite. The thickness of each $MoSi_2$ layer was kept constant by using the same amount of $MoSi_2$ powder between the layers. These stacked samples were vacuum hot pressed at 1700 °C for 40 min under a pressure of 40 MPa. Similarly, fibrous aligned composites containing coated and uncoated niobium filaments (0.127 and 1.0 mm in diameter) were also fabricated. Compositional analysis was performed using a JEOL JXA 733 microprobe and pure molybdenum, silicon, nickel, aluminum and zirconium as standards; the oxygen content was determined as the balance.

The fracture toughness of the composites was determined by a four-point bending test on chevron-notched specimens using a hydro-servo-controlled MTS machine at a cross-head speed of 4×10^{-4} mm s^{-1}. The dimensions of the specimen were 3.81 mm × 5.08 mm × 25.4 mm; the chevron notch on the laminated composites was cut perpendicular to the foil plane using a diamond wafering saw. The crack propagation process in the chevron-notched sample ·during the four-point bending test was investigated by unloading the samples at various loads. The unloaded samples were sectioned and investigated for crack geometry.

3. Results and discussion

3.1. Chemical compatibility between $MoSi_2$ and coating materials

The chemical compatibility of the coating materials (Al_2O_3, ZrO_2 and mullite) with an $MoSi_2$ matrix was assessed experimentally via microstructural and compositional analyses of the samples after hot pressing powder mixtures of commercial $MoSi_2$ and the coating materials. Figure 1 shows the microstructural and the corresponding elemental compositional profiles near the Al_2O_3–$MoSi_2$ interface of a sample annealed at 1600 °C for 100 h after hot pressing at 1700 °C for 40 min. The compositional profiles show two very distinctive types of interface: a relatively sharp interface with a thickness less than the distance between two consecutive scanning points of the electron microprobe (2 μm), and a relatively diffuse interface about 7 μm thick. Also, the diffuse interface layer is rich in silicon, aluminum
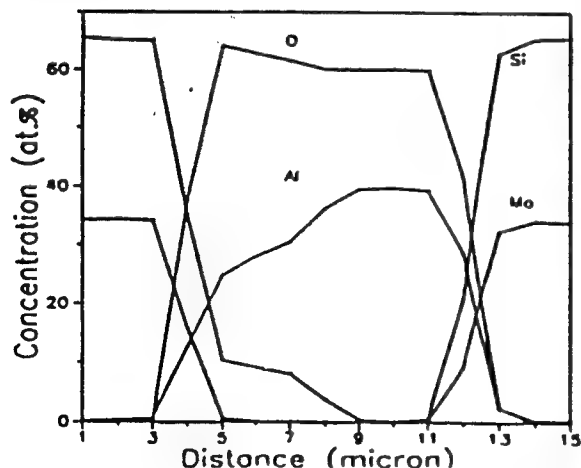

Fig. 1. Compositional profiles across an Al_2O_3 particle in an $MoSi_2$ matrix.

and oxygen, with little or no molybdenum. When the annealing temperature was varied from 1400 to 1600 °C, the general appearance of both interfaces and their thicknesses remained almost the same. In a related study, microstructural analysis of vacuum hot-pressed $MoSi_2$ samples, fabricated from the commercial $MoSi_2$ powders, revealed the presence of small second-phase particles distributed randomly thoughout the matrix, as shown in Fig. 2. Transmission electron microscopy analysis indicated that these particles were amorphous SiO_2 [7]. Consequently, it is believed that the interaction layer at the diffuse interface is due to a reaction between Al_2O_3 and SiO_2 impurity particles. This suggests that $MoSi_2$ and Al_2O_3 may be chemically compatible within the temperature range considered (1400–1600 °C).
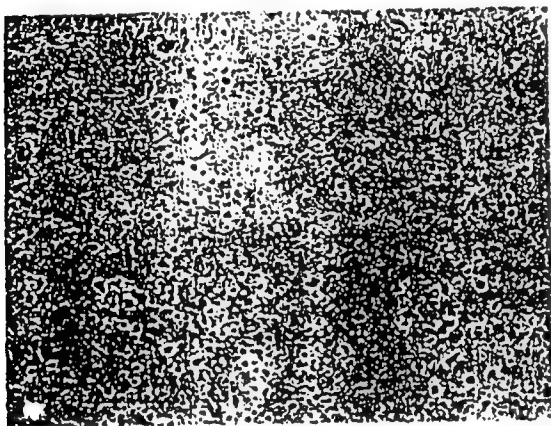
Fig. 2. Optical micrograph of $MoSi_2$ produced by the hot pressing of commercial powders.

Compositional analysis of $MoSi_2$–ZrO_2 and $MoSi_2$–mullite fiber* composites indicated a very sharp particle–matrix interface, with no apparent interaction zone. This is illustrated by the compositional profile and the corresponding microstructure of an $MoSi_2$–mullite composite (Fig. 3). Similar to $MoSi_2$–Al_2O_3, the interface remained sharp with no appreciable increase in its thickness upon annealing.

3.2. Effectiveness of the inert coatings as a diffusion barrier

In addition to the chemical compatibility of a coating with the matrix and the reinforcement, it must act as a diffusion barrier for the elemental constituents of the composite. In order to evaluate the effectiveness of the various oxide coatings as diffusion barriers, niobium filaments coated with ZrO_2 and Al_2O_3 were mixed with $MoSi_2$ powder and hot pressed at 1700 °C for 40 min. ZrO_2-coated niobium filaments (Fig. 4) exhibited a limited interaction layer on the niobium side of the coating, but not on the $MoSi_2$ side. The thickness of the interaction layer was around 4 μm, which is considerably less than that observed for the uncoated filament–matrix interface produced under similar hot-pressing conditions. For the latter, the layer thickness was 30 μm. In addition, compositional analysis indicated that the reaction product at the Nb–ZrO_2 interface was Nb_5Si_3

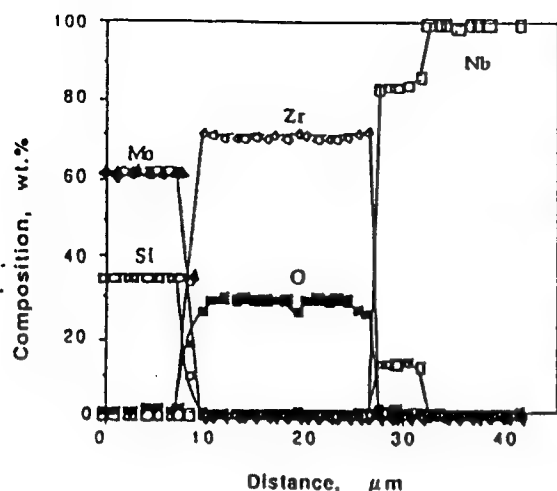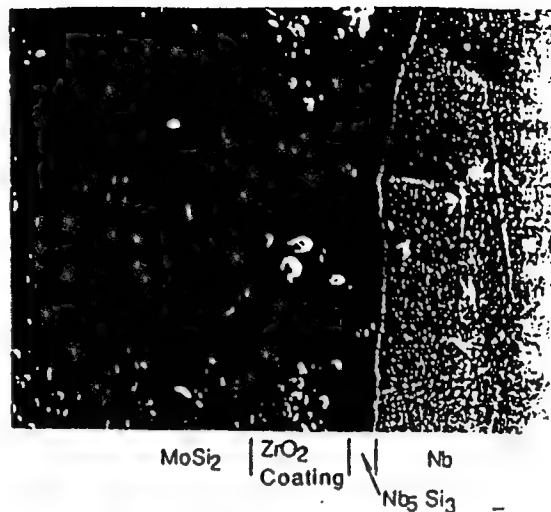*The mullite fibers were produced by M. D. Sacks et al. at the University of Florida.

Fig. 3. The interface microstructure and the corresponding compositional profiles of an $MoSi_2$–mullite composite.

Fig. 4. The microstructure and the corresponding compositional profiles across a (ZrO$_2$-coated Nb)–MoSi$_2$ interface.

compared with (MoNb)$_5$Si$_3$ which formed at the uncoated Nb–MoSi$_2$ interface.

The growth of the interaction layer (Nb$_5$Si$_3$) at 1300 °C was measured after annealing the samples for 25 and 100 h. As shown in Fig. 5, the layer thickness was increased to 6 μm after annealing for 100 h and followed a parabolic function of the annealing time. The results indicated that the growth rate of the Nb$_5$Si$_3$ at the Nb–ZrO$_2$ interface is controlled by the diffusion of silicon through the Nb$_5$Si$_3$ rather than through the ZrO$_2$ coating.

A similar interfacial interaction was observed upon coating niobium with Al$_2$O$_3$, as shown in Fig. 6. The thickness of the interaction layer formed on the niobium side of the Nb–Al$_2$O$_3$ interface was measured to be around 5 μm after hot pressing and the layer was again determined to be Nb$_5$Si$_3$. These results indicate that, even though ZrO$_2$ and Al$_2$O$_3$ are chemically compatible with niobium and MoSi$_2$, the coatings are not perfect barriers for silicon diffusion. Nevertheless, the coatings are effective in retarding the niobium and molybdenum diffusions and hence substantially reduce the growth rate of the reaction layers.

An order-of-magnitude calculation of silicon diffusivity through ZrO$_2$ and Al$_2$O$_3$ made from the growth rate of the interaction layers indicates that the apparent silicon diffusivity must be larger than 1.0×10^{-9} cm^2 s^{-1} in ZrO$_2$ at 1300 °C and larger than 2.0×10^{-8} cm^2 s^{-1} in Al$_2$O$_3$ at 1400 °C. These values are considerably higher
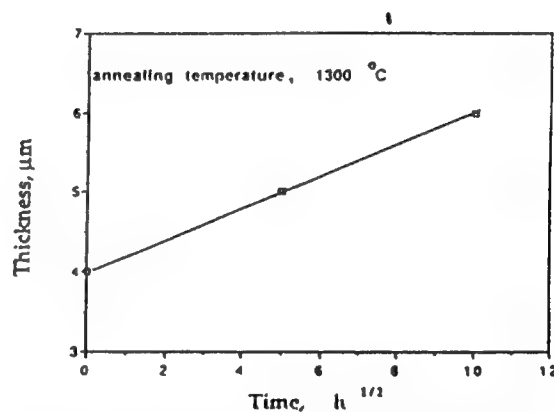
Fig. 5. The thickness of the interaction product in an MoSi$_2$-(ZrO$_2$-coated Nb) composite as a function of the square root of the annealing time.

than the bulk diffusivities of silicon in these ceramic materials [8]. It is possible that silicon diffusion in the coatings was enhanced along the grain boundaries, or processing defects such as pinholes generated during the sol-gel coating process.

3.3. Fracture toughness of ductile-phase-reinforced composites

The fracture toughness of the brittle matrix composite was calculated from the peak load of the load–displacement curves of chevron-notched samples tested in four-point bending. Typical load–displacement curves for an unreinforced matrix and an uncoated composite reinforced with 20 vol.% Nb foil are shown in Fig. 7.
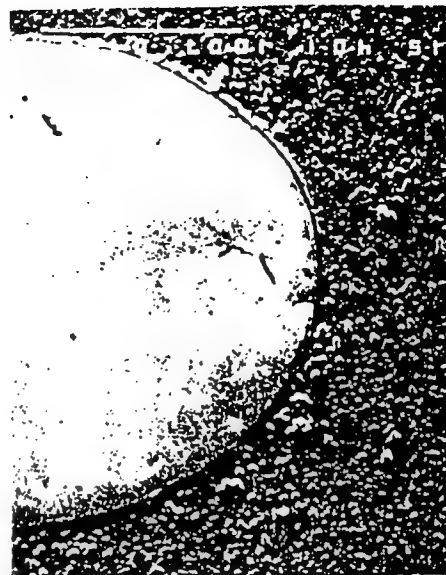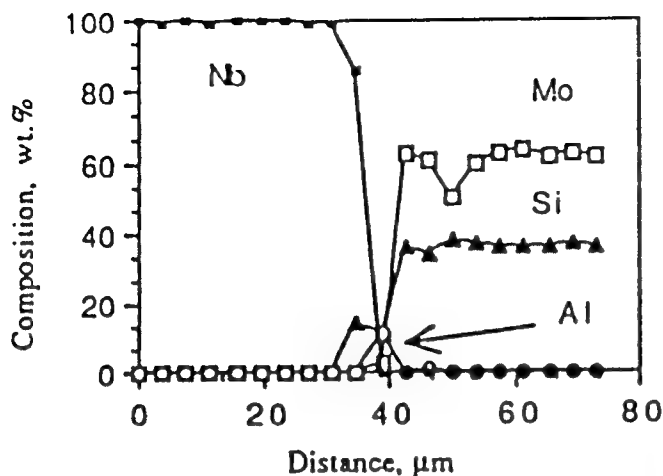
Fig. 6. The microstructure and the corresponding compositional profiles of Al_2O_3-coated niobium filaments in $MoSi_2$.
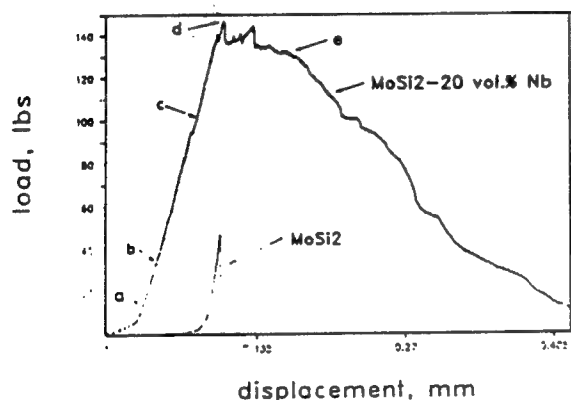

Fig. 7. Typical load–displacement curves of chevron-notched monolithic $MoSi_2$ matrix and uncoated niobium-foil-reinforced composite specimens. The letters on the composite curve indicate the approximate unloading load levels for the microstructures shown in Fig. 8.

As can be seen, the peak load of the composite specimen is more than three times higher than that of the matrix. The fracture toughness calculated using a model derived by Munz *et al.* [9] indicated that the fracture toughness K_{IC} of the composite was around 15 MPa m$^{1/2}$ compared with 3.3 MPa m$^{1/2}$ for monolithic $MoSi_2$. Also the work of fracture of the composite specimen has increased significantly over that of the matrix.

In order to investigate the crack propagation in the matrix, the chevron-notched composite specimens were unloaded at five different load levels,

indicated by points a–e in Fig. 7. The unloaded specimens were sectioned parallel to the crack propagation but perpendicular to the direction of the foil alignment and then examined for the extent of crack propagation. Figures 8(a)–(e) show the nature of crack propagation in the samples at the corresponding load levels indicated in Fig. 7. For the sample loaded up to 15 lbf (point a in Fig. 7) which is approximately 10% of the peak load of the composite, a crack was observed at the tip of the chevron notch, which had propagated in a stable manner as shown in Fig. 8(a). When the load was increased to 35 lbf (point b in Fig. 7), which is about 23% of the peak load, the result indicated that the crack had already propagated throughout the entire thickness of the matrix.

The extensive cracking of the matrix at a load level considerably below the peak load of the composite may be explained using the principle of strain compatibility in composite materials. During the initial loading and prior to cracking of the matrix, most of the applied load is carried by the matrix because the elastic modulus of $MoSi_2$ matrix (380 GPa) is much higher than that of niobium foils (105 GPa). For the niobium foils to carry the same stress as the matrix, they need to be elongated three times more than the matrix (assuming no constrained deformation). On the basis of the strain compatibility criteria, this is clearly impossible unless the matrix fractures.
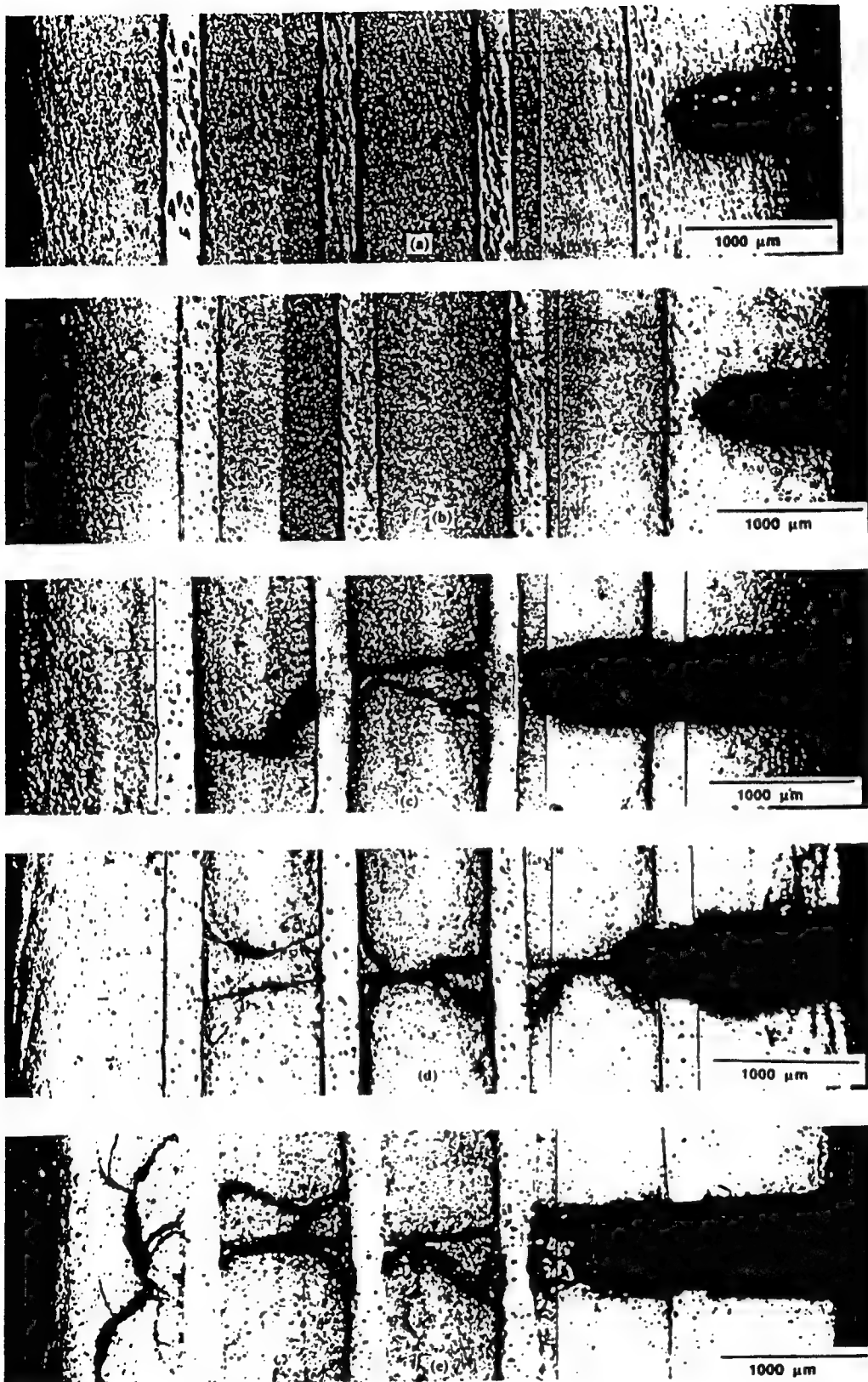
Fig. 8. The propagation of the cracks in uncoated niobium-foil-reinforced MoSi$_2$ composites at various load levels in Fig. 7.
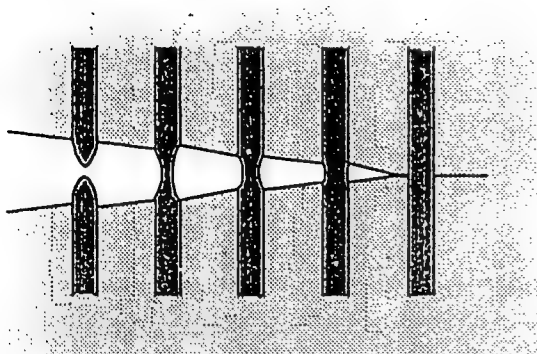
Fig. 9. Crack propagation in a ductile-phase-reinforced brittle matrix composite. The reinforcements located farther behind the crack tip are strained much more to carry the applied stress.

Therefore the reinforcement with a lower elastic modulus will carry a minor part of the load until a matrix crack has opened appreciably to allow the reinforcement to strain. This is schematically shown in Fig. 9, where the reinforcements which are farther behind the crack tip are strained much more than those closer to the tip or ahead of the crack. Obviously, the required level of the crack opening for the additional straining of the reinforcement will depend on the length of debonded section of the reinforcement: the larger the debonding length, the larger is the reinforcement section which is being strained, and the larger is the required crack opening. Moreover, the latter will also depend on the relative values of the elastic moduli of the matrix and the reinforcement. The thick (0.25 mm) niobium foils and the large distance between the foils (about 800 μm) may also have contributed to the premature failure of the matrix. It is clear that the value calculated from the peak load (point d in Fig. 7) may be interpreted as an indicator of the damage tolerance of the composite.

3.4. Interaction of cracks with uncoated niobium reinforcements

Closer examination of Fig. 8 reveals interesting aspects of the interaction between cracks and niobium foils in the composites reinforced by the uncoated niobium foils. At the early stages of loading, there is only one primary crack propagating in the matrix. This primary crack propagates through the matrix in a stepwise manner, instead of propagation on one crack plane (Fig. 8(b)). The stepwise crack propagation in the matrix may be explained through geometrical

effects of the niobium reinforcement foils. In these laminated composites, as a crack ends on one side of the niobium foils, it needs to renucleate on the other side, making the crack propagation discontinuous in nature. Let us consider, moreover, the crack nucleation mechanism: because of a statistical distribution of crack nucleation sites on the other side of the foil, it is not necessary that the renucleation be coplanar with the original crack. In fact, it may be expected that the renucleated crack will most probably not be coplanar with the original crack. The net result is the observed stepwise crack propagation.

As the load level is increased, the niobium foils at the opening of the primary crack become stretched and secondary cracks start to nucleate as shown in Fig. 8(c). On further increase in load, additional secondary cracks continue to form and propagate throughout the matrix, creating a region at the interface which may be termed "virtual debonding" as shown in Fig. 8(e). In this area, the matrix-imposed constraints are relaxed and the foil can deform freely in a unidirectional tensile stress state until it fails in a ductile manner.

When the geometry of the niobium reinforcements is changed from foils to filaments, the crack propagation in the matrix is also expected to change. For filament-reinforced composites, the crack can propagate continuously throughout the matrix without the need for renucleation. Therefore the crack will propagate on the plane of the maximum stress intensity and the secondary cracks are not expected to form. Figure 10 shows the fracture surface of an uncoated niobium-filament-reinforced composite. As seen in the figure, there is no appreciable debonding at the reinforcement–matrix interface and the filaments have failed in a brittle cleavage manner. The brittle fracture of the filaments is believed to occur because of the lack of decohesion at the reinforcement–matrix interface due to strong bonding and because of the absence of the virtual decohesion by secondary cracks as in the laminated composites. As a result, the filaments are constrained by the matrix and, under a triaxial state of stress, lead to a brittle fracture of the filaments.

3.5. Effect of coating on the crack–reinforcement interaction

When niobium foils were coated with Al_2O_3, the cracks in the laminated composites propagated in a manner similar to the uncoated

TABLE 1

Damage tolerance of the niobium-reinforced MoSi$_2$ matrix composites

| | Damage tolerance (MPa m$^{1/2}$) | | | |
	Uncoated	Al$_2$O$_3$ coated	ZrO$_2$ coated	Remarks
Laminated composites	15.5	14.0	8.6	Nb foil reinforcement
Fibrous composite	12.2			Nb filament reinforcement

ment composite was higher than the ZrO$_2$-coated niobium-foil-reinforced composite, which may again be related to the character of the interface bond.

4. Summary and conclusions

The main effort in this study was focused on the control of the reinforcement–matrix interface interactions as well as the interface mechanical properties in Nb–MoSi$_2$ composites. The approach was to coat the niobium reinforcements with inert diffusion barriers. A chemical compatibility study of MoSi$_2$ with Al$_2$O$_3$ as a potential coating material showed that they are chemically compatible in the absence of SiO$_2$ impurity particles. The presence of SiO$_2$ was found to cause extensive reaction between the second phase (SiO$_2$) and Al$_2$O$_3$. ZrO$_2$ and mullite were also found to be chemically compatible with MoSi$_2$.

When Al$_2$O$_3$ and ZrO$_2$ coatings were applied on niobium prior to incorporation in MoSi$_2$, they were effective in eliminating niobium and molybdenum diffusion, and retarding the interaction between niobium and MoSi$_2$.

Investigation on the crack propagation in the niobium-reinforced MoSi$_2$ composite indicated that the matrix cracked at a load level considerably below the peak load of the load–displacement curve. This early crack propagation through the matrix is believed to be due to low elastic modulus of the niobium reinforcement compared with that of the matrix and the strain compatibility requirements in the composite. Thus it was suggested that the fracture toughness of the composite determined from the peak load of the four-point bending test should be interpreted as

an indicator of the damage tolerance of the composite.

Composites containing uncoated and Al$_2$O$_3$-coated niobium foils showed an improved damage tolerance, with K_{Ic} around 14–15 MPa m$^{1/2}$. On the contrary, the composites reinforced by ZrO$_2$-coated niobium foils showed a lower damage tolerance (8.6 MPa m$^{1/2}$) with a brittle cleavage fracture of the foils.

The geometry of the reinforcements was also found to affect the crack propagation in the matrix. In the laminated composites, the crack propagation was discontinuous, leading to a stepwise crack propagation of a primary crack and nucleation of secondary cracks. On the contrary, the crack in a fibrous composite propagated continuously on one plane, and the filaments failed in a brittle cleavage manner.

References

1 E. Fitzer, in R. A. Bradley, D. E. Clark, D. C. Larsen and J. O. Stiegler (eds.), *Whisker- and Fiber-Toughened Ceramics*, American Society for Metals. Metals Park, OH, 1988, 165.
2 C. K. Elliott, G. R. Odette. G. E. Lucas and J. W. Sheckherd, *DARPA Annu. Rep.*, 1987 (University of California, Santa Barbara. CA) (Defense Advanced Research Projects Agency Contract).
3 L. S. Sigl, P. A. Mataga, B. J. Dalgleish, R. M. McMeeking and A. G. Evans, *Acta Metall.*, 36 (1988) 945–953.
4 S. Kunz-Douglass, P. W. R. Beaumont and M. F. Ashby, *J. Mater. Sci.*, 15 (1980) 1109–1123.
5 L. Xiao, Y. S. Kim and R. Abbaschian, *Intermetallic Matrix Composites, Proc. Materials Research Society Spring Meet., San Francisco, CA, April 16–21. 1990*, Materials Research Society, Pittsburgh, PA, 1990. p. 399.
6 A. G. Metcalfe and M. J. Klein. *Composite Materials*, Vol. 1, *Interfaces in Metal Matrix Composites*, Academic Press, New York, 1974, p. 146.
7 J. D. Cotton, Y. S. Kim and M. J. Kaufman, *Mater. Sci. Eng.*, 144 (1991) 281.
8 W. D. Kingery, H. K. Bowen and D. R. Uhlman, *Introduction to Ceramics*, Wiley, New York, 1976, p. 240.
9 D. G. Munz, J. L. Shannon. Jr., and R. T. Busey, *Int. J. Fracture*, 16 (1980) R137–141.

Control of the Interfacial Reactions in Nb-Toughened MoSi₂

Leon Shaw* and Reza Abbaschian*

Department of Materials Science and Engineering, University of Florida, Gainesville, Florida 42611

Toughening of MoSi₂ for high-temperature applications can be achieved by incorporating ductile refractory-metal reinforcements, provided that a coating is applied to prevent interdiffusion and reaction between the matrix and the reinforcements. In the present study, three different coating techniques for applying a thin Al₂O₃ film on Nb reinforcements as a diffusion barrier have been studied. The techniques consisted of (i) sol–gel coating; (ii) physical vapor deposition (PVD); (iii) hot dipping in molten Al, followed by anodizing Al to form Al₂O₃. The processing parameters for the techniques were evaluated and the effectiveness of each coating as a diffusion barrier was assessed. For the present MoSi₂ matrix which contains SiO₂, PVD coatings provided the most effective diffusion barrier for processing MoSi₂/Nb composites.

I. Introduction

AMONG intermetallics, MoSi₂ is one of the most promising candidates for high-temperature structural applications. It has a higher melting point (2020°C) than other intermetallics, such as the aluminides of iron, nickel, and titanium, and has excellent resistance to oxidation and hot corrosion up to 1500°C. Its density is 6.26 g/cm³, nearly 25% lower than that of the nickel-base superalloys. However, like other intermetallics, a major problem which impedes the use of MoSi₂ as a high-temperature structural material is its brittleness at low temperatures. Therefore, to make MoSi₂ a viable structural material, its low-temperature fracture toughness must be improved.

Numerous studies have shown that fracture toughness of brittle matrices can be improved by the incorporation of a ductile second phase.[1-11] Niobium is a suitable ductile reinforcement for MoSi₂ because of its high melting temperature and thermal expansion coefficient close to that of MoSi₂, reducing the potential for matrix cracking upon thermal cycling during processing and in service. Our previous studies[12-14] and other results[15,16] have demonstrated that such a composite system indeed exhibits a substantial increase in toughness compared to the matrix alone. However, a major problem in using such a composite system is the reactions between the matrix and ductile reinforcement at high temperatures, which lead to the formation of brittle interfacial products.[12-14,17-19] The formation of the interfacial compounds on continuous ductile phases degrades the toughening effect[20] by introducing notch effect. Therefore, using an inert diffusion barrier coating on the reinforcement prior to processing of the composites is essential to reduce the interfacial reactions during processing, as well as to maintain the integrity of the reinforcements at elevated service temperatures.

Although several attempts have been made to apply inert diffusion barrier coatings in MoSi₂/Nb composites,[12,14,17,19] none have succeeded in completely eliminating the formation of interfacial reaction products. The present study was aimed at developing a feasible processing method to apply Al₂O₃ coatings onto the surface of Nb to minimize interfacial reactions between MoSi₂ and Nb at high temperatures. Al₂O₃ is chemically compatible with MoSi₂ up to 1700°C[21] and with Nb up to 1500°C.[9,22] It also has a thermal expansion coefficient close to those of both MoSi₂ and Nb, thus reducing the potential of interfacial crack initiation upon thermal cycling during processing and in service. Three coating methods were evaluated in the present study: (i) sol–gel coating; (ii) physical vapor deposition, using electron-beam-heated Al₂O₃ sources; and (iii) hot dipping Nb in molten Al, followed by anodizing Al to form Al₂O₃. The process control parameters and the effectiveness of each coating as a diffusion barrier were assessed.

II. Experimental Procedure

(1) Sol–Gel Coating Technique

The sol solution for the present study was an aluminum-alkoxide-derived sol (using aluminum-sec-butoxide (ASB)), hydrolyzed in excess water and peptized with aluminum nitrate, Al(NO₃)₃. The procedure for preparing the sol solution was discussed in detail by Clark et al.[23] The ratio of aluminum nitrate to ASB in the sol was from 0.04:1 to 0.07:1, a range which has been reported to produce the minimum volume gel with the highest solid concentration.[24] Solutions with ratios of water to ASB ranging from 100:1 to 25:1 were prepared to evaluate the effect of excess water on the quality of the coating. The compositions of the sols used are summarized in Table I. Glycerol was added to some sol solutions to improve the flexibility of the dried gel.[25]

The sol–gel coatings were produced by dipping Nb foils into the sol solution for 5 s or by electrophoretic deposition on the Nb surface. For the latter technique, the Nb foil was kept parallel to the anode with a separation distance of 1 cm. A constant dc voltage ranging from 0.5 to 2 V was applied across the electrodes for a total coating time of 30 min for all the experiments. All coatings were applied within 24 h after the preparation of the sol to avoid aging of the sol. Once a coating was applied, the sample was withdrawn from the sol at a rate of 10 cm/s. The coated Nb foils were suspended vertically for 48 h at the ambient temperature before hot-pressing with MoSi₂ powder. Some air-dried Nb foils were further dried at 500°C for 1 h using a heating rate of 3°C/min.

(2) Physical Vapor Deposition

Physical vapor deposition (PVD) of Al₂O₃ on Nb was conducted using an evaporator (100-0030, Thermionics Laboratory, Hayward, CA) with an electron-beam-heated source, operating in 2 × 10⁻⁸ torr (~2.7 × 10⁻⁶ Pa) vacuum. The emission current was 200 mA with a potential difference of 3 kV between the cathode and the anode, resulting in a deposition rate of approximately 10 Å/s. By changing the deposition time, 1, 2, and 3 μm thick deposits were obtained.

(3) Hot Dipping and Anodizing

Hot dipping of Nb foils into a molten aluminum bath was conducted in an alumina crucible kept inside a resistance-heated furnace. Aluminum used for preparing the molten bath

had a nominal purity of 99.999 wt% based on metallic constituents. Two different bath temperatures, 930° and 870°C, were chosen to evaluate the effects of the molten metal temperature on the thickness and uniformity of the coating. Dipping time varied from 2 to 5 min, depending on the bath temperature used. All samples were withdrawn from the bath at a rate of ~10 cm/s.

Anodizing of the hot-dipped Nb foils was conducted in an electrolyte containing 5 wt% of sulfuric acid. The process was conducted at ambient temperature, and a constant dc voltage ranging from 10 to 20 V was applied to produce current densities ranging from 5 to 25 mA/cm². Anodizing time was 30 min for most operating conditions.

(4) Fabrication of Laminated Composites

Commercially pure $MoSi_2$ powder (supplied by Johnson Matthey Inc.) was used in the present study. The median powder particle size was 1.12-μm diameter, determined by centrifugal photosedimentation. The composition reported by the vendor was Mo > 61.0%, Si 36.6%, C 0.06%, N 0.03%, O 1.22%, and metallic impurities <0.5% (in weight percent). X-ray diffraction (XRD) analysis showed only $MoSi_2$ peaks (Cu$K\alpha$ radiation, 2θ angles from 5° to 100°), indicating other phases, if present, were below the volume fraction detectable by XRD or were amorphous, such as amorphous SiO_2 thin films on the surface of $MoSi_2$ powder.

The coated and uncoated Nb foils were stacked with the $MoSi_2$ powder and vacuum hot-pressed at 1400°C for 1 h using a pressure of 40 MPa. Some of the PVD-coated Nb foils were hot-pressed between $MoSi_2$ plates which were sliced from the hot-pressed $MoSi_2$ disks and finish polished with 1-μm diamond paste. This allowed an assessment of the mechanical damage to the thin coating during the hot-pressing with the powdered matrix.

III. Results and Discussion

(1) $MoSi_2$/Uncoated Nb Composite

Detailed discussion of the reaction products formed at the $MoSi_2$/uncoated Nb interface under these processing conditions has been described in Ref. 14. In order to facilitate discussion of the current study, the previous results are briefly described below. It was shown that uncoated Nb reacted extensively with $MoSi_2$, forming various intermetallic compounds, depending on the processing conditions. The microstructure and compositional profiles of a $MoSi_2$/uncoated Nb interface hot-pressed at 1400°C are shown in Fig. 1. For this processing condition, the reaction zone consisted of three intermetallics:

$$Nb\|Nb_5Si_3\|(Nb,Mo)Si_2\|(Mo,Nb)_5Si_3\|MoSi_2$$

However, while Nb_5Si_3 and $(Nb,Mo)Si_2$ had formed as continuous layers, $(Mo,Nb)_5Si_3$ existed as discrete islands distributed in the $MoSi_2$ adjacent to $(Nb,Mo)Si_2$. Most of the $(Mo,Nb)_5Si_3$ islands tended to form around the dark areas shown in Fig. 1, which were either porosity or SiO_2. The thickness of the reaction zone was about 30 μm. The composition of the reaction products depended on the processing temperature and time. For example, when the hot-pressing temperature was 1700°C, only $(Nb,Mo)_5Si_3$ formed, instead of the three intermetallics, Nb_5Si_3, $(Nb,Mo)Si_2$, and $(Mo,Nb)_5Si_3$, formed at 1400°C. This temperature dependence of the reaction products has been attributed to the hypothesis that diffusion of Mo and Nb becomes competitive with diffusion of Si at the higher temperatures.[14]

(2) Coating via Sol–Gel Technique

The interfacial microstructures of electrophoretically sol-gel-coated Nb-reinforced $MoSi_2$ composites are shown in Figs. 2 and 3. The latter had the same processing conditions as Fig. 2(c), but was taken from a region where there was a relatively long continuous alumina coating. There are several
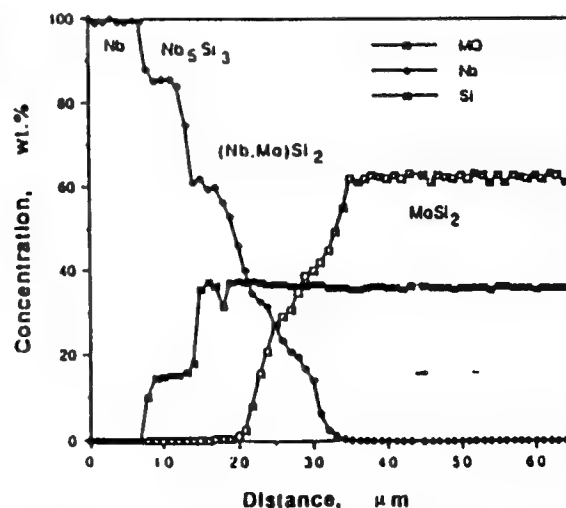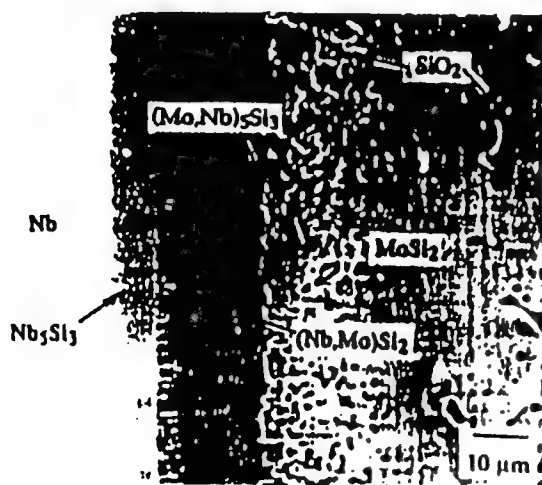
Fig. 1. Microstructure and composition profile of a $MoSi_2$/uncoated Nb interface hot-pressed at 1400°C, 40 MPa for 1 h.

was approximately 5 μm, only Nb$_5$Si$_3$ formed, whereas Nb$_5$Si$_3$, (Mo,Nb)Si$_2$, and (Mo,Nb)$_5$Si$_3$ formed during consolidation of uncoated Nb (Fig. 1). Finally, if the coating was continuous and thick enough (Fig. 3), the reaction between MoSi$_2$ and Nb could be effectively limited.

The degradation of the coatings was likely due to the presence of SiO$_2$ in the matrix. The existence of SiO$_2$ in the present specimens has been found by compositional analysis with an electron microprobe as shown in Fig. 1 and confirmed with transmission electron microscopy in a related study.[?] Most of SiO$_2$ resided at triple points and grain boundaries after consolidation.[?,?] A related study[?] also showed that in MoSi$_2$/Al$_2$O$_3$ particle composites, when a SiO$_2$ particle was adjacent to Al$_2$O$_3$, a relatively wide interface (~7 μm) formed between MoSi$_2$ and Al$_2$O$_3$, whereas a sharp interface (~1 μm) formed when MoSi$_2$ contacted Al$_2$O$_3$ directly. In the present case, therefore, the degradation of the coating was partially due to the reaction between the Al$_2$O$_3$ coating and SiO$_2$ particles at the region where the two were in contact. Another reason for the breakdown of the continuous coating could be cracking during drying and firing of the gel. When the coating was thick (> ~4 μm), as in the cases of Fig. 2(b) and (c), cracking occurred more readily during drying and firing in the furnace or even during the air drying for the case of Fig. 2(c). The addition of glycerol prevented cracking somewhat when the coating was thin, but not when it was thick. Thus, the discontinuity of the coating is primarily attributed to the attack of SiO$_2$ in the case of thin coatings and additional cracking during the drying and firing in the case of thick coatings.

The reduction in the thickness and nature of the interfacial compounds formed can be attributed to the retardation of Si diffusion and the suppression of Nb and Mo diffusion across the coating. Suppression of Nb diffusion across the coating led to the absence of reaction at the MoSi$_2$ side of the oxide coating, whereas suppression of Mo diffusion resulted in formation of only the binary silicide, instead of the ternary compound, at the Nb side. Moreover, the reduced Si diffusion across the coating favored the formation of Nb-rich binary compounds, such as Nb$_5$Si$_3$ instead of NbSi$_2$. As has been discussed in Section III(1), a similar situation arose when the availability of Nb at the reaction site became enhanced as temperature increased from 1400° to 1700°C. In contrast, when the coating was thin or there were discontinuities along the coating, the interfacial reaction product was no longer single phase, but contained at least two phases, Nb$_5$Si$_3$ and (Nb,Mo)Si$_2$, particularly near the discontinuous points.

In the presence of SiO$_2$, a thick and continuous coating is necessary, as indicated in Fig. 3. Thus, it seems that a low water/ASB ratio is more favorable. However, there is a limit to the water/ASB ratio below which bulk gelation occurs readily and AlO(OH) hardens, not responding to the electric field.[?] Therefore, there is an optimum ratio which allows for an adequate thickness of the coating without bulk gelation. For the present study, this ratio was found to be 25:1, indicated as solution SG5 in Table I. However, the cracking problem associated with the thick coating still presents a formidable processing challenge which is yet to be solved.

No obvious effect of the ratio of aluminum nitrate to ASB on the quality and thickness of the coating was observed for the two ratios investigated. Finally, the Al$_2$O$_3$ coating formed using the dip-coating technique was thinner and more porous than that produced via electrophoresis.

(3) Coating via Physical Vapor Deposition

The microstructures of MoSi$_2$ plates diffusion-bonded to PVD-coated Nb with different thicknesses of the alumina coating are shown in Fig. 4. Reaction products were detected in all cases. However, the thickness of the reaction zone was reduced dramatically from ~30 μm for uncoated samples (Fig. 1) to 15, 5, and 1 μm for PVD-coated samples with a coating of 1, 2, and 3 μm thicknesses, respectively. As the thickness of the coating increased, the capability to limit Si diffusion increased and the

(Nb,Mo)Si$_2$ layer thickness was reduced. A 2-μm coating was effective in eliminating the (Nb,Mo)Si$_2$ layer, and a 3-μm coating nearly eliminated Nb$_5$Si$_3$ formation except at local breakage in the coating. The comparison in Fig. 5 shows that the composites could also be processed using powdered MoSi$_2$ without obvious damage to the PVD coatings. Note that degradation of the coatings occurred even for the interfaces processed using polished MoSi$_2$ plates, suggesting that the degradation was most likely due to the presence of SiO$_2$.

Comparing the PVD and sol–gel coatings, the former had a much more effective Al$_2$O$_3$ barrier than the latter. In the case of sol–gel coating, the reaction zone thickness was reduced to ~1 μm only when the coating thickness reached ~10 μm. For the PVD coating, the same reaction zone thickness was observed when the coating thickness was ~3 μm. The reduction in the zone thickness is attributed to the significantly greater density of the coatings produced by PVD.

(4) Coating via Hot Dipping and Anodizing

The hot dipping of Nb into a molten aluminum produced a sharp Al/Nb interface. The compositional analysis indicated negligible interdiffusion between Al and Nb and no oxygen at the interface. The thickness of the aluminum coating produced ranged from 25 to 40 μm. Hot dipping at 870°C for 5 min produced similar coatings as hot dipping at 930°C for 2 min except that the uniformity of the coating was reduced. Figure 6 shows the microstructure and composition profile of a hot-dipped Nb after anodization with a current density of ~14 mA/cm^2 for 30 min. As seen in the figure, aluminum has been converted to alumina, and the thickness of the coating has been reduced from ~30 μm to ~10 μm. Moreover, the interface remains clean and sharp after the anodization.

Figure 7 shows the variation with time of the current density and thickness of the alumina formed for anodizing pure aluminum plates (99.999 wt%) under a constant voltage. As expected, the thickness of the alumina increased with time rapidly at the early stage of anodizing, but slowed down after about 30 min, suggesting that the alumina approached a limit thickness asymptotically for a given voltage. Correspondingly, the current density decreased rapidly at the early stage of the anodizing, and leveled off when the alumina became thick. The effect of current density on the thickness of the oxide film is summarized in Table II. As seen in the table, increasing the current density increased the thickness of the oxide film. The current density dependence of the limit thickness suggested that the oxide film formed dissolved in the electrolyte during anodizing, and the limit thickness was a result of the rate of dissolution matching the rate of formation. These results are in agreement with the literature.[?,?]

When anodizing the hot-dipped Nb, the situation was complicated by the fact that the total thickness of the coating, i.e., the (Al + Al$_2$O$_3$) layer, on the surface of Nb became thinner as anodizing proceeded, because of the dissolution of the oxide in the electrolyte.[?] If the anodizing time was too long, the entire coating would dissolve, exposing interior Nb. If the anodizing time was too short, some Al remained unconverted, which would react severely with Nb in the subsequent consolidation. Therefore, when anodizing the hot-dipped Nb, it was necessary to take into account the decrease of the thickness of (Al + Al$_2$O$_3$) layer in addition to the effect of the current density on the thickness of the Al$_2$O$_3$ film. The present study showed that for a current density of ~12 mA/cm^2 and a 5 wt% sulfuric acid electrolyte, the rate at which the thickness of (Al + Al$_2$O$_3$) layer decreased was ~0.45 μm/min. Thus, knowing the thickness of Al from the hot dipping and the current density during anodization, it is possible to calculate the anodizing time to control the coating quality.

Figure 8 shows the microstructure and corresponding composition profile for a MoSi$_2$/anodized Nb interface. The Nb foil was hot dipped in the molten aluminum at 930°C for 2 min and anodized for 45 min with a current density of ~12 mA/cm^2. As seen in the figure, the thickness of the coating and reaction zone
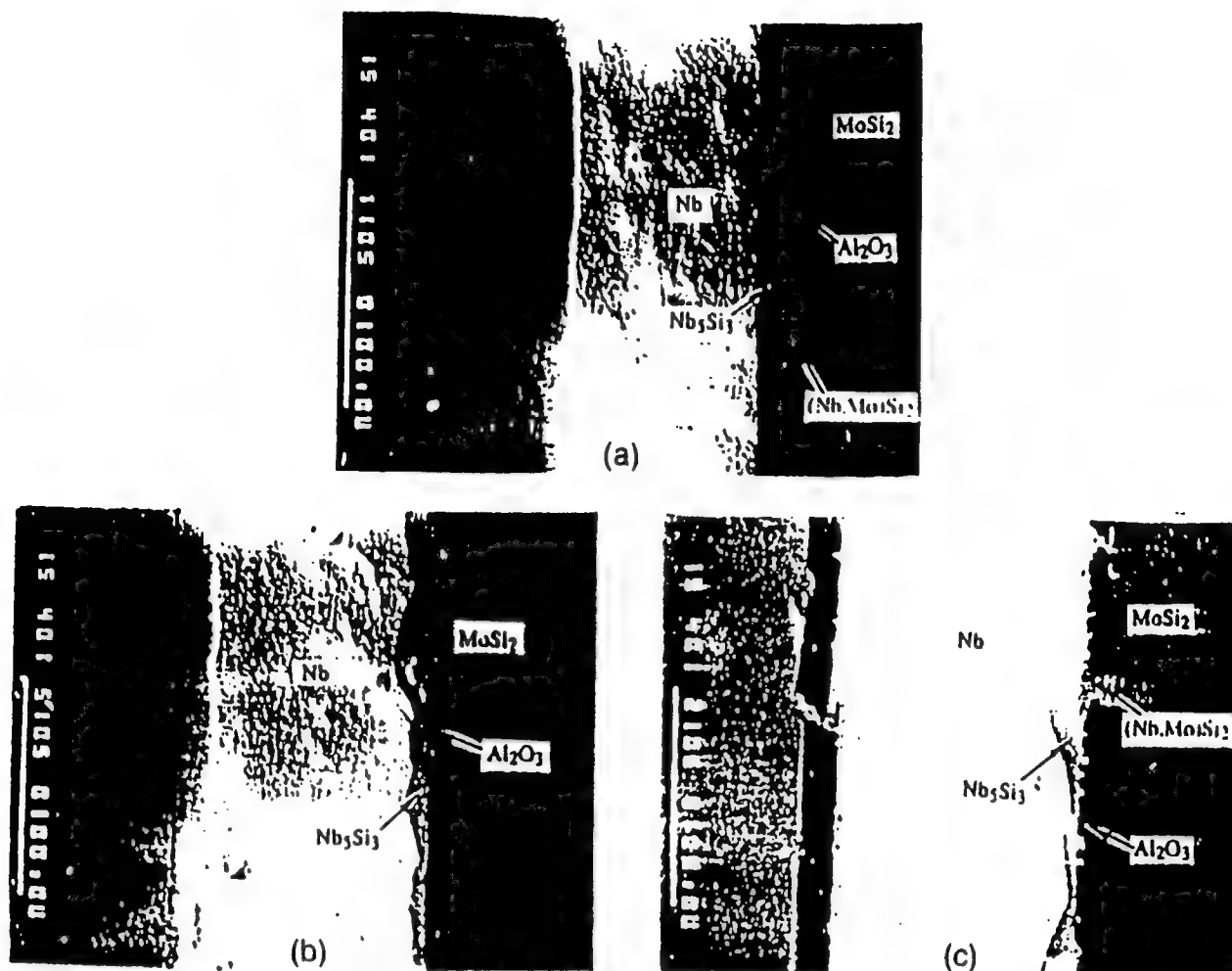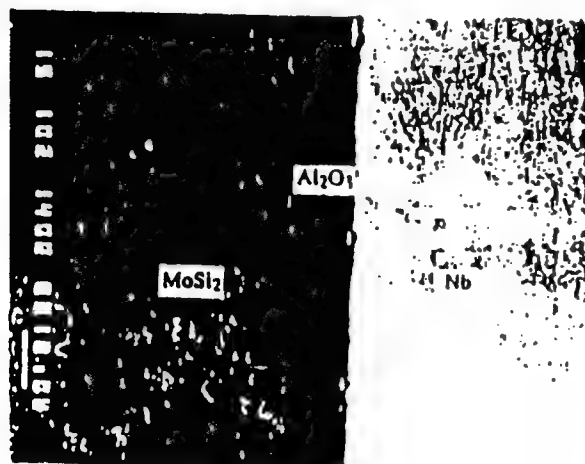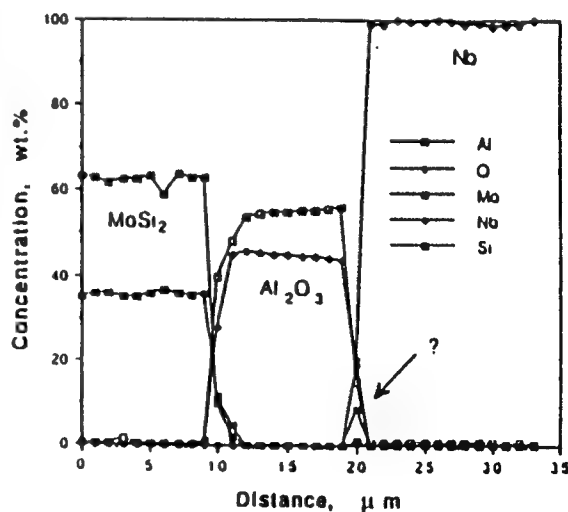
Fig. 2. Microstructures of MoSi₂/sol–gel-coated Nb interfaces hot-pressed at 1400°C, 40 MPa for 1 h. The ratios of H₂O:ASB and Al(NO₃)₃:ASB in the sols were (a) 100:1 and 0.04:1, (b) 50:1 and 0.04:1, and (c) 25:1 and 0.04:1.

prominent features in these figures. First, the thickness of the oxide coating increased with decreasing ratios of water to ASB, indicating that the higher the concentration of ASB, the higher the rate of the buildup of hydrated aluminum hydroxide colloids, AlO(OH), on the niobium surface. Second, the coatings degraded during the processing and became discontinuous, thus allowing direct contact and reaction between Nb and MoSi₂. Third, in spite of the degradation, the coatings reduced the thickness of the reaction zone between Nb and MoSi₂, e.g., from ~30 μm for uncoated samples to ~15 μm for the coated samples. Furthermore, as a result of the coating, the composition of the interfacial compounds changed. When the coating

Fig. 3. Microstructure and composition profile of a MoSi₂/sol–gel-coated Nb interface, hot-pressed at 1400°C, 40 MPa for 1 h. The coating had the same processing conditions as Fig. 2(c).
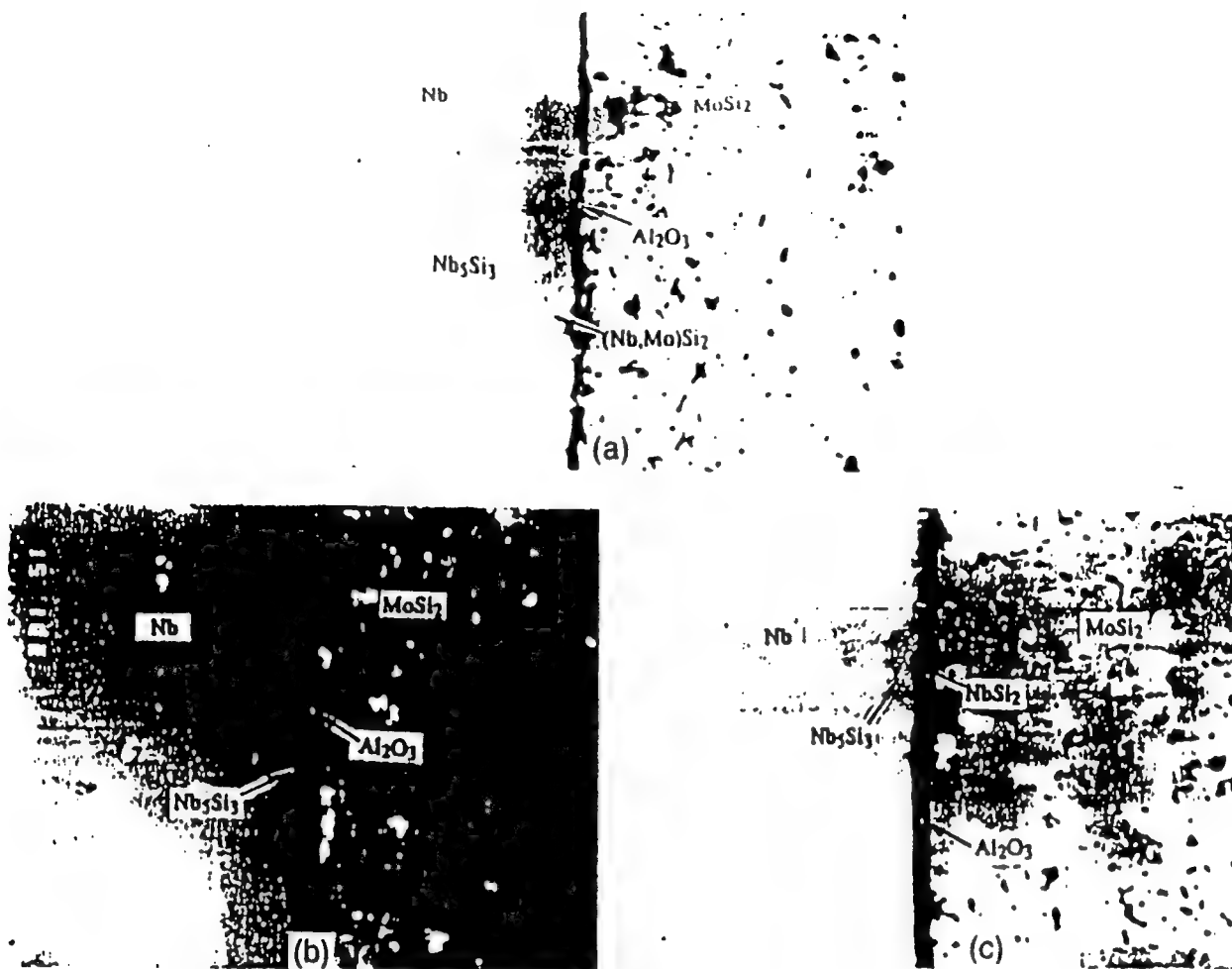
Fig. 4. Microstructures of MoSi$_2$/PVD-coated Nb interfaces, hot-pressed at 1400°C, 40 MPa for 1 h. (a) 1-μm Al$_2$O$_3$ coating; (b) 2-μm Al$_2$O$_3$ coating; (c) 3-μm Al$_2$O$_3$ coating.
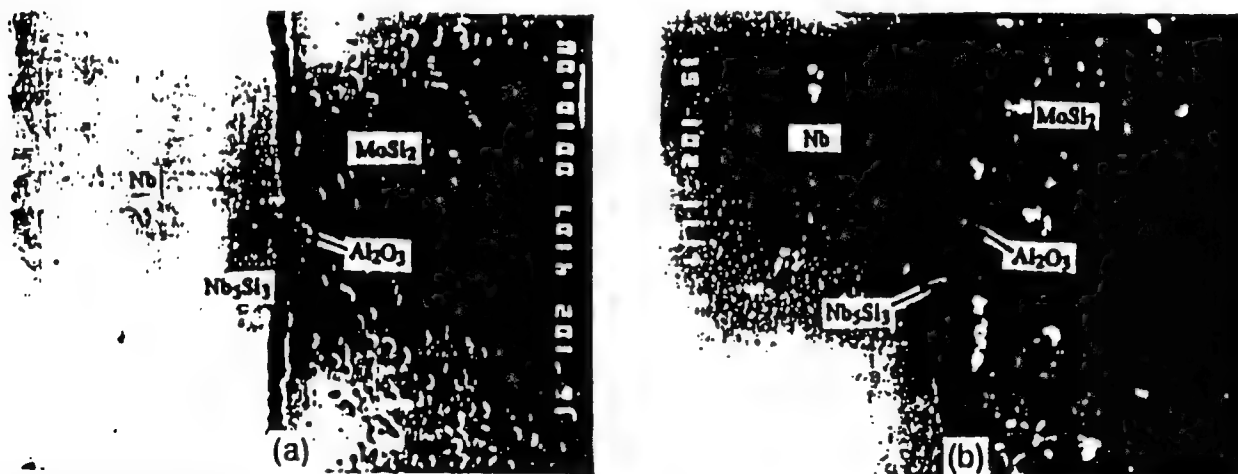
Fig. 5. Effect of the contact of the thin oxide coating with MoSi$_2$ powder and plates on the integrity of the coating. (a) The coating in contact with the powder; (b) the coating in contact with the prepolished plate.

was ~10 and ~4 μm, respectively. The reaction product at the Nb/Al$_2$O$_3$ interface was Nb$_5$Si$_3$, as observed with coatings derived by the sol–gel technique and physical vapor deposition. Note that, for the sol–gel coating technique, when the coating was ~10 μm, the reaction zone was limited to ~1 μm, indicat-

ing that the coating produced via sol–gel processing is denser than that produced via the hot dipping and anodizing. Anodizing current densities of 20 mA/cm^2 were also investigated, but the Al$_2$O$_3$ films produced were more porous and resulted in a thicker reaction zone.
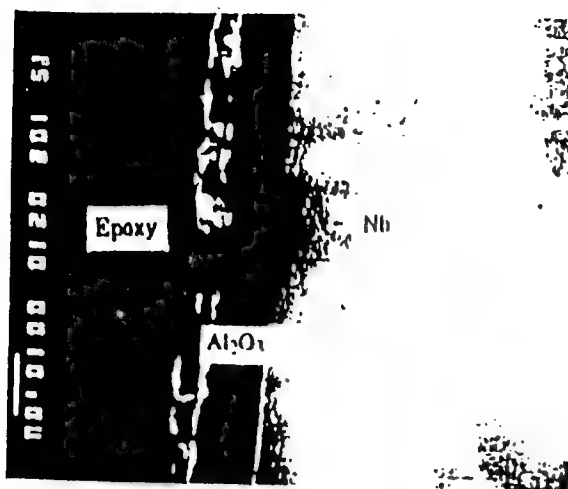
Fig. 6. Microstructure and composition profile of Al₂O₃/Nb interface after a hot-dipped Nb has been anodized with a current density of 14 mA/cm² for 30 min.
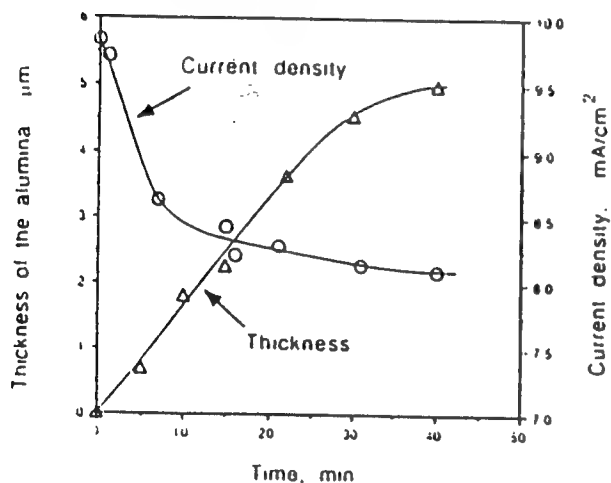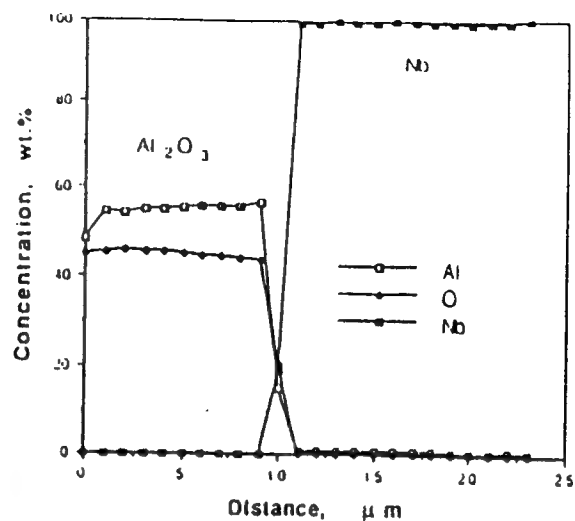
Fig. 7. Current density and thickness of the alumina film vs time during anodizing with a constant voltage.

Table II. Thickness of Al₂O₃ Layer as Function of the Current Density during the Anodizing of Pure Al Plates

Current density (mA/cm²)	Anodizing time (min)	Thickness (μm)
5–7	30	~2
8–10	30	~5
12–14	30	~10
23–25	30	~25

IV. Concluding Remarks

In the present study, three different coating techniques for applying thin Al₂O₃ coatings on Nb have been studied. The techniques were (i) sol–gel coating technique; (ii) physical vapor deposition of Al₂O₃; (iii) hot dipping the metal in molten Al, followed by anodizing Al to form Al₂O₃. Of the three techniques, PVD provided the most dense coating and was the most effective diffusion barrier for processing MoSi₂/Nb composites. Coatings formed by the hot dipping and anodizing were the most porous, while the sol–gel-derived coatings were cracked. Such defects promoted extensive formation of Nb₅Si₃. PVD coatings of 3-μm thickness effectively minimized the reaction product formation. The presence of SiO₂ in the MoSi₂ matrix
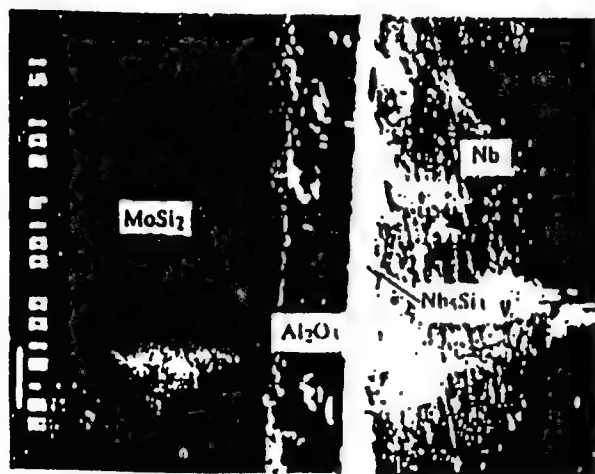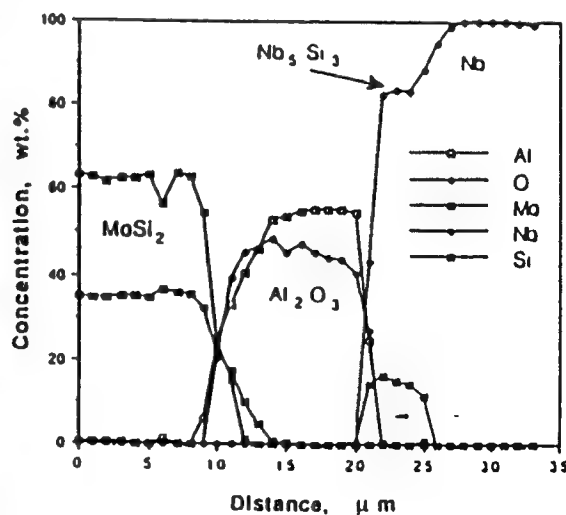

Fig. 8. Microstructure and composition profile of MoSi₂/anodized Nb interface. Processing condition: Nb foil was hot dipped at 930°C for 2 min, anodized with a current density of ~12 mA/cm² for 45 min, and finally hot-pressed with MoSi₂ at 1400°C, 40 MPa for 1 h.

can contribute to the dissolution of thin Al_2O_3 coatings and provide a significant source of silicon to react with the Nb reinforcement. Thus, improvements in matrix chemistry should be pursued to improve composite performance.

References

[1] L. Chermant and F. Osterstock, "Fracture Toughness and Fracture of WC-Co Composites," *J. Mater. Sci.*, 11 [10] 1939-52 (1976).

[2] C. O. McHugh, T. J. Whalen, and M. Humenik, Jr., "Dispersion-Strengthened Aluminum Oxide," *J. Am. Ceram. Soc.*, 49 [9] 486-91 (1966).

[3] A. V. Virkar and D. L. Johnson, "Fracture Behavior of ZrO_2-Zr Composites," *J. Am. Ceram. Soc.*, 60 [11-12] 514-19 (1977).

[4] D. T. Rankin, J. J. Stiglich, D. R. Petrak, and E. Ruh, "Hot-Pressing and Mechanical Properties of Al_2O_3 with an Mo-Dispersed Phase," *J. Am. Ceram. Soc.*, 54 [6] 277-81 (1971).

[5] P. Hing and G. W. Groves, "Strength and Fracture Toughness of Polycrystalline Magnesium Oxide Containing Metallic Particles and Fibers," *J. Mater. Sci.*, 7 [4] 427-34 (1972).

[6] V. V. Krstic, P. S. Nicholson, and R. G. Hoagland, "Toughening of Glasses by Metallic Particles," *J. Am. Ceram. Soc.*, 64 [9] 499-504 (1981).

[7] C. K. Elliott, G. R. Odette, G. E. Lucas, and J. W. Sheckherd, "Toughening Mechanisms in Intermetallic γ-TiAl Alloys Containing Ductile Phases"; pp. 95-102 in *High Temperature, High Performance Composites*. Proceedings of MRS Symposium. Edited by F. D. Lemkey, S. G. Fishman, A. G. Evans, and J. R. Strife. Materials Research Society, Pittsburgh, PA, 1988.

[8] M. F. Ashby, F. J. Blunt, and M. Bannister, "Flow Characteristics of Highly Constrained Metal Wires," *Acta Metall.*, 37 [7] 1847-57 (1989).

[9] H. C. Cao, B. J. Dalgleish, H. Deve, C. Elliott, A. G. Evans, R. Mehrabian, and G. R. Odette, "A Test Procedure for Characterizing the Toughening of Brittle Intermetallics by Ductile Reinforcements," *Acta Metall.*, 37 [11] 2969-77 (1989).

[10] H. E. Deve, A. G. Evans, G. R. Odette, R. Mehrabian, M. L. Emiliani, and R. J. Hecht, "Ductile Reinforcement Toughening of γ-TiAl: Effects of Debonding and Ductility," *Acta Metall. Mater.*, 38 [8] 1491-502 (1990).

[11] E. Fitzer, "Fiber Reinforced Ceramic Composites"; pp. 165-92 in *Whisker- and Fiber-Toughened Ceramics*. Edited by R. A. Bradley, D. E. Clark, D. C. Larsen, and J. O. Stiegler. ASM International, Metals Park, OH, 1988.

[12] L. Xiao, Y. S. Kim, R. Abbaschian, and R. J. Hecht, "Processing and Mechanical Properties of Niobium-Reinforced $MoSi_2$ Composites," *Mater. Sci. Eng.*, A144 [1] 277-85 (1991).

[13] L. Xiao, Y. S. Kim, and R. Abbaschian, "Ductile Phase Toughening of $MoSi_2$—Chemical Compatibility and Fracture Toughness"; pp. 399-404 in *Intermetallic Matrix Composites*, Proceedings of MRS Symposium. Edited by D. L. Anton, P. L. Martin, D. B. Miracle, and R. McMeeking. Materials Research Society, Pittsburgh, PA, 1990.

[14] L. Xiao and R. Abbaschian, "Interfacial Modification in $Nb/MoSi_2$ Composites and Its Effects on Fracture Toughness," *Mater. Sci. Eng.*, A155 [1] 135-45 (1992).

[15] L. Xiao, "Study of the Flow Behavior of Constrained Ductile Phases—II. Modeling"; pp. 359-69 in *Developments in Ceramic and Metal-Matrix Composites*. Edited by K. Upadhya. The Metallurgical Society, Warrendale, PA, 1992.

[16] L. Xiao, "Study of the Flow Behavior of Constrained Ductile Phases—I Experiment"; pp. 115-24 in *Developments in Ceramic and Metal-Matrix Composites*. Edited by K. Upadhya. The Metallurgical Society, Warrendale, PA, 1992.

[17] L. Xiao and R. Abbaschian, "Role of Matrix/Reinforcement Interface in the Fracture Toughness of Brittle Materials Toughened by Ductile Reinforcements," *Metall. Trans.*, 23A [10] 2863-72 (1992).

[18] T. C. Lu, A. G. Evans, R. J. Hecht, and R. Mehrabian, "Toughening of $MoSi_2$ with a Ductile (Niobium) Reinforcement," *Acta Metall. Mater.*, 39 [8] 1853-62 (1991).

[19] T. C. Lu, Y. G. Deng, C. G. Levi, and R. Mehrabian, "Y_2O_3 Coatings as Diffusion Barriers in $MoSi_2$–Nb Composites"; pp. 11-19 in *Advanced Metal Matrix Composites for Elevated Temperatures*. Edited by M. N. Guongor, E. J. Lavernia, and S. G. Fishman. ASM International, Metals Park, OH, 1991.

[20] A. G. Metcalfe and M. J. Klein, "Effect of the Interface on Longitudinal Tensile Properties"; pp. 125-68 in Composite Materials, Vol. 1, *Interfaces in Metal Matrix Composites*. Edited by A. G. Metcalfe. Academic Press, New York, 1974.

[21] J. L. Pentecost, "Coating Materials and Coating Systems"; pp. 10-109 in *High-Temperature Inorganic Coatings*. Edited by J. Huminik. Reinhold Publishing Corporation, New York, 1963.

[22] W. Mader and M. Ruhle, "Electron Microscopy Studies of Defects at Diffusion-Bonded Nb/Al_2O_3 Interfaces," *Acta Metall.*, 37 [3] 853-66 (1989).

[23] D. E. Clark, W. J. Dalzell, and D. C. Folz, "Electrophoretic Alumina Sol-Gel Coatings on Metallic Substrates," *Ceram. Eng. Sci. Proc.*, 9 [9-10] 1111-18 (1988).

[24] B. E. Yoldas, "Alumina Gels that Form Porous Transparent Al_2O_3," *J. Mater. Sci.*, 10 [11] 1856-60 (1975).

[25] J. J. Lannutti, "Applications of Alumina Gels"; M.S. Thesis, University of Florida, Gainesville, FL, 1984.

[26] J. D. Cotton, Y. S. Kim, and M. J. Kaufman, "Intrinsic Second-Phase Particles in Powder-Processed $MoSi_2$," *Mater. Sci. Eng.*, A144 [1] 287-91 (1991).

[27] J. P. A. Lofvander, J. Y. Yang, C. G. Levi, and R. Mehrabian, "Microstructural Development of $MoSi_2$ Fiber Composites Prepared by Slurry Processing Methods"; pp. 1-10 in *Advanced Metal Matrix Composites for Elevated Temperatures*. Edited by M. N. Guongor, E. J. Lavernia, and S. G. Fishman. ASM International, Metals Park, OH, 1991.

[28] S. Maloy, A. H. Heuer, J. Lewandowski, and J. Petrovic, "Carbon Additions to Molybdenum Disilicide: Improved High-Temperature Mechanical Properties," *J. Am. Ceram. Soc.*, 74 [10] 2704-706 (1991).

[29] R. B. Schwarz, D. R. Srinivasan, J. J. Petrovic, and C. J. Maggiore, "Synthesis of Molybdenum Disilicide by Mechanical Alloying," *Mater. Sci. Eng.*, A155 [1-2] 75-83 (1992).

[30] W. J. Dalzell, "Alumina Sol-Gel Coatings Formed by Electrophoretic Deposition"; M.S. Thesis, University of Florida, Gainesville, FL, 1988.

[31] R. M. Burns and W. W. Bradley, *Protective Coatings for Metals*; pp. 556-65. Reinhold Publishing Corporation, New York, 1955.

[32] *Metals Handbook*, Vol. 2, 8th ed; pp. 620-27. American Society for Metals, Metals Park, OH, 1964.

[33] G. C. Wood, "Porous Anodic Films on Aluminum"; pp. 167-279 in *Oxides and Oxide Films*, Vol. 2. Edited by J. W. Diggle. Marcel Dekker, New York, 1973.

BOOK II

Section 2

Mechanical Alloying

of

MoSi$_2$

Principal Investigator: **M.J. Kaufman**

Mechanical Alloying of MoSi$_2$

Principal Investigator: M. J. Kaufman

Objective

The objective of this work was to investigate the microstructure and property relationships in MoSi$_2$-based composites produced by mechanical alloying and to compare with those in similar composites produced using more conventional schemes such as powder mixing and subsequent consolidation. It was hoped that this mechanical alloying process might provide a means of producing MoSi$_2$ with enhanced mechanical properties and that processing might be achieved at lower temperatures; this was considered important for the production of fiber-reinforced materials where chemical and mechanical compatibility issues are critical factors and where high temperature excursions are undesirable.

Mechanical Alloying

The high melting point of MoSi$_2$ precludes conventional ingot metallurgy techniques for its synthesis due to problems associated with crucible wall reactions and high power requirements for those temperatures. Even conventional powder metallurgical techniques require relatively high processing temperatures. Our initial efforts were therefore aimed at reducing the consolidation temperature. Towards this end, solid state synthesis of stoichiometric MoSi$_2$ through the mechanical alloying of elemental Mo and Si powders was attempted, since it would achieve the dual objective of fine powder sizes (and therefore lower processing temperatures due to higher specific surface area of the powders) and room temperature compound synthesis with the desired stoichiometric control. Our results indicated that (1) mechanical alloying results in the formation of tetragonal MoSi$_2$ along with some hexagonal MoSi$_2$ and elemental Mo, (2) consolidation is possible as low as 1200°C to produce a material with submicron grain

sizes, and (3) that, although consolidation was complete at these temperatures, considerable amount of silica was incorporated into the material due to the high specific area of the powders, which tended to form a thin layer of oxide on their surfaces. As opposed to other siliceous materials such as SiC and Si_3N_4 where the silica displays a low dihedral angle and, consequently, a wetting behavior at the grain boundaries, the silica in $MoSi_2$ displays non-wetting characteristics and tends to spheroidize at triple junctions. Furthermore, the silica tends to coarsen with elevated temperature exposure and also limits grain growth by grain boundary (Zener) drag.

Silica Reduction

It was thought that the presence of silica would not be beneficial to the elevated temperature properties due to its softening characteristics at elevated temperatures above 1200°C. Continuous grain boundary glass films have been shown to promote Rachinger sliding (both liquid-enhanced sliding and solution-precipitation creep) with the resultant degradation in properties at elevated temperatures above the softening temperature. Unfortunately, little is known about the effect of a non-wetting, discrete, and discontinuous soft phases on the elevated temperature properties. Likewise, the presence of silica particles could potentially degrade the ambient toughness of the material.

Consequently, our efforts were focused toward the removal of silica from the material. It was felt that the elevated temperature properties of silica-free material needed to be addressed before efforts were made to improve the high temperature strength through compositing approaches. In addition, the issue of the DBTT of $MoSi_2$ was clouded by the softening effect of silica, and hence it was hoped that the processing of silica-free material would lend useful insights into the DBTT issue.

The well known, carbothermal reduction of silica was selected initially for the deoxidation process. Deoxidation was achieved simply through the addition of appropriate amounts of carbon powder to the elemental mixture of Mo and Si followed by mechanical alloying, since mechanical alloying would lead to the uniform dispersal of the deoxidant throughout the matrix. This combination led to the successful removal of silica and the formation of SiC via the reaction $SiO_2 + 3C \rightarrow SiC + 2CO(g)$. It should be pointed out that this scheme is effective and produces SiC which can be used

to enhance the mechanical properties of this compound as well as to lower its effective coefficient of thermal expansion (CTE) as desired for $MoSi_2$ matrix composites containing reinforcements with lower CTEs (e.g. Mo and Ta).

It should be emphasized that considerable care should be exercised while adding carbon to $MoSi_2$, as increasing carbon additions would cause the overall composition to diverge into the three phase $MoSi_2$ + SiC + Mo_5Si_3C (Nowotny) phase field. Furthermore, the product gases of the deoxidation (carbothermal reduction) reaction of silica such as (SiO?), CO, CO_2, must be effectively removed for complete deoxidation, as well as ensuring the processing of gas-pore free samples. Thus, the initial process of forming oxygen-free $MoSi_2$ would involve a vacuum hot pressing operation, although secondary operations such as hot isostatic pressing (HIP) could be carried out subsequent to hot pressing. In addition the dissociation tendencies of the silicide at elevated temperature dictated additional refinements in processing, and these are outlined in [11,13].

SUMMARY OF ACCOMPLISHMENTS

A novel processing method utilizing the combination of mechanical alloying, carbothermal reductions, and carbon additions was developed in the preceding years to synthesize silica-free $MoSi_2$ and $MoSi_2$/SiC composites[1-3,5,11,13,14]. The studies during the past year have been directed toward meeting the following objectives:

(1) Optimization of the processing sequence for various compositions corresponding to increasing volume fractions of silicon carbide in $MoSi_2$ and determination of the maximum SiC loading possible.

(2) Characterization the phase evolution sequences for the various compositions as a function of alloying time and consolidation temperature in particular, for differences associated with increasing carbon content.

(3) Extension of the processing rationale to the fabrication of silica-free, transition metal silicide/SiC and alloy silicide/ SiC system.

(4) Applications to fiber-reinforced composites processing by tailoring the matrix CTEs

(5) Mechanical property characterization.

(1) Process optimization:

Using the processing strategy outlined in [2,4,5,11,13], $MoSi_2/SiC$ composites with varying SiC contents have been fabricated. Thus far, silica-free composites with silicon carbide loadings of up to 60 v/o, and with a minimal amount of the Nowotny (CMo_5Si_3) phase have been fabricated successfully. Furthermore, near-theoretical densification has been achieved in these composites, with the open porosity being limited to 1% or less. The SiC reinforcement size in all the above composites is typically of the order of 1 μm.

In view of the tendency of the silicide to dissociate at elevated temperatures and under low total pressures, considerable modifications were made to the processing method, as outlined in references [11] and [13].

(2) Characterization of the phase evolution sequences:

A combination of DTA/TGA and x-ray diffraction (XRD) techniques have been utilized to study the phase evolution sequences during mechanical alloying and consolidation. Significant differences have been noted in the microstructural evolution sequence with changes in the nominal powder composition. For instance, while intermetallic formation during mechanical alloying is predominant for the lower carbon content alloys, the high carbon alloys evolve by initially forming carbides (such as molybdenum and silicon carbide) during mechanical alloying. These, in turn, lead to significant differences in the phase evolution sequence during powder consolidation. These findings are elaborated in [4].

(3) Extension of the processing rationale to other silicide systems:

(a) Alloy silicide/ SiC system:

The extension of the processing scheme to other alloy silicide/silicon carbide composites has also been attempted. Since $MoSi_2$ and WSi_2 are isomorphous, *in-situ* composites of the $(Mo,W)Si_2/SiC$ system, with W substituting for Mo in the disilicide, have been produced. Further improvements in the high temperature strength are anticipated in this system due to the synergistic effects of solid solution strengthening and dispersion strengthening. Thus far, silica-free $(Mo,W)Si_2/SiC$ composites with 20

v/o SiC, containing 25 and 50 mole percent of WSi_2 in the matrix have been synthesized successfully. The mechanical alloying approach makes it possible to vary the alloying levels (in the matrix) and the SiC content (in the composite) independently. Room temperature strength and fracture properties of the *in-situ* $(Mo_{0.5}W_{0.5})Si_2/20$ v/o SiC composites were characterized and compared against monolithic $(Mo_{0.5}W_{0.5})Si_2$ of similar grain size processed by mechanical alloying. Details of the processing of these composites along with the room temperature mechanical property characterization are found in [7]. The higher density of WSi_2 necessitates any property improvements to be considered on a density-compensated basis.

(b) Other transition metal silicide/ SiC systems:

In addition to the Mo-W-Si-C system, ternary phase equilibria data of many other transition metal- silicon-carbon systems reveal striking similarities to the Mo-Si-C system (see Fig. 1). Since many of these systems share the same processing-related difficulties such as high silicon dissociation pressures and silica contamination that are typical of the Mo-Si-C system, it was decided to extend the *in-situ* composite processing rationale, as outlined in earlier reports [2,11,13], to these systems. This was all the more important since some systems such as $TiSi_2$-SiC are thought to have potential electronic substrate applications. Thus far, we have successfully fabricated *in-situ* $NbSi_2$/SiC, $TaSi_2$/SiC, $ZrSi_2$/SiC, and $TiSi_2$/SiC composites, all with SiC loadings of 20 v/o. Details regarding the processing and microstructures are forthcoming in [9,13].

(4) Applications to fiber-reinforced composites processing by tailoring the matrix CTEs

As outlined in [2], one of the major problems precluding the development of fiber reinforced composites is the cracking of the matrix due to the CTE mismatch between the matrix and the fiber. While one solution is to reduce the magnitude of the mismatch stresses by reducing the reinforcement size, another involves reducing the overall matrix CTE through the addition of a second phase having a lower CTE than the matrix. Through the precise control of the powder composition so as to lie along the two-phase field between $MoSi_2$ and SiC by mechanical alloying and *in-situ* displacement reactions, we have been able to produce composite matrices with differing

amounts of SiC, thereby varying the overall CTE accordingly. One thus tailors the initial powder alloy composition depending on the CTE of the reinforcement being used. Thus the production of CTE tailored, fiber-reinforced composites is a one-step process involving the hot consolidation of the prealloyed powder and the desired fiber, instead of having to contend with an additional step involving the dispersion of a CTE lowering reinforcement. In the case of $MoSi_2$, the matrices thus derived are also silica-free, thus enhancing the efficacy of the process. Fig. 2 shows the experimental dilatometric data derived from mechanically alloyed powders corresponding to 50 and 60 v/o SiC reinforcement. The literature data of $MoSi_2$ and SiC are also shown for comparison.

(5) Mechanical property characterization:

Efforts were made to evaluate the ambient and elevated temperature properties of the silica-free $MoSi_2$/SiC composites and to compare them with composites processed by conventional blend and consolidate techniques. It was anticipated that the absence of the grain boundary silica and the presence of micron-sized SiC will lead to improved elevated temperature strengthening due to increased resistance to grain boundary sliding and potential dispersion strengthening effects [2]. The effect of the intergranular silica particles on the room temperature fracture was also investigated.

Two classes of $MoSi_2$/SiC composites were studied in the course of this investigation. The first group of materials was fabricated using conventional "blend and consolidate" approaches, wherein starting powders of $MoSi_2$ (Johnson Matthey, -325 mesh) and SiC (Cerac, average size 1 μm) were blended in ratios corresponding to the target reinforcement volume fraction in the composite. Since no attempt was made to limit oxygen pickup during fabrication, these composites had significant amounts of silica (~5v/o) in them. The second group of materials were the silica-free $MoSi_2$/SiC composites prepared through mechanical alloying and in-situ displacement reactions. Details regarding the processing of these materials are reported elsewhere [2,5].

(a) Room Temperature Fracture Measurements

Room temperature fracture toughness measurements were conducted on in-situ

and conventionally processed composites containing 20 and 40 v/o SiC particulate reinforcements in order to elucidate the effect of SiC loading and the intergranular glass phase on the room temperature properties. Monolithic $MoSi_2$ derived from commercially available powders (Johnson Matthey, -325 mesh) was also used in these studies as a baseline for comparison. Evaluations were conducted at room temperature using the Indentation Crack Length method, Strength Indentation method and fractographic techniques. The details of these experiments and the results obtained are described in [6].

(b) High Temperature Measurements:

These measurements were primarily made to elucidate the effect of the intergranular phase on the elevated temperature properties of the $MoSi_2$/SiC composites. Testing was confined to reinforcement loadings of 20 v/o SiC. It should be mentioned that efforts were made to keep the $MoSi_2$ grain size and reinforcement size consistent between the CP and ISP samples in order to derive meaningful and valid comparisons.

(i)   Fracture Measurements:

In view of the two classes of microstructures tested (silica-free and silica-containing) and possible notch radius effects on measured fracture toughness values, the controlled surface flaw (indent strength in bending) technique was used to follow the trends in fracture behavior as a function of temperature. An additional advantage of the surface flaw technique is that the strength characteristics of the material are also obtained in addition to the toughness. The indent strength technique also has the added advantage of simulating service flaws that would normally occur in the material.

For the fracture toughness measurements, rectangular bars of nominal dimensions 4 x 3 x 25 mm were electro-discharge machined from hot pressed billets for four point flexure testing. The surfaces of the bars were polished and chamfered. The prospective tensile faces of each test bar were polished to 1 μm diamond finish, and were indented with a 25 Kg Vickers indent, such that the diagonal (hence one of the radial-median cracks) was perpendicular to the tensile axis. The residual stresses associated with the indent were subsequently removed by annealing the indented bars at 1300°C (150°C

above the highest test temperature) for 1 hour under a vacuum of 10^{-3} torr or better. Besides relieving the residual stress around the indent, the annealing treatment insured the elimination of microstructural variations due to varying test temperatures. Thus, strength variations for comparable flaw sizes were studied as a function of test temperature for both classes of materials, without the added concerns of flaw size distributions and their effects. The results (showing the variation of indented and annealed strength vs. temperature) are shown in Fig. 3. Additional fractographic analyses of the fracture surfaces are currently being undertaken to determine the flaw sizes and, hence, the toughnesses and these will be published elsewhere [8]. Since the indent loads were the same for all the samples, the flaw sizes are likely to be nearly identical, and hence, as a first approximation, the trends in strengths can be taken to roughly represent the trends in toughness. It is seen that the strengths are almost constant throughout the entire test temperature range, up to the DBTT. Furthermore, the silica-free material shows a lower strength (hence a lower toughness) than the silica-containing material over the entire range of test temperatures. These trends in toughness conform to our earlier measurements, and possible explanations are given elsewhere [5]. The toughnesses are seen to taper off at higher temperatures, but the magnitude of these changes suggests that this drop-off could most probably be attributed to changes in the modulus rather than changes in the microstructure.

(ii)   Bend Strength Measurements:

Flexure strength measurements were conducted on four-point bend bar specimens having nominal dimensions of 4 x 3 x 25 mm, with an inner span of 10 mm and an outer span of 20 mm, using SiC test fixtures. These tests spanned the temperature range from 1200°C to 1400°C. In all cases, the specimens displayed yield characteristics and elongations between 5-10% (outer fiber) under constant load (hence constant outer fiber stress). A typical load-displacement curve obtained in the ductile regime is shown in Fig. 4. All tests were conducted at a constant crosshead speed of 50.8 µm/minute, under flowing argon. The results of the yield stress and flow stress variations of both classes of materials are shown in Figs. 5 and 6. The silica-free material displayed a higher strength than the silica-containing material over the entire temperature range. The

activation energy derived from the flow stress measurements is ~ 97 kJ/mole for the silica-free material, and ~ 84.5 kJ/mole for the silica-free material. These values are far lower than the activation energies reported in the literature which were derived from creep experiments.

(iii)   Compression Tests (Single Strain Rate and Strain Rate Change Tests):

These tests were conducted on the ISP and CP composites (MoSi$_2$/20SiC), primarily to check for the possibility of superplasticity, as well as to gain insight into the deformation mechanisms both in the presence and absence of the intergranular glass phase. The results of these experiments, as well as their implications are discussed in an accompanying report [10].

Publications:

1. S. Jayashankar and M. J. Kaufman, "In-situ Reinforced MoSi$_2$ Composites by Mechanical Alloying", Scripta Metallurgica et Materialia, vol.26, pp. 1245-50, 1992

2. S. Jayashankar and M. J. Kaufman, "Tailored MoSi$_2$/SiC Composites by Mechanical Alloying", Journal of Materials Research, vol.8, no. 6, pp. 1428-41, 1993

3. A. Costa e Silva, S. Jayashankar, P. Krishnan and M. J. Kaufman, "Novel Processing of Intermetallic Composites by in-situ Displacement Reactions", in Processing and Fabrication of Advanced Materials for High Temperature Applications -II, TMS, 1993.

4. S. Riddle, S. Jayashankar and M. J. Kaufman, "Microstructural Evolution in Compositionally Tailored MoSi$_2$/SiC Composites", in "High Temperature Silicides and Refractory Alloys", Materials Research Society Symposium Proceedings, vol. 322, B.F. Bewlay, J.J. Petrovic, C.L. Briant, A.K. Vasudevan and H.A. Lipsitt eds. (1994).

5. S. Jayashankar, S. Riddle and M.J. Kaufman, "Processing and Properties of in-situ MoSi$_2$/SiC Composites", in "High Temperature Silicides and Refractory Alloys", Materials Research Society Symposium Proceedings, vol. 322, B.F. Bewlay, J.J. Petrovic, C.L.Briant, A. K. Vasudevan and H.A. Lipsitt eds. (1994).

6. S. Jayashankar, M.J. Kaufman and J.J. Mecholsky, "The Room Temperature

Fracture Resistance of MoSi$_2$/SiC Composites", in preparation.

7. C.Santos, Jr., S. Jayashankar, and M. J. Kaufman, "Processing and properties of (Mo,W)Si$_2$/SiC Composites, in preparation.

8. S. Jayashankar and M. J. Kaufman, "Effect of Siliceous Intergranular Phase on the Elevated Temperature Fracture Resistance of MoSi$_2$/SiC Composites", in preparation.

9. S. Jayashankar and M. J. Kaufman, "Fabrication and Properties of *in-situ* Transition Metal Silicide/SiC Composites", in preparation.

10. S. Jayashankar and M. J. Kaufman, "Superplastic Molybdenum Disilicide?", in preparation.

Patents:

11. S. Jayashankar and M.J. Kaufman, "Composite Silicide/Silicon Carbide Mechanical Alloy", Serial # 08/069,730, Application allowed. Assigned to the University of Florida.

12. "Refractory Metal Reinforced MoSi2/SiC Composites with Matched Coefficients of Expansion", Serial # 08/069,706, Application allowed. Assigned to the University of Florida.

13. S. Jayashankar and M.J. Kaufman, "Composite Silicide/Silicon Carbide Mechanical Alloy", Continuation-In-Part, Application in progress.

14. S. Jayashankar and M. J. Kaufman, "Method of Near-Net Shape Forming of High Strength MoSi$_2$/SiC Composites", Work in Progress.
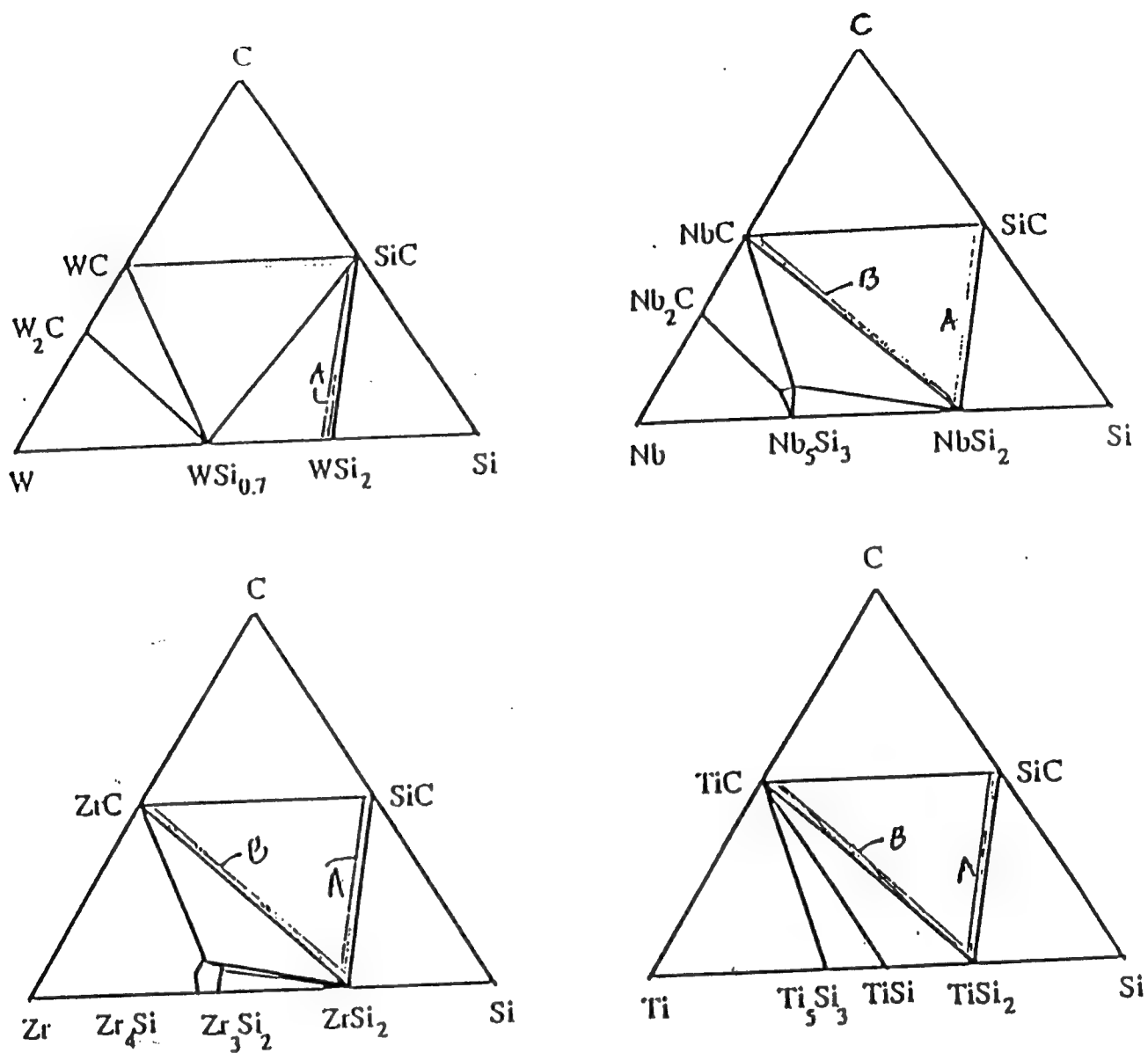
Figure 1   Transition metal – Silicon – Carbon systems sharing similarities
with the Molybdenum – Silicon – Carbon system
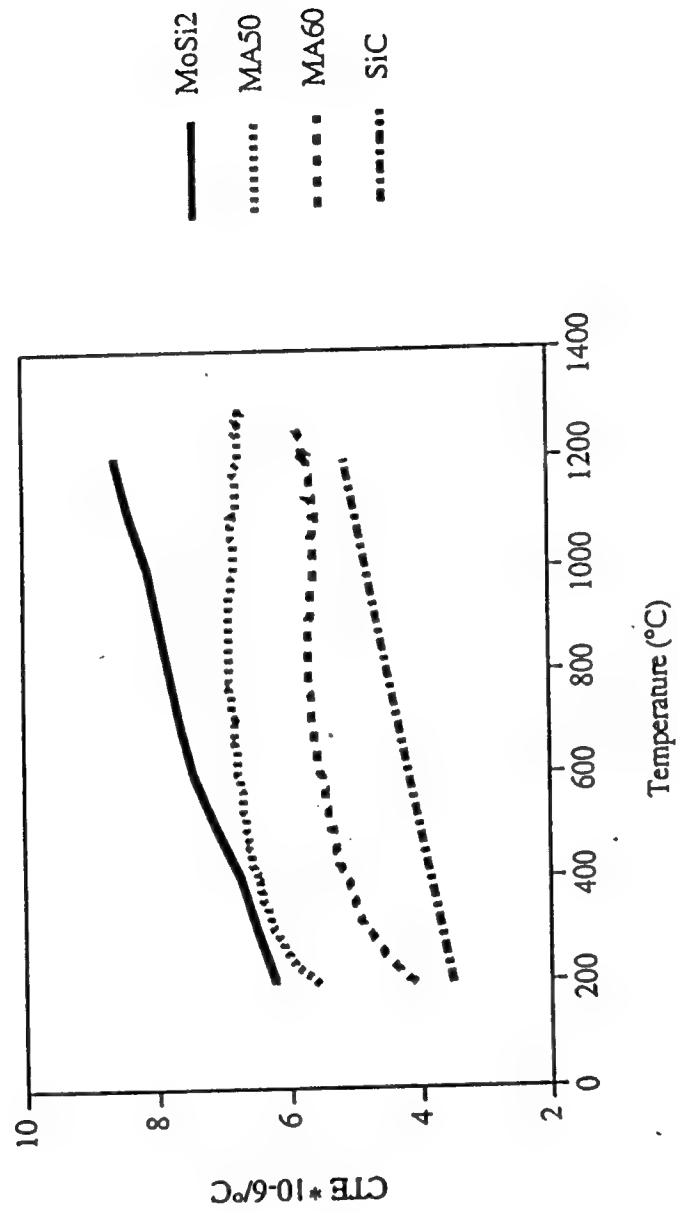
Figure 2   Coefficient of Thermal Expansion versus temperature.

Fig. 3 Indented and Annealed Fracture Strengths of MoSi2/20 v/o SiC (CP and ISP)
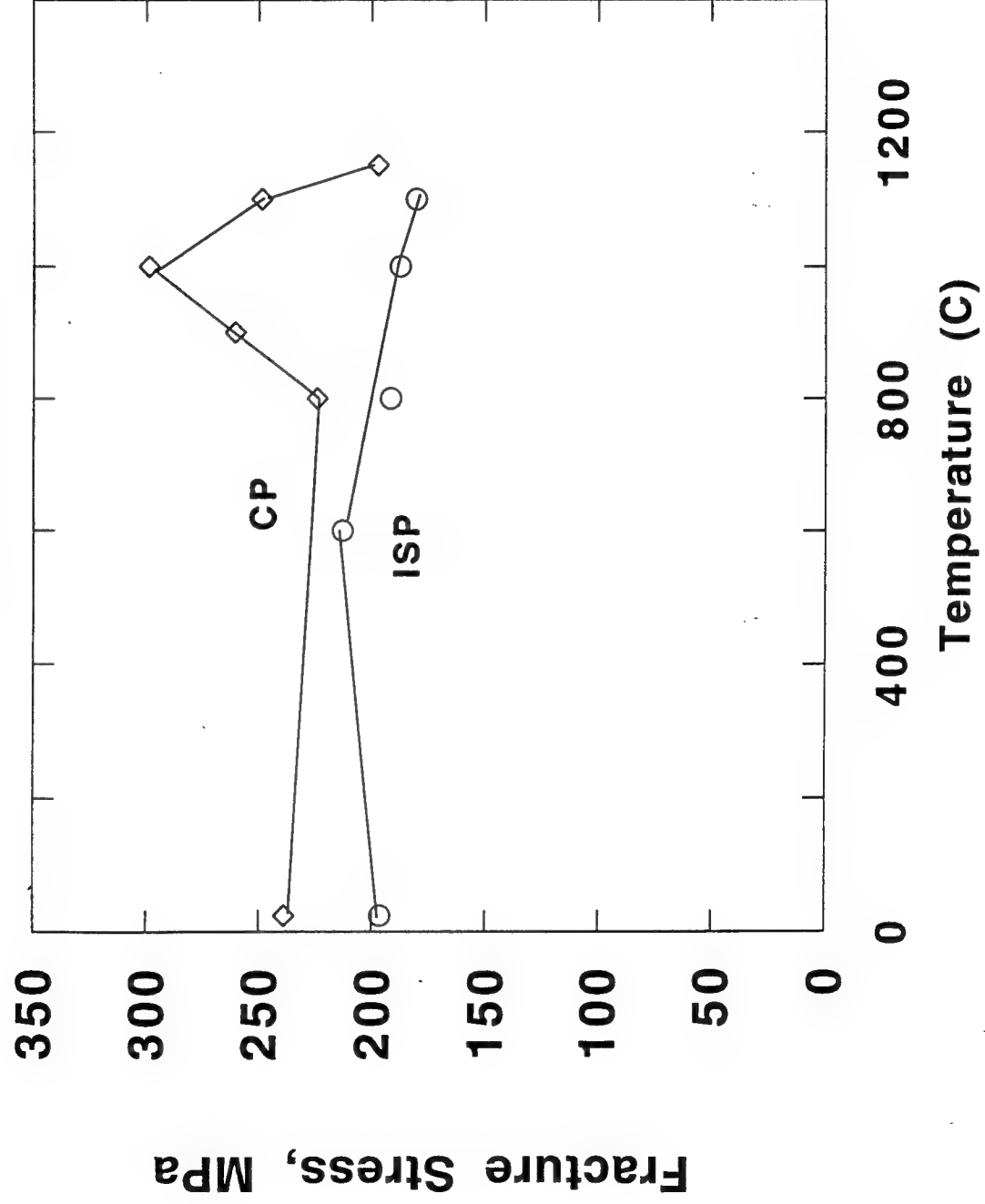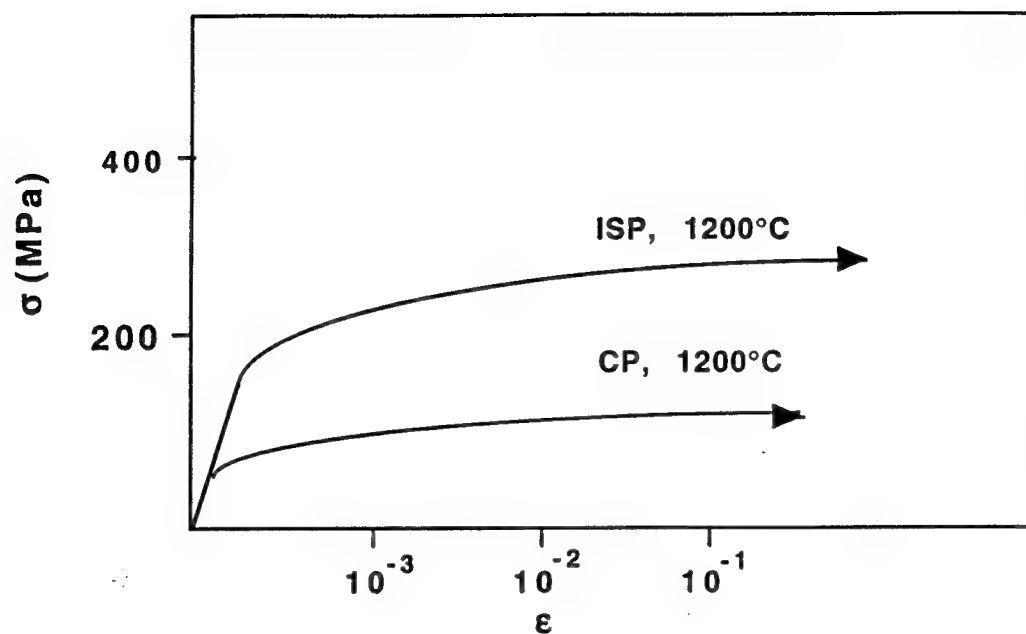
Fig. 4 Schematic of the stress-strain curve of the outer fiber for ISP and CP materials four-point bend tested at 1200°C showing large deformation at constant stress.
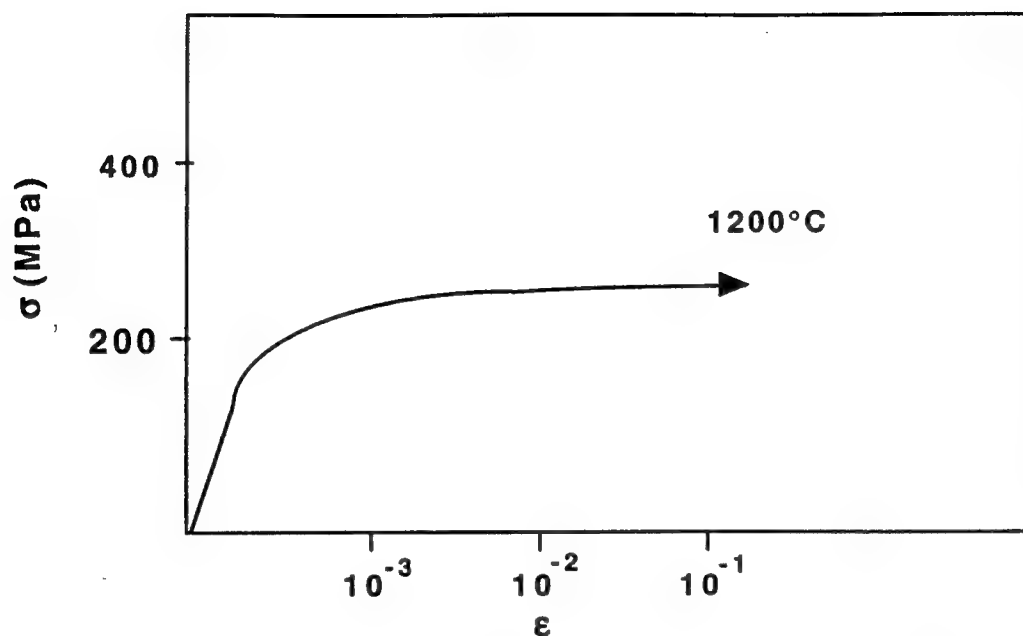
Fig. 4 Stress-strain curve of the outer fiber for ISP and CP materials four point bend tested @T~ 1200°C showing deformation at constant stress.

Fig. 5 Temperature Dependence of Yield Stress for Conventionally Processed (CP) and In-situ Processed (ISP) MoSi2/ 20 v/o SiC
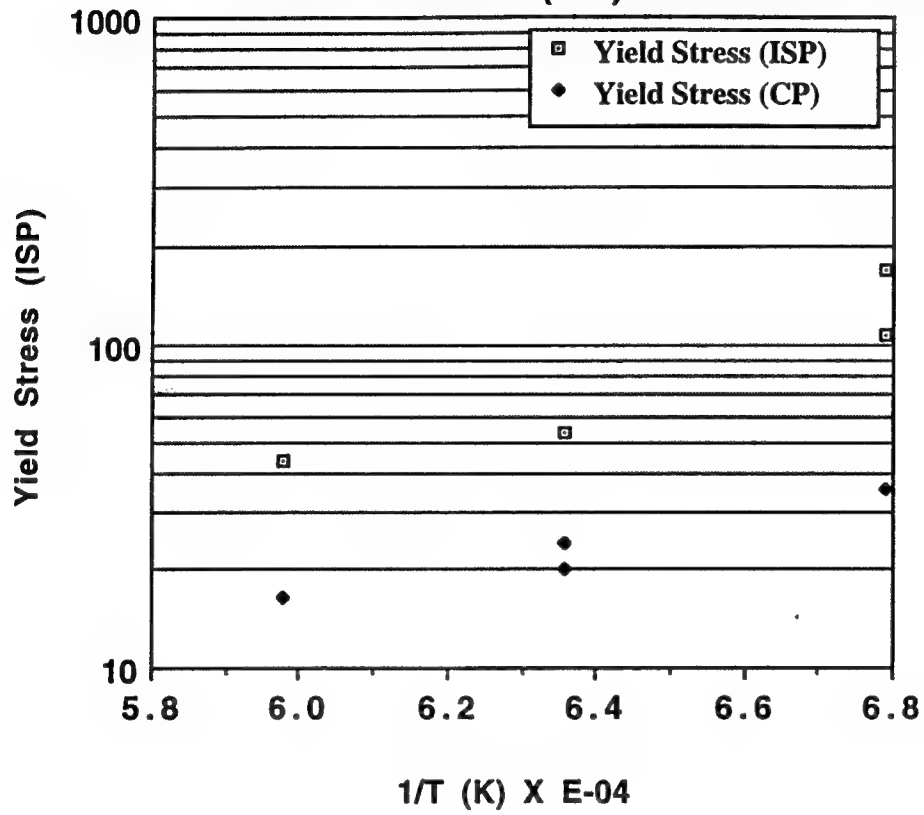
Fig. 6 Temperature Dependence of flow stress for conventionally processed (CP) and in-situ processed (ISP) MoSi2/20 v/o SiC
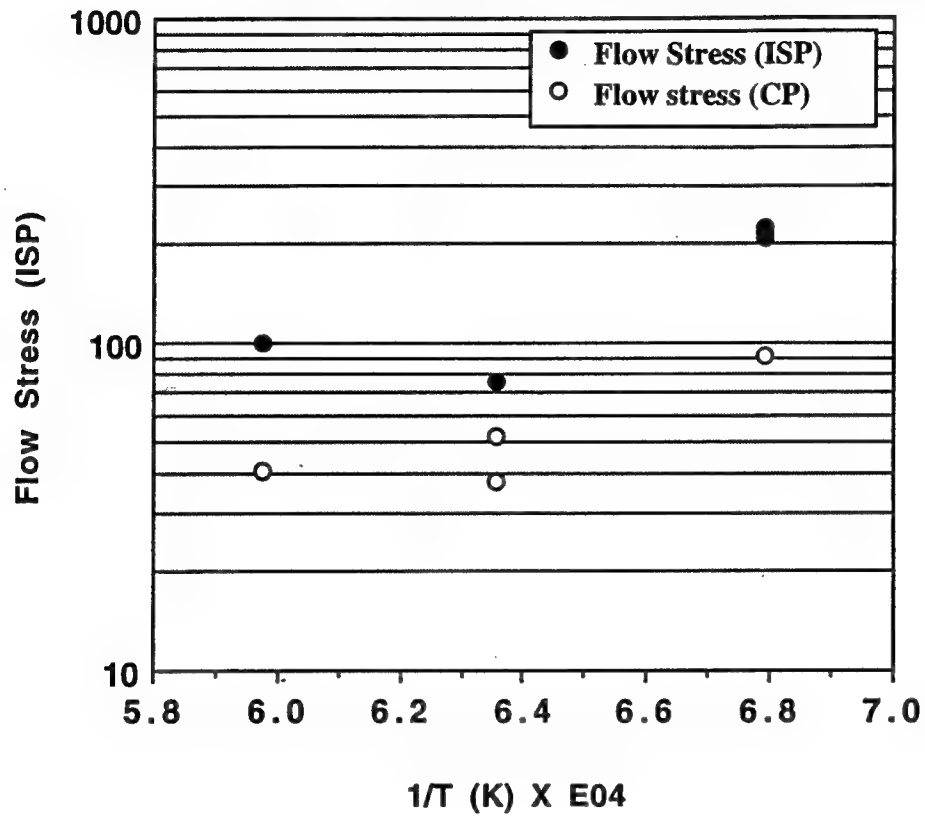
Tailored $MoSi_2$/SiC composites by mechanical alloying

S. Jayashankar and M. J. Kaufman
Department of Materials Science and Engineering, The University of Florida,
Gainesville, Florida 32611-2066

$MoSi_2$-based composites have been synthesized through the mechanical alloying (MA) of elemental molybdenum and silicon powders with and without carbon additions. The interplay between the phase formation sequence in the powders and the microstructural evolution in the consolidated samples is described. It is shown that the glassy SiO_2 phase characteristic of conventional powder processed $MoSi_2$ can be effectively eliminated by combining mechanical alloying, carbon additions, and an *in situ* carbothermal reduction reaction. Using this approach, composites consisting of uniformly distributed micron-size SiC in an $MoSi_2$ matrix can be formed. The effect of important processing variables such as the extent of carbon additions, extraneous iron pickup during MA, partial pressures of oxygen, consolidation temperatures, and consolidation atmospheres is discussed based on the evidence obtained from DTA, TGA, TEM, and XRD.

I. INTRODUCTION

The intermetallic $MoSi_2$ has long been considered a potential material for high-temperature structural applications due to its high melting point, excellent oxidation and corrosion resistance, low density, and good electrical and thermal conductivity. Similar to many other high-temperature intermetallics, the use of $MoSi_2$ is limited as a structural material due to its low ambient temperature fracture toughness and poor elevated temperature strength.

A number of approaches for the processing of this intermetallic are unsuitable due to its high melting point and owing to the fact that it exists as a line compound. Furthermore, the relatively high dissociation pressures of $MoSi_2$ at elevated temperatures result in uncontrolled second phase formation due to silicon volatilization.[1,2] In view of these characteristics, powder processing appears to be the preferred fabrication route due to the lower processing temperatures that it affords; unfortunately, it also results in the incorporation of silica (originally formed as a surface layer on the powder particles[3]) into the consolidated samples. The presence of grain boundary silica either as a continuous film or as discrete particles is expected to be detrimental, since the particles may serve as crack nucleation sites at lower temperatures, while enhancing deformation via grain boundary sliding at temperatures above 1200 °C where the silica softens appreciably. In fact, recent studies have shown that low silica polycrystalline $MoSi_2$ demonstrates negligible "plasticity" below 1400 °C.[4] Silica formation also alters the matrix stoichiometry and results in the formation of Mo_5Si_3. Such stoichiometric deviations degrade the intermediate temperature oxidation resistance[5] of the silicide. Finally, silica has also been reported to cause the degradation of the diffusion barrier coatings at the fiber-matrix interface in ductile fiber-reinforced $MoSi_2$.[6]

In attempting to control the oxygen content of $MoSi_2$ by varying the starting powder size and by intentional carbon additions (deoxidant), Maxwell[7] found that a fine-grained material with carbon additions had better creep properties and lower high-temperature plasticity than a similar grain-size material without carbon. More recently, Maloy *et al.*[8] also reported improved elevated temperature fracture toughness with varying levels of carbon additions. However, substantial (~40%) weight losses were reported on consolidating these samples, resulting in uncontrolled formation of Mo-rich second phases. Hardwick and co-workers[9] attempted to process oxygen-free $MoSi_2$ by conducting all the powder handling and consolidation steps under vacuum or inert gas atmospheres. However, these approaches[9,10] are impractical from the standpoint of processing bulk structural parts, due to the difficulties involved in the scale-up of the evacuation systems, as well as the excessive costs that would be associated with such processes.

It is therefore clear that further enhancements in the properties of $MoSi_2$ and $MoSi_2$-based composites are possible only with the elimination of silica (and oxygen) in the matrix along with close control of the overall stoichiometry, through the use of simple and economical processing schemes that do not necessitate elaborate care during powder handling. Thus, the major focus of the present study was to achieve the above-mentioned objectives through a combination of mechanical alloying and carbothermal reductions for the silica-free synthesis

of $MoSi_2$. While mechanical alloying (MA) would result in the formation of a microstructurally uniform and compositionally homogeneous alloy of the desired stoichiometry, the carbothermal reduction process[11,12] would utilize the reducing effect of carbon to convert silica to silicon carbide. Furthermore, mechanical alloying would enable the homogeneous dispersion of carbon in the matrix to facilitate these reactions.

II. BACKGROUND

A. Phase equilibria

Optimizing the processing conditions and understanding the microstructural evolution requires a knowledge of the phase equilibria and crystal chemistry of the binary Mo–Si and the ternary Mo–Si–C systems; these are summarized in Table I. It should be pointed out that many of the earlier thermodynamic and structural determinations of these systems were in error due to oxygen and carbon contamination of the samples, as well as due to the high melting points of the compounds.

Ternary isotherms of the Mo–Si–C system, as shown in Fig. 1(a), were constructed by Nowotny and co-workers[16] at 1600 °C and by Brewer and Krikorian[20]

at around 1727 °C. Subsequently, van Loo and co-workers[21] constructed a 1200 °C isotherm [see Fig. 1(b)] after examining arc-melted alloys and diffusion couples. The only ternary phase in the Mo–Si–C system is the "Nowotny phase" which has the approximate formula, $C_{<1}Mo_{<5}Si_3$, and a relatively wide homogeneity range.[16,17,20,21] Minor additions of carbon to Mo_5Si_3 destabilize its tetragonal structure and result in the formation of a carbon stabilized hexagonal Nowotny phase. These Nowotny phases have the general formula, $T_3^I T_{<2}^{II} M_3 X_{<1}$, where T denotes a transition metal, M represents Ge or Si, and X denotes a nonmetal such as C, O, B, or N.[17] The presence of carbon-centered tetrahedra is characteristic of the Nowotny phases and accounts for their stability. While the isotherms of Nowotny et al. and Brewer and Krikorian are in good agreement with each other in their prediction of the existence of a three-phase field between $MoSi_2$, $C_{<1}Mo_{<5}Si_3$, and SiC, the results of Van Loo indicate the coexistence of Mo_5Si_3, SiC, and $C_{<1}Mo_{<5}Si_3$ at 1200 °C. Recently, it has been postulated by Costa e Silva and Kaufman[22] that the van Loo and Brewer diagrams are consistent with each other only if a class II, four-phase reaction ($MoSi_2$ + Nowotny → SiC + Mo_5Si_3) exists between the temperatures at which these isotherms were constructed, i.e., 1200 °C and 1727 °C.

TABLE I. Summary of the binary and ternary phases of the Mo–Si–C system.

| System	Formula	Temp. (°C)	Crystal system	Structure	Lattice parameters (nm)	Ref.	Comments
Mo–Si	Mo_3Si	2025	Cubic	$Pm\overline{3}n$	$a = 0.4890$	14	Forms by the peritectic reaction, L + $\alpha \rightleftarrows Mo_3Si$
	Mo_5Si_3	2100	Tetragonal	$I4/mcm$	$a = 0.9648$ $c = 0.4910$	14	Incorrectly identified as Mo_3Si_2 until Aronson.[18] Solubility range ~3 at. %.
	α–$MoSi_2$	1900	Tetragonal	$I4/mmm$	$a = 0.3202$ $c = 0.7843$	14	α–β transformation is polymorphic. However, Ref. 13 considers β decomposition to α and Mo_5Si_3 through a eutectoid reaction. β may be stabilized by impurities, e.g., Ti.
	β–$MoSi_2$	2020	Hexagonal	$P6_2 22$	$a = 0.4642$ $c = 0.6529$	14	
Si–C	α–SiC	~2800	Hexagonal	$P6_3 mc$	$a = 0.3081$ $c = 1.511$	15	Numerous other polytypes exist.
	β–SiC	~2800	Cubic	$F\overline{4}3m$	$a = 0.4358$	15	
Mo–C	β–Mo_2C	2650	Hexagonal	$P6_3/mmc$	$a = 0.2932$ $c = 1.097$	16	Forms by the peritectic reaction, L + MoC $\rightleftarrows Mo_2C$
	MoC	2520	Hexagonal	$P6_3/mmc$	$a = 0.3006$ $c = 0.4753$	15	Other metastable forms which are slightly carbon rich such as α– and η–carbides exist at high temperatures and transform at lower temperature by eutectoid reaction to β–Mo_2C + C.
Mo–Si–C	$C_{<1}Mo_{<5}Si_3$	2000–2060 (composition dependent)	Hexagonal	$P6_3/mcm$	$a = 0.7286$ $b = 0.7287$ $c = 0.5002$	17	c/a changes slightly with carbon content. First structure determination made by Schachner et al.,[19] but incorrectly identified as Mo_5Si_3.
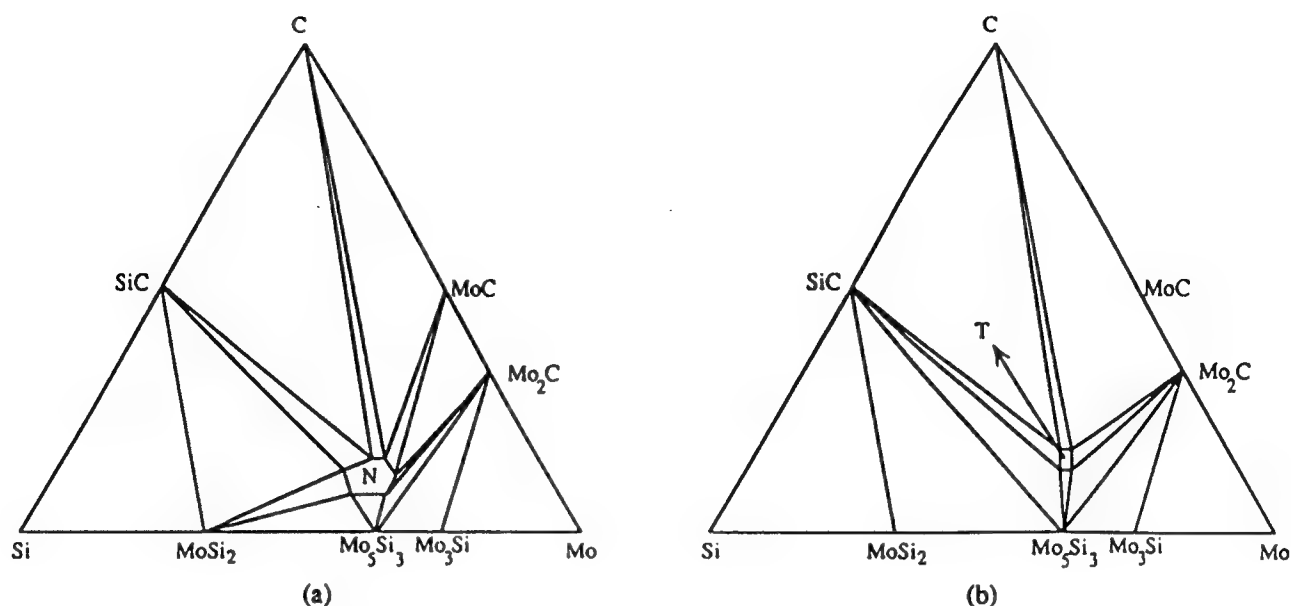
FIG. 1. Schematic of the ternary isotherms of the Mo–Si–C system as proposed by (a) Nowotny *et al.*[16] at 1600 °C and (b) van Loo *et al.* at 1200 °C.[21] N in (a) and T in (b) denote the $C_{<1}Mo_{<5}Si_3$ phase.

B. Processing rationale

Based on the 1600 °C isotherm of Nowotny and the 1727 °C isotherm of Brewer, it is clear that ternary powder alloys within the composition limits established by the $MoSi_2 + C_{<1}Mo_{<5}Si_3 + SiC$ three-phase field should form a *thermally stable*, three-phase microstructure when consolidated at these temperatures, provided that the powders are sufficiently homogeneous to minimize the diffusion length scales so as to establish equilibrium within the short time frames of the consolidation process. Here, it is assumed that the nature of the isotherms is unaltered by the presence of small amounts of oxygen present as surface SiO_2 on the powders. While part of the carbon would take part in the deoxidation/carbothermal reduction reactions, the unreacted residual carbon would exist in equilibrium, as dictated by the isotherm.

For the formation of $MoSi_2/SiC$ composites with a minimal amount of the Nowotny phase, it is necessary to start with nominal compositions slightly to the Mo-rich side of the $MoSi_2$–SiC tie line; this ensures that the compositional variations (carbon and silicon losses) due to the carbothermal reduction reactions do not shift the overall composition to the adjacent $Si + MoSi_2 + SiC$ field, where the Si phase would experience incipient melting above ~1400 °C and thus result in the degradation of the high temperature mechanical properties. Bearing this in mind, it is possible to vary the amount of the reinforcing SiC phase in the $MoSi_2$ matrix by simply choosing compositions at various points along the tie line. Note that the formation of the thermodynamically expected microstructures may also be limited by various

kinetic constraints. Similarly, processing related effects such as porosity should also be appropriately controlled in view of the gaseous by-products formed as a result of the carbothermal reduction reaction.

It is worth noting that the deoxidation of commercial $MoSi_2$ by carbon additions without a commensurate increase in the silicon content[7,8] would result in compositional shifts along an imaginary line between $MoSi_2$ and C and a corresponding increase in the amount of the Nowotny phase, according to the diagrams by Nowotny and Brewer [Fig. 1(a)].

In the present study, two powder compositions were chosen for mechanical alloying (MA). One corresponded to stoichiometric binary $MoSi_2$ as a baseline for comparison, and the other was a ternary alloy in the $MoSi_2 + C_{<1}Mo_{<5}Si_3 + SiC$ three-phase field, according to the Nowotny diagram [Fig. 1(a)].

III. EXPERIMENTAL PROCEDURE

The compositions investigated by mechanical alloying in this study were Si–28Mo–14C and Si–33.33Mo (stoichiometric binary $MoSi_2$) (all compositions in atomic percent). Mechanical alloying was performed in a water-cooled Szegvari attrition mill (planetary type) using hardened steel balls as the milling media and a ball to charge ratio of 5:1. Elemental powders of commercial purity molybdenum (purity 99.9%, 2–4 μm) and silicon (purity 98%, <44 μm) obtained from Cerac and high-purity carbon powder (99.5% pure, −300 mesh, amorphous) obtained from Johnson Matthey were the starting materials. To minimize oxygen contamination during processing, high-purity titanium-

gettered argon (oxygen content less than 4 ppm) under a slightly positive pressure was maintained in the attritor. The progress of MA was monitored by withdrawing small amounts of powder samples from the same attrition batch after 0, 0.5, 7, 17, 29, 40, and 42 h of milling. The powders were characterized for structure and morphology by SEM and XRD. In addition, powders obtained after 17 and 40 h of milling were analyzed by TEM. For the TEM analysis, powders were ultrasonically dispersed in acetone, and a small droplet was spread on a holey carbon film. The fine size (<1 μm) of the powders ensured their electron transparency.

Consolidation of the MA binary and ternary powders was carried out by hot pressing under a vacuum of 10^{-2} Torr or less in an inductively heated graphite die at both 1450 °C and 1600 °C at a pressure of 35 MPa for 1 h. To prevent cracking of the sample, the pressure was released prior to cooling. Samples for microstructural characterization were diamond-saw cut, ground, and polished to a 1 μm diamond finish. Thin foil TEM samples were prepared from the bulk samples following standard procedures of dimpling and argon ion-milling at 4.5 kV. Microstructural analysis of the consolidated samples as well as the MA powders was performed using a JEOL JSM 6400 SEM equipped with a Tracor Northern EDS unit with light element detection capabilities and JEOL 200CX and JEOL 4000FX TEM's, the latter equipped with a Princeton Gamma Tech EDS unit with a light element detector.

The transformation characteristics of the MA powders were monitored by differential thermal analysis (DTA) and thermogravimetric analysis (TGA). DTA/TGA was performed under flowing gettered argon (1 cc/min, oxygen content less than 4 ppm) on a Netzsch STA-409 system with heating/cooling rates of 10 °C/min. Errors due to the differing specific heats of the sample and the reference were eliminated by using commercial MoSi₂ powder that had been previously calcined under gettered argon at 500 °C as the reference. For more detailed investigations, powders were heated at 10 °C/min under gettered argon above each DTA exotherm, held at that temperature for less than a minute, and rapidly cooled for subsequent analysis. Structural analysis of the powders and the consolidated samples was carried out using a Philips ADP 3720 diffractometer operated at 40 kV and 20 mA with Cu K$_\alpha$ radiation and digital data acquisition over 2Θ ranges of 5°–100°.

IV. RESULTS AND DISCUSSION

A. Powder microstructure

The development of the powder morphology with increasing milling times is shown in Fig. 2. After 0.5 h of milling [Fig. 2(c)], large particles with a diameter of 5–6 μm are predominant. Refinement of the powder continues through 7 h of milling [Fig. 2(d)], beyond which the reduction in powder size is gradual. The powder size stabilizes around 1 μm after 29 h [Fig. 2(e)] and remains constant thereafter [Fig. 2(f)].

Structural evolution studies of the powders as a function of milling time (Fig. 3) indicated the formation of traces of β–MoSi₂ (hexagonal form) after short milling times [0.5 h, see Fig. 3(a)]. Further milling [7 h, Fig. 3(b)] results in a slight increase in the amount of β–MoSi₂ along with the gradual appearance of α–MoSi₂ (tetragonal form). Further increases in the amount of α–MoSi₂ continue through 17 h of milling [Fig. 3(c)], at which time elemental molybdenum and silicon are still present. Milling beyond 17 h through 29 h [Fig. 3(d)] results in the almost complete disappearance of the silicon peaks, along with a considerable broadening of the α–MoSi₂ peaks; this is presumably due to the decrease in the crystallite size of α–MoSi₂ rather than the effect of lattice strain since MoSi₂ is brittle at the milling temperatures. This was confirmed by TEM observations. Beyond 29 h, milling has little effect on the structure of the powders, a fact which was also corroborated by the SEM observations, which showed particle size stabilization after 29 h.

Powders were characterized for their microstructure by TEM. A dark-field TEM micrograph of a MA MoSi₂ powder particle milled for 40 h is shown in Fig. 4(a). Close examination reveals a fine distribution of crystallites, the sizes of which are between 4 and 7 nm. In addition, the surfaces of the powder particles appear to be covered with a layer of amorphous oxide, the projected thickness of which varies from 5 to 15 nm. The selected area diffraction pattern (SADP) [Fig. 4(b)] from this powder indexes to the interplanar spacings of Mo and α–MoSi₂. X-ray diffractograms [Figs. 5(a) and 5(b)] from these powders not only confirm the presence of the predominant phases (Mo and α–MoSi₂) determined in the SADP's, but also reveal traces of the metastable β–MoSi₂, which reportedly occurs only above 1900 °C under equilibrium conditions. The formation of the β–MoSi₂ at lower temperatures is not surprising and has been reported during the annealing of amorphous Mo–Si multilayers prepared by sputtering,[23,24] as well as in ion-implanted MoSi₂ films.[25] The presence of Mo and MoSi₂ in the as-milled powders suggests that silicon is dissolved in the MoSi₂ and Mo crystallites; this is also a metastable effect caused by mechanical alloying, since the terminal solubilities of Si in Mo and MoSi₂ are negligible at room temperature although both Mo and MoSi₂ are known to exist over a certain homogeneity range above ~1500 °C.[13,14] The possibility of amorphization of part of the silicon was considered, but was eliminated in view of the experimental evidence against it.[26] The fine
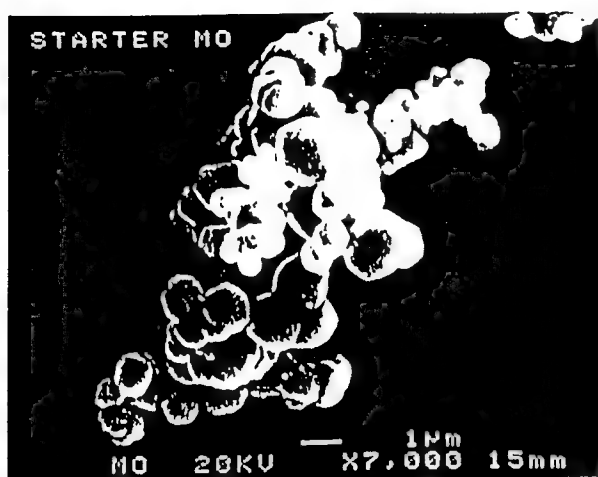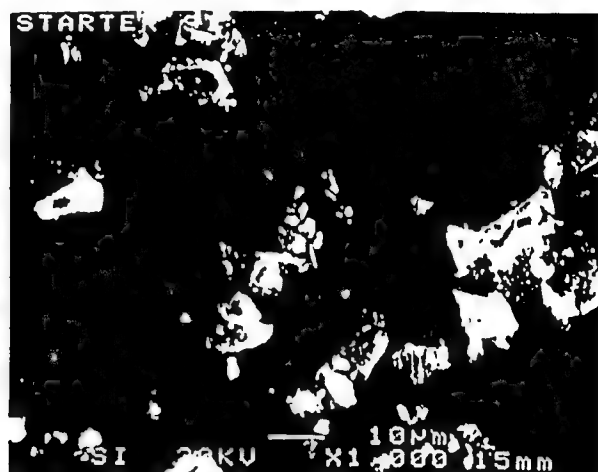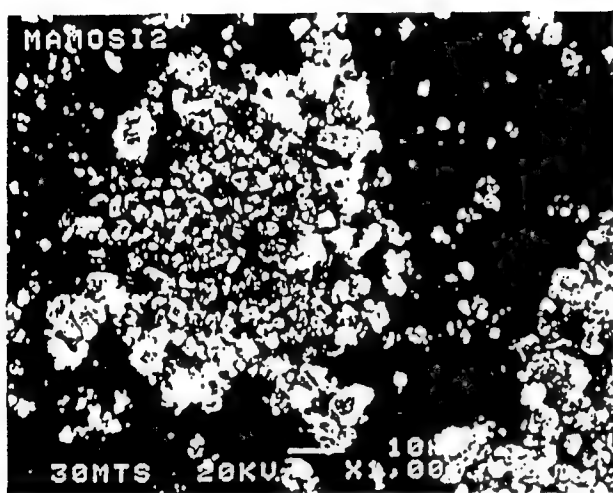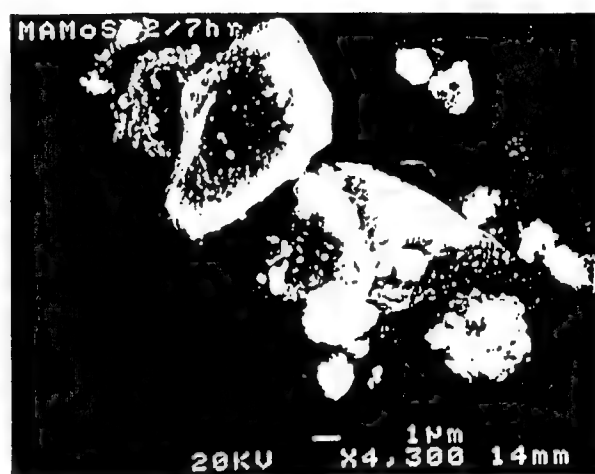
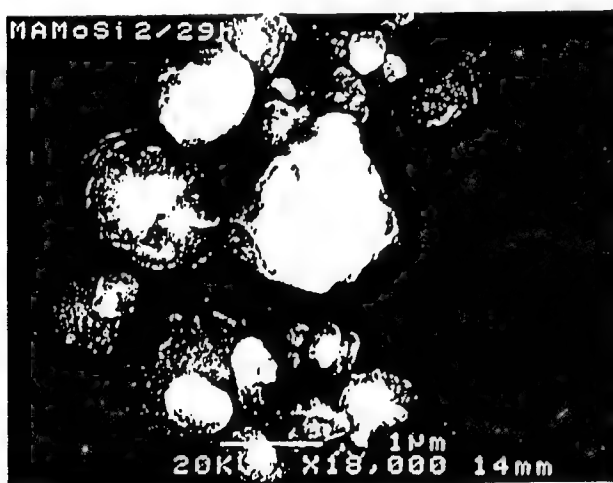FIG. 2. Morphological evolution of the MA MoSi₂ powders as a function of milling time: Elemental Mo (a) and Si (b) powders prior to milling (0 h), (c) after 0.5 h of milling, (d) after 7 h of milling, (e) after 29 h of milling, and (f) after 40 h of milling.
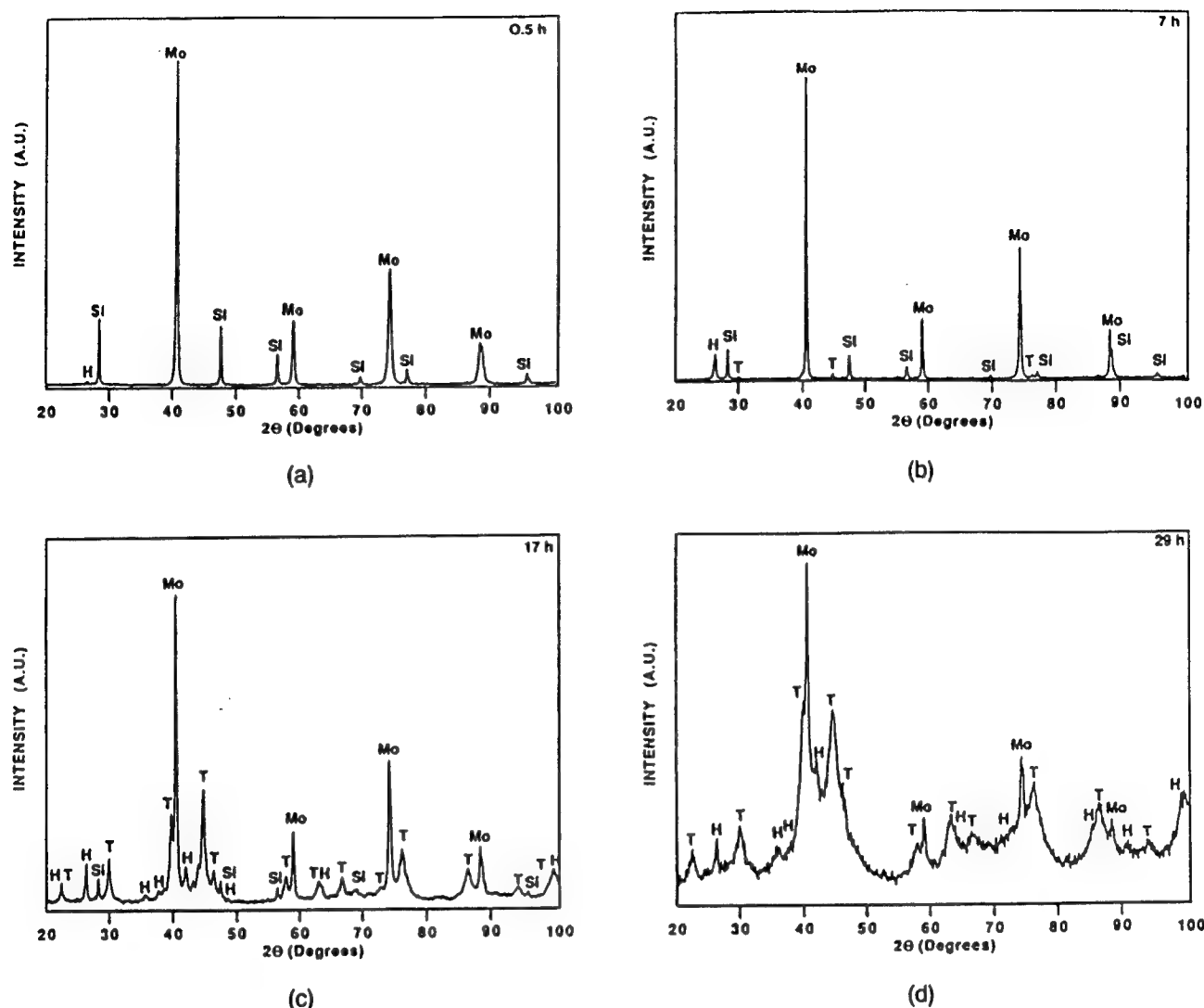
FIG. 3. Structural evolution of the ternary MA MoSi₂ powder as a function of milling time. XRD patterns of the powders milled for the indicated times: (a) 0.5 h (b) 7 h (c) 17 h and (d) 29 h (Mo is molybdenum, Si is silicon, T is tetragonal α-MoSi₂, and H is hexagonal β-MoSi₂).

scale of the powder microstructures and the intermetallic compound formation during mechanical alloying suggest a homogeneous distribution of alloying elements. EDS analysis of the powders also revealed the presence of trace amounts of iron impurities that were probably picked up from the hardened steel balls used for milling.

In order to ascertain the effects of carbon additions on the final structure of the MA powders, XRD patterns from the binary [Fig. 5(a)] and ternary samples [Fig. 5(b)] after 40 h of milling were compared. It can be seen on the basis of the relative intensities of the molybdenum and α-MoSi₂ peaks that the formation of α-MoSi₂ is suppressed by the carbon additions.

B. Phase evolution

The phase evolution of the binary and ternary MA MoSi₂ powders as a function of temperature was studied by DTA. A typical heating trace of the binary MA MoSi₂ powder is shown in Fig. 6, where weak exotherms corresponding to 580 °C, 780 °C, and 1020 °C are apparent. The transformations corresponding to these exotherms were studied by XRD analysis of powders heated to temperatures above the end of each exotherm under identical heating conditions (10 °C/min under flowing argon), and the results are shown in Fig. 7. Comparison of the room temperature and the 690 °C XRD patterns [Fig. 5(a) and Fig. 7(a), respectively] showed that the mild 580 °C exotherm is associated with the formation of more α-MoSi₂, as is evidenced by the change in the relative intensities of the α-MoSi₂ and Mo peaks. Likewise, comparison of the 690 °C and 950 °C XRD patterns shows that the 780 °C exotherm corresponds to the simultaneous growth of α-MoSi₂ and Mo₅Si₃ (tetragonal). The 1020 °C exotherm appears to be as-
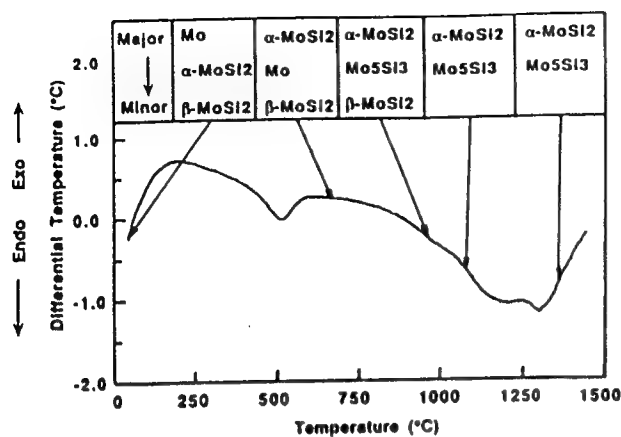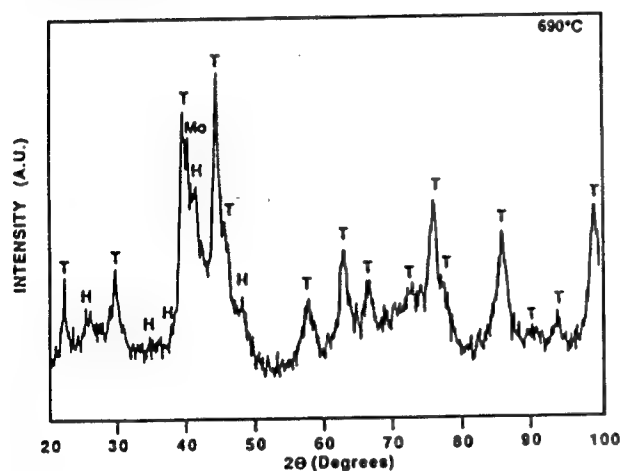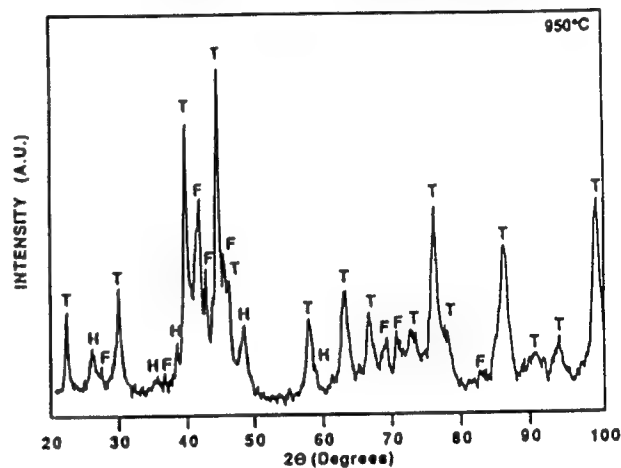
FIG. 6. DTA of binary stoichiometric MoSi₂ under flowing Ar at a heating rate of 10 °C/min, along with the corresponding phases observed by XRD.

transformation of the Nowotny phase and β-MoSi₂ to the more stable α-MoSi₂, as evidenced by a comparison of the 935 °C and 1070 °C XRD patterns [Figs. 9(b) and 9(c), respectively]. Heating to higher temperatures [1400 °C, Fig. 9(d)] results in a decrease in the amount of the Nowotny phase and an increase in α-MoSi₂. The DTA cooling curves of the binary and the ternary powders were flat in nature, thereby indicating stable structures.

The low-temperature formation of the carbon-stabilized Nowotny phase instead of the thermo-dynamically preferred α-MoSi₂ phase is probably related to its greater ease of nucleation and growth. The stability of the β-MoSi₂ up to 1030 °C is also not surprising. Hexagonal β-MoSi₂, formed by isothermal annealing of sputtered Mo-Si multilayers, has been reported to be stable up to 800 °C. The higher tem-

(a)

(b)
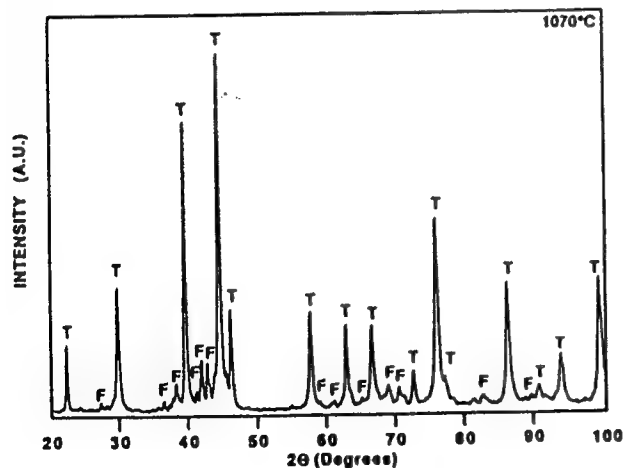
(c)
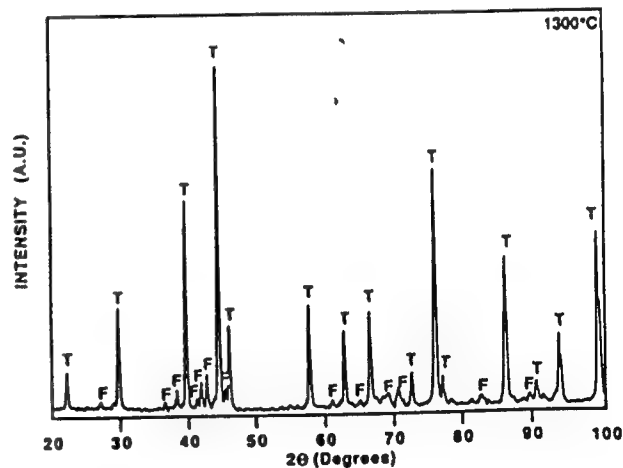
(d)

FIG. 7. XRD of the MA binary stoichiometric MoSi₂ powders heated at 10 °C/min under flowing argon to the temperatures indicated: (a) 690 °C (b) 950 °C (c) 1070 °C and (d) 1400 °C (Mo is molybdenum, Si is silicon T is α-MoSi₂, H is β-MoSi₂, and F is the tetragonal Mo₅Si₃ phase).
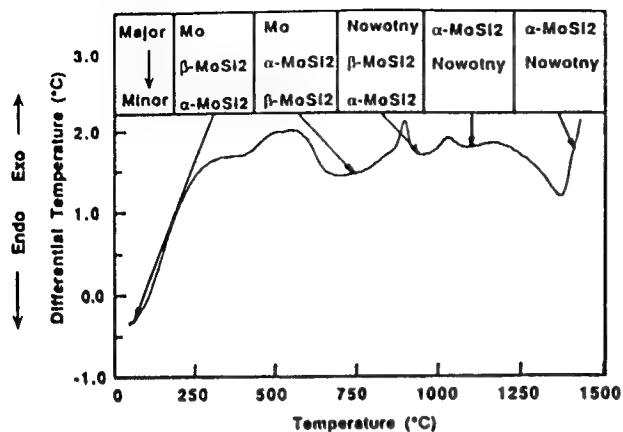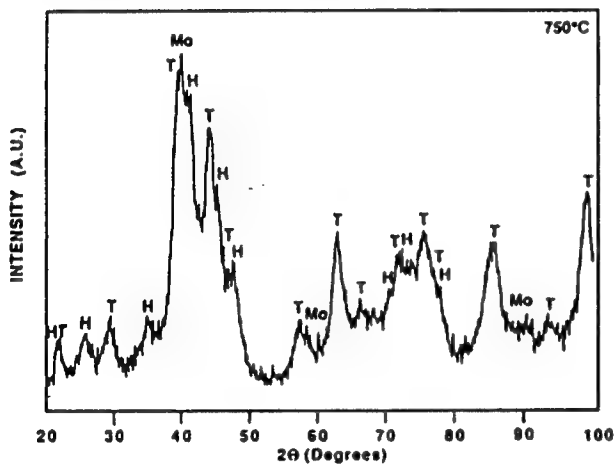
FIG. 8. DTA of ternary MoSi₂ under flowing argon at a heating rate of 10 °C/min, along with the corresponding phases identified by XRD. ("Nowotny" refers to the Nowotny phase, $C_{<1}Mo_{<5}Si_3$.)

perature stability of the β phase in this study is probably related to the presence of iron and oxygen impurities rather than the relatively high heating rates of the powders; this is consistent with the experimental evidence obtained from the isothermal annealing of the MA binary and ternary powders (820 °C for a period of 1 h), which demonstrated the stability of the β–MoSi₂ phase.

C. Consolidated microstructures

Figure 10 shows the microstructures of a hot-pressed specimen derived from the MA nominally stoichiometric MoSi₂ powders. Considerable amounts of second-phase particles with volume fractions of about 0.15 are present in the MoSi₂ matrix. TEM/EDS analysis of these samples (Fig. 11) revealed the presence of submicron-sized grains of MoSi₂ and second-phase particles which were amorphous and silicon-rich, indicating the presence of
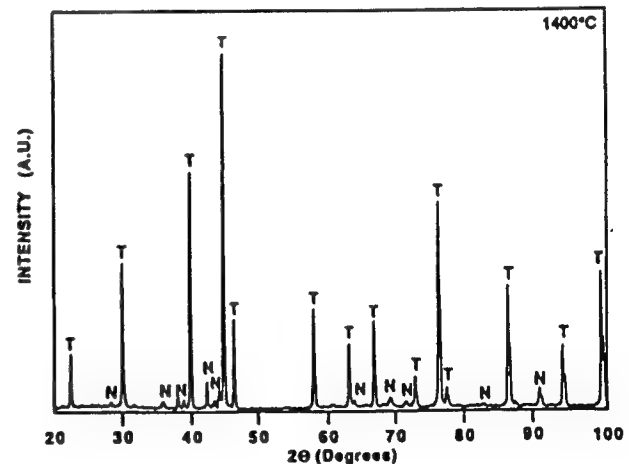

(a)
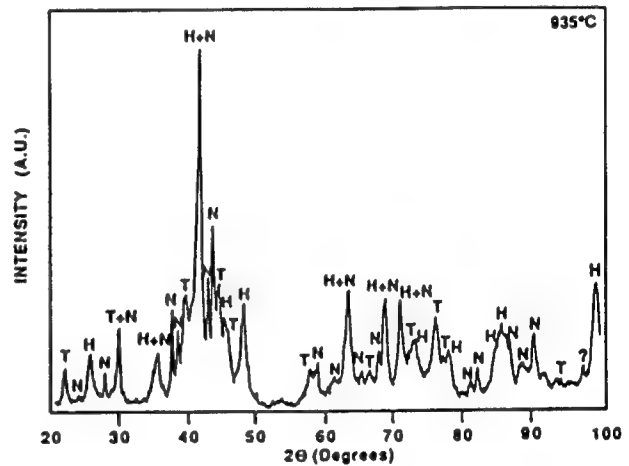
(b)
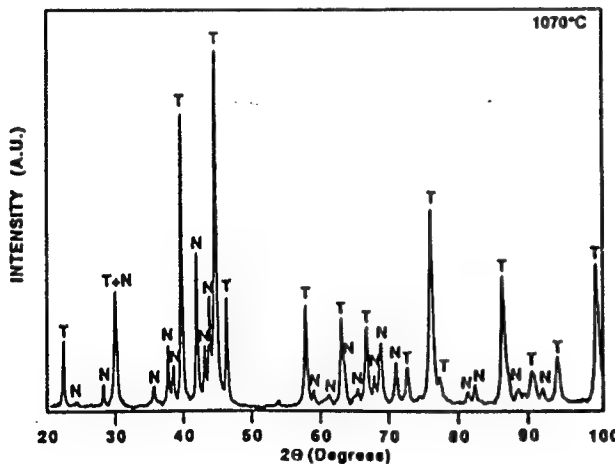
(c)

(d)

FIG. 9. XRD of the MA ternary MoSi₂ powders (Si–28Mo–14C) heated at 10 °C/min under flowing argon to the temperatures indicated: (a) 750 °C, (b) 935 °C, (c) 1070 °C, and (d) 1400 °C (Mo is molybdenum, Si is silicon, T is α–MoSi₂, H is β–MoSi₂, and N is the hexagonal Nowotny phase).
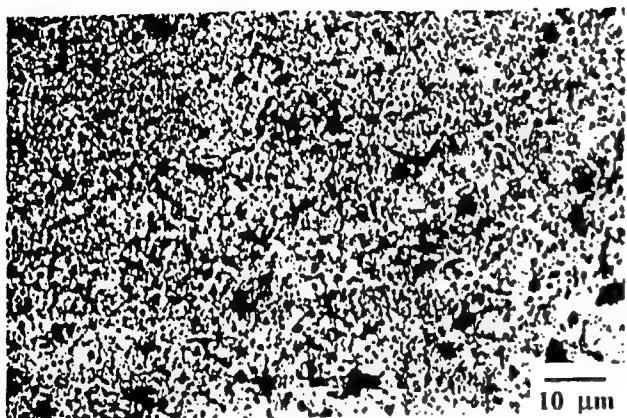
FIG. 10. Scanning Electron Micrograph (SEM) showing the microstructure of the hot-pressed binary MA MoSi$_2$.

a glassy silica phase. The silica was present at the grain boundaries and triple points. In addition, very fine
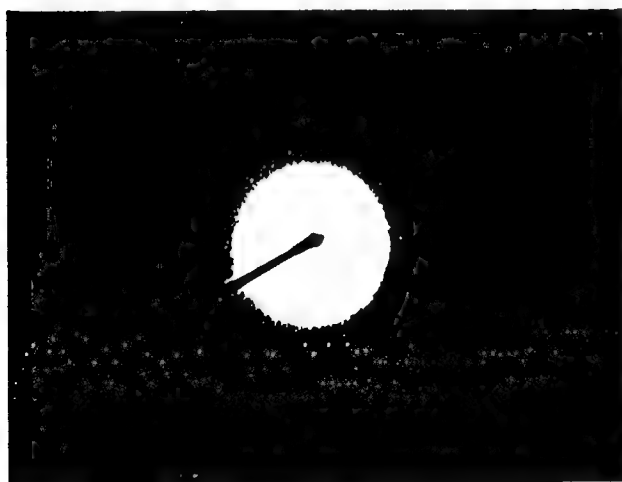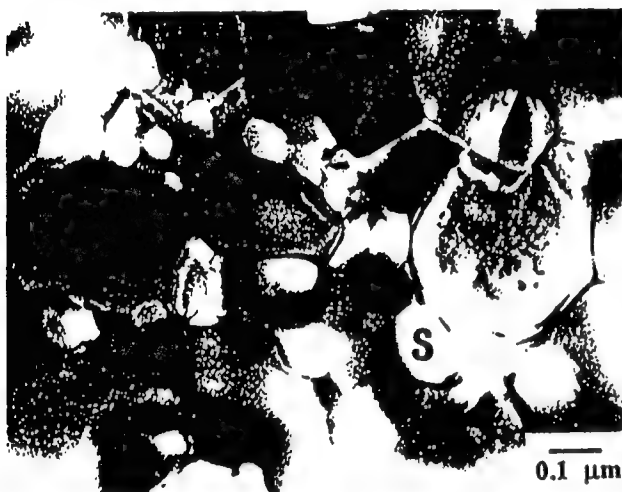

FIG. 11. Bright-Field Transmission Electron Micrograph (BFTEM) and SADP of silica particles in hot-pressed binary MA MoSi$_2$. S denotes a typical silica particle.

(10 nm) dispersoids were found within the MoSi$_2$ grains, along with occasional grains of Mo$_5$Si$_3$.

Figure 12 shows a backscattered electron image of a hot-pressed specimen derived from the carbon-modified MA MoSi$_2$ powder. Considerable improvement in the overall homogeneity and cleanliness of the microstructure is apparent in comparison with the samples derived from the binary MA MoSi$_2$ powder. Based on the atomic number (Z) contrast, it is apparent that the material has three phases.

Following qualitative analysis by EDS, the compositions of each of these phases, as well as the overall matrix composition, were determined by electron microprobe analysis. In addition, quantitative estimation of the volume fraction of these phases was obtained using standard point count techniques. These results are summarized in Table II. The data indicate the presence of SiC (low Z phase), MoSi$_2$ (intermediate Z phase), and an iron-containing Nowotny phase $C_{<1}(Mo, Fe)_{<5}Si_3$ (high Z phase) in the microstructure, and thus seem to support the isotherms proposed by Nowotny et al. and Brewer and Krikorian[16,20] [see Fig. 1(a)] rather than that of van Loo et al.[21] [see Fig. 1(b)]. Furthermore, the volume fractions of these phases are in reasonable agreement with the location of the nominal compositions in the MoSi$_2$ + SiC + $C_{<1}Mo_{<5}Si_3$ three-phase field in the Nowotny diagram. As mentioned earlier, the source of the iron is believed to be the hardened steel milling media. Interestingly, no iron was detected in the MoSi$_2$, despite the fact that it has a limited amount of solubility for iron.[27] The preferential location of iron in the Nowotny phase is probably related to the greater affinity of iron toward the carbon-centered octahedra of this phase. The relatively small size differences between the atomic radii of Mo and Fe, together with the low
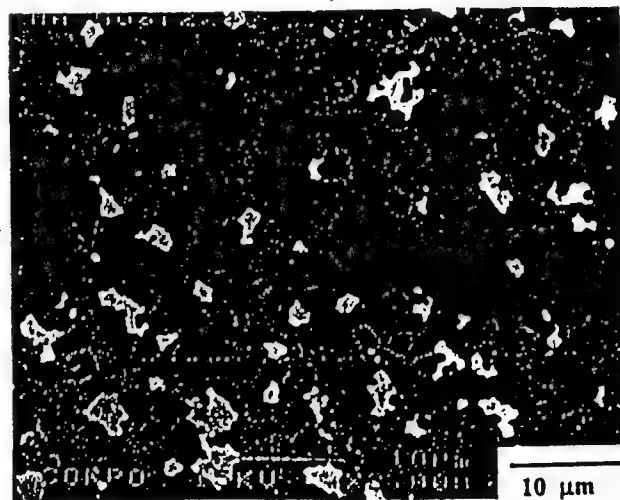

FIG. 12. Backscattered electron image of the hot-pressed ternary MA MoSi$_2$ (Si–28Mo–14C).

TABLE II. Microstructural characteristics of the consolidated samples derived from the ternary MA MoSi₂ powders.

Phase	Composition (at. %)				Volume fraction (%)
	Si	Mo	C	Fe	
MoSi₂	64.55	35.45	0.0	0.0	79.15
SiC	0.0	48.29	50.20	0.0	11.83
Nowotny	54.91	35.26	5.22	4.59	9.028
Overall	58.16	31.7	9.765	0.37	
Initial	58.00	28.00	14.00		

levels of the iron impurity, make iron substitution on the molybdenum sites easy, since the resulting lattice strains would be small. It is also apparent that the Nowotny phase tends to adjoin the SiC grains, thereby suggesting that its origin is probably due to local deviations from stoichiometry resulting from either SiO₂ or SiC formation.

TEM analysis of the carbon-modified material revealed a homogeneous microstructure with uniformly distributed second phases such as those marked A and B in Fig. 13(a). The average grain size of the MoSi₂ was between 3 and 5 μm, which is much larger than that of the material without carbon. The larger grain size is a temperature-related effect as ternary powder samples consolidated at 1450 °C exhibited submicron grain sizes. EDS microanalysis, with an ultrathin polymeric window, of region A showed the presence of silicon and carbon alone, indicating that these regions correspond to the dark (low Z) regions, such as those shown in Fig. 12. SADP's were obtained along the major zone axes from these and other silicon-rich regions [Fig. 13(b)] and were consistently indexed to the cubic β–SiC structure (with $a = 0.4359$ nm). The β–SiC was present in the form of 1 μm-sized particles located predominantly along grain boundaries and at triple-point regions. Furthermore, the SiC particles were easily distinguishable based on the internal twinning observed (Fig. 14). Although the microstructural origin of these SiC particles is presently not well understood, it is probable that their formation would involve the following reactions: (A) the carbothermal reduction of silica to SiC, and (B) the cooperative displacements of Si and C from MoSi₂ and $C_{<1}Mo_5Si_3$ to form SiC. While the reaction mechanisms for. (A) have been discussed previously[11], the results of the phase evolution studies on the ternary powders do not indicate the formation of SiC within the limits of detection of the XRD. However, the fact that these studies were conducted on loosely packed powders, at atmospheric pressures under flowing argon, as opposed to the consolidation conditions that involve densely packed powders under highly reducing atmospheres, might have precluded effective conversion of silica to SiC. On the other hand, direct reaction between

cooperatively displaced Si and C is also feasible above 1435 °C, based on the DTA data of Singh.[28] In addition to β–SiC, grains of the iron-containing Nowotny phase (region B) were also easily distinguishable, based on their lower ion-milling rates. Most importantly, the grain boundaries also appeared to be free of silica (Fig. 15), although a small amount was occasionally observed within the grains. Contrary to Maxwell's hypothesis that molybdenum carbides would be present in the matrix as a reduction product of MoO₃[7] and in accordance with the 1600 °C isotherms of Nowotny, none of the molybdenum carbides such as MoC and Mo₂C were detected.

D. Thermogravimetric analysis

The results of the thermogravimetric analysis (heating and cooling rates of 10 K/min) of the MA binary (solid line) and ternary powders (dotted lines) are shown in Fig. 16. The top and bottom curves in each set represent the weight changes of the powders during heating and cooling, respectively. While both the samples experienced weight losses above 1200 °C, those exhibited by the C-modified ternary MA MoSi₂ powders were much higher than those of the binary MA MoSi₂ at all temperatures. Examination of the XRD patterns of the binary MA MoSi₂ at temperatures above 1200 °C [Fig. 7(d)] revealed minor amounts of tetragonal Mo₅Si₃, indicating a silicon depleted powder. With the knowledge that the oxygen content of micron-sized MoSi₂ powders is about 1.5 at. %,[7] it is quite possible that the weight losses above 1200 °C are caused by the dissociation of SiO₂ (under very low partial pressures of oxygen) to the volatile SiO. On the other hand, the higher weight losses in the C-modified MA MoSi₂ powders can be ascribed to the presence of carbon. However, the mechanism in this case is the reduction of SiO₂ by carbon to volatile oxides such as CO, CO₂, and SiO.
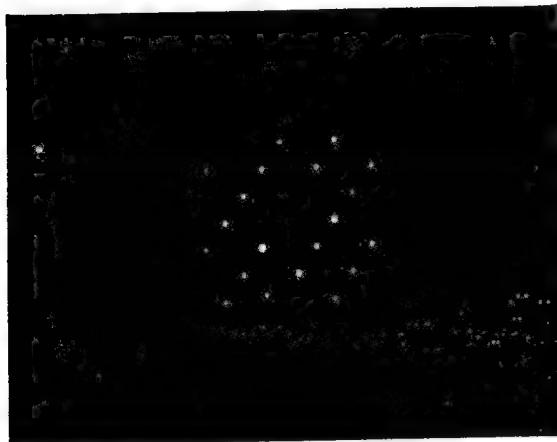
The above data are consistent with the weight losses experienced during the actual hot consolidation of the ternary MA MoSi₂ samples. Vacuum hot pressing of the C-modified samples at temperatures of 1550 °C and

(a)
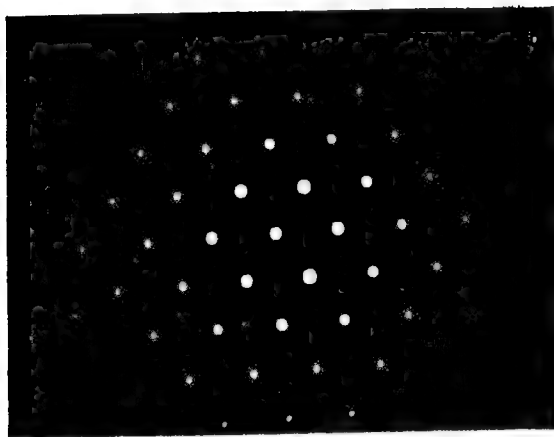
(b)

(c)

FIG. 13. (a) BFTEM of the ternary MA MoSi₂. (b) SADP of β-SiC along $B = [011]$ (region A). (c) SADP of the Nowotny phase along $B = [10\bar{1}0]$ (region B).

below resulted in weight losses near ~ 4%, while higher consolidation temperatures (1700 °C) resulted in a near doubling of the weight loss (~ 8%). However, it should
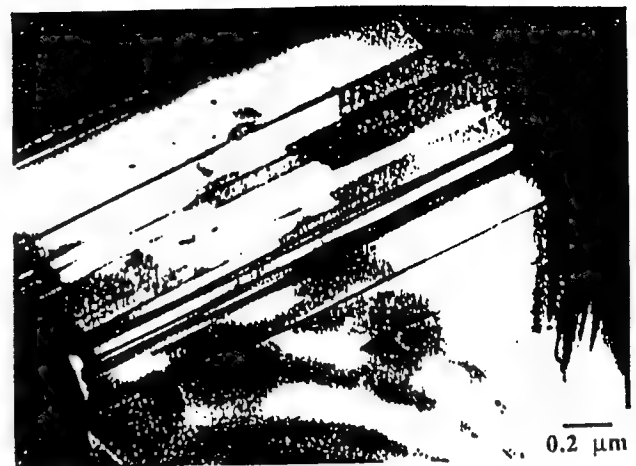

FIG. 14. BFTEM of a β-SiC particle formed in situ in the ternary MA MoSi₂.
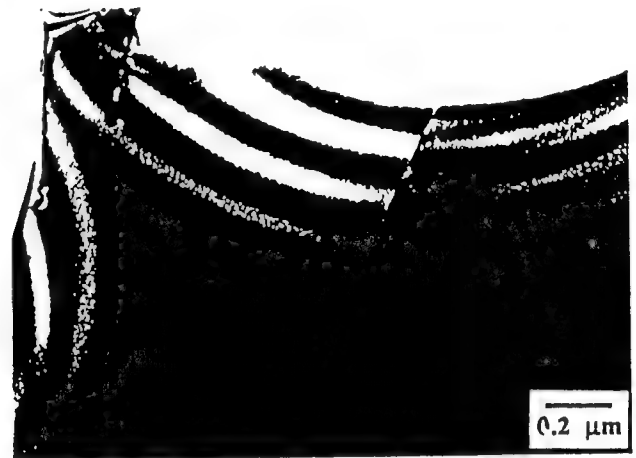

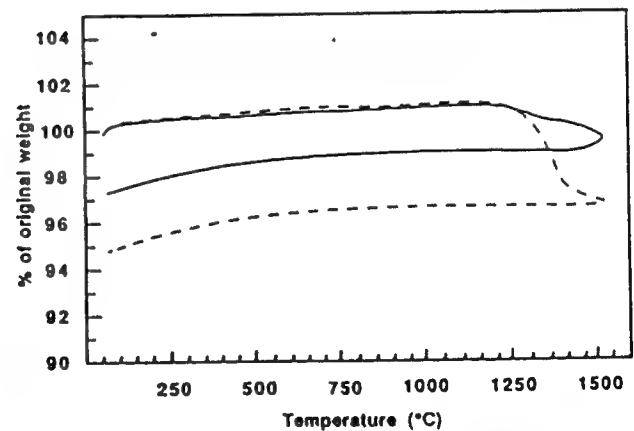FIG. 15. BFTEM of the ternary MA MoSi₂ showing the absence of grain boundary silica.

FIG. 16. TGA of the binary stoichiometric MA MoSi₂ (—) and ternary MA MoSi₂ (Si-28Mo-14C) (---) under flowing argon at a heating and cooling rate of 10 °C/min. The top curve in each set represents heating while the bottom curve represents cooling.

be recognized that the weight losses at temperatures above 1700 °C are caused by the volatilization of silicon from MoSi₂ due to the relatively high vapor pressures of silicon over MoSi₂,[1,2] rather than by the carbothermal reduction of the SiO₂. This implies that while relatively minor weight losses (up to 5%) due to carbothermal reduction of silica are unavoidable, careful control of the consolidation temperature and vacuum levels can be used to prevent substantial weight losses (~40%), such as those reported in previous studies.[8]

E. Significance of the *in situ* reactions

The ability to form silica-free MoSi₂ and MoSi₂-based composites containing micron-sized SiC reinforcements opens up some exciting possibilities. Uniformly dispersed SiC in a modified MoSi₂ matrix should lead to considerable elevated temperature strengthening in addition to improved fracture properties, due to the enhanced resistance to grain boundary sliding brought about by the SiC particles dispersed along silica-free grain boundaries. It is also conceivable that the synthesis of MoSi₂/WSi₂ alloys with carbon additions by means of mechanical alloying would result in improved strengthening due to the synergistic effects of solid solution and dispersion strengthening with *in situ* formed SiC or WC.

Utilization of this strategy holds promise in refractory metal (Nb, Mo, W) toughening also. In these systems, the major problems encountered are the degradation of the diffusion barrier coatings due to reactions with silica, and the severe residual stresses caused by the mismatch in the coefficients of thermal expansion (CTE) between the matrix and the reinforcement phases. Through the use of the ternary MA MoSi₂ powders, it should be possible to form the desired volume fraction of SiC reinforcements *in situ* so as to tailor the effective CTE of the matrix to match that of the reinforcement. For example, the CTE of a refractory metal such as molybdenum or tungsten is intermediate between that of MoSi₂ and SiC. As has been shown by Maloney and Hecht,[29] controlled additions of micron-sized SiC lower the effective CTE of the MoSi₂−SiC composite in accordance with the rule of mixtures and enable the use of refractory metals that have better strength retention at elevated temperatures (such as Mo and W), but are otherwise limited in their use due to their low CTE's. Such an *in situ* modified matrix would also have the added advantage of being free of silica and silicon, compared to composites processed using commercial powders; this should prevent the coating degradation and enhance the useful life of these composites.

V. SUMMARY AND CONCLUSIONS

A processing strategy utilizing carbothermal reduction reactions, mechanical alloying, and carbon additions has been developed for the synthesis of silica-free MoSi₂ and MoSi₂/SiC composites. Using this approach, MoSi₂ and MoSi₂/SiC composites have been fabricated starting from pure elemental molybdenum and silicon powders with and without carbon additions. The structural and morphological evolution of the powders has been studied as a function of milling time. It has been shown that complete attrition is achieved after 29 h of alloying. The resultant powders are micron-sized and contain 4 to 7 nm crystallites of molybdenum, α−MoSi₂, and traces of β−MoSi₂. The addition of carbon to the starting elemental powder mixture suppresses the formation of α−MoSi₂ in the fully milled powders. Minor amounts of iron impurities were also found in the powders due to the contamination from the milling media.

The phase evolution studies of the binary and ternary MoSi₂ powders indicated that β−MoSi₂ is stable to 1020 °C at heating rates of 10 °C/min, in contrast to previous studies on the isothermal annealing of Mo−Si multilayers which demonstrated stabilities to only 800 °C. While minor amounts of tetragonal Mo₅Si₃ were evolved as an intermediate transformation product in the binary MA MoSi₂ powders, the evolution of the ternary MoSi₂ powders showed the formation kinetics of the Nowotny phase $C_{<1}Mo_5Si_3$ to dominate that of tetragonal α−MoSi₂ at lower temperatures. However, temperatures above 1000 °C resulted in the progressive decrease in the amount of these higher molybdenum phases.

Complete consolidation of the MA powders was achieved at 1450 °C. Amorphous silica that is found in all conventional powder-processed matrices was essentially eliminated through *in situ* carbothermal reactions brought about by the additions of carbon through mechanical alloying. It is shown that composites consisting of uniformly distributed micron-sized SiC particles with varying volume fractions can be formed using this approach. Significant grain size differences exist between the microstructures processed from the binary powders and those of the ternary powders, probably due to the higher consolidation temperatures used in the latter. The formation of the iron and molybdenum containing Nowotny phase of the approximate composition $C_{<0.5}Mo_{<4.4}Fe_{0.4}Si_3$ is also reported. The co-existence of the Nowotny phase with MoSi₂ and SiC is in agreement with the isotherm proposed by Nowotny *et al.*, rather than that proposed by van Loo and co-workers.

The possibilities of utilizing MA powders to overcome the CTE mismatch and coating degradation problems in ductile phase composites are discussed. The use of these *compositionally tailored* powders would alter the matrix CTE so as to match that of the ductile reinforcements, thus minimizing the problems of matrix cracking. The absence of silica should also improve the stability of the diffusion barrier coatings of these composites.

ACKNOWLEDGMENTS

REFERENCES

1. T. G. Chart, Metal Science 8, 344 (1974).
2. A. W. Searcy and A. G. Tharp, J. Phys. Chem. 64, 1539 (1960).
3. J. B. Berkowitz-Mattuck, P. E. Blackburn, and E. J. Felten, Trans. Metall. Soc. AIME 233, 1093 (1965).
4. R. M. Aikin, Jr., Scripta Metall. 26, 1025–1030 (1992).
5. P. J. Meschter, Metall. Trans. 23A, 1763–1772 (1992).
6. L. Xiao and R. Abbaschian, Mater. Sci. Eng. A155, 135 (1992).
7. W. A. Maxwell, NACA RM E52B06, 1952.
8. S. Maloy, A. H. Heuer, J. J. Lewandowski, and J. J. Petrovic, J. Am. Ceram. Soc. 74, 2704 (1991).
9. D. A. Hardwick, P. L. Martin, and R. J. Moores, Scripta Metall. 27, 391 (1992).
10. R. B. Schwarz, S. R. Srinivasan, J. J. Petrovic, and C. J. Maggiore, Mater. Sci. Eng. A155, 75 (1992).
11. G. C. Wei, J. Am. Ceram. Soc. 66, C-111 (1983).
12. K. Ishizaki, Acta Metall. Mater. 38, 2059 (1990).
13. Atomic Energy Review, special issue No. 7, edited by L. Brewer (International Atomic Energy Agency, Vienna, Austria, 1980).
14. A. B. Gokhale and G. J. Abbaschian, J. Phase Equilibria 12, 493 (1991).
15. P. Villars and L. D. Calvert, Pearson's Handbook of Crystallographic Data for Intermetallic Phases (ASM, Metals Park, OH, 1985), Vols. 1 and 2.
16. H. Nowotny, E. Parthe, R. Kieffer, and F. Benesovsky, Monatsh. Chemie 85, 255 (1954).
17. E. Parthe, W. Jeitschko, and V. Sadagopan, Acta Crystallogr. 19, 1031 (1965).
18. B. Aronson, Acta Chem. Scand. 9, 1107 (1955).
19. H. Schachner, E. Cerwenka, and H. Nowotny, Monatsh. Chemie 85, 245 (1954).
20. L. Brewer and O. Krikorian, J. Electrochem. Soc. 103, 38 (1956).
21. F. J. J. van Loo, F. M. Smet, and G. D. Rieck, High Temp. High Press. 14, 25 (1982).
22. A. Costa e Silva and M. J. Kaufman, submitted to Metall. Trans., 1993.
23. O. B. Loopstra, W. G. Sloof, Th. H. de Keijser, E. J. Mittemeijer, S. Radelaar, A. E. T. Kuiper, and R. A. M. Wolters, J. Appl. Phys. 63, 4960 (1988).
24. C. M. Doland and R. J. Nemanich, J. Mater. Res. 5, 2854 (1990).
25. F. M. d'Heurle, C. S. Petersson, and M. Y. Tsai, J. Appl. Phys. 51, 5976 (1980).
26. C. C. Koch, personal communication, 1992.
27. G. V. Raynor and V. G. Rivlin, Int. Metals Rev. 30, 68 (1985).
28. M. Singh, presented at the 94th Annual Meeting of the American Ceramic Society, Minneapolis, MN, 1992.
29. M. J. Maloney and R. J. Hecht, Mater. Sci. Eng. A155, 19 (1992).

MICROSTRUCTURAL EVOLUTION IN COMPOSITIONALLY TAILORED MoSi₂/SiC COMPOSITES

S.E. RIDDLE, S. JAYASHANKAR AND M.J. KAUFMAN
University of Florida, Department of Materials Science and Engineering, Gainesville, FL 32611

ABSTRACT

Compositionally tailored MoSi₂/SiC composites with silicon carbide content ranging from 0 to 60 volume percent were synthesized through a novel processing scheme involving the mechanical alloying of elemental molybdenum, silicon, and carbon. The effects of important processing parameters such as the nominal powder composition and the processing temperature on the microstructural evolution during mechanical alloying and subsequent heating are described based on the results obtained from DTA and XRD.

INTRODUCTION

The intermetallic MoSi₂ has long been considered as a potential material for high temperature structural applications [1] due to its high melting point and good oxidation resistance. However, it has low room temperature fracture toughness and limited strength at elevated temperatures. This may be partly due to the presence of grain boundary silica in powder-processed MoSi₂ and MoSi₂-based composites. Accordingly, various techniques have been implemented successfully to reduce the silica content in polycrystalline MoSi₂. They include silica reduction through suitable deoxidants including carbon [1-4], in-situ displacement reactions, ultra-clean processing, and hydrogen surface etching of the powders prior to consolidation.

Recently, a novel processing technique involving carbon additions, mechanical alloying, and in-situ displacement reactions has been used to synthesize silica-free MoSi₂-based composites [4] starting from elemental molybdenum, silicon, and carbon powders. Through the modification of the starting composition, it is possible, using this technique to synthesize MoSi₂/SiC composites with varying amounts of reinforcement.

The aim of this study was to characterize the microstructural evolution of the components during milling and subsequent heating as a function of the nominal SiC composition; such information should allow for better microstructural control during consolidation.

EXPERIMENTAL PROCEDURE

Based on the 1600°C isotherm of Nowotny and co-workers (Fig. 1) [5] and the 1727°C isotherm by Brewer and Krikorian [6], it is clear that ternary powder alloys within the composition limits established by the MoSi₂ + C<1Mo<5Si₃ + SiC three-phase field should form thermally stable microstructures when consolidated at these temperatures. Further description of the processing rationale can be found elsewhere [4]. Accordingly, in the present study, ternary powder alloys were chosen for mechanical alloying in the MoSi₂ + C<1Mo<5Si₃ + SiC three-phase field, with varying amounts of nominal silicon carbide, according to the Nowotny diagram (Fig. 1). The compositions are listed in Table I.

Mechanical alloying was performed in a water cooled Szegvari (planetary type) attrition mill using hardened steel balls as a milling media and a ball to charge ratio of 5:1. Elemental powders of commercial purity molybdenum (99.9 % purity, 3 - 7 μm),

Table I. Nominal composition of ternary powders.

Alloy	Volume % SiC	Atomic Percent
MA 20	20	Si–25.1Mo–12.3C
MA 40	40	Si–17.8Mo–23.2C
MA 50	50	Si–14.4Mo–28.3C
MA 60	60	Si–11.3Mo–33.1C

MA (Mechanically Alloyed)

silicon (99.5% purity, -325mesh), and carbon (99% purity, -325 mesh, crystalline) were obtained from Johnson Matthey and used as starting materials. To minimize contamination during processing, a positive pressure of high purity titanium-gettered argon (oxygen content less than 4 ppm) was maintained in the attritor. The progress of the mechanical alloying process was monitored by withdrawing small amounts of powder after 0, 0.5, 1, 2, 5, 10, 15, 20, 30, 45, and 60 h of milling. The powders were then characterized for structure by XRD.

The transformation characteristics of the fully mechanically alloyed powders were monitored by differential thermal analysis (DTA), which was performed under flowing argon (1cc/min, oxygen content less than 4 ppm) on a Dupont 910-DSC system with heating and cooling rates of 10°C/min. For more detailed

FIG. 1. Schematic of ternary isotherm @ 1600°C of the Mo-Si-C system proposed by Nowotny *et al* [5].

analysis, the fully mechanically alloyed powders of various compositions were heated at 10°C/min under flowing, titanium-gettered argon at 100°C intervals between 400°C and 1400°C and cooled rapidly for subsequent XRD analysis. Structural analysis of the as-alloyed and heat treated powders was carried out using a Phillips APD 3720 diffractometer operated at 40kV and 20mA with CuK_α radiation and digital data acquisition over 2θ ranges from 5–100°.
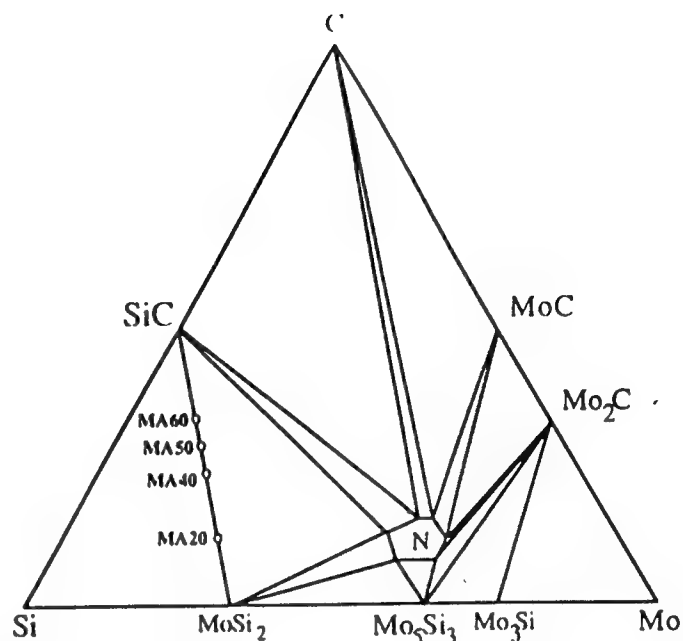
RESULTS AND DISCUSSION

Structural Evolution During Milling

Structural evolution studies of the higher carbon containing powders MA50 and MA60 as a function of milling time, shown in Fig. 2, indicate that only short milling times are required before all carbon goes into solution (0.5 h, see Fig. 2a), while the silicon peaks decrease significantly. Further milling results in a slow decrease in free silicon, probably because silicon is reaching its maximum metastable solubility in molybdenum. This occurs until between 5 and 10 h when the carbides Mo_2C (hexagonal) and SiC (cubic) as well as the intermetallic compounds α–$MoSi_2$ (tetragonal), Mo_5Si_3 (tetragonal), and $C_{<1}Mo_{<5}Si_3$ (hexagonal) are observed (see Fig. 2c). In previous studies, no evidence of carbide formation was observed during mechanical alloying [4], presumably because the compositions were lower in carbon content, in the middle of the $MoSi_2$ + $C_{<1}Mo_{<5}Si_3$ + SiC three-phase field, and away from the $MoSi_2$+SiC two phase field. Milling for 20 h results in the disappearance of Mo_2C and almost complete disappearance of the silicon peaks (Fig. 2d), along with considerable broadening of the α–$MoSi_2$ and SiC peaks; this is probably due to a decrease in the crystallite size rather than lattice strain [7] since α–$MoSi_2$ and SiC are brittle at the milling temperatures [4]. Continued milling through 60 h (Fig. 3c) resulted in a decrease in the molybdenum peaks and minimal increases in peak broadening. Comparing this to 20 h, Fig. 2d and 30 h (not shown) it can be concluded that milling is complete between 20 and 30 h. In order to ascertain the effects of compositional variations along the $MoSi_2$+SiC field, XRD patterns of all fully milled powder compositions were compared using previous work on mechanically alloyed $MoSi_2$ as a reference [4]. Increasing the nominal SiC content tends to suppress the formation and
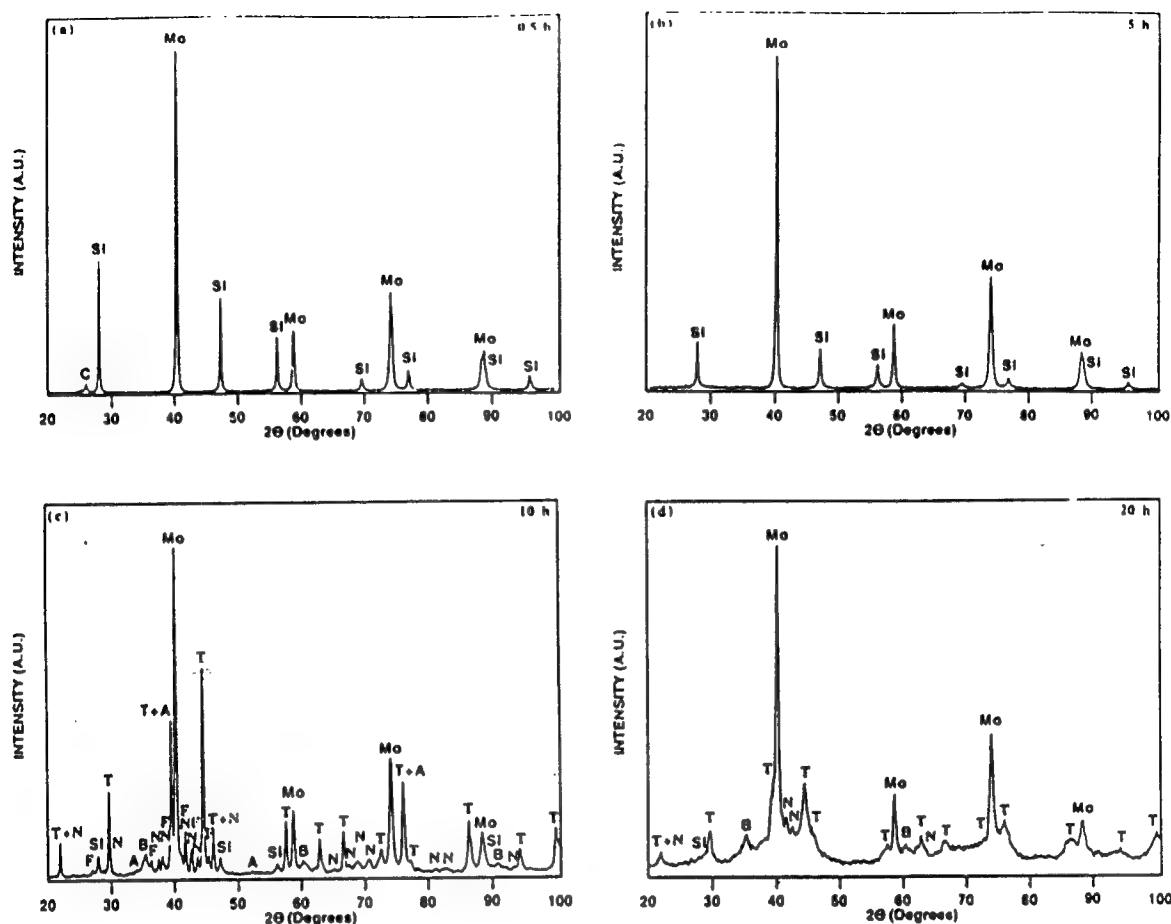
FIG. 2. Structural evolution of MA50 powders as a function of milling time. XRD patterns of the powders milled for the indicated times: (a) 0.5 h (b) 5 h (c) 10 h (d) 20 h (Mo is molybdenum, Si is silicon, C is carbon, A is hexagonal Mo_2C, B is cubic SiC, F is tetragonal Mo_5Si_3, T is tetragonal α–$MoSi_2$, and N is the hexagonal Nowotny phase).

stabilization of both α–$MoSi_2$ and β–$MoSi_2$ while simultaneously promoting the formation of SiC and $C_{<1}Mo_{<5}Si_3$ as seen by comparing the relative peak intensities of the aforementioned phases in Figs. 3a through 3d. It is also important to note that peak broadening increases with increasing nominal silicon carbide content.

Phase Evolution Upon Heating

The phase evolution of all compositions was studied by DTA. A typical heating trace of the MA20 ternary powder is shown in Fig. 4a, where strong exotherms at 480°C, 810°C, 960°C, and 1130°C (peak temperatures) are apparent. The transformations corresponding to these exotherms were studied by XRD analysis of powders heated to temperatures at the end of each exotherm using heating conditions similar to the DTA measurements (10°C/min.). Comparison of the room temperature and 700°C XRD patterns showed the 480°C exotherm is associated with the growth of β–$MoSi_2$ at the expense of molybdenum and dissolved silicon. Likewise, a comparison of the XRD patterns for 700°C and 900°C shows the 810°C exotherm corresponds to the growth of α–$MoSi_2$ and the Nowotny phase at the expense of molybdenum and dissolved silicon and carbon. The minor exotherm at 960°C appears to be associated with the transformation of molybdenum and
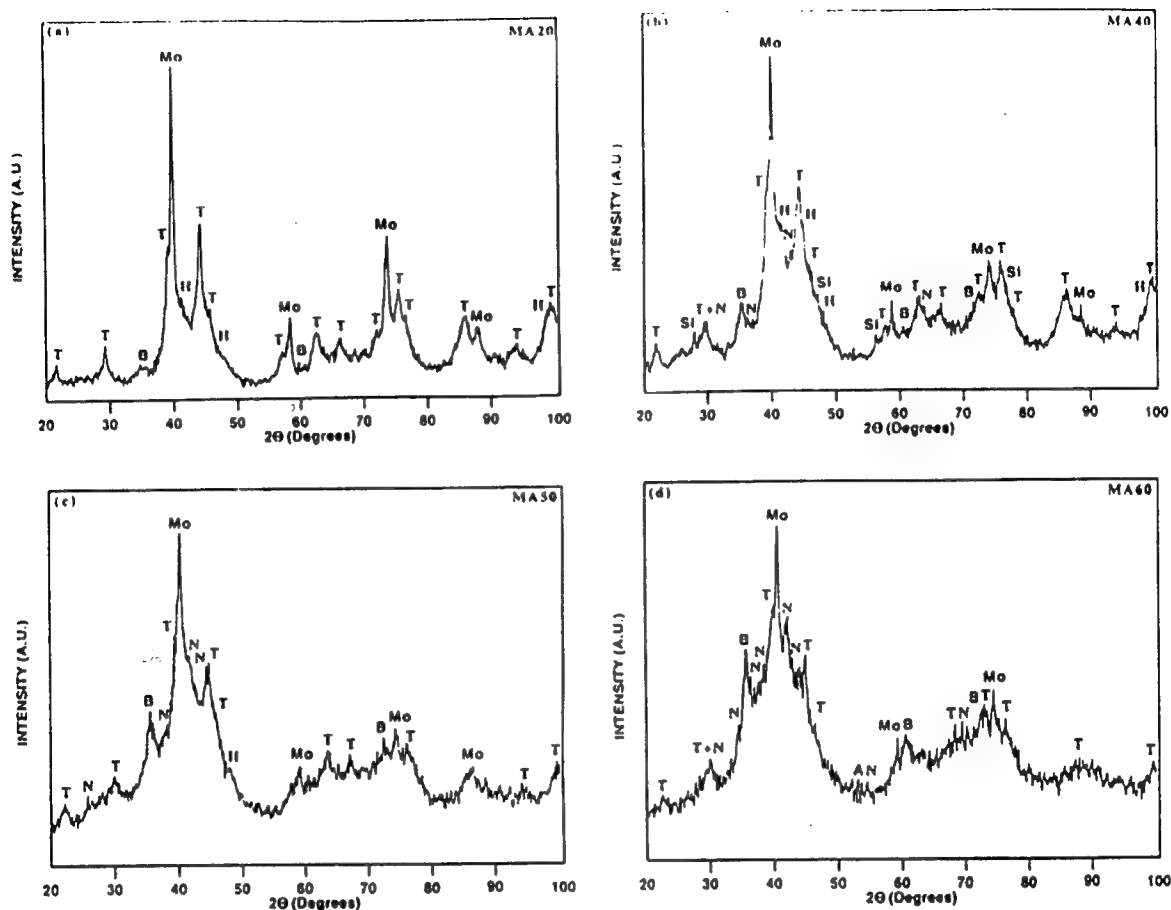
FIG. 3. XRD patterns of fully MA powders: (a) MA20, (b) MA40, (c) MA50, and (d) MA60. Note the relative peak intensities of the various phases present (Mo is molybdenum, Si is silicon, T is tetragonal α–MoSi$_2$, H is hexagonal β–MoSi$_2$, B is cubic SiC, and N is the hexagonal Nowotny phase).

β–MoSi$_2$ to α–MoSi$_2$. Further heating to 1400°C, resulted in a transformation of the Nowotny phase to α–MoSi$_2$ and SiC for the 1130°C isotherm.

Figure 4b shows the DTA trace of the MA60 ternary powder. The evolution is characterized by a weak exotherm at 440°C and strong exotherms at 760°C, 955°C, and 1270°C. The transformation sequences of these powders were monitored in the same manner as the MA20 powders. Comparison of the room temperature and 700°C XRD patterns showed the 440°C exotherm is associated with a partial transformation of molybdenum and the dissolved silicon and carbon into the Nowotny and α–MoSi$_2$ phases. Likewise, a comparison of the XRD patterns for 700°C and 900°C shows the 760°C exotherm corresponds to the growth of the Nowotny phase at the expense of molybdenum and α–MoSi$_2$. The minor exotherm at 955°C appears to be associated with the transformation of β–MoSi$_2$ and Mo$_2$C to α–MoSi$_2$, molybdenum and the Nowotny phase. This was apparent by the reappearance of the molybdenum peaks and the disappearance of the β–MoSi$_2$ peaks. Further heating to 1400°C resulted in a complete transformation of the Nowotny phase to α–MoSi$_2$ and SiC. This 1270°C exotherm is similar to that at 1130°C for the MA20 powders, indicating the greater stability of the Nowotny phase in the higher SiC containing powders. The other two compositions (MA40 and MA50) exhibited exotherms similar to the MA60 powders. XRD analysis between 400°C and 1400°C was performed at 100°C intervals to confirm these similarities and provide any indications of differences in phase stability/constitution. The stability range of β–MoSi$_2$ and the Nowotny phase show the most noticeable differences as a
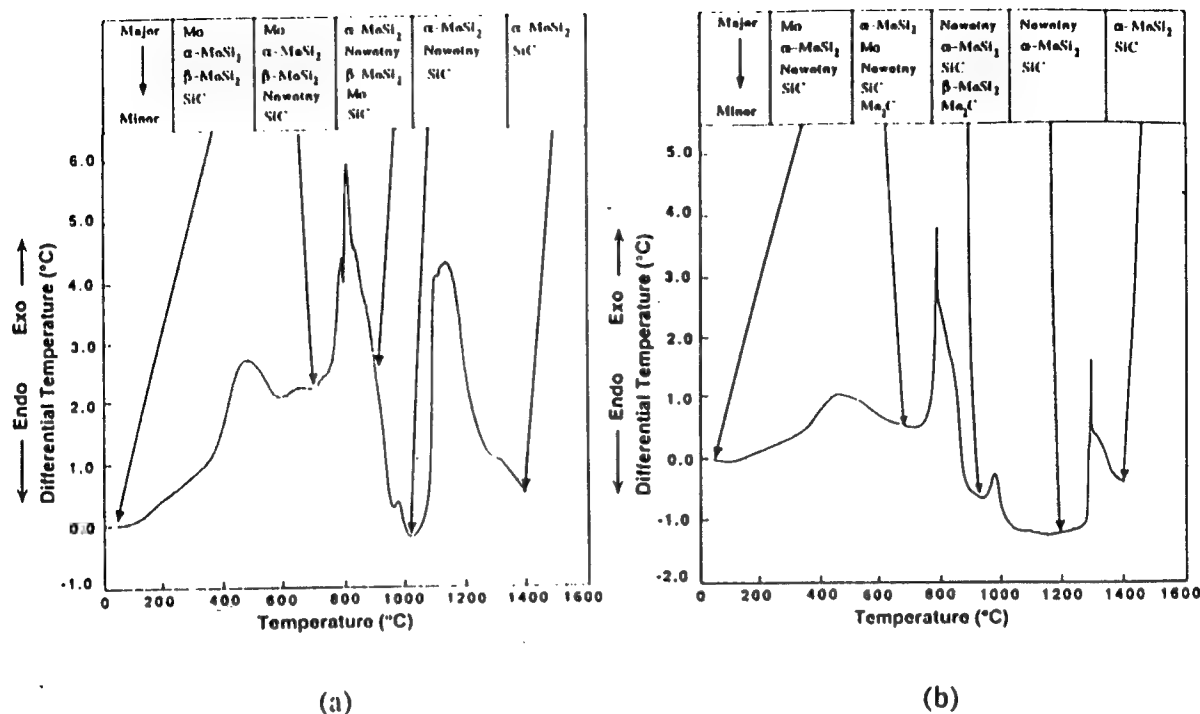
FIG. 4. DTA of MA powders under flowing argon at a heating rate of 10°C/min., along with the corresponding phases identified by XRD: (a)MA20 (b)MA60. ("Nowotny" refers to the Nowotny phase, $C_{<1}Mo_{<5}Si_3$)

function of silicon carbide content. For example, growth of the β–$MoSi_2$ peaks in the MA20 powders occurs up to 800°C and disappears around 1000°C while in the MA40 powders, β–$MoSi_2$ is absent in the as-milled powders but appears by 400°C and continues its growth until between 900°C and 1000°C before it eventually disappears by 1100°C. In the MA50 powders, β–$MoSi_2$ does not appear until 500°C and grows over a larger range to 1000°C before it disappears between 1100°C and 1200°C. Finally, in the MA60 powders, this phase appears only between 700°C and 1000°C. β–$MoSi_2$ has previously been reported to be stable up to 1030°C during mechanical alloying for an alloy with composition Si-28Mo-14C [4] and to 800°C for the isothermal annealing of Mo-Si multilayers [8, 9].

For all compositions, molybdenum is the predominant phase below 800°C while α–$MoSi_2$ becomes dominant above 800°C for both the monolithic $MoSi_2$ [4] and MA20 alloys. Increasing the nominal SiC content above 20% allows for the dominance of the Nowotny phase in the range 800°C–1000°C for MA40, 800°C–1100°C for MA50, and 800°C–1300°C for MA60. The temperature ranges over which the Nowotny phase is dominant was not the only difference observed as a function of silicon carbide content. The appearance, growth, and disappearance of the Nowotny phase are also affected. This phase does not appear until 700°C in MA20 and 400°C in MA40, while it is present in the as-milled MA50 and MA60 powders. The earlier this phase forms, as stated above, the larger is the temperature range over which it is stable. Even with the differences in appearance, growth and dominance, the Nowotny phase is always observed until 1300°C.

While the stability of β–$MoSi_2$ and the Nowotny phase are both affected by an increase in nominal SiC content, the stability of cubic SiC is not. This phase slowly grows to 1400°C with peak refinement above 800°C for all four of the compositions studied.

SUMMARY AND CONCLUSIONS

A novel processing strategy has been developed utilizing carbothermal reduction reactions, mechanical alloying, and carbon additions for the synthesis of $MoSi_2$ composites containing up to 60 volume percent silicon carbide particulate. The microstructural evolution during milling and consolidation has been studied. It has been shown that milling is complete after approximately 20 h. Structural evolution studies during milling have shown that an increase in the nominal SiC content along the narrow $MoSi_2$+SiC field tends to suppress the formation of α–$MoSi_2$ and β–$MoSi_2$ while increasing the formation of SiC and the Nowotny phase ($C_{<1}Mo_{<5}Si_3$) in the fully milled powders. While the milling studies showed the suppression of β–$MoSi_2$ in the fully milled powders, the phase evolution studies indicated an increase in the stability of β–$MoSi_2$ to between 1100°C and 1200°C in the MA50 powders, in contrast to 1020°C in previously reported studies [4] and 800°C reported for the isothermal annealing of Mo-Si multilayers [8, 9]. While the stability of the β–$MoSi_2$ phase increases with increasing nominal SiC content, the Nowotny phase becomes the dominant phase (instead of α–$MoSi_2$) to 1300°C in the MA60 powders.

ACKNOWLEDGMENTS

REFERENCES

1. W. A. Maxwell, *NACA RM E52B06* , (1952).
2. S. Jayashankar, M. J. Kaufman, *Scripta Metallurgica et Materialia* **26**, 1245-1250 (1992).
3. S. A. Maloy, A. H. Heuer, J. J. Lewandowski, J. J. Petrovic, *J. Am. Cer. Soc.* **10**, 2704-2706 (1991).
4. S. Jayashankar, M. J. Kaufman, *J. Mater. Res.* **8**, 1428-1441 (1993).
5. H. Nowotny, E. Parthe, R. Kieffer, F. Benesovsky, *Monatsh. Chemie* **65**, 255 (1954).
6. L. Brewer, O. Krikorian, *J. Electrochem. Soc.* **103**, 38 (1956).
7. B. D. Cullity, Eds., *Elements of X-Ray Diffraction* (Addison-Wesley, Menlo Park, California, (1978).
8. O. B. Loopstra, et al., *J. Appl. Phys.* **63**, 4960 (1988).
9. C. M. Doland, R. J. Nemanich, *J. Mater. Res.* **5**, 2854 (1990).

SYNTHESIS AND PROPERTIES OF *IN-SITU* MoSi$_2$/SiC COMPOSITES

S. JAYASHANKAR, S.E. RIDDLE, AND M. J. KAUFMAN
Department of Materials Science and Engineering, University of Florida,
Gainesville, FL 32611

ABSTRACT

Compositionally-tailored, silica-free, MoSi$_2$/SiC composites with SiC content ranging from 0 to 40 percent were synthesized through a novel processing scheme involving mechanical alloying and *in-situ* reactions for the formation of the reinforcement. Room temperature indentation fracture toughness and hardness measurements were obtained from these silica-free composites and were compared with values obtained from silica-containing, conventionally-processed MoSi$_2$/SiC composites.

INTRODUCTION

Conventional powder processing techniques for the fabrication of MoSi$_2$ result in the incorporation of silica (originally present as a surface layer on the powders) into the consolidated samples. The presence of silica is believed to be detrimental, since the particles may serve as crack nucleation sites at lower temperatures, while enhancing grain boundary sliding at temperatures above the softening point of silica. Additionally, the overall matrix stoichiometry is altered. Considerable efforts have therefore been made to eliminate or control the silica content through the addition of deoxidants such as carbon [1-4] and erbium [5], through clean processing [6,7], and through surface etching of the powders prior to consolidation [1].

In order to achieve the dual objective of silica elimination and control of the stoichiometry, a novel process combining mechanical alloying with the carbothermal reduction of silica has been used to synthesize MoSi$_2$/SiC composites [2,4]. While mechanical alloying would result in a microstructurally uniform and compositionally homogeneous alloy of the desired stoichiometry, the carbothermal reduction would reduce the silica to SiC. Furthermore, MoSi$_2$/SiC composites with varying amounts of SiC could be produced by suitable control of the starting compositions of the powders derived from the mechanical alloying process.

EXPERIMENTAL

Processing

The study focused on the processing and property evaluation of silica-free MoSi$_2$/SiC composites with reinforcement contents of 20 and 40 volume percent (v/o) produced through mechanical alloying and in-situ displacement reactions. For this purpose, elemental powders of molybdenum (3-7 μm, Johnson Matthey), silicon (98% pure, -325 mesh, Cerac), and carbon (99.5 % pure, -300 mesh, Johnson Matthey) were subjected to mechanical attrition for a period of at least 24 hours. The choice of powder compositions was based on the 1600°C isotherm of the Mo-Si-C system as proposed by several workers [8,9] (see Fig. 1). Nominal compositions were chosen in the MoSi$_2$ + SiC + CMo$_5$Si$_3$ (Nowotny phase) three phase field, close to the

MoSi$_2$-SiC tie line so that the volume fraction of undesirable phases would be kept to a minimum; these corresponded to 20 and 40 v/o SiC (hereafter designated as MA20 and MA40). Details concerning the processing rationale and the microstructural evolution during mechanical alloying and hot consolidation can be found elsewhere [4, 10].

To achieve the optimum microstructure in the MA materials, the consolidation process is carried out in two stages. The MA powder is loaded in dies and a very low pressure (less than 10 MPa) is applied on the cold compact, so that the sample has sufficient open porosity for the entrapped gases to escape during the degassing and silica reduction reactions. The sample is ramped up to 1500°C and held at that temperature for at least 30 minutes to deoxidize the matrix. Subsequently, it is heated to 1650°C under an argon environment (7 psi) and densified for an hour under a uniaxial pressure of 35-40 MPa. The pressure on the compact is subsequently released and the sample cooled to room temperature at 10°C/min.

It should be noted that processing variables such as the temperature and the partial pressures need to be carefully controlled while processing

Fig.1 Schematic of the ternary Mo-Si-C isotherm at 1600°C as proposed by Nowotny et al. [9].

MoSi$_2$ and MoSi$_2$/SiC composites. As Fig. 2a clearly indicates, the equilibrium dissociation pressure of Si over MoSi$_2$ increases rapidly above 1650°C [11,12]. Thus, conditions typically present during vacuum hot pressing, such as high temperatures and low vacuum levels would
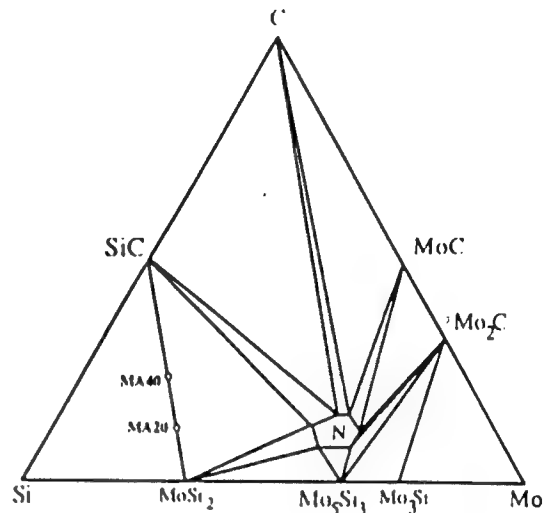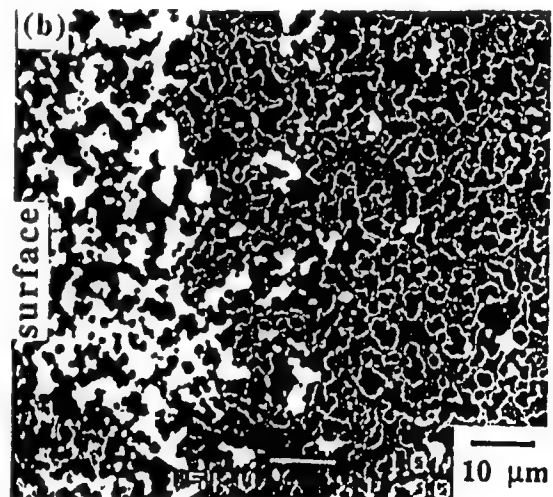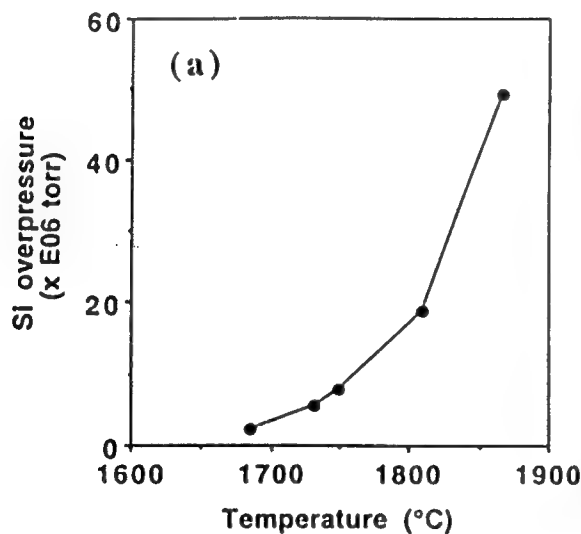

Fig. 2.(a) Equilibrium dissociation pressures of Si over MoSi$_2$, as adapted from [12].
(b) BEI of the surface of a MA40 sample hot pressed at 1700°C, showing silicon depletion. Light phase is the Nowotny phase, grey phase is MoSi$_2$ and dark phase is SiC.

result in the progressive volatilization of elemental silicon from the silicide and result in substantial weight losses. Such a volatilization reaction would be exemplified by the loss of elemental silicon from the surface of the sample, and the resultant formation of a Mo-rich phase

such as Mo_5Si_3 or the Nowotny phase. Fig. 2b is a backscattered electron image of the surface of the MA40 material that had undergone silicon volatilization after being hot pressed under a vacuum of less than 10^{-3} torr at 1700°C for 1 h. Similar effects have been reported during the processing of monolithic $MoSi_2$ [13].

For purposes of comparison, composites with 20 and 40 v/o SiC reinforcement were fabricated using the conventional approach of dry blending $MoSi_2$ (99.9% pure, -325 mesh, Johnson Matthey) and SiC powders (< 1 μm average diameter, 99.9% pure, Cerac) in the appropriate proportions followed by hot consolidation (hereafter designated as C20 and C40). Monolithic $MoSi_2$ was also processed from commercial $MoSi_2$ powder (99.9% pure, -325 mesh, Johnson Matthey). In order to facilitate the meaningful comparison of properties between the conventionally processed and compositionally tailored in-situ composites produced by mechanical alloying, the size distribution of the SiC powders was chosen such that they matched the reinforcement sizes in the *in-situ* processed material. Hot pressing of the conventionally processed composites was performed in graphite dies under a vacuum of 10^{-3} torr or better, with a pressure of 35 MPa at 1600°C for a hold time of 1 h. Subsequently, samples were cooled at the rate of 10°C/min to room temperature.

Specimens for microstructural characterization and Vickers indentation measurements were electro discharge machined, ground to remove the recast layer, and polished to a 1 μm diamond finish. Microstructural analysis of the consolidated samples was performed on a JEOL 6400 SEM equipped with a Tracor Northern EDS unit with light element detection capabilities, while phase analysis of the consolidated mechanically alloyed samples was conducted by XRD using Ni-filtered Cu K_α radiation on a Philips APD 3720 diffractometer with digital data acquisition. Since $MoSi_2$ responds well to polarized light, grain size measurements in the composites and the monolithic material were performed using cross-polarized light microscopy. Bulk density and open porosity measurements were also made on all the hot pressed samples using the Archimedes method with deionized water as the liquid medium.

Hardness and Fracture Toughness

Vickers microhardness indentations, each at least 3 mm apart (to minimize interactions between neighboring cracks) were made on the surfaces of the samples polished to 1 μm diamond finish. The indentation loads spanned a range from 49 N to 245 N for a contact time of 15 s, with a minimum of 4 indentations per indent load per sample. The minimum indentation loads were selected so as to achieve a minimum value of 2 for the ratio of the half penny crack radius (c) and half the diagonal of the Vickers impression, a requirement recommended in conventional practice for toughness measurements by indentation. In the case of the monolithic $MoSi_2$ (examined as a control sample), extensive microcracking around the indenter prevented the formation of well defined cracks for loads up to 196 N, in part due to the large grain size. The lengths of the indent diagonals (2a) and the radial cracks (2c) were measured and the hardness (H) and fracture toughness (K_c) were calculated using the following equations [14]:

$$H = P / \alpha a^2 \tag{1}$$

and

$$K_c = \delta (E/H)^{1/2} (P/c)^{3/2} \tag{2}$$

where P is the peak indentation load, $\alpha = 2$ for a Vickers indenter, δ is a material independent constant ($\delta = 0.016$) and E is the Young's modulus of the material. The Young's moduli of the

composites were calculated using literature values for MoSi$_2$ [15] and SiC [16] and assuming the rule of mixtures behavior (Voight bound).

RESULTS AND DISCUSSION

Bulk density measurements of the various composites prepared during this study show that near full densities (99% or greater) were achieved for the in-situ composites and the conventionally processed (CP) composites for compositions up to 40 v/o SiC. It should be noted that the estimation of the theoretical density of the in-situ composites was made after determining the actual volume fraction of SiC in the composite through standard point count techniques. The results of near-complete densification for the in-situ composites are significant from the standpoint of processing, since it involved the deoxidization of SiO$_2$ and the effective removal of the product gases CO and CO$_2$ in order to avoid gas porosity in the samples.

Microstructures

Fig. 3a shows a backscattered electron image of the hot pressed specimen MA20. The microstructure consists of a uniform distribution of 1-2 μm sized low Z particles dispersed in an intermediate-Z matrix. XRD and EDS analysis together indicated that the low Z phase is SiC, while the intermediate Z phase is MoSi$_2$. In addition, minor amounts (< 1 v/o) of the high Z Nowotny phase were observed. Furthermore, the relative volume fractions of these phases were found to agree very well with the location of the nominal powder compositions in the 1600°C Mo-Si-C isotherm of Nowotny. The grain size of the MoSi$_2$ was relatively uniform and between 6-8 μm. Polarized light microscopy indicated that the SiC particles were located primarily at the MoSi$_2$ grain boundaries. Occasionally, large SiC grains were also observed. Previous TEM analysis of similarly processed material [4] revealed that the grain boundaries were free of the siliceous intergranular phase.

The microstructure of the hot-pressed MA40 alloy (Fig. 3b) shows a dispersion of SiC in the MoSi$_2$ matrix. However, the SiC size is considerably larger and the distribution considerably more inhomogeneous than the MA20 material, possibly due to the diffusion-controlled coarsening of SiC brought about by the smaller interparticle spacing associated with high volume fraction of SiC. Indeed, the presence of necks between adjacent SiC particles as in Fig 3b is indicative of coarsening by coalescence. This coarsening leads to a wider size distribution and a higher mean particle size, and results in a wide variation in the MoSi$_2$ grain size distribution due to varying Zener drag on the grain boundaries. The MoSi$_2$ grain size varies between 2 and 7 μm, with the mean grain size close to 5 μm The SiC is irregularly shaped, with a size range from 1 -10 μm.

The microstructures of the conventionally-processed (CP) composites C20 and C40 are shown in Figs. 4a and 4b and are typified by an inhomogeneous distribution of the SiC particles. These microstructures are characterized by particle-free islands of MoSi$_2$ surrounded by a network of irregularly shaped SiC particles. It should be recognized that in this case, the inhomogeneous distribution is due to the relative starting powder sizes of the MoSi$_2$ and SiC. The size of the SiC is much greater than the initial starting size of less than 1 μm, indicative of its coarsening during consolidation. Both of these microstructures are exemplified by a wide distribution of matrix and reinforcement grain sizes. The C20 composite has a MoSi$_2$ grain size range ranging from 2 - 10 μm, with a mean of 7 μm, while for the C40 composite, these values

range from 2 - 8 μm, with a mean of around 5 μm. These relatively wide distributions in the matrix and reinforcement grain sizes are significant since they may enhance the magnitude of the thermal mismatch stresses between the two phases.
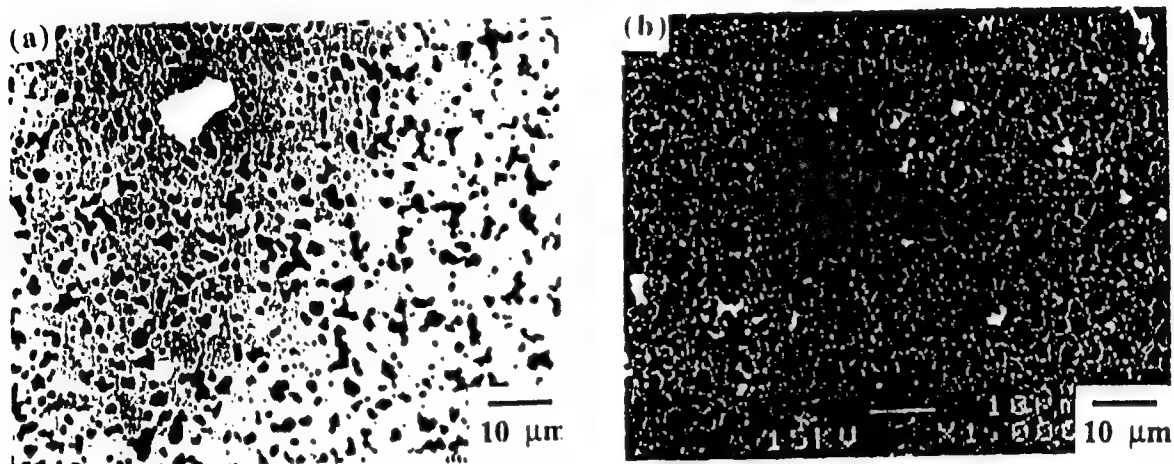

Fig. 3 BEI of (a) MA20 and (b) MA40. Phase designations are the same as that of Fig. 2b.
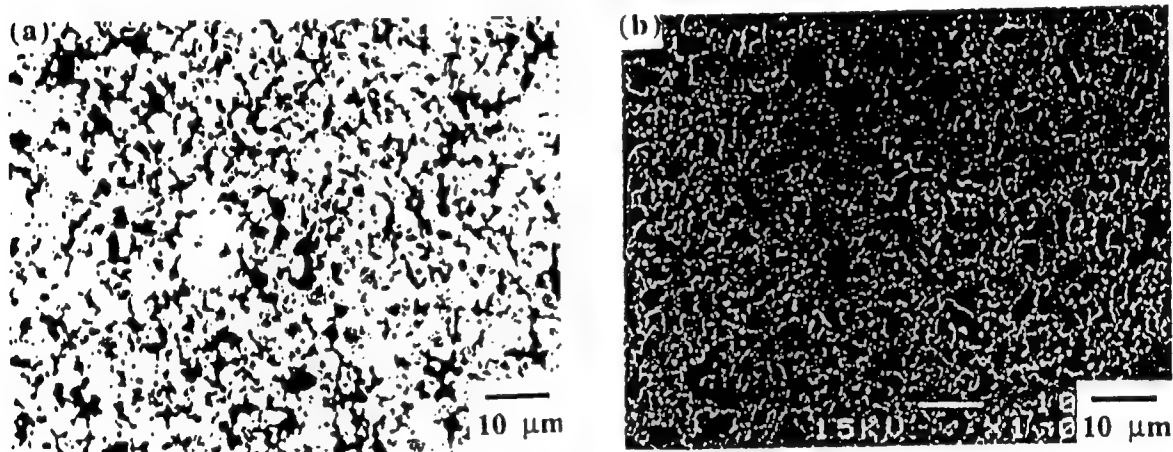

Fig. 4 Secondary Electron Image of (a) C20 and (b) C40.

Properties

Fig. 5 shows the variation of the Vickers Hardness as a function of reinforcement content of the composites. For the purpose of comparison, the hardness of the composites as predicted by a simple rule of mixtures is also plotted. It should be noted that while the hardness values of single phase $MoSi_2$ (~20 μm grain size) studied in this investigation is 8.56± 0.5 GPa, a slightly higher value was used in the rule of mixtures calculation in order to account for the smaller grain size of the matrix in the composites (~10 μm or less). Indeed, previous studies [13] on monolithic $MoSi_2$ have shown the hardness to be structure sensitive, with slight increases with decreasing grain size. The hardness value of SiC used in the rule of mixtures estimation was 25 GPa [17].

The results show that the room temperature hardnesses of the $MoSi_2$/SiC composites increase with increasing SiC content. For all reinforcement contents, the hardnesses of the in-situ composites were slightly higher than the CP composites, with the difference increasing with increasing reinforcement content. Microstructural comparison between the CP and in-situ processed composites at 40 v/o SiC loading show no marked differences in the matrix or

reinforcement grain sizes or in their spatial distribution to account for the observed differences. However, it may be of significance that the content of the intergranular silica phase in these composites are substantially different, with the MA material containing little or no silica. Specifically, the presence of the viscous glass phase at elevated temperatures might play a significant role in the relaxation of the thermal contraction stresses generated during cooldown by the CTE mismatch between the reinforcement and matrix phases.

Fig. 5 Vickers Hardness of CP and MA composites as a function of SiC content.

Figs. 6a and 6b shows the variation of the fracture toughness with SiC content for the in-situ processed and CP composites respectively for various indentation loads, with each data point representing the average of at least 4 indentations. It is seen that the fracture toughness of the in-situ composites monotonically increases through 40 v/o of reinforcement, while the toughnesses of the CP composites seems to saturate at around 20 v/o and remains constant thereafter. This trend in the toughness variations with increasing reinforcement content for the conventionally processed material is consistent with earlier data [18]. Furthermore, the peak toughness values obtained in the composites processed using the CP as well as the MA approaches are almost identical at around 4.5 MPa. m$^{1/2}$. This is possibly the limit of toughening for SiC particulate reinforced MoSi$_2$.

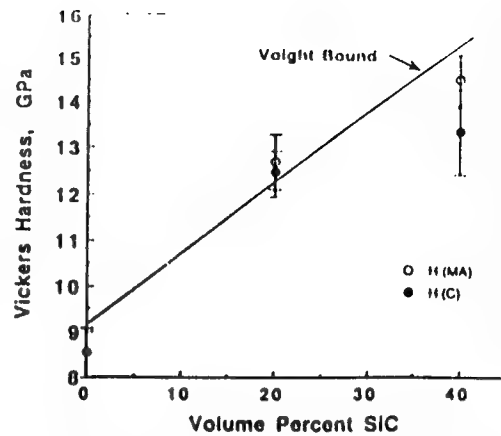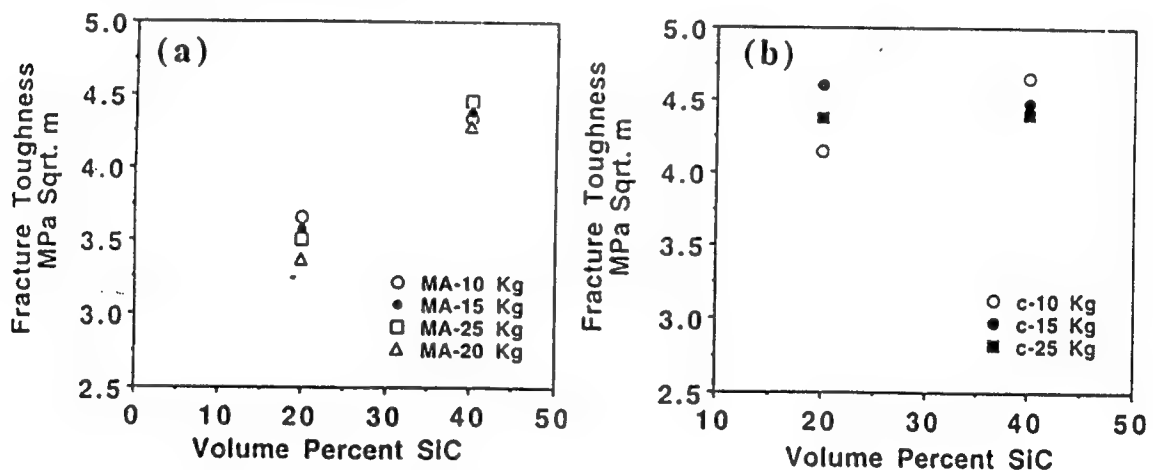Fig. 6 Indentation fracture toughnesses of (a) MA and (b) CP MoSi$_2$/SiC composites as a function of SiC content.

The data in Figs. 6a and 6b also indicates that the toughnesses are constant and do not show any variations with the crack length, at least for the range of indentation loads used in this investigation. The only possible exception to this trend is the indentation response of the C20 material, which seemingly shows a marginal increase in K$_c$ with indentation load.

Microstructural observations of the crack path seem to support the trends in the toughness values. Examination of the crack path of the MA20 material under polarized light as well as in

the SEM (Fig. 7a) revealed that the crack propagation was relatively straight, with a substantial portion of the crack length being transgranular and through the silicide matrix. A limited amount of crack deflection was also evident. For the most part, the cracks appeared to propagate through the matrix, and in some instances, the crack cut through the SiC particles. The absence of any interfacial debonding along the MoSi$_2$/SiC interface suggests that the strength of this interface is high and hence, does not contribute to toughening.
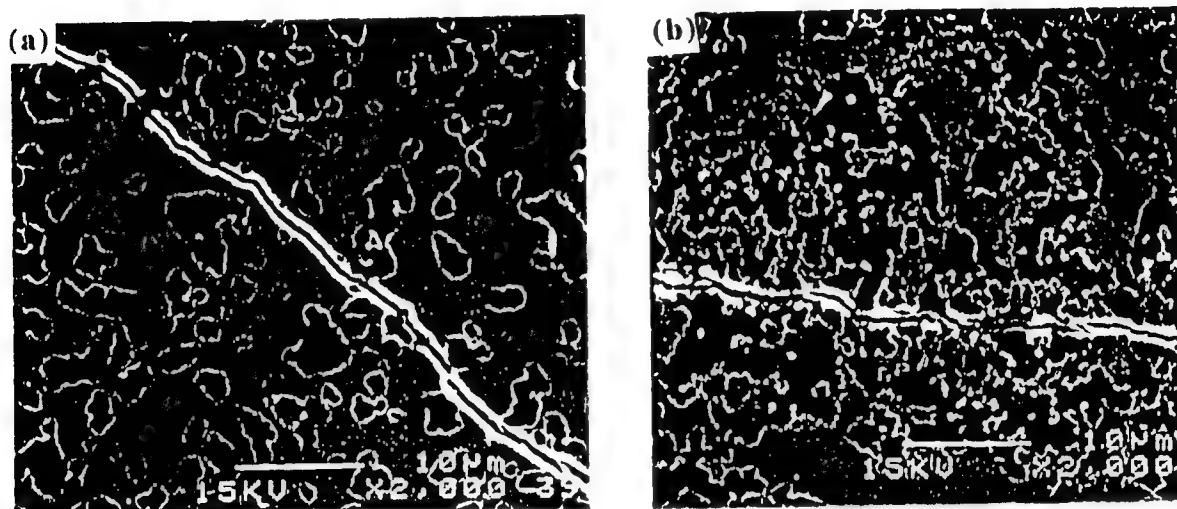

Fig. 7 Crack path arising from a Vickers indentation in (a) MA20 and (b) C40 composite.

Investigation of the crack path in the microstructures of the C20, C40 and MA40 materials showed that all three materials displayed similar crack-microstructure interactions. Considering the C40 material as a representative example (Fig. 7b), a small amount of crack deflection due to the SiC particles is observed. Evidence of some crack branching is seen, although it does not appear to be extensive. A larger portion of the crack segments were observed to run along the MoSi$_2$/SiC interface as well as through the SiC particles, when compared to the MA20 material. Presumably, these differences could have contributed to the increased toughness in the case of the C20, C40 and MA20 materials. Alternatively, it is also conceivable that the large differences in the CTEs between the MoSi$_2$ and SiC at the processing temperatures ($\Delta\alpha = \sim 4 \times 10^{-6}$ at 1000°C) could lead to thermally-induced microcracking, thereby contributing to increased toughnesses, with the magnitude of the thermal mismatch stresses being higher for a wide grain size distribution, such as the C40 and MA40 materials than for a uniform, fine grained microstructure such as the MA20. The propagation of the cracks through the SiC particles rather than being deflected around them is also not surprising since the lower CTE of the SiC particles compared to the matrix would cause radial compressive stresses within the SiC particles and tensile hoop stresses around the SiC particle in the MoSi$_2$ matrix thereby causing the crack to be attracted towards the particles [19].

The results of the room temperature indentation fracture toughness measurements thus seem to indicate that the intergranular glass phase does not influence the toughness as much as the uniformity of the microstructure. However, it should be noted that K_c determinations based on direct crack length measurements are rather inaccurate and have a high degree of error. Additional testing using at least one other large crack technique will be necessary to verify the trends in toughnesses.

SUMMARY AND CONCLUSIONS

$MoSi_2/SiC$ composites containing up to 40 v/o SiC have been fabricated using a novel processing technique involving mechanical alloying, carbothermal reduction of silica and in-situ displacement reactions. These composites are essentially free of grain boundary silica that is otherwise present in powder processed $MoSi_2$ matrix composites which have not been deoxidized. Homogeneous distributions of the reinforcing phase are observed for SiC contents up to 20 v/o, while higher loadings lead to inhomogeneities brought about by the diffusion-controlled coarsening of the SiC due to reduced interparticle distances. Preliminary property evaluations using indentation measurements indicate that the peak room temperature fracture toughnesses for the silica-free $MoSi_2/SiC$ composites are similar to those of the CP composites indicating that microstructural uniformity, rather than the presence or absence of silica, controls the toughnesses in these composites.

ACKNOWLEDGMENTS

REFERENCES

1. W.A. Maxwell, NACA RM E52B06, 1952.
2. S. Jayashankar and M. J. Kaufman, Scripta Metallurgica et Materialia, 26, 1245 (1992).
3. S.A. Maloy, A.H. Heuer, J.J. Lewandowski and J.J. Petrovic, J. Am. Ceram. Soc. 74, 2704 (1991).
4. S. Jayashankar and M. J. Kaufman, Journal of Materials Research, 8, 1428 (1993).
5. D.P. Mason and D.C. Van Aken, Mat. Res. Soc. Symp.Proc. 273, 289 (1992).
6. D.A. Hardwick, P.L. Martin and R. J. Moores, Scripta Metall. 27, 391 (1992).
7. R. B. Schwarz, S.R. Srinivasan, J. J. Petrovic and C. J. Maggiore, Mater. Sci. Eng. A155, 75 (1992).
8. A. Costa e Silva and M. J. Kaufman, to appear in Met. Trans. 25A (1994).
9. H. Nowotny, E. Parthe, R. Kieffer and F. Benesovsky, Monatsh. Chemie 85, 255 (1954).
10. S. E. Riddle, S. Jayashankar and M.J. Kaufman, Mat. Res. Soc. Symp. Proc. (this proceedings).
11. T. G. Chart, Metal Science 8, 344 (1974).
12. A.W. Searcy and A. G. Tharp, J. Phys. Chem. 64, 1539 (1960).
13. R. K. Wade and J. J. Petrovic, J. Am. Ceram. Soc. 75, 3160 (1992).
14. G.R. Anstis, P. Chantikul, B.R. Lawn and D. B. Marshall, J. Am. Ceram. Soc. 64, 533 (1981).
15. M. Nakamura, S. Matsumoto, and T. Hirano, J. Mat. Sci 25, 3309 (1990).
16. "Engineering Property Data on Selected Ceramics, Vol. 2, Carbides", Metals and Ceramics Information Center Report No. MCIC-HB-07 vol II, Batelle Columbus Laboratories, Columbus, Ohio, (1979).
17. Y. Ohya, M.J. Hoffman, and G. Petzow, J. Am. Ceram. Soc. 75, 2479 (1992).
18. A. K. Bhattacharya and J.J. Petrovic, J. Am. Ceram. Soc. 74, 2700 (1991).
19. R. Rice, Ceram. Eng. Sci. Proc. 8, 605 (1987).

Superplastic MoSi$_2$/SiC Composites?

S. Jayashankar and M. J. Kaufman

DRAFT

High temperature bend tests were conducted on the conventionally-processed (CP) and the *in-situ* processed (ISP) MoSi$_2$/SiC composites (20 v/o). The tests revealed an abrupt transition from brittle to ductile behavior between 1100°C and 1200°C for both the conventionally processed and the *in-situ* composites, such that the tensile surface of the bend bar exhibited strains between 5 and 10% (Fig. 1). Furthermore, the outer fiber stresses (i.e., the applied load) remained constant for the entire duration of the deformation, suggesting the likelihood of superplasticity.

To further investigate the possibility of superplastic flow and to gain insight into the mechanisms of flow in this temperature range, compression tests were conducted in argon at 1300°C. Compression strain rate change (SRC) tests were performed to determine the value of the stress exponent, n. Rectangular parallepiped specimens of nominal dimensions 4 x 4 x 8 mm were prepared by electrodischarge machining specimens, such that the testing direction was perpendicular to the hot pressing direction. Tests were performed on both the silica-free and silica-containing composites at 1300°C at strain rates ranging from 4×10^{-6} sec^{-1} to 4×10^{-4} sec^{-1}. Other single strain rate (SSR) compression tests were also performed, with the aim of validating the flow stress values (and hence the stress exponents) obtained from the SRC tests. The stress-strain curves for the SRC and SSR tests exhibited yielding behavior at 1300°C, with the flow stress remaining constant thereafter. In the case of the silica-free material, some flow softening occurred for strain rates at or above $\sim 1.2 \times 10^{-4}$ sec^{-1} in the SRC tests, indicative of concurrent microstructural damage. The silica-containing material, on the other hand, did not exhibit flow softening, even at the highest strain rates tested. The flow stress for each strain rate was determined after the sample had undergone a minimum strain of 0.03 to 0.04 at the desired strain rate. Stress exponents were

determined by analysis of the flow stress - strain rate relationships.

The underlying assumptions behind the assessment of the deformation mechanisms based on SRC experiments are (a) the deformation of a prior stage of the SRC test has no effect on the deformation (hence the flow stress) of the subsequent stages (assumption of no prehistory effect on the deformation) and (b) the flow stress after 0.03-0.04 strain at each strain rate is indicative of the steady state corresponding to that strain rate. Excellent agreement was obtained between the flow stress values obtained at the highest strain rates of the SRC test with those obtained with the corresponding strain rate in the SSR test, thus validating the assumption of no prehistory effects on subsequent deformation. Strain rate decrement tests were conducted subsequent to the incremental strain rate tests, and, in this case, the flow stresses corresponding to each strain rate (upchange and downchange) showed reasonable agreement, indicating that these flow stress values could be used with reasonable certainty to establish the stress exponents and flow mechanisms.

The results of these SRC experiments are plotted in Fig. 2. The reader is cautioned that these results are preliminary at this point in time and that additional mechanical testing and microstructural analysis are underway to validate the accuracy and reproducibility of the measurements reported, as well as to clearly elucidate the deformation mechanisms. Nevertheless, the significance of our preliminary results warrant their inclusion in this report.

Several inferences can be drawn from this figure and these are described below:

(1)   Conventionally-processed $MoSi_2/20$ v/o SiC material (silica containing): The stress exponent for creep starts around ~ 3.5 to 3.7 for low strain rates (from 4×10^{-6} to 1.6×10^{-5} sec^{-1}) and transits to ~2.3 at higher stresses and strain rates. The microstructure of the conventionally processed composite is exemplified by a matrix whose grain size ranges from 2 μm to 10 μm, with the mean grain size of around 7 μm. The microstructure is characterized by the presence of particle free islands of the matrix surrounded by regions of SiC particles.

(2)   In-situ processed $MoSi_2/$ 20 SiC (silica-free) material: The deformation behavior

of this material is characterized by a stress exponent which gradually varies from ~2.7 at low strain rates (~10^{-6}sec^{-1}) to ~2 at strain rates of 10^{-5} - 10^{-4} sec^{-1}. It should be noted that the matrix grain size of this material is between 5 and 7 μm and the reinforcement size is between 1 and 3 μm. Furthermore, the SiC particles are located at the grain boundaries and triple points.

(3)   Creep exponent behavior: The stress exponent of most metals and ceramics normally increases with increasing stress and strain rate. In the case of the present materials, both of which are relatively fine grained (~ 5 to 7 μm), the stress exponents decrease with increasing stress and strain rate, contrary to the normally expected behavior, and to the trends of stress exponents on coarse grained (~ 30 μm) MoSi$_2$ and MoSi$_2$/SiC composites reported by other investigators. The decreasing stress exponents probably imply a set of deformation processes which act in series, with the slowest process determining the rate of deformation. The transition in slopes would therefore imply a shift in the slowest mechanism from one process to another. It remains to be explored whether the transit from one slope to the next occurs at a definitive stress level, and whether the silica content in the matrix has any influence on the magnitude of this transit stress for a constant grain size of matrix and reinforcement. It is as yet unclear whether the non-wetting intergranular phase wets the grain boundaries at elevated temperatures or whether it spreads as a thin film. Regardless of the deformation mechanism and the wetting behavior, the present results clearly indicate that the intergranular glass phase effects the flow properties of the MoSi$_2$SiC composites in the range of grain sizes explored. The interplay between the grain size and the silica content in effecting the deformation modes is also unknown, although it is conjectured that the effect of non-wetting silica on grain boundary sliding mechanisms would progressively diminish at larger grain sizes. It is also likely that increasing grain sizes in the silica-free material would lead to a transition from diffusional processes to dislocational processes at a particular temperature.

(4)   Superplastic behavior?: The trends in the stress exponents (n values tending close to 2) of both the conventionally processed material as well as the in-situ material

are indicative of a high strain rate sensitivity. This stems from the deformation mechanism which is normally associated with stress exponents close to 2, namely, grain boundary sliding, accommodated by either grain boundary or bulk diffusional mechanisms. A common prerequisite for superplastic flow (structural as opposed to transformation superplasticity) in most materials is a high strain rate sensitivity (m ~0.5 to 1, i.e., n = 1/m ~ 1 to 2), a relatively high homologous temperature of deformation ($T_h > 0.5$) and a relatively fine grain size of less than 10 μm. The first requirement is mandated by the need for uniform neck-free deformation, which necessitates a large dependence of the flow stress on the strain rate (and hence high strain rate sensitivities), while the latter requirements are based on the need to accommodate the deformation due to grain boundary sliding (typical of superplastic flow), by concurrent bulk (Nabarro-Herring) or grain boundary (Coble) diffusional processes, with the appropriate grain size dependencies of the creep rate (p=3 for Coble creep, and p=2 for Nabarro Herring Creep). From a physical perspective, continuity of adjacent grains during deformation by grain boundary sliding has to be accommodated for by the diffusion of atomic species within the length scale of the boundaries and within the time scale as dictated by the imposed strain rate on the process. These requirements would be met by a combination of factors such as fine grain sizes (and hence small diffusional distances) and / or high diffusivities (brought about by high homologous temperatures). It is to be noted that for the case of compounds and intermetallics, the diffusivity requirement of the *slowest* moving species *must* be met in order to achieve accommodated grain boundary sliding.

Yet another requirement for tensile superplasticity is the need for a lack of intergranular brittleness, since large deformations would otherwise not be possible. In the case of $MoSi_2$, numerous single crystal studies have shown the activation of sufficient slip systems at these temperatures in order for this requirement to be satisfied.

In the case of most ceramic systems such as Al_2O_3, ZrO_2, and SiC which have been shown to exhibit superplasticity, the low diffusivities and the high melting points dictate that the diffusional distances be short for accommodated grain boundary sliding. This is perhaps why these materials exhibit superplastic flow in the regime of ultrafine (<1 μm) grain sizes. Our results on $MoSi_2$ indicate the possibility of accommodated

grain boundary sliding processes in grain size regimes between 5 -10 μm at 1573°C (T_h~0.7). These are perhaps indicative of the relatively high diffusivities of the major species in this system, viz. Mo and Si at these temperatures.

Another noteworthy point is the fact that the high strain rate sensitivity is exhibited at moderate strain rates in both the materials at a temperature of 1300°C. The silica-free material with an average grain size of 5 μm shows promise of superplastic workability within the processing window at temperatures of 1350°C. While the focus of our present experiments was in obtaining silica-free microstructures without any consideration whatsoever being given to minimize the grain size while processing, it is quite conceivable that the workable temperature range of the silica-free material would be lowered, if adequate reductions in the grain size were achieved from their present levels. It should be mentioned that the optimum working temperature range that would be desired for hot working would be in the range of 1200°C, since the tooling capabilities that exist for the working of molybdenum and nickel based alloys could then be used. Even with the current grain size levels of 5 μm, an increase in temperature by about 50 to 100°C from the current 1300°C levels would make superplastic deformation feasible at reasonably economical strain rates and low flow stresses for the silica-free material, as defined by the processing window in Fig. 2. Improvements in the creep strength and lowering of the creep rates subsequent to superplastic working could be achieved by appropriate grain growth treatments that would shift the deformation mechanism from the grain boundary sliding regime to one involving dislocation creep. The limiting grain size that could be derived through grain growth would, of course, be controlled by the volume fraction and particle size of the SiC, approximately following the Zener relation, $R_{MoSi2} = (4r_{SiC})/(3f_{SiC})$. The volume fraction of SiC desired for optimum creep strength could then be controlled by simply controlling the composition of the mechanically alloyed powder as detailed elsewhere.

It should be pointed out that flow softening has been reported in $MoSi_2$ for temperatures as low as 900°C and that deformation under constant flow stress has been reported in plasma sprayed $MoSi_2$/SiC at 1300°C. The former was attributed to large scale microcracking during the compressive deformation of large grain samples due to unaccommodated grain boundary strains possibly resulting from an insufficient number

of slip systems at these temperatures. The latter is presumably due to substantial amounts of silica in these materials. While the latter would also lead to high strain rate sensitivities, it seems probable that the deformation in this case is due to liquid enhanced sliding due to the viscous glass phase (Rachinger sliding). Such a scenario could imply the high temperature strength of the material would be indirectly dictated by the strength of the deforming phase, i.e. silica, thereby questioning the viability of the processing routes. Thus, our results on high strain rate sensitivity in silica-free $MoSi_2/SiC$ composites are thus perhaps the first demonstrable evidence of superplasticity due to diffusionally accommodated grain boundary sliding in the $MoSi_2$ system, with the concomitant possibilities of superplastically forming a material with superior properties above 1200°C.

It should also be noted that the flow stresses for the ISP composite, having a comparable grain size to the CP composite, are significantly higher than that of the CP composite at all strain rates, with the magnitude of the difference increasing at higher strain rates, within the range of our experimental results. Our results also run counter to the only known investigation of the effect of a non-wetting phase on the creep properties, where it was reported that the deformation mechanisms remained unchanged in deformation experiments performed across the melting temperature of the non-wetting intergranular phase.

In an earlier report, it was conjectured that the formation of in-situ SiC reinforcements on the grain boundaries and triple points, resulting from the carbothermal reduction of silica, would enhance high temperature strength by virtue of the SiC particles serving to pin the grain boundaries against sliding. The current work seemingly demonstrates the operation of the grain boundary sliding process in both classes of materials, especially the in-situ composites, thus negating this hypothesis. However, it is quite possible that the SiC particles do enhance the resistance to grain boundary sliding, which in turn would be manifest in higher activation energies for the process, when appropriately measured.

Finally, it should be pointed out that the processing route has a significant bearing on the properties measured in this section of the investigation. As noted in the early sections of this report and elsewhere, structural superplastic flow requires uniform

deformation which imposes stringent requirements on the material microstructure insofar as near uniform grain sizes and uniform chemical homogeneity are required; otherwise shear bands might be nucleated at heterogeneities which, in turn, would lead to non-uniform deformation and subsequent loss of superplastic characteristics. The current investigation utilized the mechanical alloying, characteristically producing fine powders not only of precise and homogeneous composition and stoichiometry, but also of uniform structure; this, in turn, insured the formation of the chemically and microstructurally homogeneous fine grained microstructures so very essential for the properties demonstrated in this work. The use of the fine powders derived from mechanical alloying would also enable the use of lower consolidation temperatures and thence to a fine grain sized material and superplasticity.

The possibility of superplasticity in the silica-containing material, while having negating implications in the high temperature regime (T>1200°C), nevertheless has important applications in the processing of $MoSi_2$-based materials for use in the lower temperature regimes below the softening temperature of silica. As has been clearly demonstrated in this and numerous earlier reports, the presence of the viscous intergranular phase promotes grain boundary sliding, thus enhancing the formability of the material at lower temperatures through superplastic forming mechanisms. This work has also demonstrated that the presence of the non-wetting intergranular phase has a negligible (if not a benefic) effect on the fracture properties extending from room temperature up to the BDTT. Also considering the passivity of the silica to most chemical environments in addition to all the above mentioned facts, it would be well worth considering forming fiber reinforced, silica-containing, fine grained $MoSi_2$ based composites for low temperature (600°C< T <1000°C) applications, with the fiber reinforcement providing the necessary toughening at the lower temperatures. Such a process would of course exploit the superplastic forming characteristics endowed by the silica on the forming process. Considering other important factors such as fiber stability and fiber-matrix interactions that would accrue at the high processing temperatures, it should be possible to further lower the superplastic forming temperature by modifying the glass transition temperature (hence the superplasticity onset temperature) through the addition of suitable network modifiers to the silica.

The likelihood of the existence of a viable superplastic forming regime at reasonably low temperatures around 1350°C for $MoSi_2$ opens up a plethora of processing-related opportunities. For instance, it would be possible to perform a whole range of operations ranging from sinter forging to net shape extrusion and diffusion bonding of $MoSi_2$-based composites, besides unlocking avenues in the superplastic forming of SiC fiber reinforced composites. The major drawback limiting the use of SiC fibers such as Nicalon* in the reinforcement of high temperature materials has been their poor elevated temperature stability due to their high oxygen content. This imposes severe processing constraints in attempts to incorporate them into matrices. For instance, Nicalon* can withstand a processing temperature of 1425°C for a maximum of 20 minutes of infiltration by silicon, before suffering irrecoverable degradation. Consequently, the use of fibers is restricted to relatively low temperature processes such as CVD, CVI, RVI, plasma spraying, reactive melt infiltration, and similar net-shape capable processes, which do not expose the fibers to such high processing temperatures, but are nevertheless plagued by such factors as slow deposition/reaction rates and incomplete reactant conversion, which consequently limit their utility in scale-up efforts. With the apparent superplastic phenomenon in the silica-free $MoSi_2$SiC composites, it should be possible to form SiC fiber reinforced $MoSi_2$/SiC composites by the alternate stack-up of $MoSi_2$/SiC laminates interspersed with layers of SiC fiber tows, followed by a diffusion bond operation at a relatively benign temperature (~1350°C) in the superplastic flow regime, where the fibers are apt to retain their stability for prolonged periods of time. The vast difference in the CTE between the SiC fibers and the $MoSi_2$ would require precautions while processing to eliminate cracking. As has been demonstrated earlier, the cracking problem could be tackled by adopting a two-pronged approach as follows: (a) lowering the effective CTE of the $MoSi_2$/ SiC laminates through control of the composition, as has been demonstrated elsewhere and (b) use of fine diameter fibers, since the magnitude of the CTE mismatch stresses (and hence cracking) is significantly reduced at fine reinforcement sizes. Fine diameter fibers also have the added advantage of possessing higher strength and hence, better ease in handling and processing operations. Caution should be exercised, however, while applying the principle of superplastic forming to the net shape processing of fiber

reinforced composites, as the nature of the forming process would considerably distort and alter the fiber inter-layer and intra-layer spacings, thereby leading to variations in the material properties, in addition to the likelihood of fiber damage. These challenges could nevertheless be tackled through appropriate reverse-engineering of the fiber layup and forging processes.

The present study also serves as a case-in-point to demonstrate that significant improvements in the high temperature strength can be derived through a proper understanding and control of the matrix microstructure, and that such additional improvements in strength could be obtained without blind recourse to compositing approaches. While it is an undeniable tenet that compositing approaches are necessary in order to impart the strength and toughness required for futuristic materials applications, it is equally imperative that the importance of fundamental microstructural parameters such as the grain size and second phase morphology / distribution, and the effect of artificial / in-situ reinforcements on the above-mentioned microstructural parameters be reemphasized and carefully manipulated in the successful optimization of the microstructural design of such composites, aside from the thermodynamic stability and interface design considerations that govern composite design.
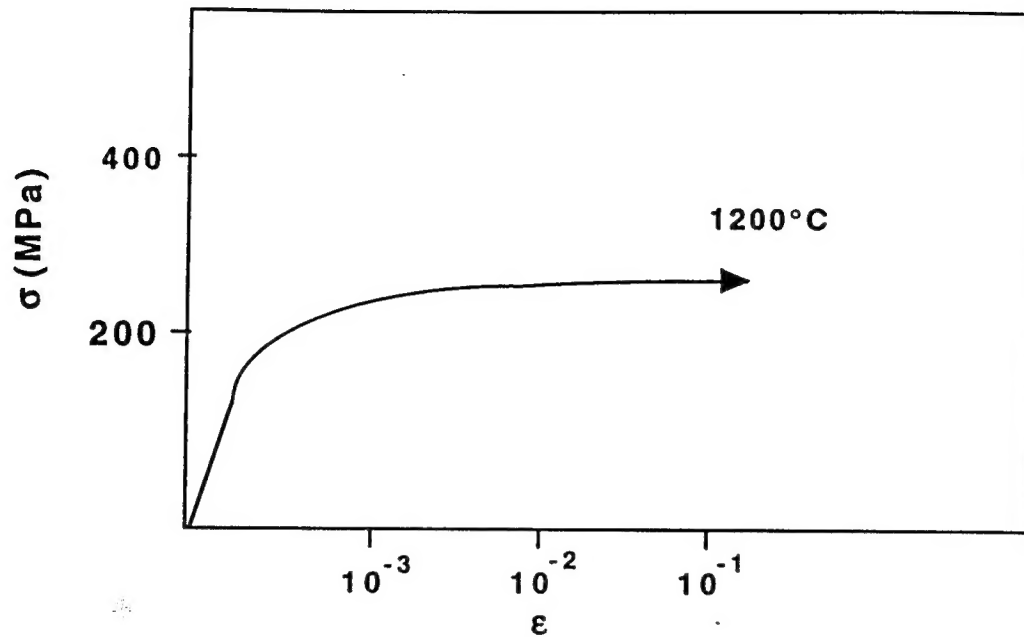
Fig. 1 Stress-strain curve of the outer fiber for ISP and CP materials four point bend tested @T~ 1200°C showing deformation at constant stress.
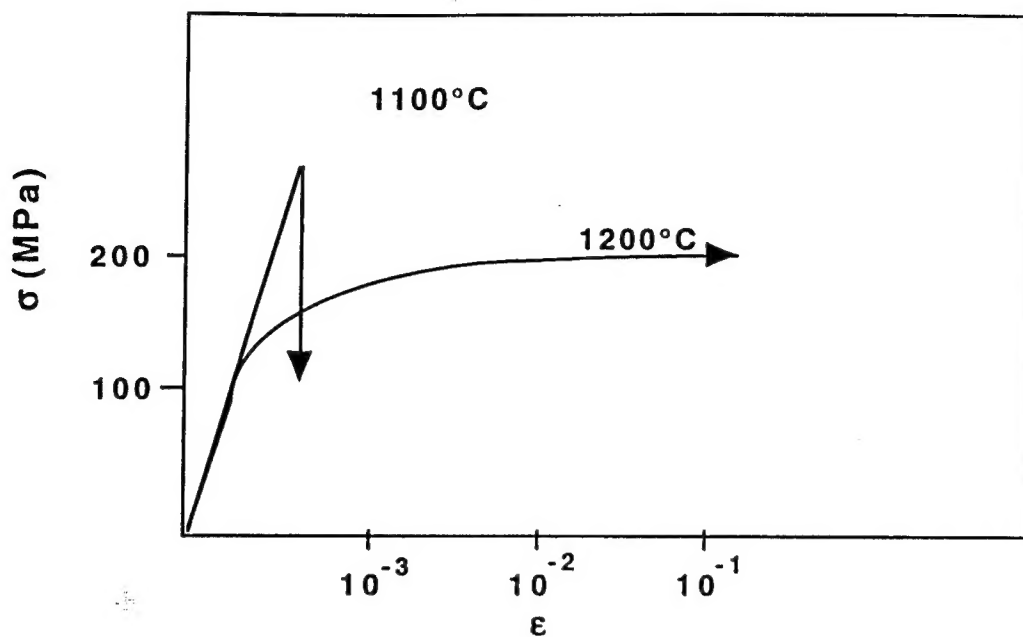
Fig. 1a Schematic stress-strain curves of the outer fiber for four-point bend tested ISP material showing the transition in behavior between 1100°C and 1200°C.
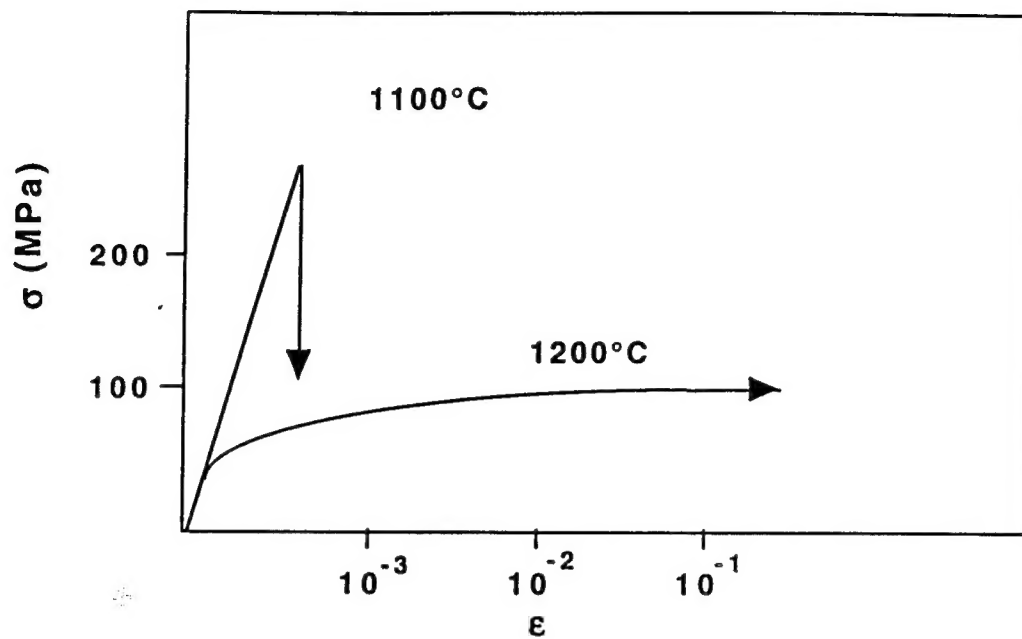
Fig. 1b Schematic stress-strain curves of the outer fiber for four-point bend tested CP material showing the transition in behavior between 1100°C and 1200°C.

Fig.2 Strain rate - Flow Stress Relationship at 1573 K for MoSi2/SiC Composites.